



HAL
open science

Exploring the capability of the LII technique to characterize titanium dioxide nanoparticles in flame synthesis

Junghwa Yi

► **To cite this version:**

Junghwa Yi. Exploring the capability of the LII technique to characterize titanium dioxide nanoparticles in flame synthesis. Fluid mechanics [physics.class-ph]. Université Paris-Saclay, 2023. English. NNT : 2023UPAST035 . tel-04083107v2

HAL Id: tel-04083107

<https://hal.science/tel-04083107v2>

Submitted on 15 May 2023

HAL is a multi-disciplinary open access archive for the deposit and dissemination of scientific research documents, whether they are published or not. The documents may come from teaching and research institutions in France or abroad, or from public or private research centers.

L'archive ouverte pluridisciplinaire **HAL**, est destinée au dépôt et à la diffusion de documents scientifiques de niveau recherche, publiés ou non, émanant des établissements d'enseignement et de recherche français ou étrangers, des laboratoires publics ou privés.

Exploring the capability of the LII technique to characterize titanium dioxide nanoparticles in flame synthesis

*Exploration de la capacité de la technique LII
à caractériser la synthèse de nanoparticules
de dioxyde de titane dans une flamme*

Thèse de doctorat de l'université Paris-Saclay

École doctorale n° 579 : Sciences mécaniques et énergétiques,
matériaux et géosciences (SMEMaG)
Spécialité de doctorat : Combustion
Graduate School : Sciences de l'ingénierie et des systèmes.
Référént : CentraleSupélec

Thèse préparée dans la unité de recherche **Laboratoire EM2C
(Université Paris-Saclay, CNRS, CentraleSupélec)**,
sous la direction de **Benedetta FRANZELLI**, Chargée de recherche,
la co-direction de **Nasser DARABIHA**, Professeur émérite,
le co-encadrement de **Christopher BETRANCOURT**, Maître de Conférences

Thèse soutenue à Gif-sur-Yvette, le 28 mars 2023, par

Junghwa YI

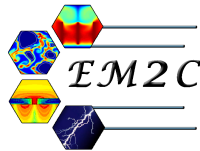
Composition du jury

Kyle Daun Professeur, University of Waterloo, Canada	Rapporteur et Examineur
Silvana De Iuliis Chargée de Recherche, CNR-ICMATE, Milan, Italie	Rapporteuse et Examinatrice
Yann Leconte Directeur du Recherche, DRF/IRAMIS/NIMBE/LEEL, CEA Saclay	Président
Timothy Sipkens Chargé de Recherche, National Research Council, Ottawa, Canada	Examineur

*"Der Vogel kämpft sich aus dem Ei. Das Ei ist die Welt.
Wer geboren werden will, muß eine Welt zerstören."*

— Hermann Hesse, Demian: Die Geschichte von Emil Sinclairs Jugend

Acknowledgements



I would like to express my heartfelt gratitude to everyone who has been a part of this journey to successfully finish my PhD.

I would like to start by thanking the members of the jury for their time, valuable feedback, and constructive critiques during the defense. I am honored to have had the opportunity to defend my work in front of such a distinguished panel. I extend my special thanks to the rapporteurs, Prof. Kyle Daun and Dr. Silvana De Iuliis, for their detailed reports, comments, and exchanges, which significantly improved my research. I would also like to thank Dr. Yann Leconte, who chaired the defense, and Dr. Timothy Sipkens, who attended remotely, for their instructive feedback. Finally, I extend my appreciation to Dr. Gilles Bruneaux and Dr. Alessandro Faccinetto for their presence and high-quality contributions during the defense.

I am also grateful to my advisors, who have been instrumental in guiding and mentoring me throughout my PhD journey. First and foremost, I thank my director and mentor, Dr. Benedetta Franzelli, for her unwavering support, patience, expertise, and energy. She taught me the invaluable knowledge necessary to be a good researcher and always motivated me during the many late nights we spent writing this thesis and other papers together. I also thank Prof. Nasser Darabiha for his guidance and advice throughout my thesis, and Dr. Christopher Betrancourt for his support in perfecting our experiments and helping me with some of the more challenging concepts in LII. Their consistent support and contributions have been invaluable, and I could not have reached this momentous milestone without these amazing advisors.

I cannot forget to thank the permanent staff and technicians in EM2C laboratory for their tireless efforts in creating a conducive environment for research. I am grateful to Prof. Sebastien Decruix and Prof. Choongsik Bae (from KAIST) for their support which afforded me the opportunity to come to France. Special thanks go to Laurent Zimmer and Antoine Renaud, who took care of me during my stay in France for my master's degree. I also extend my appreciation to Gabi-Daniel Stancu, Ronan Vicquelin, Christian Tenaud, Clément Mirat, Aymeric Vie, Sean McGuire, Morgan Chabanon, Benoit Fiorina, Christophe Laux to be always so kind and supportive with me throughout my time in EM2C laboratory. I really want to thank to the EM2C technical staff (Yannick Le Teno, Erika Jean-Bart, Sébastien Turgis, Hubert Jubeau, and Jean-Michel Dupays) for their priceless insights, technical expertise, and support. I would also like to thank the administrative staffs, Brigitte Llobel, Noï Lavaud, and Nathalie Rodriguez, not only for

their administrative proficiency but also for their kindness and thoughtfulness in my daily life in France, as if I were their own Korean daughter.

I am grateful to my colleagues for creating a warm and positive atmosphere that made my journey more enjoyable. Specifically, I am deeply grateful to my drama team members, Victor Boniou and Véranika Latour, for their countless encouragements every night going back to home. I would also like to extend my earnest thanks to Preethi Rajendram Soundararajan for introducing me to the delightful world of Indian cuisine and for her true friendship. Furthermore, I am grateful to Victorien Blanchard, Gilhem Lavabre, Luc Lecointre, Corentin Grimaldi, and Valentin Lechner for engaging in numerous discussions and sharing this special moments with me, which were indispensable in making my PhD life more joyful. Additionally, I would like to thank my ancient lab students, Renaud Gaudron, Claire Beauchesne, David Mercier, Mathieu Roussillo, Thomas Epalle, Hernando Maldonado Colman, Arnaud Gallant, Erwan Pannier and Nicolas Minesi, for their unrequited helps, insightful comments and feedback during my thesis. I am also thankful for the enlightening conversations I have had with Axel Ivaldi, Pierre Mariotto, Maxime Leroy, Ulysse Dubuet (even though I never attended your concert), Olivier Destrian, Maxime Delort-Laval, Artur Carvalho Santos, Marie Truffot, and others. Special thanks go to the students in the coffee office for sharing a cup of Nespresso coffee with me: Yacine Bechane, Tan Phong Luu (and his nice hairstyle), Aurora Maniffa, Yanis Bendali, and Samuel Dillon (the first Aussie in my life). I cannot forget to express my gratitude to SOTUF members: Suzane Pereira, Geoffrey Guy, Yuri Ogata and my lovely co-bureau members, including Karl Topperwien, Gael Parant, Jean Maillard, Alexandre Fougny, and Malo Hustache whose friendship, support, and camaraderie have been essential in motivating my research. Lastly, My appreciation goes to the new members who have joined me on my academic journey including Toufik Khattara, Guillaume Janodet, Cyrine Merhaben, Jean-Baptiste Perrin Terrin, Frédéric Roqué, Mragnak Singh, Julie Ben Zenou, Nicolas Vaysse, Stéphane Wang, Renaud Galbier and Nicolas Gasnier.

Special thanks to Dr. Francesco Saverio Marra and Dr. Fabien Onimus for their presence during my defense. Their presence until the end (even questions!) with great heart and patience was a huge encouragement to me.

I am deeply grateful to my friends and family for their support, love, and understanding throughout my long journey (bac+10...). Their encouragement, especially throughout the difficult times was the driving forces behind this thesis. These include Kewin, Yang, Altynay, Jangmi and my friends from the KAIST Mechanical Engineering 2012 cohort, among so many others. Thank you for keeping me sane and providing a positive and supportive environment.

This project was supported by the European Research Council (ERC) under the European Union's Horizon 2020 research and innovation program (grant agreement No. 757912).

Finally, I want to express my heartfelt gratitude to Constantin Nguyen Van, ma petite fée, for his unwavering support in various forms such as beautifully sliced apples in the morning, lunch boxes, hot dinners, keeping the house clean, correcting all of my French writing, helping me with code and Chemkin, and being there for me on all the nights when I needed someone to say 'it's okay'. His selflessness and generosity have been greatly appreciated and continue to motivate me. I cannot thank him enough for being the best partner and for supporting me throughout my PhD journey. My appreciation for him knows no bounds.

Résumé

Le marché global des nanoparticules représente une production de 11 millions de tonnes par an d'après la Commission européenne. Parmi les différentes méthodes de production, la synthèse de celles-ci dans des flammes est considérée comme une technologie très prometteuse permettant un contrôle fin des caractéristiques des particules produites. Dans ce contexte, l'objectif de ce travail est de développer des diagnostics d'optiques permettant l'étude de l'évolution spatiale des caractéristiques d'une population de particules de TiO_2 produites le long de la flamme ; cela, afin, à la fois de mieux comprendre leur mécanisme de formation, et de créer une base de données pour le développement de modèles numériques. Tout d'abord, l'émission induite par laser (LIE) de nanoparticules de dioxyde de titane (TiO_2) est étudiée pour montrer la faisabilité de la technique d'incandescence induite par laser (LII) sur celles-ci. Cette technique permet de caractériser de façon quasi-non intrusive la fraction volumique des particules f_v et la taille de particules primaire. Elle est classiquement utilisée pour la caractérisation in-situ de la formation de suies dans les flammes, mais sa faisabilité sur de nanoparticules de TiO_2 reste encore à démontrer. Dans le cas où elle le serait, elle pourrait fournir de nouvelles informations sur le processus de synthèse des oxydes métalliques dans les flammes spray et permettre ainsi une description spatiale de la production de nanoparticules de TiO_2 .

Pour vérifier la faisabilité de la technique LII, on considère à la fois des nanoparticules de TiO_2 de haute pureté et des nanoparticules de TiO_2 générées par une flamme d'hydrogène en utilisant deux systèmes de génération de particules : l'un injecte directement des particules dans un milieu non réactif et l'autre synthétise les particules via un milieu réactif. Pour ce dernier, une version inspirée du brûleur de Yale est utilisée. Elle permet la stabilisation de flamme de diffusion pré-vaporisée d'isopropoxyde de titane (TTIP)/ H_2 /Ar. Dans les deux systèmes, les particules sont irradiées à l'aide d'un laser de type top-hat dans la gamme UV, assurant ainsi l'absorption et le chauffage des particules. Un système de détection équipé d'un spectromètre et d'un tube photomultiplicateur (PMT) est également utilisé pour identifier les caractéristiques spectrales et temporelles de LIE des nanoparticules de TiO_2 . Différentes fluences du laser et durées d'acquisition sont prises en compte pour observer les différentes contributions du signal provenant des nanoparticules TiO_2 . La nature du signal est étudiée en la comparant aux résultats théoriques et à des résultats de référence obtenus à partir de nanoparticules de noir de carbone. Plus précisément, l'émission induite par laser des nanoparticules de TiO_2 présente des composantes non-LII pendant les 100 premières nanosecondes après l'interaction avec le laser. A faible fluence laser, le signal peut être interprété comme une fluorescence induite par laser (LIF). Pour une fluence laser élevée, la spectroscopie par claquage induit par laser sélectif en phase

(PS-LIBS) peut se produire en raison d'une éventuelle vaporisation de la surface des particules. Comme les signaux LIF et PS-LIBS sont caractérisés par une courte durée de vie, une acquisition retardée est envisagée pour éviter ces interférences. La nature LII du signal d'émission décalée dans le temps est démontrée premièrement, en confirmant le comportement spectral d'un corps noir. Deuxièmement, l'évolution temporelle du taux de décroissance du signal et de la température inverse est analysée et confirme un comportement du type LII. Dans les configurations considérées, une présence de carbone sur les nanoparticules de TiO_2 est peu probable. De ce fait, la contribution de matériaux carbonés au signal LII peut être supposée négligeable, démontrant ainsi la faisabilité de la technique LII pour des particules de TiO_2 .

Ensuite, une caractérisation quantitative de la production de nanoparticules de TiO_2 dans des flammes a été réalisée. Pour cela, le signal LII est converti en fraction de volume f_v . Cela nécessite donc la connaissance de la température effective T_{eff} atteinte par les particules pendant l'irradiation du laser et de la fonction d'absorption $E(m_\lambda)$. Les deux grandeurs étant fortement liées, il est nécessaire de disposer d'une information sur l'une pour estimer la deuxième. Cependant, une grande variabilité caractérise les données de la littérature pour la fonction $E(m_\lambda)$ pour le TiO_2 , dont les propriétés optiques dépendent fortement des caractéristiques des particules telles que leur géométrie, la structure cristalline et l'état de la matière. Afin de répondre à cette problématique, une nouvelle approche pour estimer la forme spectrale de la fonction d'absorption est proposée à partir des mesures LII. Cette méthode est d'abord validée pour les nanoparticules de noir de carbone pour lesquelles des données sont disponibles dans la littérature. Elle est ensuite appliquée aux nanoparticules de TiO_2 de haute pureté et de TiO_2 synthétisées via la flamme. Une fois l'information sur $E(m_\lambda)$ disponible, la température effective des particules peut être déduite. Enfin, les effets de la distribution spatiale de la température effective et de la fonction d'absorption sur la mesure de la fraction volumique de TiO_2 dans notre flamme de référence ont été étudiés. Les résultats issus des mesures sont comparés à ceux issus d'une simulation numérique représentative de l'état-de-l'art sur le sujet en termes de modélisation. Les comparaisons des champs de f_v normalisés fournissent une première indication pour l'amélioration des modèles numériques.

Abstract

The global market for nanoparticles represents a production of 11 million tons per year according to the European Commission. Among different production methods, flame synthesis is considered a promising technology for producing nanoparticles with fine control over their characteristics. In this context, the goal of this thesis is to develop optical diagnostics to study the spatial evolution of characteristics of a population of TiO_2 particles produced along the flame, in order to better understand their formation mechanism and create a database for the development of numerical models. First, laser-induced emission (LIE) of titanium dioxide (TiO_2) nanoparticles is studied to demonstrate the feasibility of laser-induced incandescence (LII) technique on these particles. LII is a quasi-non-intrusive technique that characterizes the volume fraction of particles (f_v) and primary particle size. It is traditionally used for in-situ characterization of soot formation in flames, but its feasibility on TiO_2 nanoparticles remains to be demonstrated. If feasible, it could provide new insights into the synthesis process of metal oxide nanoparticles in spray flames and thus allow a spatial description of the production of TiO_2 nanoparticles.

To verify the feasibility of the LII technique, both high-purity TiO_2 nanoparticles and hydrogen flame-generated TiO_2 nanoparticles are considered using two particle-generation systems: the first directly injects particles into a non-reactive environment, and the second synthesizes particles via a reactive environment. The latter applies a new version of the Yale diffusion burner that stabilizes the pre-vaporized diffusion flame of titanium isopropoxide (TTIP)/ H_2 /Ar. In both systems, the particles are irradiated with a top-hat laser in the UV range, thus ensuring absorption and heating of the particles. A detection system equipped with a spectrometer and a photomultiplier tube (PMT) is also used to identify the spectral and temporal characteristics of the LIE of the TiO_2 nanoparticles. Different laser fluences and acquisition times are considered to observe the different signal contributions from the nanoparticles. The nature of the signal is investigated by comparing it to theoretical results and reference results obtained from carbon black nanoparticles.

Specially, the laser-induced emission of TiO_2 nanoparticles exhibits non-LII components during the first 100 nanoseconds after the laser interaction. At low laser fluence, these features can be interpreted as laser-induced fluorescence (LIF). With high laser fluence, phase-selective laser-induced breakdown spectroscopy (PS-LIBS) can occur due to possible surface vaporization of the particles. As LIF and PS-LIBS signals are characterized by a short lifetime, delayed acquisition is considered to avoid these interferences. The LII nature of the temporally delayed emission signal is demonstrated first by confirming the spectral behavior of a black body. Secondly, the temporal evolution of the signal decay rate and the inverse temperature is analyzed and

confirms as an LII-type behavior. In the considered configurations, the presence of carbon on the nanoparticles of TiO_2 is unlikely. Therefore, the contribution of carbonaceous materials to the LII signal can be assumed negligible, thus demonstrating the feasibility of the LII technique for TiO_2 nanoparticles.

Next, a quantitative characterization of the production of titanium dioxide nanoparticles in flames is carried out. For this, the LII signal is converted into a volume fraction f_v , which requires the knowledge of the effective temperature T_{eff} reached by the particles during the laser irradiation and of the absorption function $E(m_\lambda)$. Since these two quantities are strongly related, it is necessary to have information on one in order to estimate the other. However, there is a large variability in the literature data for the absorption function $E(m_\lambda)$ for TiO_2 , whose optical properties strongly depend on particle characteristics such as geometry, crystalline structure, and state of matter. To address this issue, a new approach to estimate the spectral dependence of the absorption function is proposed from LII measurements. This method is first validated for carbon black nanoparticles, for which data are available in the literature. It is then applied to high-purity and flame-synthesized TiO_2 nanoparticles. Once the information on $E(m_\lambda)$ is available, the effective temperature of the particles can be deduced. Finally, the spatial distribution effects of the effective temperature and the absorption function on the measurement of the volume fraction of TiO_2 in our reference flame are studied. The results of the measurements are compared to those from a numerical simulation representative of state-of-the-art modeling. The comparisons of normalized f_v fields provide a first indication for improving numerical models.

Contents

Résumé	vii
Abstract	ix
Introduction	1
I Nanoparticle synthesis and characterization	7
1 Nanoparticles	9
1.1 Definition	10
1.2 Properties and applications	11
1.3 Manufacturing methods	15
1.3.1 Liquid phase process	17
1.3.2 Gas phase process	18
1.4 Titanium dioxide	26
1.4.1 Crystal phase	26
1.4.2 Key features and applications	27
1.4.3 Laboratory-scale TiO ₂ synthesis in flame reactor	29
1.4.4 Industrial manufacturing processes of TiO ₂	29
1.5 Conclusion	30
2 Nanoparticle formation process in flame synthesis	31
2.1 Terminology	32
2.2 Nanoparticle production processes	35
2.2.1 Nucleation	35
2.2.2 Surface growth	35
2.2.3 Coagulation	36
2.2.4 Sintering	36
2.3 Conclusion	37
3 Techniques for the characterization of nanoparticle morphology and composition	39
3.1 Ex-situ methods	40

3.1.1	Scanning electron microscopy (SEM) and transmission electron microscopy (TEM)	40
3.1.2	X-ray diffraction (XRD)	42
3.1.3	Brunauer–Emmet–Teller (BET)	43
3.2	On-line methods	44
3.3	In-situ methods	45
3.3.1	Elastic light scattering	45
3.3.2	Raman spectroscopy (RS)	47
3.3.3	Small-angle x-ray scattering (SAXS)	48
3.3.4	Laser-induced fluorescence (LIF)	49
3.3.5	Laser-induced breakdown spectroscopy (LIBS)	51
3.3.6	Laser-induced incandescence (LII)	51
3.4	Conclusion	52
 II Characterization of the Laser-Induced Emission of TiO₂ nanoparticles: Feasibility of Laser-Induced Incandescence		55
4	Laser-Induced emission (LIE) of TiO₂	57
4.1	Laser-induced Fluorescence (LIF)	58
4.1.1	Effect of experimental parameters on LIF of TiO ₂	60
4.2	Laser-induced breakdown spectroscopy (LIBS)	65
4.2.1	Phase-selective laser-induced breakdown spectroscopy on TiO ₂	66
4.3	Laser-induced incandescence (LII)	69
4.3.1	Basics on LII	69
4.3.2	LII signal and volume fraction	71
4.3.3	Information on particle size distribution	74
4.3.4	Challenges of laser-induced incandescence on TiO ₂	75
4.4	Conclusion	81
5	Characterization of the LIE of TiO₂ nanoparticles in a non-reactive environment	83
5.1	Strategy to analyze LIE	84
5.1.1	LII theory	85
5.2	Experimental set-up	88
5.2.1	Particle dispersion	88
5.2.2	Laser setting	90
5.2.3	Signal detection	90
5.3	Results and discussion	92
5.3.1	General characteristics and comparison with carbon black	92
5.3.1.1	Spectral analysis	93
5.3.1.2	Temporal evolution	95
5.3.2	Characterization of prompt LIE from TiO ₂	96
5.3.3	LII nature of delayed LIE from TiO ₂	99
5.4	Conclusion	105

6	Characterization of the LIE of TiO₂ nanoparticles in a reactive environment	107
6.1	Experimental set-up	107
6.1.1	Yale diffusion burner (YDB)	107
6.1.2	Pre-vaporization system	108
6.1.3	Flame configuration	109
6.2	Results	111
6.2.1	General characteristics	112
6.2.1.1	Spectral emission	112
6.2.1.2	Temporal emissions	113
6.2.2	Characterization of prompt LIE from flame-generated TiO ₂	115
6.2.3	LII nature of delayed LIE from flame-generated TiO ₂ nanoparticles	118
6.3	Discussion and conclusion	121
 III Towards quantitative characterization of TiO₂ production in flames based on LII measurements		129
7	Methodology for quantifying spectral properties of absorption function $E(m_\lambda)$	131
7.1	Determining the spectral form of $E(m_\lambda)$	131
7.1.1	Post-processing procedure	134
7.1.2	Results	137
7.1.2.1	Feasibility on carbon black particles in non-reactive environment	137
7.1.2.2	Application to TiO ₂ nanoparticles in non-reactive environment	141
7.1.2.3	Application to flame-synthesized TiO ₂ nanoparticles	143
7.2	Derivation of the absolute value of $E(m_\lambda)$	146
7.2.1	Assuming spectrally-constant $E(m)$	147
7.2.2	Assuming spectrally-variable $E(m_\lambda)$	151
7.3	Conclusion	157
8	On the dependence of absorption function $E(m_\lambda)$ and effective temperature T_{eff} in analyzing TiO₂ nanoparticles volume fraction in flame synthesis	159
8.1	Set-up	160
8.1.1	Experimental set-up for 2D spatial distribution	160
8.1.2	Numerical simulation	164
8.2	Spatially-constant effective temperature and $E(m_{\lambda_{em}})$	166
8.3	Spatially-constant $E(m_{\lambda_{em}})$ and non-uniform effective temperature	168
8.3.1	Spatial evolution of effective temperature	169
8.3.2	Spatial evolution of f_v^*	174
8.4	Non-uniform $E(m_{\lambda_{em}})$ and non-uniform effective temperature	176
8.4.1	Spatially non-uniform absorption function	176
8.4.2	Spatial evolution of f_v^*	178
8.5	Conclusion	180

Conclusion	183
A Industrial manufacturing process of TiO₂	187
A.1 Sulfate process	187
A.2 Chloride process	187
B LII modeling process	189
B.1 Important parameters in LII model	189
B.2 Heat transfer model	190
B.2.1 Absorption	191
B.2.2 Conduction	191
B.2.3 Vaporization	193
B.2.4 Thermal radiation	194
C Flame structure parametric study	195
D Characterization of prompt/delayed LIE from flame-generated TiO₂	197
References	227

List of Tables

1.1	Differences between the furnace reactor and spray flame pyrolysis.	25
1.2	Properties of anatase, rutile, and brookite. For the refractive index, values are given for the three coordinate axes in the order of least, intermediate, and greatest index (for brookite) [108, 112]. For the lattice parameter, see Fig. 1.16 for the coordination.	27
2.1	Overview of aerosol growth processes with their effect on each design parameter. d_{pp} is the primary particle diameter, n_{pp} the number of primary particles in an aggregate, D_f fractal dimension, S total surface concentration, N total number concentration, number density, and f_v volume fraction. The symbol + signifies a favorable effect, - a decrease in that stage, = same level as previous steps or invariant in that stage, +/- depending on the operating condition. . . .	37
3.1	Summary of the measurable parameters with various experimental techniques. .	53
4.1	List of studies of Phase-selective Laser-induced breakdown Spectroscopy (PS-LIBS) and Laser-induced Breakdown Spectroscopy (LIBS) on TiO_2	68
4.2	Properties of carbon black and TiO_2 nanoparticles.	75
5.1	Characteristics of the laser-induced emissions of TiO_2 nanoparticles in terms of operating fluence range, and characteristics time (at 1 atm)	85
5.2	Detectable LIE signals with our detection system for different laser wavelengths for carbon black and pure TiO_2 nanoparticles.	92
6.1	Operating conditions for the preheated hydrogen and precursor (TTIP) coflow flame. The inflow velocity is 1.9 m/s, and the coflow velocity is 0.55 m/s in high-temperature conditions.	110
7.1	T_{min} and T_{max} and corresponding $E(m)$ at 355 nm ($= E(m_{\lambda_{laser}})$) at three acquisition delay times for carbon black, high-purity TiO_2 and flame-generated TiO_2 nanoparticles. When the maximum estimated temperature is higher than the sublimation (or boiling) temperature, the sublimation (or boiling) temperature was selected for the calculation.	152

- 8.1 Effective temperature of the flame-generated TiO_2 nanoparticles at three flame heights (HAB = 30, 45, 60 mm) calculated with the two-color pyrometry at 650 nm and 710 nm. Four different values of $\frac{E(m_{710nm})}{E(m_{650nm})}$ are considered corresponding to: constant $E(m)$, minimum and maximum $E(m_\lambda)$ function obtained in Chap. 7, $E(m_\lambda)$ from Liu et al. [285]. The temperatures at prompt and at 100 ns are calculated using prompt and time-delayed LIE signals. 170

List of Figures

1	The Solar Keyboard Folio with the solar panels on the bottom, which can charge from ambient light. Image from Sarah Tew/CNET.	1
1.1	Schematic representation of various nanomaterials, adapted from [5].	10
1.2	Examples for 0D, 1D, 2D, and 3D nanostructures [38].	11
1.3	Different colors of gold nanoparticles with potential applications in biomedicine. (a) Gold nanorods, (b) silica–gold core-shell nanoparticles, and (c) gold nanocages [45].	12
1.4	Configuration of gas sensors with two electrodes [57].	14
1.5	Nanoparticle production strategy: Top-down and bottom-up process.	15
1.6	TEM images (top) and illustrations of the corresponding crystal forms (bottom) of various shapes of ZnMgO nanoparticles produced by chemical vapor deposition (a), metal combustion (aerosol process) (b), and sol-gel method (c). Zn is highlighted by green color, MgO is colored in blue, and light blue for ZnMgO in the illustration [63].	16
1.7	Schematic drawing of the sol-gel process for ceramic materials, adapted from [70].	17
1.8	SHYMAN’s continuous hydrothermal apparatus, (1) autoclave, (2) mixing zone, (3) formulation stage [49].	18
1.9	Schematic drawing of arc discharge particle formation process [73].	19
1.10	Schematic drawing of laser ablation particle formation process [76].	20
1.11	Schematic drawing of chemical vapor deposition by hot-wall heating, adapted from [80].	20
1.12	Schematic drawing of particle formation pathways during the aerosol synthesis [90].	22
1.13	Flame spray pyrolysis: a spray jet is introduced into the flame through a two-phase nozzle, supported by pilot flamelets on the face of the burner to ensure stable combustion. A flame is generated from the main jet, where particle formation takes place by nucleation, coagulation, and coalescence or agglomeration (left side). The formation of different particle configurations via the gas-to-particle mechanism for single and multicomponent systems is illustrated at the right side [93, 36].	23

1.14	Illustration of the typical aerosol reactor in (a) furnace [100] and (b) spray flame pyrolysis [101]. In the aerosol reactor in the furnace, the gas-to-particle transition occurs inside a high-temperature furnace heated by a heating source. In spray flame pyrolysis, the flame itself is both a heating source and the particle formation zone at the same time.	25
1.15	Three crystal forms of titanium dioxide in nature [111].	26
1.16	Three-dimensional representation of crystal structures of TiO ₂ rutile, brookite, and anatase polymorphs [109]. Ti atoms are represented in round blue balls, and O is described in red point.	27
1.17	The mechanism of semiconductors acting as photocatalysts. Typical oxidation and reduction reactions are shown. Oxidation of water by an electron-hole forms hydroxyl radicals OH·, which are powerful oxidizing agents.	28
2.1	Schematic of particle formation in a flame [136].	31
2.2	Processes by which colliding particles join together. Each particle is illustrated as a spherical monomer for ease of description, but it could also apply to the collision between two aggregates/agglomerates	32
2.3	Overview of the evolution of aerosol growth. d_{pp} is the primary particle diameter, d_c is the collision diameter. Adapted from [78].	33
2.4	Evolution of aggregate mobility d_m and primary particle diameter d_{pp} during sintering of aggregates. Adapted from [141].	34
3.1	TEM images of the carbon-coated TiO ₂ particles generated in H ₂ /O ₂ /Ar multiple diffusion flame with TTIP precursor in a carrier gas C ₂ H ₄ are shown [134]. The presence of C ₂ H ₄ in the flame promotes the formation of carbon coating around the TiO ₂ particles. (a) The growth of a spherical carbon-coated TiO ₂ particle is observed. (b) A uniform carbon coating is observed around TiO ₂ particles, with a high-resolution TEM (HRTEM) image of the carbon coating (3 – 5 nm) shown in the bottom-right inset. (c) The growth of two TiO ₂ particles from the same experimental run is shown, where one is coated with carbon and the other is not coated. (d) A HRTEM image shows that the coated particle is crystalline (left) while the other particle is amorphous (right) without the carbon coating.	40
3.2	X-ray diffraction (XRD) patterns of TiO ₂ nanoparticles synthesized in a curved wall-jet burner with C ₂ H ₄ /Air premixed flame at different equivalence ratios (ϕ). The peaks labeled as A and R correspond to the anatase and rutile phases of TiO ₂ , respectively. As seen in the figure, at high ϕ values, only the anatase phase is detected, while as the ϕ value decreases, the rutile phase appears. The intensity ratio of the anatase and rutile peaks is often used as an indicator of the crystallinity of the synthesized TiO ₂ nanoparticles. [160].	42
3.3	BET specific surface area (m ² /g) of spray flame-made silica from HMDSO/ethanol mixture (0.1 molar ratio) as a function of air and oxygen volumetric flow rates [132].	43
3.4	Light scattering regimes as a function of the wavelength and particle radius [179].	45

-
- 3.5 (a) The measured scattering intensity at 90° (I_{90}) as a function of axial distance (dashed line with a solid inverted triangle). The mean particle diameter determined by TEM imaging is also shown (dashed line with open square). The calculated normalized particle number concentration N' assuming Rayleigh scattering as intensity $\propto Nd_{pp}^6$ (dotted line with open circle) is compared to that using monodisperse coagulation theory [183] (solid line with solid circle) [178]. (b) Normalized scattering intensity (I/I_0) as a function of the scattering wave vector (q) at different axial positions X (mm) from the burner outlet. Calculated R_g and D_f are shown inside the legend. 46
- 3.6 In-situ Raman spectra of TiO_2 nanoparticles synthesized by low-pressure axisymmetric, stagnation premixed flame at different distances from the substrate (0 mm) along the axial centerline [187]. The burner exit is located at 40 mm. Known modes for Anatase is marked in "A". Gas-phase temperature was measured by LIF on OH. The figure shows the anatase (A) content of the nanoparticles increases as they approach the substrate. 47
- 3.7 Scattered intensity as a function of the scattering vector q measured in-situ for silica nanoparticles produced by a premixed flame at $\text{HAB} = 40$ mm [198]. The circles represent the measured scattered intensity. The global unified fit (gray) is shown with component curves such as the Porod regime for primary particles (solid black line), the Guinier regime for primary particles (dash-dotted line), and aggregates (dash-double dotted line). The appearance of a weak power-law regime (dashed line) indicates that these particles are mass fractal. 49
- 3.8 Spatial profiles of TiO number density for various flame equivalence ratios, with a constant total flow rate of H_2 and O_2 in low pressure stagnation flow flame. Adapted from [205]. 50
- 4.1 Schematic demonstrating the typical progression of the LIF, LII and LIBS signals and particle temperature as a function of the laser fluence, adapted from [12]. 57
- 4.2 Partial energy-level diagram for a fluorescent (photoluminescent) molecule, often called a Jablonski diagram [203]. 59
- 4.3 Absorption and LIF emission of anatase TiO_2 particles at two excitation wavelengths (250 and 364.6 nm) [236]. 60
- 4.4 Time-resolved LIF spectra of rutile TiO_2 monitored at 820 nm and 77 K. The excitation wavelengths are 300, 333, 360, and 390 nm with a duration of $\sim 2 \mu\text{s}$ [237]. 61
- 4.5 (a) Low-temperature LIF emission spectra of pure TiO_2 film in the temperature range of 9–300 K. A five-peak fit of the LIF spectra with the temperature of (b) 9 K, (c) 100 K, (d) 200 K, and (e) 300 K. Note that the inset (f) shows the temperature dependence of the corresponding peak/shoulder positions. Broadening shoulders are indicated by the symbol asterisk (*). Adapted from [238]. 62

4.6	LIF spectra of commercial TiO ₂ of different crystalline structures. (a) A 325 nm He-Cd laser was used for excitation in an ambient air environment. (1) anatase, (2) Anatase that was calcined at 900 °C for 6 h, (3) anatase that was calcined at 1200 °C for 24 h, and (4) rutile [240]. (b) A 355 nm laser was used for excitation in an aqueous solution. (1) anatase (Merck), (2) anatase (Ishihara Co., ST11), (3) rutile (Ishihara Co., CR-EL), (4) rutile (Toho Titanium Co., NS51) [241]. . .	63
4.7	Absorption and fluorescence spectra of colloidal TiO ₂ particles: (a) specimen A (TiO ₂ concentration 0.015 g/L), (b) specimen B (TiO ₂ concentration 0.015 g/L), and (c) specimen C (TiO ₂ concentration 0.3 g/L). The excitation wavelength at 270 nm [244].	64
4.8	(a) Schematic illustration of the temporal variation of laser pulse irradiation and plasma behavior [246], (b) Schematic illustration of the emission spectra of the laser-induced plasma for different time delays with respect to the irradiation of the laser pulse [217].	65
4.9	Comparison between the two-dimensional resonance-enhanced PS-LIBS snapshots (up) and the simulated particle volume fraction (bottom) in the laminar flame [255].	66
4.10	(a) Ti atomic emission. Emissions from Ti I are colored in black and emissions from Ti II are colored in blue. (b) O atomic emission. Emissions from O I are colored in black and emissions from O II are colored in blue [258].	67
4.11	Scattering efficiency of TiO ₂ clusters with 532 nm laser excitation (black squares) and atomic emission intensity of titanium at 498.17 nm with 532 nm laser (blue triangles) and 1064 nm laser excitation (red circles) at different laser intensities. The inset shows the comparison of scattering signals of clusters (black squares) and gases (green circles) with 532 nm laser excitation [259].	68
4.12	Typical fluence dependence of the maximum LII (left) and temperature (right) of soot particles generated in ethylene/air laminar diffusion flame. LII signal is recorded at 681.8 nm and the laser wavelength of 532 nm was used [267]. . . .	71
4.13	Absorption function $E(m_\lambda)$ of (a) carbonaceous particles [287, 288, 289, 290, 291, 292, 293, 294, 295, 296] and (b) TiO ₂ nanoparticles (in log scale) [285, 286, 297, 214]. Liu et al. [148] synthesized nanofilms by mist chemical vapor deposition using TTIP and annealing to transform anatase to rutile. Jellison et al. [286] generated TiO ₂ nanofilms by RF magnetron sputter deposition. Siefke et al. [297] used atomic layer deposition with TTIP at a deposition temperature of 100 °C to create nanofilms. De Iuliis et al. [214] measured the extinction coefficient (ex-situ) for flame-synthesized nanoparticles	76
4.14	Temporal profiles of laser-induced emission of soot particles in the methane diffusion flame, adapted from [305]. Blue triangles represent the total laser-induced emission from soot particles using a 532 nm laser. The red round points indicate the laser-induced incandescence signal from soot particles using a 1064 nm laser. The black dotted line shows the subtracted part between blue and red points, signifying the LIF part from the PAH species of the flame.	77

4.15	Ratio of liquid and solid phase $E(m_\lambda)$. Si and Fe from [12]; solid Au, Ag, and Ni from [12] and liquid Au, Ag and Ni from [26]; Al, Cu from [26]; Al_2O_3 from [315].	79
4.16	Laser-induced light emission under different laser fluences at HAB = 2 cm in TiO_2 nanoparticle flame spray synthesis at prompt detection timing, adapted from [215]. C_2 and C_3 bands from [312].	80
5.1	Schematic of the particle phase information related to the temperature (top) and to the LIE characteristic emission duration (bottom) as a function of the typical fluence range of different LIE signals.	84
5.2	Effect of the temperature on LII emission spectra $S_{LII}(\lambda_{em}, T_p(t))$, normalized by maximum value between 400-700 nm.	86
5.3	Schematic presentation of the experimental set-up developed to investigate the laser-induced emission from TiO_2 nanoparticle-laden aerosol using a pulse YAG laser at 355 nm with a top-hat spatial profile (bottom-right). The laser profile is captured in 500 individual shots, and the resulting images are averaged to create a top-hat image.	88
5.4	Microscopy image of commercial nanoparticles used in this study. (a) SEM image of carbon black nanoparticle. (b) TEM image of TiO_2 nanoparticles (provided by nanografi).	89
5.5	Histogram of laser fluence viewed by the detection optics across the laser beam.	90
5.6	Calibration function for spectral detection via spectrometer.	91
5.7	Effect of laser fluence F on laser-induced emission spectra at prompt for (a) carbon black and (b) TiO_2 nanoparticles. The temperature in the legend for carbon black particles is obtained from the spectrum fitting of the Planck function. Spectra are normalized by the value at 650 nm, except for the case of TiO_2 $F = 0.06 J/cm^2$ and $F = 0.10 J/cm^2$, whose normalization is based on the maximum value at 470 nm for visualization purpose.	93
5.8	Temporal evolution of laser-induced emission of (a) carbon black and (b) TiO_2 nanoparticles at 450 ± 10 nm detection wavelength. Each profile is normalized by its maximum value.	95
5.9	Emission spectra of TiO_2 nanoparticles at prompt under laser fluence $F = 0.06 J/cm^2$ (black round points). The LIF emission spectra (square and start symbol) are from gaussian fitted spectra (green dashed line from Paul et al. [335], red dotted lines from Santara et al. [243]).	97
5.10	Normalized emission spectra of TiO_2 for $F = 0.19 J/cm^2$ with (a) gaussian fit of band emission of LIF from literature [236, 244, 243, 238, 335, 336] and (b) Ti and O atomic emissions from NIST [258] corresponding to peak location of emission spectra. The intensities of each transition are adapted for a clear view with the curve, not expressing the relative intensities.	98

5.11	Effect of gate delay (gate width = 20 ns) on emission spectra of laser-induced emissions of (a,c,e) carbon black nanoparticles and (b,d,f) rutile TiO ₂ nanoparticles. The temperature given inside the legend for carbon black particles is from spectrum fitting. Spectra are normalized with the value of the spectrum at 650 nm.	100
5.12	Normalized temporal evolution of carbon black nanoparticles at different laser fluences at detection wavelengths of (a) 450± 10 nm, (b) 570± 10 nm, (c) 640± 10 nm and (d) 710 ± 10 nm. All profiles are normalized with the value of the signal at 100 ns.	101
5.13	Normalized temporal evolution of high-purity TiO ₂ nanoparticles at different laser fluences at detection wavelengths of (a) 450 ± 10, (b) 550 ± 10, (c) 650 ± 10 and (d) 710 ± 10 nm. All profiles are normalized with the value of the signal at 100 ns.	102
5.14	Decay characteristic times of LIE signal for (a) carbon black and (b) TiO ₂ as a function of detection wavelength. The R^2 value inside the legend represents the coefficient of determination for the fitting procedure. The dotted lines are the results of the linear fitting.	103
5.15	Time evolution of ΔT^{-1} of carbon black nanoparticles LIE for three laser fluences at (a) $F = 0.06$, (b) $F = 0.12$ and (c) $F = 0.23$ J/cm ²	104
5.16	Time evolution of ΔT^{-1} of pure TiO ₂ nanoparticles LIE for three laser fluences at (a) $F = 0.19$ and (b) $F = 0.24$ J/cm ²	104
6.1	Schematic of the burner configuration, D_i is the inner tube diameter, D_o is the coflow diameter [337].	108
6.2	(a) Injection system of liquid precursor. (b) Schematic of the vaporization system.	109
6.3	Picture of targeting diffusion coflow argon-diluted hydrogen flames before (a) and after (b) injecting TTIP precursor. The camera exposition is adapted for better visualization for each figure. (c) Schematic illustration of H ₂ /Ar/TTIP flame.	110
6.4	Effect of laser fluence on laser-induced emission spectra of TiO ₂ nanoparticles at HAB = 45 mm. Measurements are done at prompt, i.e., at peak signal. Spectra are normalized with the value of 650 nm for each curve with different fluence.	112
6.5	Temporal evolution of laser-induced emission of flame-synthesized TiO ₂ nanoparticles at HAB= 45 mm, detected at 500 ±10 nm. Each signal is normalized by its maximum value.	113
6.6	Temporal evolution of laser-induced emission of flame-synthesized TiO ₂ nanoparticles at (a) $F = 0.06$ J/cm ² and (b) $F = 0.24$ J/cm ² detected at 450 ±10 nm and 710 ±10 nm. Each graph is normalized by its maximum value. The change of decay mode is expressed with arrows.	114
6.7	Emission spectrum of flame-generated TiO ₂ at prompt under laser fluence $F = 0.24$ J/cm ² , normalized by the value of 650 nm of each curve. The C ₂ and C ₃ bands are from [356].	115

- 6.8 Normalized emission spectra of flame-generated TiO_2 nanoparticles at prompt under laser fluence of $F = 0.24 \text{ J/cm}^2$ with (a) Gaussian fit of sub-band emissions (peak location μ and $\pm\sigma$) of the LIF from literature [236, 336, 335, 238, 243, 244] and (b) Ti and O atomic emission from NIST [258] corresponding to peak location of emission spectra. The intensities of each transition are adapted for a clear view with curve, not expressing the relative intensities. The curves are normalized by its value at 650 nm. 117
- 6.9 Effect of gate delay (gate width =20 ns) on emission spectra of laser-induced emission of TiO_2 particles in flame synthesis at HAB = 45 mm. Laser fluence $F = 0.15 \text{ J/cm}^2$ was applied. Spectra are normalized with the value of each curve at 650 nm. 118
- 6.10 Normalized time evolution of flame-generated TiO_2 nanoparticles at HAB=45mm at different laser fluences at a detection wavelength of (a) $650 \pm 10 \text{ nm}$ and (b) $710 \pm 10 \text{ nm}$. All graphs are normalized with the value of each curve at 100 ns. The reverse tendency between $F = 0.15 \text{ J/cm}^2$ and 0.19 J/cm^2 in (b) is from the normalization process. 119
- 6.11 Decay characteristic time τ of LIE signal at HAB = 45 mm at $F = 0.15 \text{ J/cm}^2$. To determine τ , the LIE signals between 100 ns - 400 ns after the peak signal have been fitted using a log function. The R^2 value inside the legend represents the coefficient of determination for the fitting procedure. The dashed lines are the results of the linear fitting. 120
- 6.12 Evolution of ΔT^{-1} with of flame-synthesized TiO_2 nanoparticles LIE for two wavelengths for $F = 0.15 \text{ J/cm}^2$ at HAB = 45mm. 120
- 6.13 Flame emission intensity as a function of wavelength at different heights above the burner. 121
- 6.14 Emission spectra of TiO_2 nanoparticles from the optical cell (non-reactive, white square) and flames (reactive, at HAB= 45mm, green triangle symbol) at prompt under laser fluences of (a) 0.06 J/cm^2 , (b) 0.10 J/cm^2 , (c) 0.19 J/cm^2 122
- 6.15 (a) PS-LIBS spectra of carbon-metal oxide (CMO) nanocomposites (black line) and pure soot particles (blue line) are shown, along with the Voigt fitting curves (red dotted lines) for Ti atomic emission (NIST database, represented as black columns) and C_2 Swan band [265]. (b) The emission spectra from the current study are displayed for carbon black nanoparticles in the optical cell (blue line), high-purity TiO_2 nanoparticles in the optical cell (black line), and flames-synthesized TiO_2 nanoparticles (at HAB= 45mm, green line) at prompt under a laser fluence of 0.24 J/cm^2 124
- 6.16 Comparison of emission spectra between high-purity TiO_2 and flame-generated TiO_2 nanoparticles. Emission spectra of TiO_2 nanoparticles from the optical cell (non-reactive, white square) and flames (reactive, at HAB = 45 mm, green triangle symbol) have been shown with delayed acquisition time at (a) around 50 ns (60 ns for the high-purity TiO_2 case) and (b) 100 ns, under laser fluence of 0.19 J/cm^2 for non-reactive case and 0.15 J/cm^2 for the reactive case. Both spectra are normalized by the value of each curve at 650 nm. 125

6.17	The evolution of ΔT^{-1} at 650 nm and 710 nm of (a) TiO ₂ nanoparticles from the optical cell (non-reactive) and (b) flame (reactive); laser fluence of 0.19 J/cm ² for the non-reactive case and 0.15 J/cm ² for the reactive case. The value of τ/λ_{em} is written inside the legend.	126
7.1	Post-processing method to apply two-color pyrometry from spectral information: (a) Calculation of averaged values of emission spectra for each 20 nm and (b) linear fitting of selected data. Data correspond to LIE from carbon black nanoparticles at $F = 0.06$ J/cm ² and a delay of 100 ns from laser excitation (blue line). The effect of data filtering (orange line) is illustrated.	134
7.2	Post-processing method to calculate the possible range of $\varepsilon^*(\lambda)$: (a) Estimation of possible effective temperature values from Eq. (7.3) and (b) corresponding $\varepsilon^*(\lambda)$ region (blue zone) extended to sublimation temperature (red zone). Both results from the raw and filtered spectra are shown. Data correspond to LIE from carbon black nanoparticles at $F = 0.06$ J/cm ² and a delay of 100 ns from the peak.	135
7.3	Effect of $\Delta\lambda$ on the estimation of maximum and minimum effective temperatures. Data correspond to LIE from carbon black nanoparticles at $F = 0.06$ J/cm ² and a delay of 100 ns from the peak (blue line).	136
7.4	$\varepsilon^*(\lambda, t)$ for carbon black nanoparticles using LIE at $F = 0.06$ J/cm ² and different acquisition delay times: (a) 0, (b) 60, (c) 100, (d) 200 ns. Values of T_{min} and T_{max} are shown in the legend. The values $\varepsilon^*(\lambda)$ found in the literature are also presented [364, 25, 303, 287, 361, 362, 261].	138
7.5	$\varepsilon^*(\lambda, t)$ for carbon black nanoparticles using LIE at $F = 0.12$ J/cm ² and different acquisition delay times: (a) 0, (b) 60, (c) 100, (d) 200 ns. Values of T_{min} and T_{max} are shown in the legend. The values $\varepsilon^*(\lambda)$ found in the literature are also presented [364, 25, 303, 287, 361, 362, 261].	139
7.6	$\varepsilon^*(\lambda, t)$ for carbon black nanoparticles using LIE at $F = 0.23$ J/cm ² and different acquisition delay times: (a) 0, (b) 60, (c) 100, (d) 200 ns. Values of T_{min} and T_{max} are shown in the legend. The values $\varepsilon^*(\lambda)$ found in the literature are also presented [364, 25, 303, 287, 361, 362, 261].	140
7.7	$\varepsilon^*(\lambda, t)$ for high-purity TiO ₂ nanoparticles using LIE at $F = 0.19$ J/cm ² and different acquisition delay times: (a) 0, (b) 60, (c) 100, (d) 200 ns. Values of T_{min} and T_{max} are shown in the legend. T_{min} is bigger than melting point of TiO ₂ (2128 K [282]) so estimated $\varepsilon^*(\lambda, t)$ are for liquid state particles.	141
7.8	$\varepsilon^*(\lambda, t)$ for high-purity TiO ₂ nanoparticles using LIE at $F = 0.24$ J/cm ² and different acquisition delay times: (a) 0, (b) 60, (c) 100, (d) 200 ns. Values of T_{min} and T_{max} are shown in the legend. T_{min} is bigger than melting point of TiO ₂ (2128 K [282]) so estimated $\varepsilon^*(\lambda, t)$ are for liquid state particles.	142
7.9	$E(m_\lambda)$ normalized at 451 nm for high-purity TiO ₂ nanoparticles from LIE at $F = 0.19$ J/cm ² and 100 ns from prompt. Results are compared to literature data [285, 214]. T_{min} is bigger than melting point of TiO ₂ so it should be in liquid state. 143	

- 7.10 $\varepsilon^*(\lambda, t)$ for flame-synthesized TiO_2 nanoparticles using LIE at $F = 0.15 \text{ J/cm}^2$ and different acquisition delay times: (a) 0, (b) 50, (c) 100, (d) 150 and (e) 250 ns. Values of T_{\min} and T_{\max} are shown in the legend. T_{\min} is bigger than melting point of TiO_2 (2128 K [282]) so estimated $\varepsilon^*(\lambda, t)$ are for liquid state particles. 144
- 7.11 $E(m_\lambda)$ normalized at 451 nm for flame-synthesized TiO_2 nanoparticles from LIE at $F = 0.15 \text{ J/cm}^2$ and 100 ns from prompt. Results are compared to literature data of solid TiO_2 [285, 214]. T_{\min} is bigger than melting point of TiO_2 so it should be in liquid state. 145
- 7.12 (a) Effective temperature as a function of laser fluence from LIE of carbon black nanoparticles at three acquisition times ($t=0$ ns, 60 ns, and 100 ns). The observed reduction at $F = 0.23 \text{ J/cm}^2$ appears to be due to the sublimation effect. (b) Estimation of $E(m_{\lambda_{\text{laser}}})$ when using the effective temperature calculated at a given time t from LIE of carbon black nanoparticles for $F = 0.06 \text{ J/cm}^2$, where the plateau regime does not seem to be reached yet. The blue dashed lines are for the $E(m_{\lambda_{\text{laser}}})$ obtained at each instant (left axis), black dashed line is the average for all instants (left axis), and the red dotted line for the temperature considered for the calculation (right axis). 148
- 7.13 (a) Effective temperature as a function of laser fluence obtained from LIE of high-purity TiO_2 nanoparticles at three acquisition times ($t=0$ ns, 60 ns, and 100 ns). (b) Estimation of $E(m_{\lambda_{\text{laser}}})$ when using the effective temperature calculated at time t from LIE of high-purity TiO_2 nanoparticles for $F = 0.19 \text{ J/cm}^2$. The blue dashed lines represent the $E(m_{\lambda_{\text{laser}}})$ obtained at each instant (left axis), the black dashed line represents the average for all instants (left axis), and the red dotted line represents the temperature used for the calculation (right axis). Since the effective temperature is higher than the melting point of TiO_2 , $E(m_{\lambda_{\text{laser}}})$ is for liquid state particles. 149
- 7.14 (a) Effective temperature as a function of laser fluence from LIE of flame-synthesized TiO_2 nanoparticles at prompt (HAB = 45 mm). (b) Estimation of $E(m_{\lambda_{\text{laser}}})$ when using the effective temperature calculated at a given time t from LIE of flame-synthesized TiO_2 nanoparticles for $F = 0.15 \text{ J/cm}^2$ (HAB = 45 mm). The blue dashed line corresponds to $E(m_{\lambda_{\text{laser}}})$ obtained at each instant (left axis), black dashed line is the average for all instants (left axis), and the red dotted line corresponds to the temperature used for the calculation (right axis). Since the effective temperature is higher than the melting point of TiO_2 , the obtained $E(m_{\lambda_{\text{laser}}})$ is expected to correspond to liquid state particles. . . . 151
- 7.15 (a) $E(m_\lambda)$ for carbon black nanoparticles from LIE at $F = 0.06 \text{ J/cm}^2$ and 100 ns from prompt. Results are compared to literature data [364, 25, 303]. A linear extrapolation is considered between $E(m_{\lambda_{\text{laser}}})$ and $E(m_{\lambda_{450}})$. (b) Zoom between 0.1 - 0.5. 154

7.16	$E(m_\lambda)$ for high-purity TiO_2 nanoparticles from LIE at $F = 0.19 \text{ J/cm}^2$ and 100 ns from prompt. Results are compared to literature data [285, 286, 214]. A linear extrapolation is considered between $E(m_{\lambda_{\text{laser}}})$ and $E(m_{\lambda_{450}})$. Since the effective temperature is higher than the melting point of TiO_2 , our $E(m_\lambda)$ corresponds to liquid state.	154
7.17	$E(m_\lambda)$ for flame-synthesized TiO_2 nanoparticles from LIE at $F = 0.15 \text{ J/cm}^2$, delayed at 100 ns from prompt. Results are compared to literature data for solid TiO_2 [285, 286, 214]. A linear extrapolation is considered between $E(m_{\lambda_{\text{laser}}})$ and $E(m_{\lambda_{450}})$. Since the effective temperature is higher than the melting point of TiO_2 , our $E(m_\lambda)$ corresponds to liquid state.	155
7.18	(a), (c), (e) $E(m_\lambda)$ of high-purity TiO_2 nanoparticles from LIE at $F = 0.19 \text{ J/cm}^2$ and 100 ns from prompt. (b), (d), (f) $E(m_\lambda)$ of flame-synthesized TiO_2 nanoparticles from LIE at $F = 0.15 \text{ J/cm}^2$ and 100 ns from prompt. Results are compared to literature data [285, 286, 214]. The quantity $\frac{E(m_{\lambda_{450}})}{E(m_{\lambda_{\text{laser}}})}$ is extrapolated from available experimental data from De Iuliis et al. [214] (a, b), Jellison et al. [286] (c,d), and Liu et al. [285] (e,f).	156
8.1	Schematic of the LII set-up for TiO_2 nanoparticles in flame synthesis. The excitation and temporal detection parts are identical to those presented in Part II. An additional ICCD camera is used to obtain spatial distribution information. . . .	160
8.2	Comparison between data from two different detection devices for $\lambda_{\text{em}} = 640 \text{ nm}$: camera (spatial, red round symbol) and PMT (temporal, blue triangle symbol). Measurements were done along the flame centerline at three flame heights. . . .	161
8.3	Variability of LII signal intensity from (a) 7 sets of PMT and (b) 2 sets of camera measurements at prompt along the flame centerline. Standard deviations (σ) of each measurement are represented in colored area, the averaged values are represented in black lines.	162
8.4	Evolution of ΔT^{-1} under laser fluence at $F = 0.15 \text{ J/cm}^2$ of flame-generated TiO_2 nanoparticles for two wavelengths at (a) HAB = 30 mm, (b) HAB = 45 mm, (c) HAB = 60 mm.	162
8.5	Intensity of flame brightness (right) at the centerline along the flame height (left).	163
8.6	Comparison between flame luminosity obtained with a CANON camera (a) and numerical simulation (b,c,d). For the result of simulation, the volume fraction of TiO_2 is expressed in a yellow-red color bar, with the mass fraction of OH expressed in blue color in (b), temperature (c), and size of primary particle (d) are also shown.	165

8.7	Comparison between experimental flame luminosity outline (white line for luminous cylindrical zone and surrounding transparent flame) and numerical OH mole fraction (blue colormap) and TiO ₂ volume fraction (red-yellow colormap). The boundary of the experimental flame luminosity is taken from 30 % of the highest intensity for the middle cylindrical zone. For the colorless surrounding part, the image has been split into RGB colormap and only the blue component has been considered for defining the boundary. Numerical values are normalized by each maximum value.	165
8.8	Spatial distribution of f_v^* from (a) numerical simulation, from LIE signals (b-e) assuming spatially-uniform absorption function and effective temperature. Measurements at (b) prompt and delayed time at (c) 50, (d) 100 and (e) 150 ns are considered for Eq. (8.4).	166
8.9	Evolution of f_v^* along the flame centerline based on S_{LII} signals at 0, 50, 100 and 150 ns. The numerical simulation result is also shown.	167
8.10	Estimated $E(m_\lambda)$ range for TiO ₂ nanoparticles produced in the YDB burner. Results have been obtained in Chap. 7 using the LII spectra at HAB=45 mm under $F = 0.15 \text{ J/cm}^2$ at $t = 100 \text{ ns}$. Literature results from Liu et al. [285] are added for comparison. Note that our results are possible for liquid state nanoparticles and those of Liu et al. [285] come from solid films.	168
8.11	Effective particle temperature obtained by two-color pyrometry at 650 and 710 nm under $F = 0.15 \text{ J/cm}^2$ at different acquisition timing: (a) at HAB = 30 mm, (b) at HAB = 45 mm, and (c) HAB = 60mm. Round black symbols are for $\epsilon^*(\lambda) = 1$. The red area corresponds to $\epsilon^*(\lambda) \neq 1$. The absorption function of Liu et al. [285] is shown in black triangle symbols.	172
8.12	Evolution of temperature along the flame centerline when assuming (a) $\epsilon^*(\lambda) = 1$ and (b) $\epsilon^*(\lambda) \neq 1$	173
8.13	Spatial distribution of f_v^* obtained using numerical simulation (a) and LIE signals assuming a spatially uniform absorption function and non-uniform effective temperature from measurements at (b) prompt and (c) 100 ns delay time. Eq. (8.5) was used to calculate f_v^* in all cases.	174
8.14	Evolution of f_v^* along the centerline of the flame height is calculated from S_{LIE} at 0 ns (a) and 100 ns (b), considering $\epsilon^*(\lambda) = 1$ and $\epsilon^*(\lambda) \neq 1$. Non-uniform temperature is also considered. The numerical simulation results are also shown in blue line.	175
8.15	Estimated absorption function $E(m, z)$ at different flame heights from the effective temperature obtained in Fig. 8.11 for $\epsilon^* = 1$. Black symbols are obtained assuming a gas temperature of 1900 K, and blue symbols correspond to gas temperature from numerical simulation. Full and void symbols are obtained from LIE signals at 100 ns. (a) $E(m, z)$ value and (b) $E(m, z)/E(m, z_0)$ normalized value with the value at HAB = 30 mm.	177
8.16	Spatial distribution of f_v^* in the case of non-uniform absorption function and non-uniform effective temperature (with $\epsilon(\lambda) = 1$). (a) numerical simulation. f_v^* from measurements at (a) prompt and (c) delayed time at 100 ns.	178

8.17	Normalized volume fraction at the centerline of flame synthesis derived with spatially variable $E(m)$ (a) at prompt and (b) 100 ns after.	179
8.18	Normalized volume fraction f_v^* at the centerline of flame synthesis derived with considered strategies: spectrally constant $E(m_{\lambda_{em}})$ and T_{eff} , spectrally constant $E(m_{\lambda_{em}})$ and non-uniform T_{eff} , non-uniform $E(m_{\lambda_{em}})$ and T_{eff} and numerical simulation at prompt (a) and delayed (100 ns) (b) case.	181
8.19	(a) Absorption function and (b) effective temperature at prompt used for non-uniform $E(m_{\lambda})$ and non-uniform T_{eff} case. The values are interpolated between 30 and 60 mm.	181
C.1	The effect of fuel rate, oxidizer rate, and dilution ratio on the flame structure in the YDB burner. The fuel is a mixture of CH_4 and N_2 , and the coflow is air. The height above the burner (HAB) = 0 mm is marked by a white dashed line. . . .	196
D.1	Effect of laser fluence F on laser-induced emission spectra at prompt for flame-generated TiO_2 nanoparticles. Spectra are normalized by the value of 650 nm. . .	198
D.2	Effect of gate delay (gate width = 20 ns) on emission spectra of laser-induced emissions of flame-generated TiO_2 nanoparticles at laser fluence $F = 0.15 \text{ J/cm}^2$. Spectra are normalized with the value of the spectrum at 650 nm.	199

Introduction

Nanoparticles constitute an increasingly important area of science and technology with broad applications. The global nanomaterials market was estimated at US\$7.1 billion in 2020 and should reach US\$12.1 billion by 2026, with a compound annual growth rate (CAGR) of 9.7% [1]. Their use includes historical ink, healthcare, cosmetics, food and beverages, as well as electronics and computational devices, including semiconductors [1]. In 2014, more than 1800 nanotechnology-based consumer products were commercialized in more than 20 countries [2]. The work presented in this manuscript focuses on titanium dioxide (TiO_2) nanoparticles. They are commonly used in everyday commodities, mainly as whitening and brightening agents in food additives, or in toothpaste and sunscreen [3]. They are also considerably used in energy and environmental applications, due to their unique optical properties as semiconductors. For example, in terms of energy application, Logitech marketed an iPad keyboard powered by solar irradiation (Fig. 1), using dye-sensitized solar cells [4] with TiO_2 nanoparticles. In terms of environmental application, the photocatalytic characteristics of TiO_2 nanoparticles are also being actively investigated for wastewater treatment [5].



Figure 1. The Solar Keyboard Folio with the solar panels on the bottom, which can charge from ambient light. Image from Sarah Tew/CNET.

Among the various methods for synthesizing TiO₂ nanoparticles, spray flame synthesis is considered to be a promising technique [6] for the production of nanoparticles with advanced characteristics [6]. TiO₂ photocatalyst with improved performance [7], TiO₂ (B), a promising material for batteries and catalysts [8], or an organic vapor sensor [9] can be generated through the spray flame synthesis systems. The properties of the generated particles depend on the local conditions that nanoparticles have experienced during their forming trajectory. Thus, the high temperature gradient and short residence time in the spray flame system provide a unique environment for the generated nanoparticles, which gives them specific properties. In addition, similar to other gas-phase synthesis technologies, the spray flame synthesis system requires only a few milliseconds to form nanoparticles in a single-step process, a critical advantage in terms of industrial scaling-up.

In this framework, there is a critical need to understand the formation of nanoparticle synthesis in turbulent flow reactors for both designs of aerosol properties and mitigation of unwanted nanoparticle emissions (e.g., soot). Turbulent flames allow for the viability of larger-scale nanoparticle production in gas-phase reactors but the understanding of particle formation in turbulent flames remains challenging due to complex interactions between particles, chemical reactions, and fluid dynamics. Therefore, diagnostics capable of characterizing the properties of the temporally and spatially resolved particle population are needed to successfully investigate the underlying physical processes of nanoparticle production in turbulent flame technology.

Among the available experimental diagnostics, laser-induced incandescence (LII) is an optical diagnostic based on the thermal radiation (also called incandescence) from aerosolized nanoparticles. This technique was initially developed as a combustion diagnostic to obtain information on soot volume fraction and soot particle size in flames [10, 11]. In the LII technique, particles are heated with a high-power laser until they reach a high temperature. Then, the particles cool down to the surrounding environment emitting thermal radiation that can be measured.

Even though this technique has been well-developed for soot particles over decades, its application to nanomaterials, particularly non-soot particles [12] presents new scientific challenges. In theory, all normal matter can be heated so that it will radiate incandescent emissions. However, a high temperature is required to have enough incandescence, i.e., a signal intensity higher than the threshold level of the detection equipment. This point restricts the range of materials that can be considered for the LII. LII has more recently been explored in a broader set of materials, including metals [13, 14, 15, 16], metal oxides [17, 18, 19, 20, 21], and elemental semiconductors [22, 23, 16, 24].

Five main challenges are identified when applying LII on metal oxide TiO₂, :

1. The first point concerns the difficulty in sufficiently heating the particles to reach the incandescent temperature. One important nanoparticle property for LII mechanisms is the absorption function $E(m_\lambda)$, where the refractive index m_λ is a wavelength-dependent optical property describing the scattering and the light-absorbing capacities of a material. Being related to the particle absorption of laser energy, $E(m_\lambda)$ is important for the LII process since the particles have to absorb the incident laser beam to be heated to a sufficiently high temperature. It is well known that metal oxides, like TiO₂ nanoparticles, generally show low $E(m_\lambda)$ compared to those of soot in the visible range [12]. Thus, particle heating by laser excitation is expected to be challenging.

2. The second difficulty concerns the low level of laser-induced emission in analogy with the discussion at the previous point. A low level of LII emission signal is expected since $E(m_\lambda)$, also related to the particle emission, is found to be small in the LII detection wavelength range (400-700 nm).
3. Due to the first (small absorption property) and second points (weak incandescence signal), they are more susceptible to being contaminated by interference from other laser-induced emission sources than carbonaceous particle case [12]. The possible overlap of other atomic and molecular emissions from various sources (excited-state emission from gas or vaporized species, chemiluminescence, photoluminescence [13]) during the laser-induced process makes it even more difficult to distinguish the nature of the signal before using for particle characterization.
4. Physicochemical properties of metal oxide nanoparticles show different aspects than those of carbonaceous particles. The lower melting point of metal oxide than soot particles can drive the change of phase (solid-liquid) during the laser heating and cooling process. The melting process can, in turn, influence particle heating and cooling rates because of differences in physical properties between solid and liquid states as reported for soot [25], metal [26] and metal-oxide [27] particles. This can change the optical property related to $E(m_\lambda)$, which brings more uncertainty in the analysis of LII. With a lower boiling point, we have more chances of evaporating the particles when increasing laser fluence to have enough S/N intensity as well.
5. Finally, compared to the carbonaceous particles, the optical property of TiO_2 has high dynamic in visible range wavelength and also has high variability in literature, which increases the uncertainty in the analysis.

In this study, the laser-induced emission of TiO_2 nanoparticles has been investigated to verify if the LII technique can possibly be used to characterize their volume fraction distribution in flame synthesis. For this purpose, both commercially engineered TiO_2 nanoparticles with high purity and hydrogen flame-generated TiO_2 nanoparticles are considered for the first time to characterize the nature of laser-induced emission for TiO_2 particles.

More precisely, this thesis has three main objectives:

- Validation of the feasibility of LII of TiO_2 nanoparticles in an inert environment by comparing the LIE behavior of carbon black and TiO_2 nanoparticles.
- Development of a flame synthesis system with a pre-vaporized TTIP precursor and verification of LII emission from the flame-generated TiO_2 nanoparticles.
- The first step for illustrating how we can use the LIE for characterization of $E(m_\lambda)$ and volume fraction.

Structure of this manuscript

The manuscript is comprised of three parts:

- Part 1: Nanoparticle synthesis and characterization.
 - In **Chapter 1**, the generalities of nanoparticles are introduced. The definition, properties, and manufacturing methods are reviewed, and the general properties of the target material, titanium dioxide (TiO_2), are presented.
 - Among the different manufacturing processes of nanoparticles, spray flame synthesis

- is selected for its capacity to produce advanced nanomaterials. The formation of nanoparticles in flame synthesis is described in **Chapter 2**.
- Common diagnostics of characterizing nanoparticle synthesis in flames are summarized in **Chapter 3**. The different ex-situ, on-line, and in-situ approaches for particle characterization, especially for TiO_2 , are summarized in terms of their advantages and difficulties.
 - Part 2: Characterization of the Laser-Induced Emission of TiO_2 nanoparticle: Feasibility of Laser-Induced Incandescence.
 - In-situ characterization of the nanoparticle, especially laser-induced incandescence (LII) is a powerful in-situ characterization method. However, possible laser-induced emission (LIE) should be carefully treated. Three main LIE of TiO_2 - Laser-induced fluorescence (LIF), Laser-induced breakdown spectroscopy (LIBS), and LII- will be revised in **Chapter 4**.
 - In **Chapter 5**, the feasibility of LII on TiO_2 has been studied with high-purity commercial TiO_2 in a non-reactive environment. The experimental set-ups for the LII technique on high-purity TiO_2 nanoparticle aerosol in an inert environment are presented to avoid possible carbon intervention in the particle distribution. Based on the information about interference, spectrally-resolved LII-emissions of TiO_2 particles under different detection gate delays and laser fluences are measured to retrieve black-body-like behavior. The results show the LII-like nature of signal emission from TiO_2 nanoparticles.
 - The feasibility of LII on flame-generated TiO_2 nanoparticles in hydrogen flame is verified in **Chapter 6**.
 - Part 3: Towards quantitative characteristics of TiO_2 nanoparticles production in flames based on LII measurement.
 - To quantitatively estimate the particle volume fraction, information on optical properties is indispensable. In **Chapter 7**, methodology for deducing spectral information of absorption function $E(m_\lambda)$ is introduced.
 - In **Chapter 8**, qualitative analysis of the volume fraction in flame synthesis of TiO_2 nanoparticles is investigated. The effect of effective temperature and absorption function along the flame height is analyzed regarding the interpretation of the LII signal into volume fraction.

As already pointed out, two different aerosol-generating systems have been developed during this thesis for LII experiments for TiO_2 . Particle dispersion of commercial high-purity TiO_2 has been used for non-reactive measurements with nitrogen (in **Chapter 5**). Then, flame-generated TiO_2 nanoparticles are synthesized in argon-diluted hydrogen flame with the pre-vaporized precursor of TTIP (in **Chapter 6, 7, 8**). The comparison between soot and TiO_2 particles is used in the manuscript to interpret the LII signal of particles.

Part of this manuscript (Chap. 5) has been presented at the 10th European Combustion Meeting (ECM 2021) and 9th International Workshop on Laser-Induced Incandescence (LII) held in Glasgow (2022). The contents of Chapter 5 and Chapter 7 have both been submitted to Applied Physics B's Special Issue: Laser-Induced Incandescence with the title of "Characterization of Laser-Induced Emission of high-purity TiO_2 nanoparticles: Feasibility of Laser-Induced Incan-

descence" and "Experimental Determination of Spectral Absorption Function in LII Measurements of Flame-Synthesized TiO₂ Nanoparticles", respectively. The contents of Chapter 8 will be presented at the 11th European Combustion Meeting (ECM 2023) and have been submitted in Journal of Applications in Energy and Combustion Science with the title of "Towards the characterization of TiO₂ flame synthesis via Laser-induced Incandescence (LII) technique". This thesis has been financed by the European Research Council (ERC) support from the European Union's Horizon 2020 research and innovation program (grant agreement No. 757912).

Part I

Nanoparticle synthesis and characterization

Chapter 1

Nanoparticles

Nanotechnology is increasingly embedding itself into everyday life. Nanoparticles are everywhere; from daily life products like sunscreen, plastic odds and ends, and wall paints, to high-end technology like electronics (storage material in high-capacity batteries), biotechnology (ultra-filtration membranes, medical diagnostics, drug delivery), chemistry (highly efficient catalysts), energy technology (solar photovoltaic), and materials science (optical glasses, dense ceramics). Nanoparticles have unique physical and chemical properties, different from those of bulk materials, mainly originating from the surface layer atomic structure [28].

Nanoparticles naturally exist in many incidental processes (e.g., soot emissions in fossil fuel combustion, large-scale mining, or metal particles in welding fumes). Since the 1940s, engineered nanoparticles have been synthesized in well-defined environments to control their size-dependent properties [29]. Although the technical skills for industrial nanoparticle production have evolved in the last couple of decades, the detailed formation process remains to be discovered. The challenge of controlling the nanoparticle formation processes persists with growing demands of tailored nanoparticles for a specific purpose in diverse fields [1].

Among various nanoparticle-producing methods, we will focus on nanoparticle synthesis using flames. Ulrich [30] highlighted the importance of the flame aerosol technique in 1971 as a relatively simple process to change the operating conditions, i.e., temperature, reactant mixing, and gas composition. Consequently, a wide variety of nanoparticle commodities have been made by aerosol technology, including carbon black, fumed silica, and titanium dioxide [31]. Today, as our knowledge about flame synthesis progresses, flame-generated technique gains more significance in nanoparticle production. Especially, the flame spray pyrolysis (FSP) technique can carry out advanced nanopowders such as metastable [8, 32], multi-component [33], or coated oxides [34, 35] nanomaterials through steep temperature gradient and short characteristics time [36]. This technique can have the potential to provide precise control for fabricating advanced gas sensors, catalysts, and other high-tech applications with novel properties [37].

In this chapter, the basics of nanoparticles are presented. First, the definition of nanoparticle will be provided in Sec. 1.1. Then, some outstanding properties and their implications for applications will be discussed in Sec. 1.2. The nanoparticle production process will be revised focusing on aerosol synthesis and flame spray pyrolysis in Sec. 1.3, which is the technique under the scope of this work. Finally, the discussion will focus on titanium dioxide (TiO_2)

nanoparticles, the target of this research work. The three crystalline polymorphs, the key features with corresponding applications, and the typical laboratory and commercial fabrication methods are reviewed in Sec. 1.4.

1.1 Definition

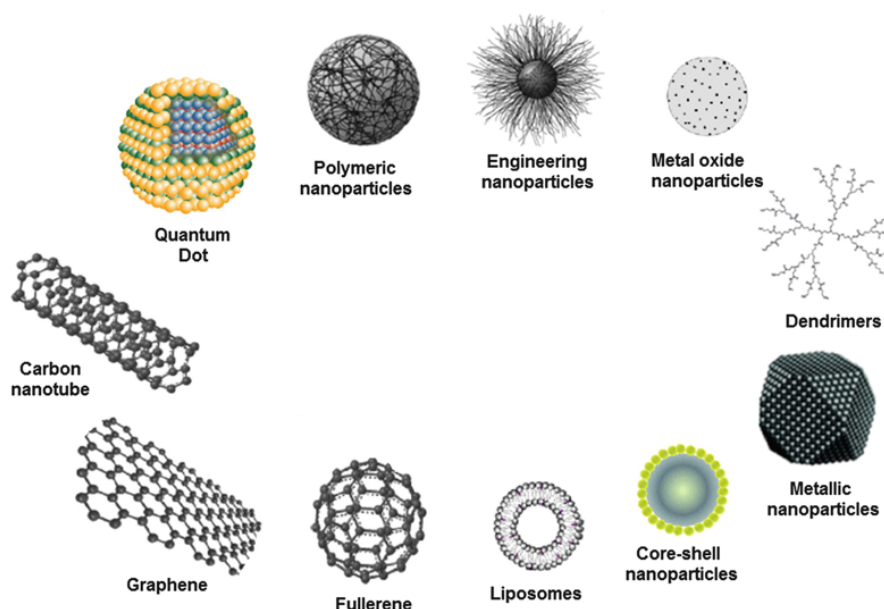


Figure 1.1. Schematic representation of various nanomaterials, adapted from [5].

Nanomaterials generally designate materials with at least one of their dimensions at the nanoscale. They include not only organic polymers (liposomes, dendrimers) and polymeric micelles but also various types of inorganic materials: metallic (nanogold, nanosilver), metal oxide (ceramic) materials, metalloid oxides, quantum dots, and carbon nanomaterials (fullerenes, carbon black or nano-tubes) as shown in Fig. 1.1. They can also be categorized into different geometric morphologies (0D sphere, 1D nanofibers, nanorod, 2D graphene, engineered layered nanomaterials, and 3D composite materials) as illustrated schematically in Fig.1.2. Each form of nanomaterials has unique chemical-physical properties utilized in various fields of applications [38].

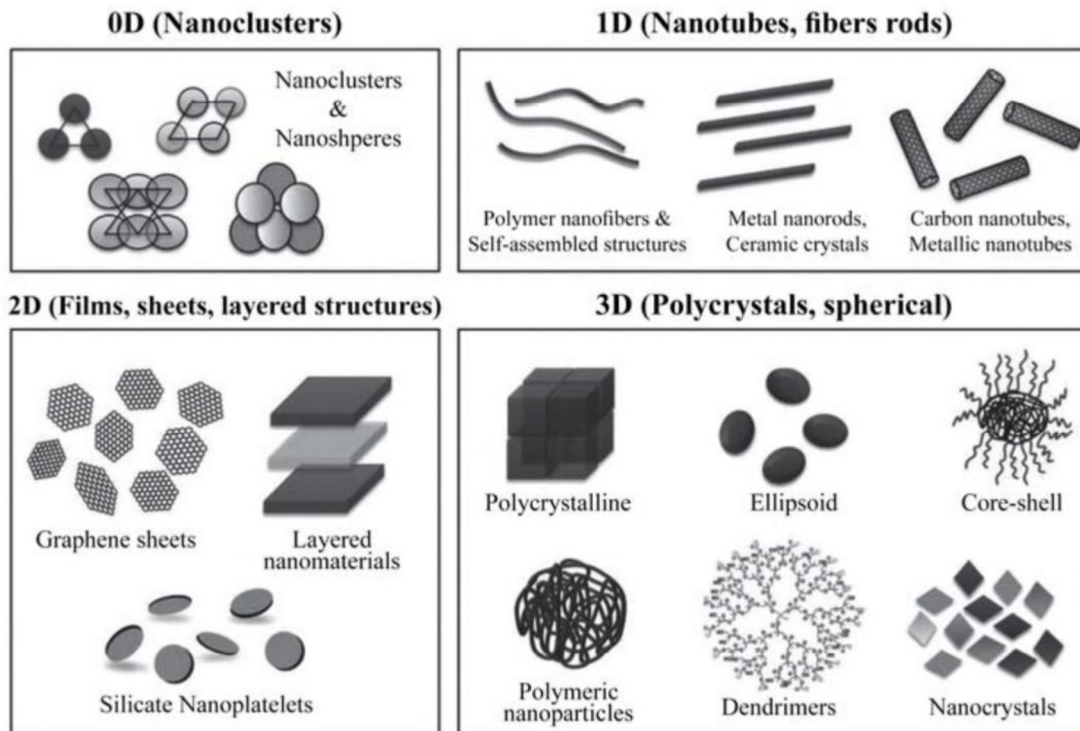


Figure 1.2. Examples for 0D, 1D, 2D, and 3D nanostructures [38].

This study focuses on nanomaterials with spherical forms, known as nanoparticles. Nanoparticles are defined as an object with all three external dimensions in the nanoscale, whose longest and shortest axes do not vary extensively, with a significant difference typically being a factor of at least 3 (International Standards Organization (ISO) technical specification 80004).

Inorganic metal oxide nanoparticles, especially titanium dioxide (TiO_2), are the focus of this study. Metal oxides nanoparticles are of interest for applications in various fields like the fabrication of microelectronic circuits [39], sensors [40], piezoelectric devices [41], fuel cells [42], and coatings against corrosion [43], and as catalysts [44].

It should be mentioned that all along the manuscript, the carbonaceous particles (carbon black and soot, commonly investigated in combustion systems) will also be considered as a reference to illustrate the unique optical properties of metal oxide particles.

1.2 Properties and applications

The great interest in using nanomaterials compared to bulk state materials is that they present a relatively larger surface-to-volume ratio. It is then possible to control the properties of the nanomaterials by adjusting their surface distribution. For example, for a cube with a volume of one cubic centimeter, the total surface area of the materials is increased 10^7 times after dividing it into 10^{21} nanocubes with one cubic nanometer. Then, many atoms (typical diameter between 0.15 and 0.6 nm) forming the nanostructure are located at the surface of the crystal structure.

Consequently, the properties originating from the surface atomic structure dominate the overall characteristics, introducing a size-shape dependency on the physicochemical properties. In this way, some unique properties appear at nanoscales, which are not found in the bulk state. One famous example is gold nanoparticles. In bulk state, the color of gold is yellow. At the nanoscale, the color changes depending on the geometry of the nanostructure. Figure 1.3 shows the different colors of gold nanoparticles with different geometric shapes. Based on their (a) aspect ratio (ratio of width to height), (b) shell thickness, and/or (c) galvanic (related to electric current) displacement, the color of nanoparticles arises from the collective excitation of their conduction electrons, also called surface plasmon resonance modes, which results in photon absorption at wavelengths that vary with the geometry of particles [45].

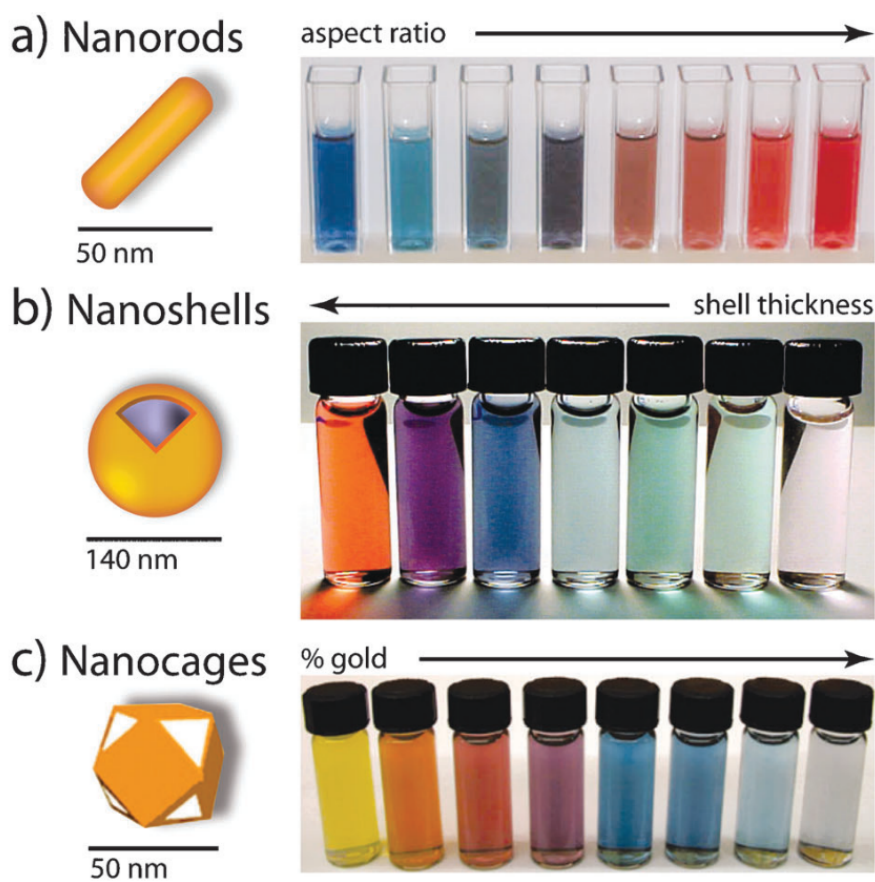


Figure 1.3. Different colors of gold nanoparticles with potential applications in biomedicine. (a) Gold nanorods, (b) silica-gold core-shell nanoparticles, and (c) gold nanocages [45].

The following sections will describe some of the unique properties of nanoparticles and their applications in industry.

Mechanical properties Mechanical properties of materials such as elastic modulus, hardness, stress, strain, adhesion, and friction can be drastically changed in nanosize. Nanoparticles can be employed for novel applications in surface coating or as reinforcement of composite materials because of those reasons [46]:

- High hardness and strength of particles.
- Migration and dislocation motion of grain boundaries can be prevented by the particles in the matrix.
- Heterogeneous nucleation effect of particles in metal or metal alloys.

In the building structure, silica nanoparticles and carbon nanotubes can be incorporated into the cement to increase their mechanical properties and abrasion resistance [47, 48]. They are also used to protect and lighten the structure of boats, to strengthen packaging and manufacture coatings, to strengthen tire structure, and to improve their grip on the ground [49]. The polymers incorporate carbon nanostructure in textiles such as sports sneakers for better mechanical strength [50].

Optical properties As described in the case of gold nanoparticles (Fig. 1.3), some noble metals have size-dependent optical properties. They show an intense ultraviolet (UV)-visible (VIS) extinction band that is not present in the spectrum of the bulk metal. The excitation band results in localized surface plasma resonance (LSPR), in which conduction electrons on the surface of the nanoparticle oscillate in resonance with incident light, as discussed previously. This results in selective wavelength absorption with an extremely large molar extinction coefficient¹. Based on this unique optical property, noble metal nanoparticles are widely used in biomedical applications - labels for antigens, drug delivery systems (tunable optical spectra in the visible (VIS)-infrared (IR) region) [45], and biosensors [51].

The refractive index, which concerns the optical behavior of the materials, can be controlled by adding inorganic nanoparticles into polymeric nanocomposites. Enhanced refractive index nanocomposite can be used in lenses, optical filters, reflectors, optical waveguides, optical adhesives, solar cells, or antireflection films [43].

Chemical properties Nanoparticles have higher surface chemical (redox, acidity) reactivity than bulk state [52]. Metal oxides are used for their redox and acid/base properties in the context of catalysts. Redox catalyst undergoes reduction and reoxidation simultaneously by giving out surface lattice oxygen anions (negatively charged ions) and taking oxygen from the gas phase in given reaction conditions. Metal oxide nanoparticles (e.g., CoO [53], CuO [54]) have stable redox potential with high energy density, making them promising electrode materials for sodium-ion or lithium-ion batteries [52].

Electrical properties Nanoparticles can be used to obtain a remarkably high electric conductivity. In bulk materials, multiple collisions of electrons during their trajectories can cause them to lose energy. The distance between two successive collisions of an electron, the electron mean

¹The extinction coefficient indicates the amount of attenuation when an electromagnetic wave propagates through a material.

free path, is the order of a few nanometers. The use of a nanometric-length metallic conductor allows each electron to cross it without collision. It is then possible to realize the ballistic transport of electrons without unnecessary energy dissipation when working at nanoscales. As an example, nanoparticles SnO_2 , WO_3 , and In_2O_3 oxides exhibit an improved n-type conductivity greater than the bulk substance [55].

The strong dependence of electrical conductivity on nanoparticle size is of great relevance for a gas-sensing device. A gas sensor comprises a heating layer, electrodes, and sensing material, as illustrated in Fig. 1.4. The conductivity of metal oxide nanoparticles can be changed upon exposure to a target gas or sudden temperature change, serving as a sensing material. A change of conductivity generates an electric signal, which is transmitted to electrodes. High reactive surface sites with a large surface-to-volume ratio of nanoparticles result in fast sensing response with high surface reactivity [52]. Many nanomaterials, such as SnO_2 , ZnO , CuO , and many other Au-doped nanomaterials are used for detecting carbon monoxide, ammonia, nitrogen oxides, and hydrogen gas [56].

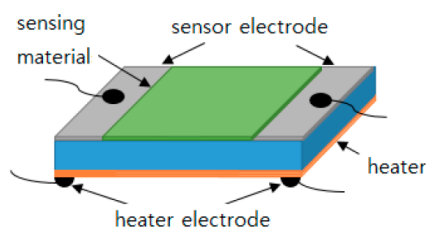


Figure 1.4. Configuration of gas sensors with two electrodes [57].

Thermal properties It is well-known that the nanoparticles have lower melting temperatures and enhanced specific heats than those in bulk states [29].

Recently, studies about nanofluids [58], fluids containing suspended solid nanoparticles, are getting attention because they can highly increase the thermal conductivity of liquid by adding solid nanoparticles with high thermal conductivity. For example, the thermal conductivity of copper at room temperature is about 400 W/m K , while that of water is 0.6 W/m K . Then, the thermal conductivity of the nanofluid is expected to display 1.5 - 3.5 times enhanced (depending on the volume fraction of particles) with their large total surface area, which is required in heat transfer fluid of a heat changer typically in solar thermal systems [59].

Magnetic properties In nanosize, the uneven electronic distribution can cause high magnetization properties than in the bulk state. Small magnetic nanoparticles, those containing metal nanoparticles and those containing Fe_2O_3 , Fe_3O_4 or ferrite nanoparticles, can be used in various biomedical applications, including MRI contrast enhancement, tissue repair and immunoassay, detoxification of biological fluids hyperthermia, drug delivery, and cell separation [60]. In terms of environmental application, superparamagnetic iron oxide nanoparticles are used to remove heavy metals (mercury, lead, cadmium) from natural water [60].

1.3 Manufacturing methods

The nanoparticle manufacturing methods can be categorized into two major processes (Fig. 1.5). One is the top-down process, where the particle size of the source material is reduced through mechanical, chemical, or thermal methods. Typical top-down manufacturing methods are mechanical ball milling for traditional ceramic products, and lithography commonly applied to the integrated electric circuits for computer chips [61].

The other is the bottom-up process based on the growth or self-assembly of single atoms and molecules by chemical or physical processes. Through the bottom-up approach, it is possible to produce selected, complex structures with precise morphology controls. Therefore, the bottom-up process is considered a powerful technique to produce identical structures with atomic precision [62].

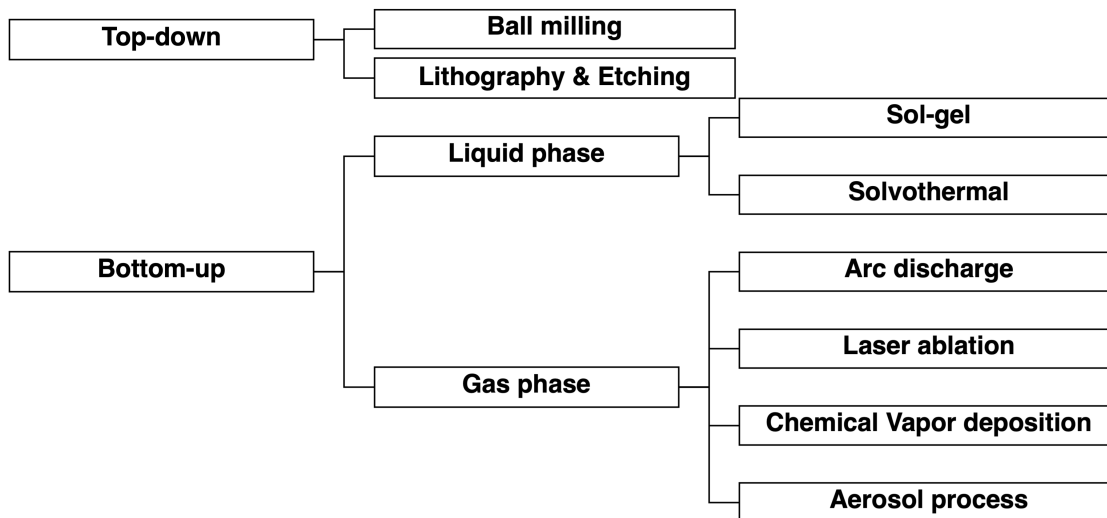


Figure 1.5. Nanoparticle production strategy: Top-down and bottom-up process.

The choice of a synthetic method results in different physicochemical characteristics of the nanoparticle, such as the size, composition, morphology, and crystal structure [63]. As an example, Fig. 1.6 illustrates the transmission electron microscopy (TEM) images of ZnMgO nanoparticles fabricated via three different synthesis methods. The left column shows the nanoparticles produced by chemical vapor deposition, the middle column displays a mixture of cubes and tetrapods generated by metal combustion (aerosol process), and the right column gives the irregular nanorods originating from the sol-gel process ZnMgO. The green color line signifies the surface segregation of Zn atoms. The three TEM images show a clear distinction in crystal structures, even though they have the same chemical formula.

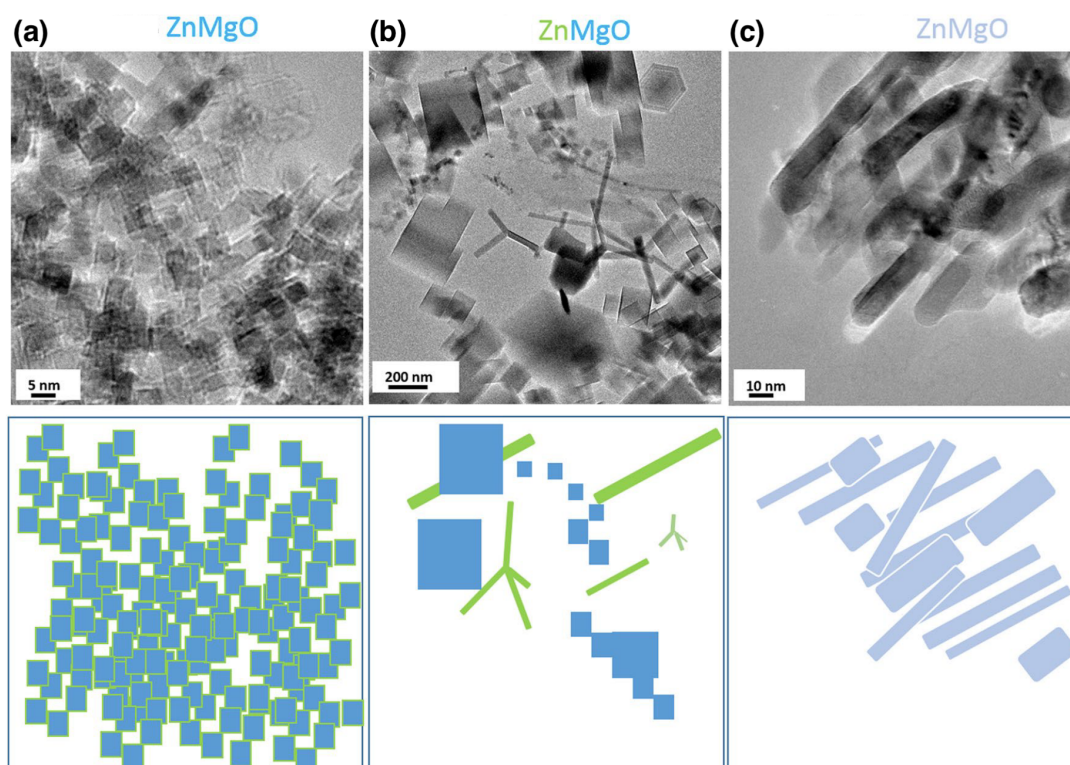


Figure 1.6. TEM images (top) and illustrations of the corresponding crystal forms (bottom) of various shapes of ZnMgO nanoparticles produced by chemical vapor deposition (a), metal combustion (aerosol process) (b), and sol-gel method (c). Zn is highlighted by green color, MgO is colored in blue, and light blue for ZnMgO in the illustration [63].

Various bottom-up processes for nanoparticle manufacturing will be presented in the following section, from a liquid phase to a gas phase-based process, with a focus on the fabrication of spherical nanoparticles. For all thin nanofilm productions, chemical vapor deposition will be presented as a representative method of film deposition technique. Detailed descriptions of other film deposition techniques like molecular-beam epitaxy [64], pulsed laser deposition [65], and atomic layer deposition [66] can be found in the literature.

1.3.1 Liquid phase process

(1) Sol-gel process

The sol-gel process is schematically presented in Fig. 1.7. First, a dispersion of solid particles in a liquid, called a sol, is created via hydrolysis² of a metallic alkoxide of precursor. Then, it gradually evolves toward the formation of a gel-like system. This gel-like solution can be transformed into discrete particles or continuous polymer networks by additional drying and heating.

This process can accurately control the kinetics during the formation in a low-temperature (< 100 °C) environment with good reproductivity. The produced oxide particles have a homogenous composition with high purity [67].

Still, there exist inconveniences of sol-gel method [68, 69] :

1. high cost of the raw materials (e.g., MgO power \$ 30/kg vs. Magnesium ethoxide (precursor) \$200/kg)
2. large volume shrinkage and cracking during drying
3. existence of organic contaminants
4. longer process time compared to gas-based methods

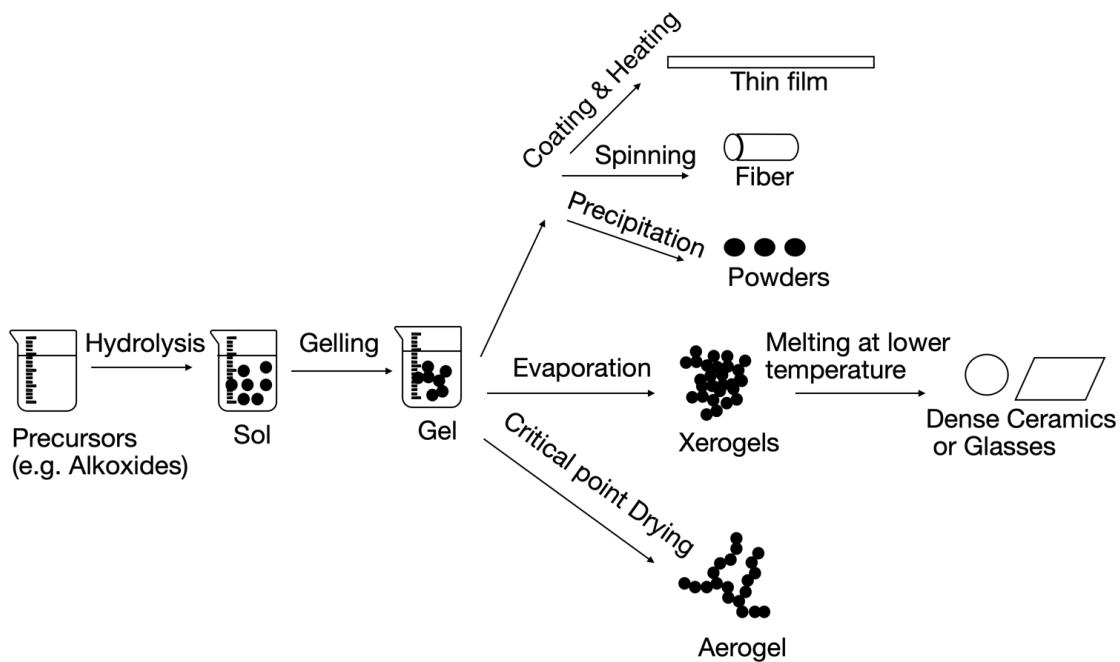


Figure 1.7. Schematic drawing of the sol-gel process for ceramic materials, adapted from [70].

²Chemical reaction in which a molecule of water breaks one or more chemical bonds.

(2) Solvothermal method

Solvothermal synthesis is based on the self-crystallizing (precipitation) of solid substances directly from high-temperature liquid solutions. The crystal growth is performed in a reactor system like in Fig. 1.8. It consists of a steel pressure vessel called an autoclave, in which a nutrient (aqueous metal salt in this case) is supplied along with solvent (water in this case). High pressures and temperatures are used to increase solid solubility and enhance the reaction rate. The advantage is that most materials can be made soluble in a proper solvent by heating and pressurizing the system close to its critical point. The higher partial vapor pressure of the solvent induces chemical reactions. Nevertheless, in terms of scale-up possibility, it is limited by its high temperature and pressure equipment. Moreover, information on the structure of materials during transient transformations is mostly unavailable [71].

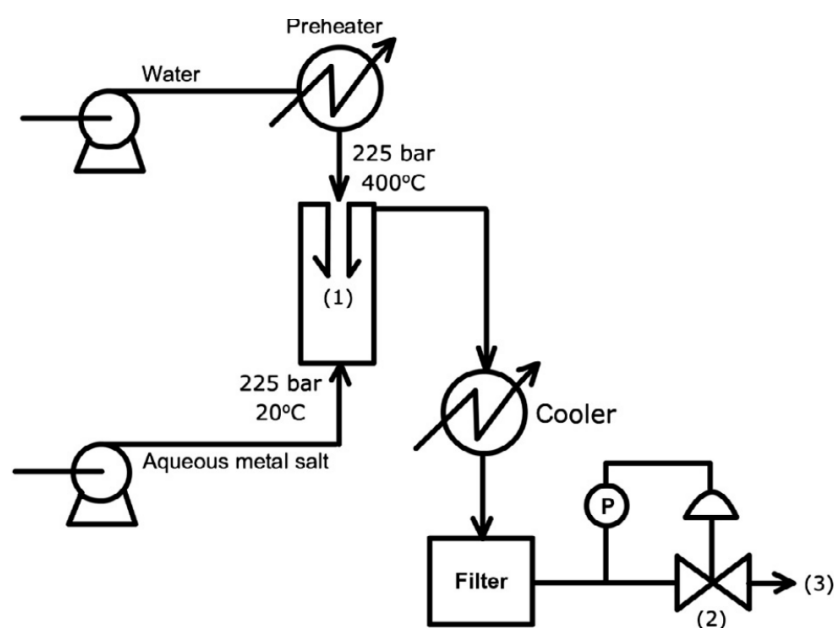


Figure 1.8. SHYMAN's continuous hydrothermal apparatus, (1) autoclave, (2) mixing zone, (3) formulation stage [49].

1.3.2 Gas phase process

(1) Arc discharge generation

Various types of plasma, spark, glow, and arc discharge can be applied to produce various nanomaterials (metal, alloy, oxide, inorganic, carbonaceous, and composite). In arc discharge generation illustrated in Fig. 1.9, a high current is applied to two metal electrodes (cathode, anode) until it reaches the breakdown voltage (a few tens of volts). The arc created across the two electrodes vaporizes a small amount of metal from one electrode to another. Then gas-phase metal nucleates in the form of nanoparticles [49].

This method can produce relatively small amounts of nanoparticles, whereas it is characterized

by good reproducibility with high-purity, inert-environment characteristics.

Nevertheless, the high-temperature environment in arc discharge causes melt electrodes and evaporates electrodes at a significant rate. This vaporization by arc leads to considerable loss of mass output rates, up to grams per hour, depending on the electrode material, gas composition, and arc current [72].

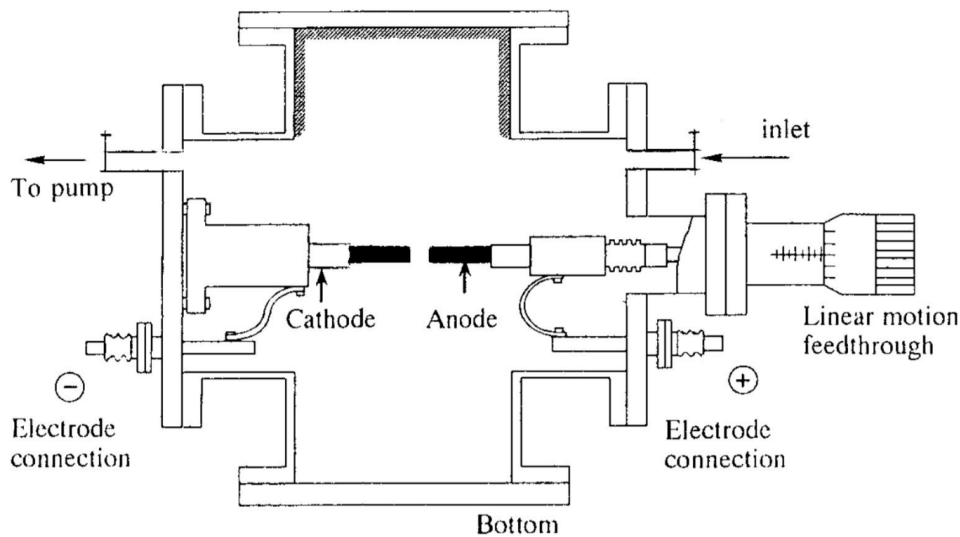


Figure 1.9. Schematic drawing of arc discharge particle formation process [73].

(2) Laser ablation process

In the laser ablation process, the target source material, whether aerosol in inert gas or colloidal solution, is selectively irradiated by laser as illustrated in Fig. 1.10. Nanoparticles are then generated by nucleation and growth of laser-vaporized species in a background gas.

This technique utilizes the absorption wavelength of material and decomposes source material into the desired nanosized product. Thus, most materials (served as precursor targets) can be first vaporized and then nucleated into nanoparticles. Moreover, particles generated from laser ablation have a narrow size distribution with variable primary particle size and shape [74]. Laser ablation can generate small nanoparticles like quantum dots ($\sim 2 - 10$ nm).

Despite its advantages and applications, the use of laser ablation has been limited to laboratory-scale nanoparticle production due to the high input energy required for a small laser-irradiating area to evaporate the target materials [75].

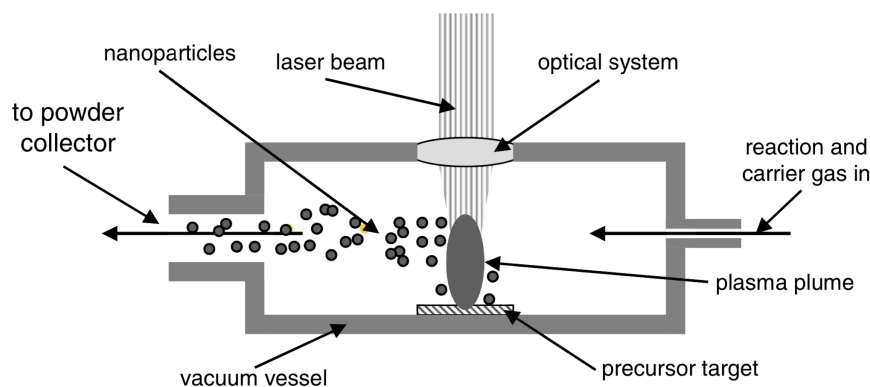


Figure 1.10. Schematic drawing of laser ablation particle formation process [76].

(3) Chemical vapor deposition

Chemical vapor deposition (CVD) is a vapor-phase process that deposits solids in the form of a film or particles by reacting gaseous components [77]. Solid substrates are heated at high temperatures and exposed to precursor materials in the gaseous state along with an inert carrier gas. Hot wall (Fig. 1.11), radiofrequency plasma, laser beam, or flame can be applied as a heating source [77]. This technique is predominantly used to deposit a thin film onto the substrate. Chemical vapor deposition has the advantages of low set-up cost, high production yield, ease of scale-up of super-hard carbide films, and heterogeneous catalysts [78]. With the capacity to produce uniform and high-quality metal oxide films in excellent reproducibility, there exist many studies to produce various nanomaterials through chemical vapor deposition [79]. However, there is a risk of safety hazards caused by the toxic, corrosive, flammable, and/or explosive precursor gases (e.g., SiH_4 , SiCl_4 or TiCl_4 gases) [77].

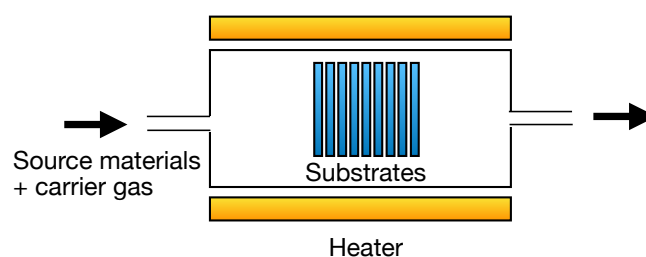


Figure 1.11. Schematic drawing of chemical vapor deposition by hot-wall heating, adapted from [80].

(4) Synthesis by Aerosol Processes

Aerosol³ based process is a common method for industrial production of nanoparticles [81]. Particle formation is driven by the generation of atoms or molecules via the chemical reaction of precursor vapors in a gas flow through a high-temperature furnace [82]. Hydrocarbon flames, joule (resistive) heating, plasmas, sputtering, ion, electron, laser beams, or hot-wall reactors are often used to provide a high-energy source in the furnace reactor [82].

Nanoparticle formation by the aerosol process through gas-to-particle conversion (illustrated at the left side in Fig. 1.12) is similar to chemical vapor deposition, except that there is no need for substrates to deposit the particles. The gaseous precursor is transformed into the final particles through a complex physical process involving nucleation, condensation of gases onto particles, and coagulation and coalescence between particles. Generated particles can be spherical or fractal-like structures with self-preserving particle size distribution [83].

Particles made by aerosol reactors can obtain high-purity powders since no additional milling process can bring impurities [84]. They are mostly thermally stable. It is considered an environmentally friendly process than the sol-gel process that results in multiple toxic byproducts [6]. Moreover, the process chain is relatively shorter than liquid sol-gel processes based on multiple batches [6].

Flame aerosol reactors have been studied for various nanoparticle production like silicon particle formation by the decomposition of silane SiH_4 [85], silica SiO_2 by the oxidation of SiCl_4 [86, 87], and titania TiO_2 by oxidation of TiCl_4 [88] and the reaction of titanium isopropoxide (TTIP) [89].

Flame spray pyrolysis (FSP) While flame aerosol reactor brought a significant production volume in nanoparticle synthesis, its preparation and handling of precursor vapor may not be trivial [36]. The continuous demands for process versatility require the replacement of vapor precursor, which is often expensive or limited in availability. This promoted a new technique - spraying liquid precursors directly into the flame - flame spray pyrolysis (FSP). Rather than injecting vapor precursors into the flame, a liquid precursor is directly sprayed by dispersion gas into the hot flame region. Then, precursor pyrolysis occurs, and particles are formed.

³An aerosol is defined as an ensemble of systems of solid or liquid particles suspended in air or other gaseous environments.

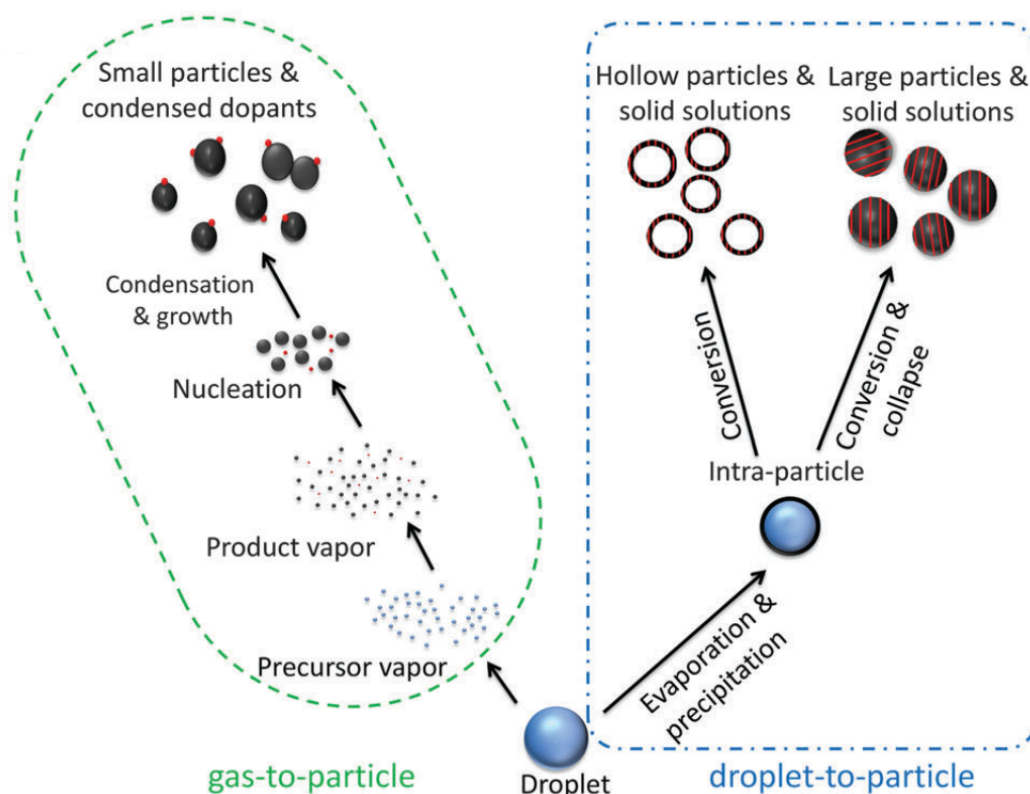


Figure 1.12. Schematic drawing of particle formation pathways during the aerosol synthesis [90].

Liquid precursor droplets can experience two pathways during the particle formation: a gas-to-particle and a liquid-to-particle mechanism, as illustrated in Fig. 1.12. In the gas-to-particle conversion mechanism, the precursor and solvent evaporate inside a high-temperature flame, forming nanoparticles through vapor phase reactions. This process is known to produce relatively homogeneous particles. This gas-to-particle conversion is promoted when droplet break-up (microexplosions) happens [91]. The droplets are divided into a much smaller size that rapidly evaporates [37]. On the other side, the droplet-to-particle conversion occurs in a relatively low-temperature environment (~ 500 °C for very porous pure or Pt-doped SnO_2 films [92]). For certain precursor-solvent mixtures, only the solvent part evaporates at low temperatures. Then the precursor precipitates on the surface of the droplets, and the rest of the solvent liquid evaporates inside the particle surface, forming hollow particles. Alternatively, large (up to micrometer) particles can be developed due to drying and solid-state densification. The droplet-to-particle conversion can result in the formation of particles that are inhomogeneous morphology and size, especially when endothermic precursors reduce the flame temperature significantly [36].

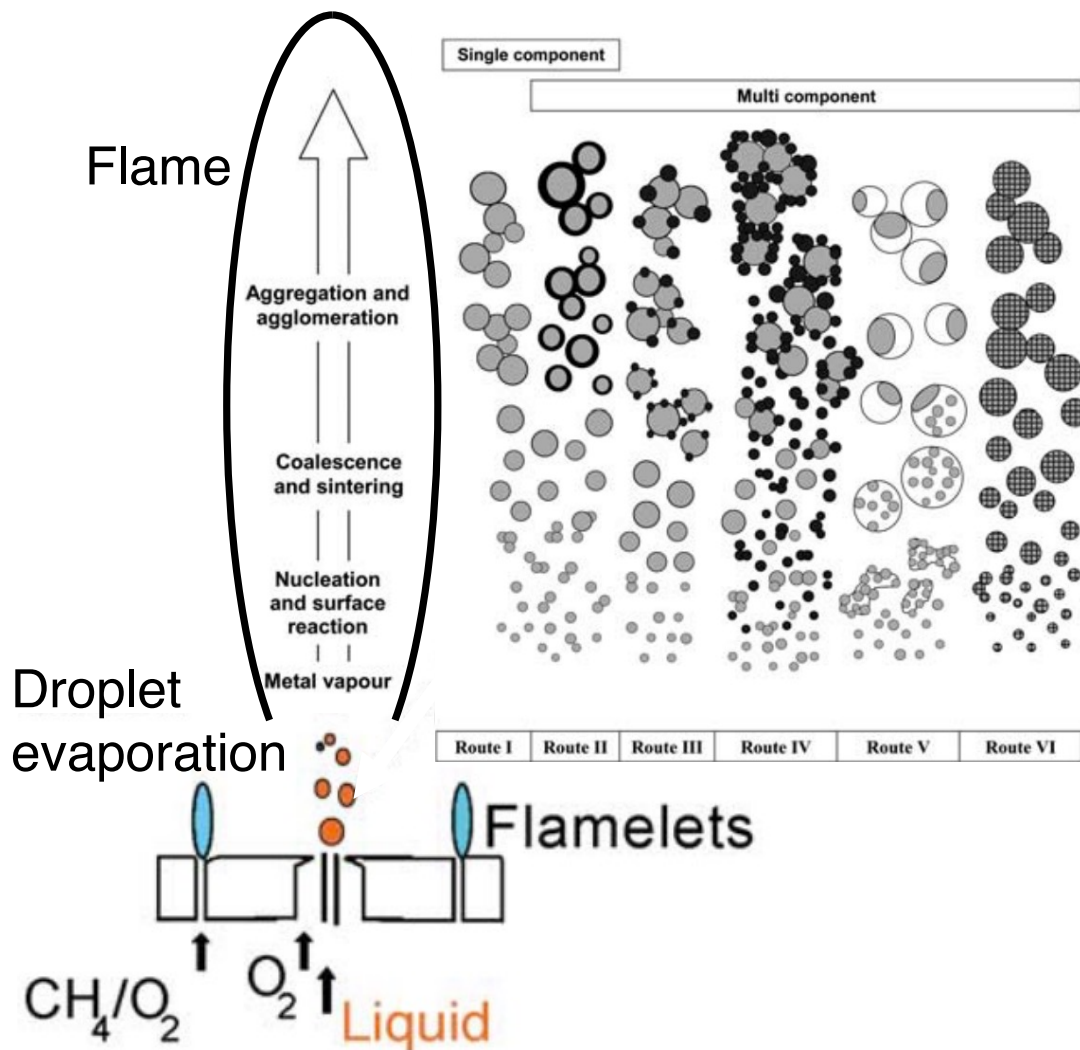


Figure 1.13. Flame spray pyrolysis: a spray jet is introduced into the flame through a two-phase nozzle, supported by pilot flamelets on the face of the burner to ensure stable combustion. A flame is generated from the main jet, where particle formation takes place by nucleation, coagulation, and coalescence or agglomeration (left side). The formation of different particle configurations via the gas-to-particle mechanism for single and multicomponent systems is illustrated at the right side [93, 36].

The structure of the flame spray pyrolysis reactor is schematically illustrated in Fig. 1.13. It consists of an atomizing nozzle (ultrasonication or pressure-assistance) for dispersion (mostly by oxygen) of the liquid metal-containing precursor-solvent mixture (mainly based on organic solvents) forming a spray flame. The center flame is surrounded by co-flow streams of gaseous fuel and oxidant feeding the pilot flame. In terms of the particle formation process, the vaporization of the liquid precursor step is added to the gas-phase aerosol process. The details for each formation step will be described in the next chapter.

The properties of the product can be varied over an extensive range of morphology and sizes by selecting precursor mixture, flame, and nozzle parameters [94]. Different formation routes for a single and multi-component particle in a gas-to-particle mechanism are described on the right side of Fig. 1.13. Each route is briefly presented below:

- Route I: Single oxides or carbonates⁴ are produced with single metal component precursors like alkaline metals.
- Route II: Nanoparticles can be covered with a surface carbon layer by limiting the presence of O₂ which is needed for the consumption of carbon sources.
- Route III: In case of introducing a secondary component whose amount is insufficient for full encapsulation or when phase segregation occurs, deposit-supported particles on other nanoparticles can be generated.
- Route IV: Different particle phases may tend to segregate completely with little miscibility⁵ allowing only physical inter-particle mixing.
- Route V: Segregation of phases could happen within a single particle; molten particles envelopes the precipitated particles, producing multi-core structures. At the same time, the encapsulation layer acts as a diffusion barrier, retarding the agglomeration and sintering of the core particles.
- Route VI: When multi-elements are highly miscible, a wide variety of configurations of materials could occur; doped materials, solid solutions (homogenous mixture of two solid states and have a single crystal structure), dispersed mixed oxides, complex metal oxides, and metal alloys.

The detailed description can be found in [36].

In this manuscript, the aerosol reactor using flame as a heating source in the furnace is distinguished from flame spray synthesis. These differences between the two production frameworks are summarized in Tab. 1.1 and Fig. 1.14. The aerosol reactor uses combustion to ensure the high temperature in the reactor. It was mainly used for manufacturing simple commodity powders such as carbon black, pigmentary titania, fumed silica, and alumina, as described above.

On the other hand, in flame spray synthesis, the flame is the principal zone where particle formation occurs, and its dynamics directly affect the quality of the produced particles. Particle properties like crystallinity or morphology are determined by the trajectory and the residence time of the particle inside the flame. For example, the longer the particle is exposed to high temperatures, the higher the final particle can feature a strong crystalline structure [95]. As a consequence, in terms of particle formation, steep temperature gradients with short residence time in the FSP are the principal distinction from furnace reactors using flames in large-scale production.

The FSP reactor can realize the sophisticated control over particle size and morphology to engineer a broad range of products, previously limited in production because of thermal stability or complicated synthesis technique. For example, in the formation of doped particles (Route II in Fig. 1.13), the FSP can be advantageous because the steep temperature gradient and short residence time prevent segregation of the dopants (Route IV in Fig. 1.13) and enhance substitutional dopant concentrations [36].

⁴Carbonates are characterized by the presence of carbonate ion CO₃²⁻

⁵Property of two substances to mix in all proportions, forming a homogeneous mixture.

Those temperature-time characteristics in the FSP process could also be beneficial to produce metastable materials like δ -bismuth oxide [96] and ϵ -tungsten oxide [97] in ambient conditions. The formation of the metastable phase results from the lack of time to recrystallize into the more stable phases during the formation trajectory of particles. For instance, a promising material for use as a battery and catalyst, $\text{TiO}_2(\text{B})$, was previously developed based on multi-step processes like sol-gel [98], or microwave [99] processes. Riad et al. [8] produced $\text{TiO}_2(\text{B})$ via flame spray pyrolysis for the first time with a one-step process.

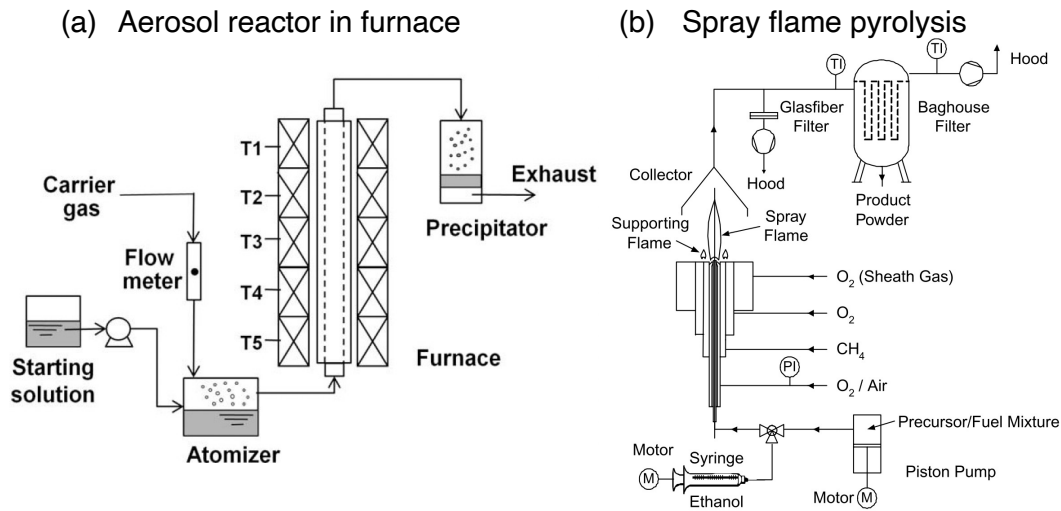


Figure 1.14. Illustration of the typical aerosol reactor in (a) furnace [100] and (b) spray flame pyrolysis [101]. In the aerosol reactor in the furnace, the gas-to-particle transition occurs inside a high-temperature furnace heated by a heating source. In spray flame pyrolysis, the flame itself is both a heating source and the particle formation zone at the same time.

Table 1.1. Differences between the furnace reactor and spray flame pyrolysis.

	Aerosol reactor in furnace	Spray Flame pyrolysis
Scale	industry	laboratory
Residence time	long	short
Temperature gradient	smooth	steep
Application	conventional mass production	development of new materials

1.4 Titanium dioxide

In this thesis, we are interested in TiO_2 particles. TiO_2 is the second largest commodity made by flame reactors. It is used in the paint, cosmetics, power, pharmaceuticals, biomedical, food, and plastic industry [3]. Three representative crystal polymorphs and some specific features of TiO_2 will be described with their applications. Then, the typical industrial manufacturing processes are presented.

1.4.1 Crystal phase

Titanium dioxides include one titanium atom in the lattice, surrounded octahedrally by six oxygen atoms. Each oxygen atom is surrounded by three titanium atoms in a trigonal arrangement. The three crystal phases correspond to different ways of linking the octahedra at their corners and edges: rutile, anatase, and brookite, illustrated in Fig. 1.15 and Fig. 1.16. They can also exist in other crystal phases like $\text{TiO}_2(\text{II})$ [102], $\text{TiO}_2(\text{H})$ [103] and monoclinic $\text{TiO}_2(\text{B})$ [104] or in amorphous state⁶.

The crystal phase can be changed by heat treatment. At temperature above 400 °C, the surface area of amorphous TiO_2 decreases with heating because of the collapse of pores in the TiO_2 powder. It causes the transformation of amorphous TiO_2 to the anatase phase [105]. Slow heating rates provide relatively mild phase transformation [106]. The anatase-to-rutile phase transformation is frequently reported to undergo in the range from 600–700°C in the air in the absence of dopants or impurities [107, 108, 109]. The transition during sintering is simulated via molecular dynamics [110]. The transition is also affected by various factors such as preparation conditions, precursors, impurities, oxygen vacancies, and the primary particle size of the anatase phase [110].

The characterization and performance evaluation of flame-made TiO_2 nanopowders depend strongly on their crystallinity. The different physicochemical properties of each phase are based on the specific molecule structure of each crystal polymorph (Fig. 1.16, and Table 1.2). As shown in Fig. 1.16, the crystal structure with different numbers of atoms per unit cell results in the distinctive geometry of each crystal. Rutile shows the highest density with the smallest unit cell volume and the highest real part of the refractive index. All the polymorphs are not soluble in water.



Figure 1.15. Three crystal forms of titanium dioxide in nature [111].

⁶The amorphous state is a non-crystalline state. It is defined as a glassy solid state lacking the long-range order in the crystal phase.

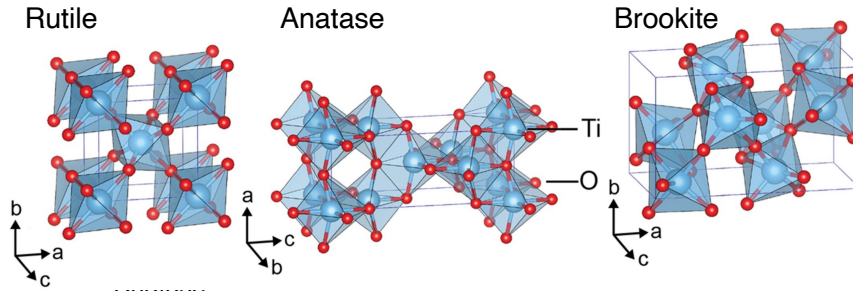


Figure 1.16. Three-dimensional representation of crystal structures of TiO_2 rutile, brookite, and anatase polymorphs [109]. Ti atoms are represented in round blue balls, and O is described in red point.

Table 1.2. Properties of anatase, rutile, and brookite. For the refractive index, values are given for the three coordinate axes in the order of least, intermediate, and greatest index (for brookite) [108, 112]. For the lattice parameter, see Fig. 1.16 for the coordination.

Property	Anatase	Rutile	Brookite
Crystal structure	Tetragonal	Tetragonal	Orthorhombic
Atoms per unit cell (Z)	4	2	8
Lattice parameters (nm)	a = 0.3785 c = 0.9514	a = 0.4594 c = 0.29589	a = 0.9184 b = 0.5447 c = 0.5154
Unit cell volume (nm^3)	0.1363	0.0624	0.264
Density (kg/m^3)	3894	4250	4170
Refractive index (real part)	2.54, 2.49	2.79, 2.903	2.583, 2.584, 2.700
Solubility in Hydrofluoric acid (HF)	Soluble	Insoluble	Soluble
Solubility in H_2O	Insoluble	Insoluble	Insoluble

1.4.2 Key features and applications

Mechanical properties

TiO_2 is a very robust material with high hardness and toughness (Rutile: Mohs hardness 6.5 - 7, Anatase: Mohs hardness 5.5 [3], Graphite: Mohs hardness 1-2 [112] for reference). Rutile has high hardness because of the highest density and the most compact atomic structure than other crystal phases of TiO_2 . It is used as an additive for strengthening the material and increasing

wear resistance [68]. It can also be used as anticorrosive coatings for steel products [29].

Optical properties

TiO₂ has a wide band-gap whose energy difference between the valence and the conductivity bands in the solid state is 3.05 eV (415 nm) for rutile and 3.29 eV (385nm) for anatase (0.18 - 1.31 for soot in a non-premixed flame [113] for reference). Due to this large band-gap, it absorbs principally electromagnetic radiation in the near UV region.

It is well known for its strong absorption in both UV-A (320-400 nm) and UV-B (280-320 nm) radiation [114], which makes it serve as a sunscreen in the cosmetic industry. It is used as a pigment, a whitener, and a shimmer brightener as it reflects the light in the visible range with a low extinction coefficient in the visible range [3].

Photocatalytic properties

TiO₂ nanoparticles are well known for their photocatalytic capacity. A photon irradiation greater than the band-gap energy generates electrons (e⁻) and holes (h⁺) in conduction and valence bands of TiO₂, respectively as illustrated in Fig. 1.17. Then, redox (reduction-oxidation) reactions can take place at the surface of these photogenerated electrons and holes.

If the TiO₂ nanoparticles are suspended in water, they form hydroxyl ions (OH⁻) (Fig. 1.17). Hydroxyl radicals can convert organic pollutants into carbon dioxide and water and destroy the cell structure of bacteria in wastewater treatment [3, 115]. Therefore, it is widely used as a self-cleaning/self-disinfecting additive in the product (e.g., cement) under sun irradiation. This photocatalytic activity is enhanced with a smaller TiO₂ particle size, with an increasing fraction of atoms located at the particle surface [116]. The degree of photocatalytic efficiency is generally higher for the anatase phase [117].

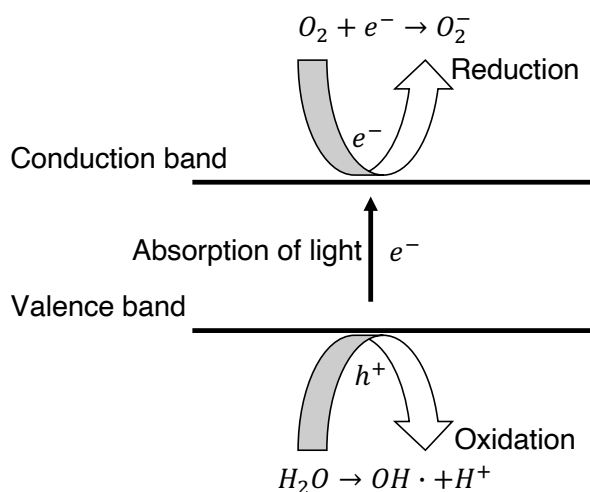


Figure 1.17. The mechanism of semiconductors acting as photocatalysts. Typical oxidation and reduction reactions are shown. Oxidation of water by an electron-hole forms hydroxyl radicals OH[·], which are powerful oxidizing agents.

1.4.3 Laboratory-scale TiO₂ synthesis in flame reactor

On a laboratory scale, the production of particles from TiCl₄ precursors has been widely investigated in various flame reactors with its relatively simple chemical structure. The kinetic mechanism of TiCl₄ oxidation has been studied both theoretically [118, 119] and experimentally [120, 121] in the flame synthesis of nanoparticles.

After the 2000s, with growing concerns against the release of hazardous chlorine HCl from the reaction, studies with safer precursor TTIP (titanium tetraisopropoxide, Ti(OC₃H₇)₄) have evolved in laboratory-scale nanoparticles productions in flame synthesis.

The synthesis in flames [30] or hot-wall reactors [122] has been extensively investigated [123]. Conditions for the preparation of well-defined size and structure of particles have been determined in terms of temperature, particle cooling rate, and precursor concentration [124].

In academic research, small laminar flames are commonly used because of their simplicity in describing nanoparticle growth models. In this study, the discussion in the following chapters will be focused on the production of TiO₂ particles in laminar co-flow flame based on TTIP precursor. Even if a deep understanding of particle formation in turbulent flames is essential for expanding the knowledge to large-scale industrial aerosol reactor design [81], laminar flames represent the fundamental first step towards such understanding.

1.4.4 Industrial manufacturing processes of TiO₂

There are two most broadly adopted production processes for pigment level titania on the industrial scale market; sulfate and chloride.

The sulfate process is a kind of sol-gel process (Fig. 1.5). The sulfate process is more economical as it uses low-grade and cheaper ores and less complicated technology to manufacture titanium dioxide. However, a large amount of waste material is generated during the process technology, increasing pollution control costs. In Europe, around 70% of the market used the sulfate process in 1995 [3].

On the other side, the chloride process, commercialized in the early 1950s, offers less waste disposal, lower cost, and quality advantages over the sulfate process [125]. It is an aerosol process (Fig. 1.5). This process mainly uses high rutile component feedstocks, like rutile and synthetic rutile (90% - 95% TiO₂), avoiding the iron sulfate waste problem [126]. Still, there exist toxicity problems with Cl₂ and TiCl₄. The North American market is mostly chloride-based, with most manufacturers adopting the chloride process (over 98% in terms of volume in 2019 [127]). The global manufacturers are focused on shifting toward the chloride process (60% in world production [126, 78]) due to environmental considerations and end-use requirements for high-quality titanium dioxide [128].

A number of industrial products require well-defined properties of TiO₂ for a specific application. The most important applications of non-pigmentary nanoscale TiO₂ are enamels and ceramics (25–30%), glass and glass ceramics (25–30%), electroceramics (10–15%), catalysts and catalyst supports (10–15%), welding fluxes (10–15%), and others [3, 129]. Especially for catalysts, Degussa already adopted flame aerosol technology to produce the P25 TiO₂ photocatalyst, which is the standard material in photocatalysis [130].

The detailed sulfate and chloride process are summarized in Appendix A.

1.5 Conclusion

This study aims to investigate flame-generated nanoparticles. In this chapter, the generalities of nanoparticles are reviewed. First, the definition and distinctive properties of nanoparticles that appear only in nanoscale materials, which bring commercial and scientific interests, have been revised. Several nanoparticle manufacturing methods have been presented with a focus on aerosol synthesis and flame spray pyrolysis (FSP). Then, the primary target material in this study, titanium dioxide (TiO_2), was presented in terms of its unique properties and laboratory/industrial scale production.

The versatility of the FSP process can lead to the breakthrough of the emerging market of nanoparticles, which demands more sophisticated and complex nanomaterials in a relatively simple way than the conventional liquid batch process. Especially for TiO_2 , whose photocatalytic capacity brings enormous potential for electrochemical applications, the FSP method can cover the needs for developing high-end nanoparticles, including multi-component based on TiO_2 that are already broadly investigated in various fields. Readers interested in further information can refer to the review paper by Liu et al. [44].

Despite all the claimed potentials of the FSP process for particle/thin film production over the last 30 years [131, 132], there is still no industrial mass-production process applying FSP. Nevertheless, the scale-up of the FSP has been demonstrated for the production of silica and titania [31], zirconium oxide as catalyst support [133] up to g/h scale. There are also several new companies and university spinoffs like Nanocerox (USA), Engi Mat (USA), HeiQ (Switzerland), TurboBeads (Switzerland), Avantama (Switzerland), Smartodont GmbH, Hemotune AG, and Anavo medical currently producing nanoparticles via flame spray synthesis for different applications.

Some points should be improved for mass production via FSP: the production costs should be reduced using economic metal salts (nitrates, chlorides, acetates) with inexpensive precursor [37]. The use of hydrocarbon fuel for combustion can risk a carbon footprint [134]. The complexity of the process due to fast particle growth is still challenging for process scale-up. Therefore, a better understanding of the particle formation mechanisms is essential for both controlling product qualities and facilitating the design and operation of flame reactors for a high production rate. In particular, how process variables affect the properties of the particles at each stage of the formation allows the synthesis of materials that are more efficient than those available by other processes. The size distribution, morphology, aggregation level, and chemical and phase composition should be attentively monitored under local operation conditions in flames (temperature, local stoichiometric conditions (lean vs. rich), and mass flow rate of fuel and oxygen) to guarantee high-quality products. The thesis is written in this context to develop an optical diagnostic to pursue the formation of TiO_2 in the flame. The detailed formation mechanisms will be discussed in the next chapter.

Chapter 2

Nanoparticle formation process in flame synthesis

Flame technology can generate advanced nanomaterials for catalysts or gas sensors [135]. The size, morphology, surface characteristics, and composition of particles strongly influence the performance of the final nanomaterials. These particle characteristics are closely related to the turbulent spray flame environment. Thus, the control of the formation of fine particles is critical for designing aerosol synthesis.

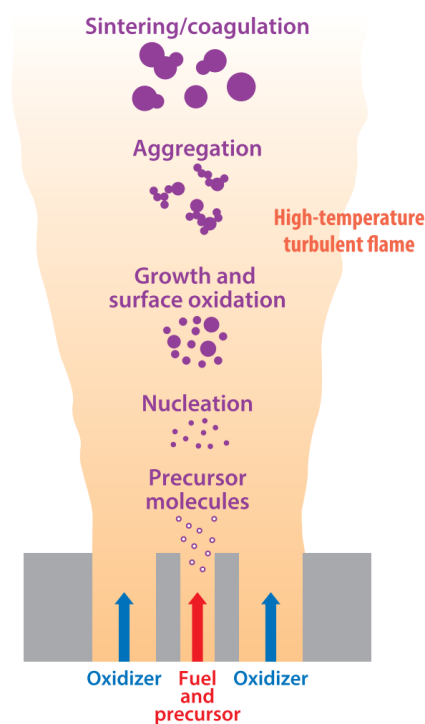


Figure 2.1. Schematic of particle formation in a flame [136].

In the flame synthesis of metal oxide nanoparticles, an oxidizer, a fuel, and a metal-containing precursor are injected into the system. The overall process is schematically illustrated in Fig. 2.1. The smallest solid phase particles in the system, nuclei, are formed from gas-phase precursors. The particles then grow in size through surface reactions and collide with each other, leading to aggregates/agglomerates. Under specific conditions (usually high temperature-flame front zone), the constituent particles inside an aggregate can partly/entirely fuse to form larger particles via sintering. The importance of each formation step to the final product depends on the type of particles and process conditions, including temperature, flow rate, and precursor loading. In the case of spray flame synthesis, the evaporation of liquid precursor spray can complicate the particle formation system. In this study, the liquid precursor will be completely vaporized by an external heating source before its injection to avoid any difficulties linked with the liquid phase and its interactions with the reactions.

In this chapter, the formation during the flame synthesis of nanoparticles will be presented. The discussion is oriented on metal oxide nanoparticle formation through flame synthesis. After introducing terminology and target design parameters to describe the particle geometry in Sec. 2.1, a detailed description of each stage of formation in a flame (nucleation, surface growth coagulation, and sintering) is presented in Sec. 2.2 with a focus on the evolution of the target parameters.

2.1 Terminology

Before presenting a detailed description of each process, it should be mentioned that terminology used to describe the processes by which two colliding particles combine to form a single particle (or aggregate/agglomerate) can be confusing due to the different use of the same term in different scientific fields. For example, the process by which two particles collide and become a single particle without changing the total surface area is called aggregation in the physics literature and agglomeration in flame-generated particles (Fig. 2.2). In this study, we will follow the same definition used in the review article of Michelsen et al. [137].

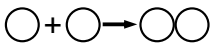
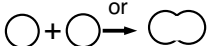
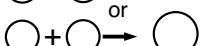
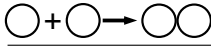
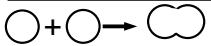
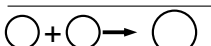
	Flame-generated particle	Keyword
  	Coagulation	“join particles together” Including coalescence, aggregation, and agglomeration
	Agglomeration	“loosely attached”
	Aggregation	“firmly bound”
	Coalescence (sintering)	“into one”, “liquid-like”

Figure 2.2. Processes by which colliding particles join together. Each particle is illustrated as a spherical monomer for ease of description, but it could also apply to the collision between two aggregates/agglomerates

The processes leading to the formation of a single particle/aggregate of surface area s as a result of the collision of two particles/aggregates of surface area s_1 and s_2 , respectively, are:

- **Coagulation:** the process by which two particles (or aggregates) stick upon collision regardless of whether they fuse ($s \leq s_1 + s_2$).
- **Agglomeration:** the combination of two existing particles into a single particle (or aggregate) without changing the total surface area, loosely attached, generating agglomerates ($s \simeq s_1 + s_2$). The clusters of (primary) particles or spherules held together by weak physical (e.g., van der Waals, electrostatic, or capillary) forces are called **agglomerates**.
- **Aggregation:** the process by which two or more particles are firmly bound together, generating aggregates ($s < s_1 + s_2$). The clusters of (primary) particles or spherules held together by strong chemical forces, with the formation of bridges or necks primary particles are called **aggregates**
- **Coalescence:** the process by which two or more particles remove any boundary between them ($s < s_1 + s_2$).

Target design parameters

Some target design parameters to describe the geometric structure of flame-generated fine particles are presented in this section. For simplicity, aggregates and agglomerates will not be differentiated in the following brief description of each particle, which is schematically shown in Fig. 2.3.

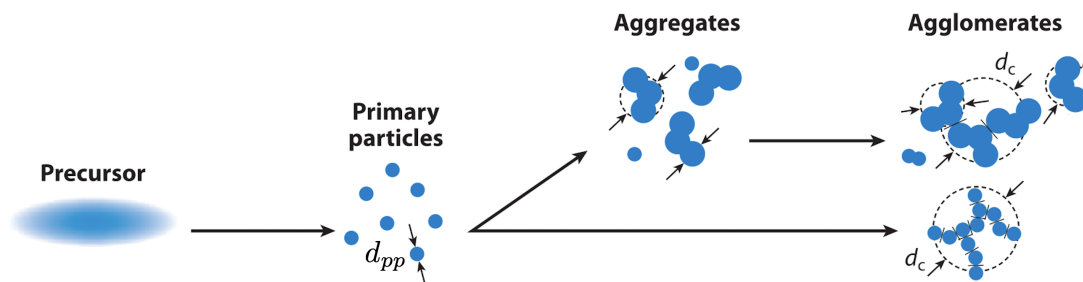


Figure 2.3. Overview of the evolution of aerosol growth. d_{pp} is the primary particle diameter, d_c is the collision diameter. Adapted from [78].

The target design parameter to describe the particles during/after the formation are :

Primary particle diameter d_{pp} The basic sub-unit constituting the aggregates/agglomerates. The primary particle diameter of flame-generated fine particles typically have a size of tens of nanometers diameter (unity [nm]).

Collision diameter d_c The collision diameter d_c [78] depends on the particle morphology. It is closely related to the collision efficiency, i.e., how frequently the particles collide and has the possibility to interact during the interaction between two particles [138, 139] (unity [nm]):

$$d_c = \sqrt{5/3} \cdot d_{pp} \left(\frac{n_{pp}}{k_0} \right)^{1/D_f} \quad (2.1)$$

where D_f is the fractal dimension, n_{pp} is the number of primary particles in the aggregate, and k_0 is the scaling prefactor.

Primary particle number n_{pp} is the average number of primary particles per agglomerate. If $n_{pp} = 1$, the particle is a geometrical sphere.

It has been shown that the primary particle number can be empirically estimated from electric mobility¹ measurement [140]:

$$n_{pp} = (d_m/d_{pp})^{0.45} \quad (2.2)$$

where d_m is mobility diameter.

Fractal dimension D_f is a parameter to characterize the morphology of aggregates/agglomerates. Large fractal dimension $D_f = 3$ denotes compact spherical geometry, while $D_f = 1$ corresponds to an open string shape (dendritic agglomerate).

The evolution of the fractal dimension D_f of aggregates produced in a furnace is illustrated in Fig. 2.4 as a function of the temperature or residence time. The longer the particles are exposed to high temperatures, the more they form a compact-spherical shape with D_f near 3. The mobility diameter d_m decreases during sintering because particles become compact in geometry while the primary particle diameter d_{pp} grows until both become identical for a fully coalesced sphere.

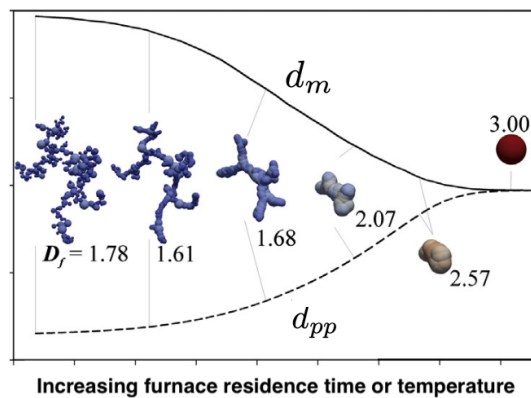


Figure 2.4. Evolution of aggregate mobility d_m and primary particle diameter d_{pp} during sintering of aggregates. Adapted from [141].

¹When a charged particle suspended in a gaseous medium is placed in an electric field, the particle experiences a force which is dependent on its charge (mobility) and the strength of the electric field.

Surface area concentration S is the total surface area of aggregates (unity $[\text{m}^2/\text{m}^3]$).

Number density/concentration N is the number of specified objects per unit volume (unity $[\#/ \text{m}^3]$).

Volume fraction/concentration f_v is the total volume of the component divided by the sum of volumes of all components used to constitute the mixture. It can also be described as the volume of particle times the number density (unity of $[\text{m}^3/\text{m}^3]$).

Particle-size distribution (PSD) describes how the particle size is distributed in the control volume². In the case of mono-dispersed particles, all particles in a control volume have the same volume. Those distributions are often described with total number concentration N , geometric mean diameter d_{geom} -which is equal to the count median diameter (d_{CMD}) in case of a log-normal distribution of particle size- and the standard deviation σ_g of particle size distribution. The geometric mean diameter d_{geom} is defined as the n^{th} root of the product of n numbers of primary particle diameter, i.e., for a set of numbers of primary particle diameter d_1, d_2, \dots, d_n , the geometric mean is defined as:

$$d_{\text{geom}} = \left(\prod_{i=1}^n d_i \right)^{(1/n)} = \sqrt[n]{d_1 d_2 \cdots d_n} \quad (2.3)$$

In the next part, each particle formation process will be described with the evolution of these target geometric parameters. Each stage will be explained based on metal oxide synthesis in flames, especially for the case of TiO_2 formation with the precursor of TTIP.

2.2 Nanoparticle production processes

2.2.1 Nucleation

Nucleation is the process of solid-particle formation from gas-phase precursors. The transition of gas-phase-precursor species to condensed-phase particles occurs when the properties (e.g., density, specific heat, and optical properties) of the particle or cluster depart from those of gas-phase species from which it is composed and begin to exhibit properties of a solid particle [137]. Spherical particles of size d_{pp} are generated. As more particles are generated in the control volume, the total number, number density N , volume fraction f_v , and total surface area S will increase.

The modeling of particle formation of nucleation remains challenging [142, 143].

2.2.2 Surface growth

Surface growth describes the process by which gas-phase species are added to the surface, increasing the mass. Surface growth can occur at any stage of formation by condensation-like

²Target space of unit volume where we consider the particle aerosol.

mechanisms, including condensation (gas-to-liquid phase transition), deposition (gas-to-solid phase transition), physical and chemical adsorption (interfacial uptake of material that is not the result of a thermodynamic phase transition) [137]. As a result, the primary particle size d_{pp} grows as well as volume fraction f_v and total surface S . The number density N is kept constant.

2.2.3 Coagulation

Coagulation is the process by which two particles stick upon collision, regardless of whether they fuse, as illustrated in Fig. 2.2. When the two particles adhere through the van der Waals forces to form larger structures, but with unchanged constituent particles, it is called **agglomeration**. The resultant particles are called agglomerates. In most high-temperature flames, pure agglomeration is rarely observed [136]. Instead, **aggregation** can occur when two or more particles are firmly bound together, generating aggregates.

During agglomeration and aggregation, the total surface S and number concentration N are reduced while the volume fraction is conserved. Generally, during particle growth by Brownian coagulation, highly concentrated nanoparticles reach an asymptotic self-preserving size distribution (SPSD) [144]. This distribution of primary particle diameter remains time-invariable, with a geometric standard deviation $\sigma_g = 1.44$ and 1.46 for the continuum and free molecule regimes, respectively [78, 145].

The aggregate/agglomerate diameter d_c increases with an increased number of primary particles n_{pp} within one aggregate/agglomerate. Previous extensive studies have described the aggregates and agglomerates with their fractal geometry D_f [141]. When particles collide without sintering, fractal-like agglomerates of gyration radius r_g are formed consisting of n_{pp} primary particle of radius r_{pp} following a power law [146]:

$$n_{pp} = k_n \left(\frac{r_g}{r_{pp}} \right)^{D_f} \quad (2.4)$$

where k_n is pre-exponential factor, D_f is the fractal dimension. The D_f value depends on the collision mechanism of the growing aggregates [123]. A mass fractal dimension $D_f = 1.8-1.9$ with pre-exponential factor $k_n = 1.4$ are common values for agglomerates [147].

2.2.4 Sintering

In metal oxide particles, when the flame temperature is higher than the melting point of the particles, the particle surface area for a given particle volume can be reduced in a liquid-like phase manner [148]. When primary particles within agglomerates sinter, they become more compact aggregates than agglomerates, eventually leading to spherical particles.

The sintering rate is highly sensitive to the surface area of the particles and the local gas-phase temperature [78]. Smaller primary particles will lead to higher sintering rates due to larger surface areas, as they are more exposed to high temperatures. On the contrary, temperature reduction or higher precursor concentrations (which will increase the particle diameter) will reduce sintering rates [136]. The sintering process dominates the growth of the aggregates through the flame front (where the combustion takes place) and is responsible for determining its final

morphology and dimensions. Through the sintering process, the size of the average primary particle diameter d_{pp} increases while the number of particles in an aggregate n_{pp} is reduced, which narrows the size distribution of the primary particles in aggregates. Eventually, the average aggregate mobility size also decreases with further sintering, as in Fig. 2.4.

2.3 Conclusion

Table 2.1 summarizes the effect of each formation stage on each parameter. The primary particle diameter d_{pp} increases during the surface growth, aggregation and the coalescence (sintering) stages. During the agglomeration process, the primary diameter is conserved whereas the number of primary particles in aggregates/agglomerates n_{pp} increases. The fractal dimension D_f evolves into a more spherical form under the coalescence and aggregation stage. For the agglomeration stage, the value of D_f will depend on other operating conditions whether to form a chain-like or more compact geometry.

The total surface S and the number N concentration will grow during the nucleation. N decreases during the coalescence and aggregation steps while the total surface S will be conserved during the agglomeration stage. In terms of volume fraction f_v of particles, it will increase during the nucleation and surface growth. The volume fraction of particles in the control volume remains constant during the coagulation process.

Note that sintering affects in a similar way to coalescence (two colliding particles/aggregates), but since it concerns the phenomenon inside one aggregate/agglomerate, the number of primary particles in an aggregate n_{pp} decreases, and the total number concentration N is conserved [149]. During sintering, f_v may change due to phase changes, such as from solid to liquid, or from one crystal polymorph to another, such as from anatase to rutile in the case of TiO_2 . Modeling the sintering of nanoparticles generally involves the conservation of volume fraction, as shown in the literature [149].

Table 2.1. Overview of aerosol growth processes with their effect on each design parameter. d_{pp} is the primary particle diameter, n_{pp} the number of primary particles in an aggregate, D_f fractal dimension, S total surface concentration, N total number concentration, number density, and f_v volume fraction. The symbol + signifies a favorable effect, - a decrease in that stage, = same level as previous steps or invariant in that stage, +/- depending on the operating condition.

Parameters	Nucleation	Surface growth	Coagulation			Sintering
			Coalescence	Aggregation	Agglomeration	
d_{pp}	constant	+	+	+	=	+
n_{pp}	1	=	=	+	+	-
D_f	.	.	+(sphere-like)	+(sphere-like)	+/-	+(sphere-like)
S	+	+	-	-	=	-
N	+	=	-	-	-	=
f_v	+	+	=	=	=	=/-

The order/importance of each formation process can vary depending on the operating conditions

and flame structure. For example, Ma et al. [150] showed via numerical simulations that by increasing the inlet oxygen/nitrogen ratio, a higher temperature zone is observed in the coagulation/coalescence stage, consequently increasing the particle size. The increase in precursor concentration results in more seed particles produced by nucleation leading to a higher collision rate and, consequently, a larger collision diameter [150]. Increasing temperature can significantly change the mean particle size even if the shape of the size distribution will not change, as already discussed, with a geometric standard deviation $\sigma_g \approx 1.4$ [151].

Finally, particle flame synthesis includes multiscale and multiphase interactions, and each of them can completely change the morphology of final product particles. A complete characterization of the gas and solid phases of each particle formation stage is needed for further development of advanced nanomaterials. In the next chapter, the major diagnostics to characterize particle formation in flames will be introduced by discussing their advantages and inconveniences.

Chapter 3

Techniques for the characterization of nanoparticle morphology and composition

The characterization of nanoparticles is essential to understand the particle formation process, to optimize the reactor, and to develop a scale-up production of nanoparticles. Since nanoparticles' size range directly influences product properties, the characterization of nanoparticles' morphology and composition is indispensable to control the quality of produced particles.

Due to the complexity of the simultaneous appearance of various physicochemical processes, aerosol measurements in high-concentration and high-temperature environments are often challenging. Accordingly, ex-situ measurements, which require extraction of particles from the zone of interest, are frequently used [6].

Alternatively, on-line measurement, which measures the particle properties in real-time but not necessarily in the synthesis location, is also of great interest for monitoring industrial synthesis processes. Yet some on-line measurements can require a dilution during the sampling [152], which might result in changes in the morphology of particles during the extraction of samples.

Therefore, the necessity of in-situ measurement, which measures particle properties during the particle synthesis in a quasi-non-intrusive feature, arises. The use of in-situ optical diagnostics that do not interfere with the reaction process can successfully describe the effect of the local environment during particle formation. However, due to the multi-scale and multi-phase nature of particle flame synthesis, the interpretation of signals can become challenging.

In this chapter, diagnostics for nanoparticle properties will be discussed in terms of morphology and composition. Typical ex-situ methods (Sec. 3.1), on-line methods (Sec. 3.2), and in-situ methods (Sec. 3.3) will be described along with their characteristics and applications, with a focus on the properties of metal oxide nanoparticles, especially those of TiO₂ nanoparticles.

3.1 Ex-situ methods

3.1.1 Scanning electron microscopy (SEM) and transmission electron microscopy (TEM)

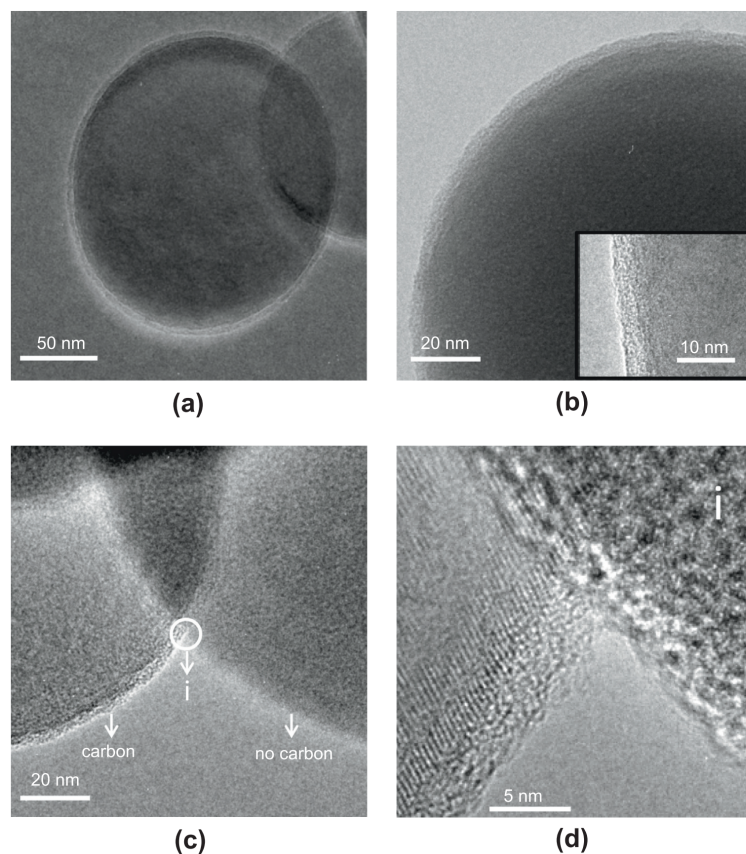


Figure 3.1. TEM images of the carbon-coated TiO_2 particles generated in $\text{H}_2/\text{O}_2/\text{Ar}$ multiple diffusion flame with TTIP precursor in a carrier gas C_2H_4 are shown [134]. The presence of C_2H_4 in the flame promotes the formation of carbon coating around the TiO_2 particles. (a) The growth of a spherical carbon-coated TiO_2 particle is observed. (b) A uniform carbon coating is observed around TiO_2 particles, with a high-resolution TEM (HRTEM) image of the carbon coating (3 – 5 nm) shown in the bottom-right inset. (c) The growth of two TiO_2 particles from the same experimental run is shown, where one is coated with carbon and the other is not coated. (d) A HRTEM image shows that the coated particle is crystalline (left) while the other particle is amorphous (right) without the carbon coating.

Transmission electron microscopy (TEM) and scanning electron microscopy (SEM) methods are widely used for particle characterization, allowing investigation of geometric primary particle diameter, aggregate size distribution, and morphology [153, 154, 155]. TEM image are often used as a reference for validating size and structure obtained from other techniques [12]. Generated particles can be filtered from the exhaust gases or harvested through thermophoretic

deposition onto surfaces such as sampling grids. These grids are inserted into the target region of interest for a short period (tens of milliseconds), during which the temperature gradient between the hot flame and the cold grid creates a thermophoretic force that deposits particles onto the grid. This deposition process can occur during the insertion and retraction phases, rather than necessarily at the target position in the flame synthesis. The deposited particles are then imaged using transmission or scanning electron microscopes (TEM/SEM). Statistical information is extracted from these images through additional image processing using various contour recognition algorithms [156, 157, 158].

The high cost and time-consuming nature of the sampling and probe preparation procedure are the main drawbacks of TEM. Due to the use of electron beams, TEM requires a high vacuum condition (<0.01 Pa) inside of microscope and is limited to studying solid matter with a thickness less than 100 nm that does not evaporate or degrade under low pressure and heating from the electron beam. Therefore, in studies of spray flames, it is generally recommended to sample particles in the droplet-free region to avoid residual droplets that can cause permanent damage to the sample grid [6].

The crystallographic information of the nanoparticles can be obtained using High-resolution transmission electron microscopy (HRTEM), which provides atomic-level structural details. Individual nanoparticle crystallinity and phase composition can be determined by analyzing Selected Area Electron Diffraction (SAED) patterns with lattice fringes [8]. In the flame synthesis of TiO_2 nanoparticles, 3-window method [159], which involves mapping of titanium, oxygen, and carbon elements and the ionization edges can be used to generate the elemental mapping. The 3-window method enables differentiation between the carbon coating and core crystal TiO_2 [134], as shown in Fig. 3.1.

3.1.2 X-ray diffraction (XRD)

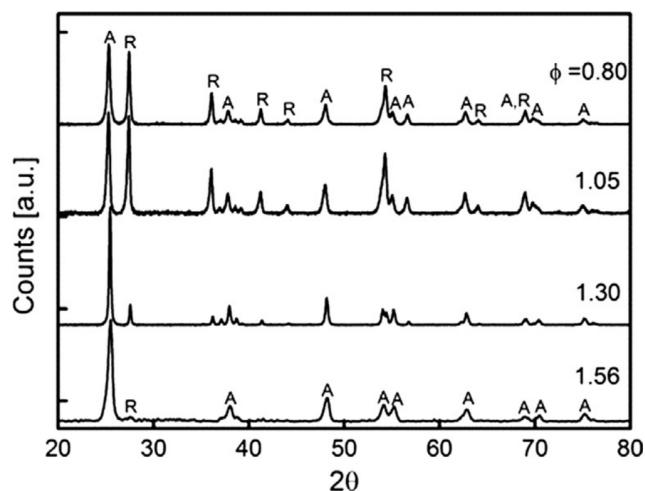


Figure 3.2. X-ray diffraction (XRD) patterns of TiO_2 nanoparticles synthesized in a curved wall-jet burner with $\text{C}_2\text{H}_4/\text{Air}$ premixed flame at different equivalence ratios (ϕ). The peaks labeled as A and R correspond to the anatase and rutile phases of TiO_2 , respectively. As seen in the figure, at high ϕ values, only the anatase phase is detected, while as the ϕ value decreases, the rutile phase appears. The intensity ratio of the anatase and rutile peaks is often used as an indicator of the crystallinity of the synthesized TiO_2 nanoparticles. [160].

X-ray diffraction (XRD) analysis is commonly used to determine the phase composition [161, 32], crystal structure [162] and crystal size [163] of crystalline materials. Each crystalline structure produces a unique X-ray pattern that can be used for identification.

In the flame synthesis of TiO_2 , XRD is often used to track the evolution of crystal phases under different process conditions such as temperature, equivalence ratio, flow rates, and TiO_2 -solvent combinations. These factors can significantly affect the properties of the crystalline product [35, 164, 165]. XRD can also differentiate between the composition of different phases of nanocatalysts consisting of multiple crystal phases [166]. The fundamental parameter approach such as Rietveld method [167, 168] is widely used to quantify the average crystal phase composition of a sample.

Figure 3.2 shows the typical XRD patterns of TiO_2 nanoparticles synthesized in a curved wall-jet (CWJ) burner with an ethylene/air flame. The crystal phase of the particles varies with the equivalence ratio ϕ of the flame mixture.

3.1.3 Brunauer–Emmet–Teller (BET)

The Brunauer-Emmett-Teller (BET) method is a widely used technique for measuring the specific surface area (m^2/g) of materials, particularly solids. The method is based on the physical adsorption of gas molecules onto the surface of a solid material, typically nitrogen gas [169]. The BET method involves exposing a sample of the material to a known quantity of nitrogen gas at a range of pressures. As the gas adsorbs onto the surface of the material, the amount of gas adsorbed is measured. By analyzing the relationship between the amount of gas adsorbed and the pressure at which it was adsorbed, it is possible to calculate the specific surface area of the material [169].

Under the assumption of monodispersed size distribution, the BET average primary particle diameter can be derived:

$$d_{p,\text{BET}} = \frac{6}{A_s \rho_p}$$

where ρ_p is the density of materials, A_s is measured specific surface area (m^2/g).

Madler and colleagues [132] applied the BET technique to investigate the evolution of specific surface area as a function of total dispersion/oxidant gas flow rate (Fig. 3.3). Initially, the decrease in residence time due to the increased flow rate slows sintering and increases the specific surface area. Then, an even higher oxidant flow rate shortens the particle formation process leading to higher temperature after particle formation, and thereby sintering is more pronounced, resulting in a lower specific surface area. These effects of fuel-oxygen correlation (equivalent ratio) to flame synthesized particles have been shown in SiO_2 [170] and TiO_2 [165, 160] either through the specific surface area or equivalent diameter.

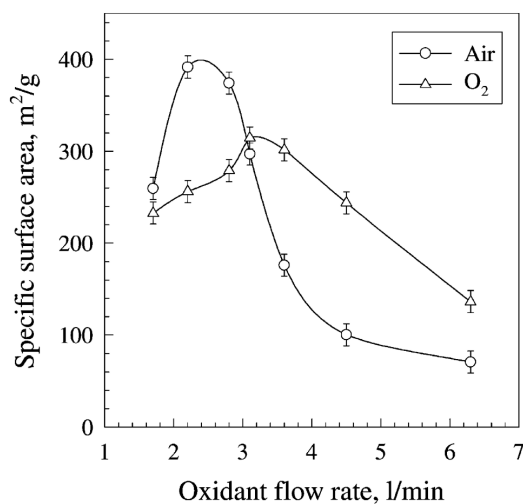


Figure 3.3. BET specific surface area (m^2/g) of spray flame-made silica from HMDSO/ethanol mixture (0.1 molar ratio) as a function of air and oxygen volumetric flow rates [132].

3.2 On-line methods

Synthesized nanoparticles can be described by sampling and analyzing the local aerosol in an on-line manner (e.g., Scanning mobility particle sizer (SMPS) from aerosol probing, Engine Exhaust Particle Size (EEPS)¹, Aerodynamic Particle Sizer (APS)² ...). Among various on-line methods, the SMPS has commonly been used to characterize the synthesis of TiO₂ nanoparticles, providing information about particle size distribution and number concentration.

SMPS is a type of instrument used to measure the size distribution of particles in gas. It works by first electrically charging particles in a sample, then applying a voltage gradient between the rod concentrically positioned and the surrounding cylinder wall. The rod sorts the particles based on their electrical mobility, which is related to their size. The SMPS can be used to measure particle sizes ranging from a few nanometers to several micrometers. It is commonly used with condensation particle counters (CPC) for counting the number concentration.

Sampling aerosols from a hot-flame environment generally requires rapid cooling to prevent further changes in morphology due to chemical reactions, particle growth, continuing aerosol coagulation, and sintering effects within the collection tubes. Therefore, significant dilution with nitrogen gas is used to quench the aerosol. The well-diluted aerosol is then sent to SMPS equipment for particle characterization.

The SMPS method provides a mobility diameter in a relatively fast sampling time, but it is not a geometric diameter. As a result, comparing results based on geometric diameter may lead to errors. For instance, for a soot aggregate, SMPS measures an equivalent mobility diameter related to the agglomerate size and fractal dimension (radius of gyration) [140]. In general, the equivalent sphere defined by the mobility diameter measured by an SMPS has a larger volume than the actual clusters due to the presence of voids of the clusters in the equivalent sphere. Smallwood et al. [152] compared LII and SMPS data obtained from diesel particulate matter (PM), showing the importance of the nature of the aggregate in interpreting SMPS size and volume fraction measurements. Krüger et al. [171] used the same techniques in a premixed laminar soot flame, showing similar results in average particle size due to the compact morphology of their soot particles.

Chen et al. [172] performed SMPS on various gas-phase synthetic nanoparticles: multiwall carbon nanotubes, welding fumes (SiO₂), and titanium dioxide. They show that the performance of the SMPS for measuring size distribution and the total number concentration depends on the type of particle.

The group of Pratsinis et al. [173] examined the correlation between geometric diameter, aggregate size, and mobility diameter of soot particles using discrete element modeling (DEM) coupled with discrete dipole approximation (DDA).

¹Engine Exhaust Particle Size (EEPS): This is another instrument used to measure the size distribution of particles, specifically those found in engine exhaust. It works on a similar principle as the SMPS but is designed for higher flow rates and larger particle sizes.

²Aerodynamic particle sizer (APS): This is a type of instrument used to measure the size distribution of particles in the air, similar to the SMPS. However, instead of sorting particles based on their electrical mobility, the APS uses aerodynamic sizing to sort particles based on their ability to move through a series of small nozzles. The APS can be used to measure particle sizes ranging from a few tenths of a micron to several tens of microns.

3.3 In-situ methods

3.3.1 Elastic light scattering

Elastic light scattering (ELS) describes an interaction between light and particles, causing a change in direction and polarization of the incident wave without a change in photon energy. As the scattering signal depends on size and geometry, this technique is closely linked to the detection of the aggregate shape of the particle. This technique has been used to study the evolution of morphology in particles of soot [174, 175, 176], Al_2O_3 [177], and TiO_2 [178] in flames, along the distance from the burner outlet/axial distance.

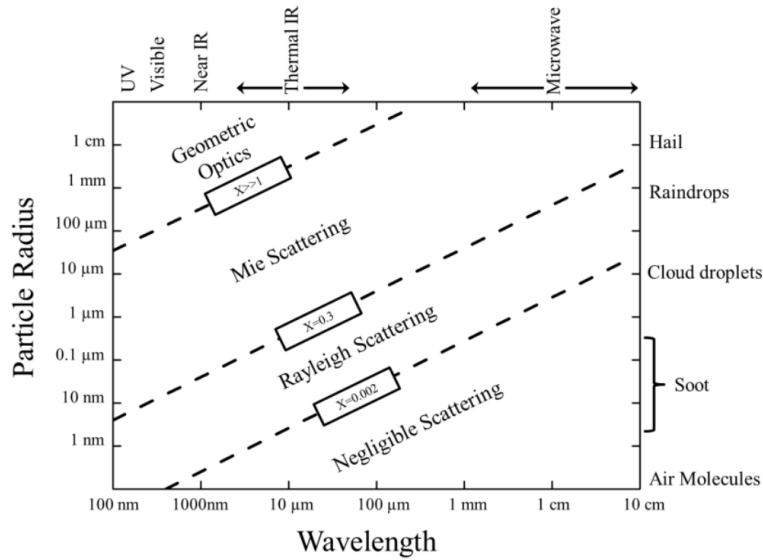


Figure 3.4. Light scattering regimes as a function of the wavelength and particle radius [179].

To describe the interaction between light and spherical particles, the ratio of the particle size d_p to incident light wavelength λ , also called the size parameter $x = \frac{\pi d_p}{\lambda}$, is often used. Depending on the value of the size parameter, the interaction can be described in Rayleigh scattering ($d_p \ll \lambda$) or Mie scattering ($d_p \sim \lambda$) as shown in Fig. 3.4. For nanoparticle synthesis, Rayleigh scattering is mostly applied as a characterization technique. It can be noted that for small particles, short wavelength range laser (UV, VIS range) results in higher scattering intensity, while the scattering becomes negligible with IR range laser irradiation.

In the Rayleigh scattering regime, the intensity of the scattered light I_s from an aggregate is given as [180]:

$$I_s \propto \frac{d\sigma}{d\Omega_{\text{agg}}} = n_{\text{pp}}^2 \frac{d\sigma}{d\Omega_p} S(q) = n_{\text{pp}}^2 k^4 a^6 F(m) S(q), \quad (3.1)$$

where $\frac{d\sigma}{d\Omega_{\text{p,agg}}}$ is the differential scattering cross-section of the primary particle/aggregate, n_{pp} is the number of primary particles per aggregate, $S(q)$ is the structure factor related to the the radius

of gyration with q denoting the scattering wave vector $q = 4\pi\lambda^{-1}\sin(\theta/2)$ [181], $k = \frac{2\pi}{\lambda}$, a is the nanoparticle radius, and $F(m) = |(m^2 - 1)/(m^2 + 2)|^2$ is the refractive index function for scattering with m denoting the complex refractive index. The scattered intensity is proportional to a^6 . Therefore, the change of scattering signal can be used to estimate the change of the particles or aggregates.

Yang and Biswas [178] used multi-angle Rayleigh scattering to establish the relationship between fractal size change and normalized area reduction in the formation of nanoscale titania particles in the premixed flame aerosol reactor. Figure 3.5(a) shows the light scattering signal at 90° as a function of height from the burner exit. The increased intensity (dashed line with triangle symbol) indicates continuing coagulation. The mean diameter based on the TEM image (dashed line with open square) shows the same tendency (right axis). The relative change in number concentration N is estimated using the mean particle size from the TEM image (dotted line with open circle) and assuming monodispersity (solid line with solid circle). The radius of gyration R_g can be obtained from the slope of the line of the normalized intensity $I(q)/I(0)$ in Fig. 3.5(b), as the structure factor $S(q)$ has a linear relationship with $I(q)$. At the region of $qR_g \ll 1$,

$$S(q)/S(0) = \left(1 - \frac{1}{3}q^2 R_g^2\right). \quad (3.2)$$

To calculate the fractal dimension D_f , the Fisher-Burford approximation [182] can be applied :

$$S(q)/S(0) = (1 + 2q^2 R_g^2/3D_f)^{-D_f/2}. \quad (3.3)$$

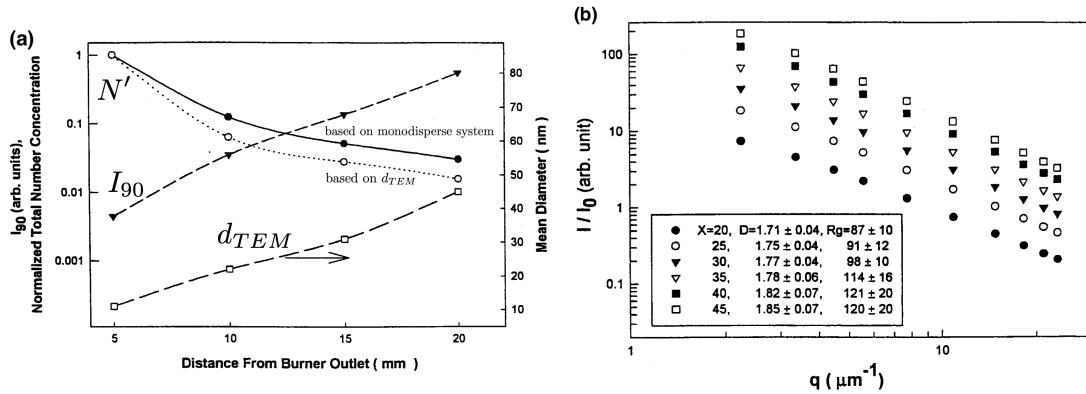


Figure 3.5. (a) The measured scattering intensity at 90° (I_{90}) as a function of axial distance (dashed line with a solid inverted triangle). The mean particle diameter determined by TEM imaging is also shown (dashed line with open square). The calculated normalized particle number concentration N' assuming Rayleigh scattering as intensity $\propto Nd_{pp}^6$ (dotted line with open circle) is compared to that using monodisperse coagulation theory [183] (solid line with solid circle) [178]. (b) Normalized scattering intensity (I/I_0) as a function of the scattering wave vector (q) at different axial positions X (mm) from the burner outlet. Calculated R_g and D_f are shown inside the legend.

In highly particle-laden streams and large-scale reactors, measurement accuracy can be affected by light attenuation caused by particles or flame emissions, which can affect both lights entering the sample volume and the detection of scattered light [184], requiring additional calibration. In addition, the Mie regime large's particles and droplets easily contaminate the ELS signal [185] so that ELS is not appropriate to describe the small metal oxide aerosol scattering in the Rayleigh regime. Therefore, in-situ aerosol measurements by ELS and RDG theory³ could be considered to obtain the aerosol properties of the droplet-free region downstream of the FSP [6].

3.3.2 Raman spectroscopy (RS)

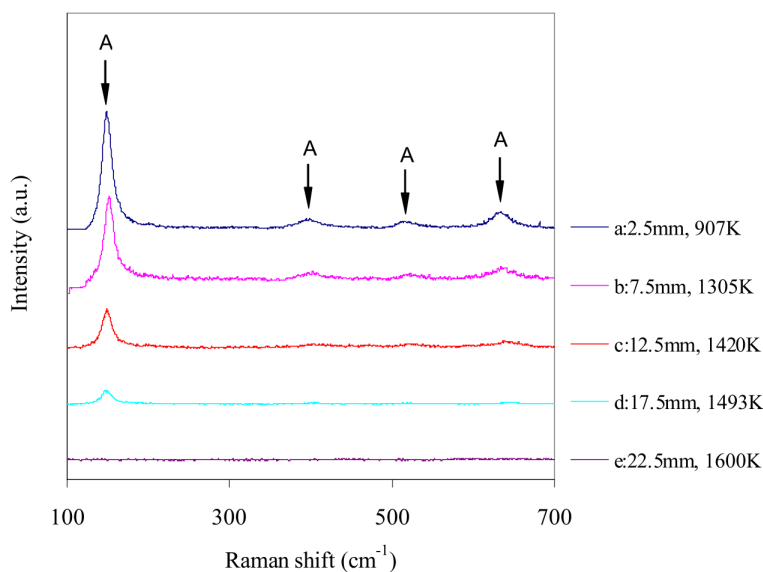


Figure 3.6. In-situ Raman spectra of TiO₂ nanoparticles synthesized by low-pressure axisymmetric, stagnation premixed flame at different distances from the substrate (0 mm) along the axial centerline [187]. The burner exit is located at 40 mm. Known modes for Anatase is marked in "A". Gas-phase temperature was measured by LIF on OH. The figure shows the anatase (A) content of the nanoparticles increases as they approach the substrate.

In the field of combustion, Raman spectroscopy (RS) is commonly used to measure the flame temperature [188] and the gas composition by comparing theoretical and measured Raman spectra [189]. However, in the presence of droplets in gas flows, this technology is not appropriate for temperature measurement because of the presence of possible laser-induced plasma around droplets due to high-energy laser pulse [6].

In nanotechnology, Raman spectroscopy measurements on solid metal oxide particles are used for the relative quantification of the crystal phase compositions of particle mixtures or to reveal information about the carbon content. The low signal intensity mostly limits the diagnosis to an

³The RDG-FA theory [175] gives analytical solutions that relate the optical cross sections to the size and morphology of particle aggregates taking into account self-interaction and multiple scattering effects [186].

ex-situ crystallinity measurement on deposited nanoparticles [190] or thin films [191, 192, 193]. Nevertheless, Liu et al. [187] conducted the first in-situ Raman diagnosis of nanoparticle aerosol formation during flame synthesis. They studied the amorphous, anatase, and rutile phase transitions using both ex-situ Spontaneous RS for the deposited nanoparticle layers and in-situ SRS of TiO_2 in flames. Nanoparticles were either seeded in a diffusion flame or synthesized from TTIP in a low-pressure premixed flame reactor to form TiO_2 . Along the centerlines of the flame, they found the transformation of TiO_2 from anatase to rutile from the seeded TiO_2 nanoparticles in the diffusion flame case. In contrast, the flame-synthesized TiO_2 (Fig. 3.6) shows increasing anatase content as the nanoparticles approach the cold substrate (far from the burner, cold substrate at 0 mm). They explained that the absence of Raman spectrum near the burner (22.5 mm, the beginning of particle generation) might be because of the production of suboxide⁴ or amorphous states without Raman signature.

3.3.3 Small-angle x-ray scattering (SAXS)

Small-angle X-ray scattering (SAXS) utilizes X-ray wavelengths ($\lambda \approx 0.1$ nm) with a very high frequency ($f \approx 10^{18}$ Hz), resulting in a refractive index close to unity and making X-ray scattering a relatively simple wave problem [175]. The collimated, monochromatic X-ray beam strikes the sample and scatters at small angles (typically between 0.1 and 10 degrees) relative to the direction of the incident X-ray beam. This results in a characteristic azimuthal ring pattern detected at a defined distance from the sample. The scattered radiation provides information about the size, shape, and distribution of particles in the sample. In materials science, SAXS is often used to study the structure of nanoparticles and nanomaterials.

SAXS data is typically analyzed using mathematical models to extract information about the size and shape of particles in the sample. The most common models used for SAXS data analysis are the Porod law [194], which describes the scattering from large particles, and the Guinier law [195], which describes the scattering from small particles. The combination of these two models allows for the determination of important parameters such as the diameter and polydispersity of primary nanoparticles, as well as average values of mass fractal dimension, radius of gyration of the aggregate, and number of primary particles per aggregate [196]. When combined with wide-angle X-ray scattering (WAXS), SAXS can also provide information about internal atomic-level structures of particles [197].

⁴Class of oxides wherein the electropositive element is in excess relative to the “normal” oxides; Titanium suboxide, TiO_x or Titanium monoxide, TiO .

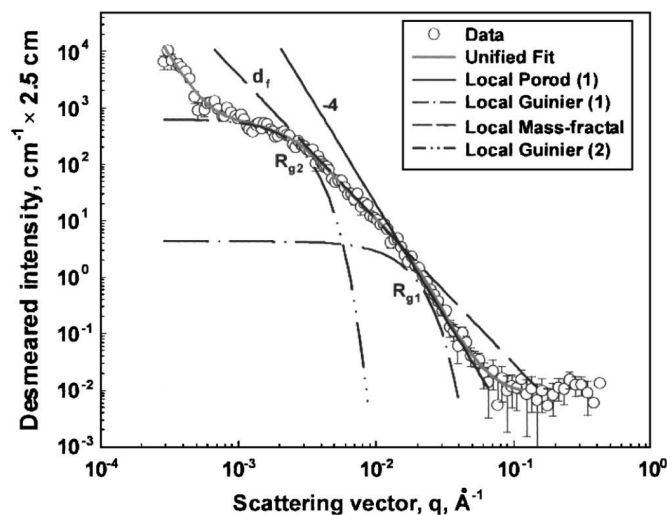


Figure 3.7. Scattered intensity as a function of the scattering vector q measured in-situ for silica nanoparticles produced by a premixed flame at $HAB = 40$ mm [198]. The circles represent the measured scattered intensity. The global unified fit (gray) is shown with component curves such as the Porod regime for primary particles (solid black line), the Guinier regime for primary particles (dash-dotted line), and aggregates (dash-double dotted line). The appearance of a weak power-law regime (dashed line) indicates that these particles are mass fractal.

SAXS has been employed for both ex-situ and in-situ measurements of flame-synthesized particles such as TiO_2 [199] and SiO_2 [196, 200]. In-situ SAXS measurements have been used to investigate the nanostructure of SiO_2 particles in flames [201, 202, 198]. Figure 3.7 shows a typical in-situ SAXS intensity-scattering vector graph for flame-synthesized SiO_2 nanoparticles. The unified fit of the data (gray) can be evaluated with component curves corresponding to several regimes describing particle geometry. However, in-situ SAXS measurements are typically required large-scale synchrotron sources, limiting their feasibility in laboratory-scale measurements [198, 6].

3.3.4 Laser-induced fluorescence (LIF)

Laser-induced fluorescence (LIF) corresponds to the emission from electronically excited molecules by absorption of photons. When atoms or molecules absorb energy, they are in a higher electronic energy state. Since the excited state is thermodynamically unstable, the atoms and molecules rapidly release the received energy and return to the fundamental energy level. Returning to its ground state, a photon is emitted.

LIF has a short lifetime (approximately ns) and is different from phosphorescence, which has a long lifetime (approximately ms). During the lifetime of LIF, the energy of the excited state is usually dissipated through various pathways before it relaxes back to the ground state and emits a photon. During this relaxation process, some of the energy is lost due to nonradiative transitions, such as vibrational relaxation and collisional quenching, which causes the emitted photon to have less energy (i.e., a longer wavelength) than the absorbed photon (detailed in Chap.

4). This energy difference between the absorbed and emitted photons is known as the Stokes shift. It can affect the sensitivity of the LIF technique because the spectrally shifted emission can be detected with high S/N ratio in low-intensity background signals [203]. The LIF signal intensity depends on temperature and pressure as well, which should be controlled attentively [204].

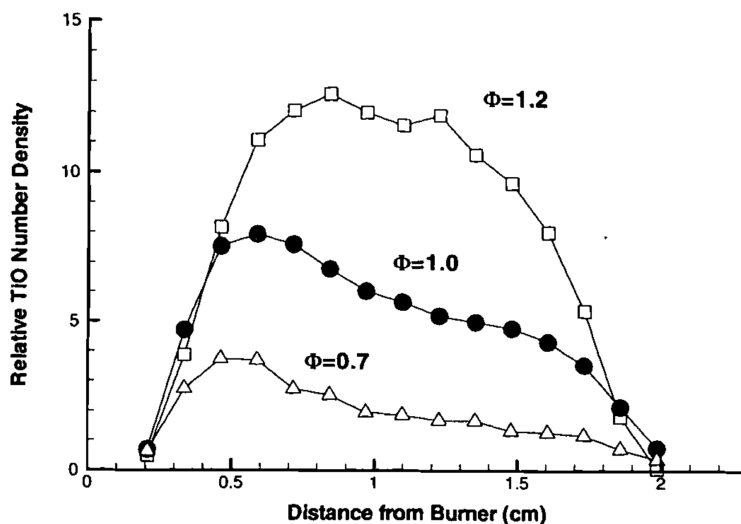


Figure 3.8. Spatial profiles of TiO number density for various flame equivalence ratios, with a constant total flow rate of H₂ and O₂ in low pressure stagnation flow flame. Adapted from [205].

LIF is a useful technique for obtaining spatially-resolved images of intermediate species during flame synthesis of nanoparticles. It has traditionally been used for visualizing the flame front, as shown by measuring OH and CH radical concentrations in the reaction zone (OH in SiO₂ synthesis [206, 207]). LIF is also commonly employed to measure flame temperature, such as using NO multiline LIF to synthesize TiO₂ [208] and Fe₂O₃ [209]. Specific atoms or naturally occurring molecules, such as Fe [209], SiO [210, 211, 212], FeO [213], AlO [205], and TiO [205] (an example of TiO species distribution in a low pressure hydrogen/oxygen flat flame is shown in Fig. 3.8), can be utilized to estimate local concentration or temperature. With additional optical calibration process, quantitative measurement is achievable [209].

In terms of LIF studies on TiO₂ nanoparticles, there have been numerous studies performed in an ex-situ way (with spectrophotometer), on the filtered powder, or in a colloid state to investigate its photocatalytic reactivity (detailed in Chap. 4). The group of Zizak [19, 20] and De Iuliis et al. [214, 215] have performed the laser-induced emission in-situ measurements on flame synthesized TiO₂ where the LIF emissions are detected at a prompt (same as laser timing) before the incandescence emissions arrive. More details will be provided in Chap. 4.

3.3.5 Laser-induced breakdown spectroscopy (LIBS)

Laser-Induced Breakdown Spectroscopy (LIBS) is an analytical method utilized to identify the elemental composition and concentration of a substance through the spectral emissions produced by the plasma resulting from laser-induced breakdown. This approach has been employed in particle synthesis to monitor nanoparticle production in various generation techniques, such as flame synthesis, laser ablation synthesis, and electrical discharge synthesis [216].

When a focused, pulsed laser beam is directed at a material, it vaporizes and atomizes the material, resulting in plasma formation on the surface of the sample. This process is accompanied by the appearance of a spark and a shock wave. After the plasma has cooled down and the continuum emission (Bremsstrahlung) from the plasma has dissipated, longer-lasting emissions from neutral and ionized species are observed. These light emissions contain information about the elemental composition of the sample, as each element emits a characteristic set of wavelengths of light when it is excited by the energy from the laser pulse. These atomic and ionic emission spectra can be analyzed using a spectrometer to determine the local elemental composition of the sample. The peak intensity can be associated with the number density of each emitting species in the plume and with the concentration of specific elements in the ablated material.

Typically, LIBS requires a laser fluence above the breakdown threshold of the material, which can vary depending on the experimental conditions [217], especially the laser wavelength [218, 219]. Because of its intrusive (destructive) nature, it has been generally used for ex-situ elemental composition analysis, rather than in-situ measurement. However, recently, it has been developed to be applied in an in-situ environment by adapting the level of plasma to the surface, without ionizing gas molecules (PS-LIBS). This in-situ LIBS can provide valuable information on the complex processes in turbulent flame reactors [220].

More details about LIBS on TiO_2 will be provided in Chap. 4.

3.3.6 Laser-induced incandescence (LII)

Laser-induced incandescence (LII) is a laser diagnostic technique based on the emission of incandescence of laser-heated particles. The heated nanoparticles emit thermal radiation, which is subsequently detected. The particles cool down to the initial temperature.

LII was originally developed for carbonaceous particles, including soot and carbon black nanoparticles. The carbonaceous particles can broadly absorb light in the UV-VIS-IR wavelength range and can be heated up to 4000 K before vaporization or sublimation. The LII technique has been extended to non-carbonaceous nanoparticles such as metals or metal oxide nanoparticles for in-situ diagnostics [12]. Since the absolute incandescent signal intensity depends on the volume fraction of the particles in the control volume, it is possible to measure the volume fraction. From the radiation signal temporal decay, it is possible to obtain information on particle size based on LII signal modeling [221]. The advantage of LII over elastic scattering is the absence of interfering signals from liquid fuel droplets. And it is also relatively easy to reject the scattered light from the surrounding environments. Therefore, LII has been used for visualization of 2D spray flame synthesis [222, 223].

It should be noted that other laser-induced emissions can be overlapped during the LII emission measurement. If the input laser fluence is too low to heat the particles up to incandescent

temperature, the detected emission can be composed of more LIF signals than LII contribution [224]. Alternatively, two emissions can exist at the same time. This phenomenon is particularly frequent in UV range excitation laser wavelength, which can easily excite molecules with higher energy than IR range laser. There have been studies using this feature to detect soot (via LII) and PAHs (Polycyclic aromatic hydrocarbon, via LIF) simultaneously in turbulent jet flames [225]. On the contrary, when too strong laser fluence is focused, it can create a breakdown so that the atomic line emission from the evaporated particle species can contaminate the LII signals [214, 226, 227], continuing in PS-LIBS regime [228]. More details will be provided in Chap. 4.

3.4 Conclusion

Ex-situ methods can provide a variety of particle properties (e.g., size, morphology, crystal phase, composition...) once the product powders are collected in the sampling filter. However, the obtained information can not describe the effect of the change in local operating conditions during the formation. On the other hand, the on-line method can offer real-time measurement of particle information during the synthesis. Still, high dilution during the extraction of particle flows can cause an additional quenching effect on the generated particles, which can result in a different geometry.

For these reasons, in-situ diagnostics are considered the most appropriate method to pursue the evolution of particle characteristics during the formation in flames. They can describe the change in local operating conditions instantaneously. Still, among in-situ techniques, not all diagnostics are feasible in studying laboratory-scale particle flame synthesis. ELS can not be employed when there exist liquid spray droplets. The emission of spontaneous Raman spectroscopy is often too weak, so a high-energy laser is required. SAXS measures also require high collimation and high photon flux for the laser. Then, among the techniques using laser-induced emission, the LII has the potential to characterize particle formation with instantaneous information on volume fraction and particle diameter. The summary of each technique is shown in Table 3.1.

At the same time, as previously observed in some pioneering works on LII on non-soot particles [214, 226], laser-induced emissions (LIEs) - LIF, LIBS, and LII - can coexist during the measurements as interferences. To properly exploit the particle information from the diagnostics using these laser-induced emissions, it is important to distinguish the different temporal/spectral characteristics of each emission. For this reason, the next part of this thesis will be dedicated to the diagnostics using these three laser-induced emissions in more detail, focusing on TiO_2 nanoparticles.

Table 3.1. Summary of the measurable parameters with various experimental techniques.

	Variables	Note	limit
SEM and TEM	d_{pp} , n_{pp} , D_f , crystal phase (HR-TEM)	geometric characteristics	ex-situ
ex-situ	XRD	crystallinity	ex-situ
	BET	size (d_{BET})	ex-situ
		monodispersed distribution assumption	
on-line	SMPS	size (d_m)	dilution effect
	ELS	size (d_{pp} , R_g), D_f	without droplet presence
	Raman	crystallinity	low signal intensity
	SAXS	size(d_{pp} , R_g), f_v , D_f	need for high-spec laser
In-situ	LIF	radical concentrations, temperature	optical calibration needed
	LIBS	atomic concentration	intrusive
	PS-LIBS	gas-to-particle conversion, f_v , Band gap	high laser fluence
	LII	f_v , size	complex interpretation of signal
		quantitative measurement with calibration	

Part II

Characterization of the Laser-Induced Emission of TiO₂ nanoparticles: Feasibility of Laser-Induced Incandescence

Chapter 4

Laser-Induced emission (LIE) of TiO_2

The light-particle interaction as a result of in-situ laser diagnostics can induce various emissions such as Laser-induced fluorescence (LIF), Laser-induced incandescence (LII), and Laser-induced breakdown spectroscopy (LIBS). Those emissions can coexist in the targeted detection volume. Consequently, it is important to distinguish each emission to apply the appropriate theory and interpret the signal for each diagnostic purpose. As schematically presented in Fig. 4.1, their occurrence depends on the laser fluence regime. The basics of these three techniques will be presented with a focus on their application on TiO_2 particles: LIF in Sec. 4.1, LIBS in Sec. 4.2, and LII in Sec. 4.3 .

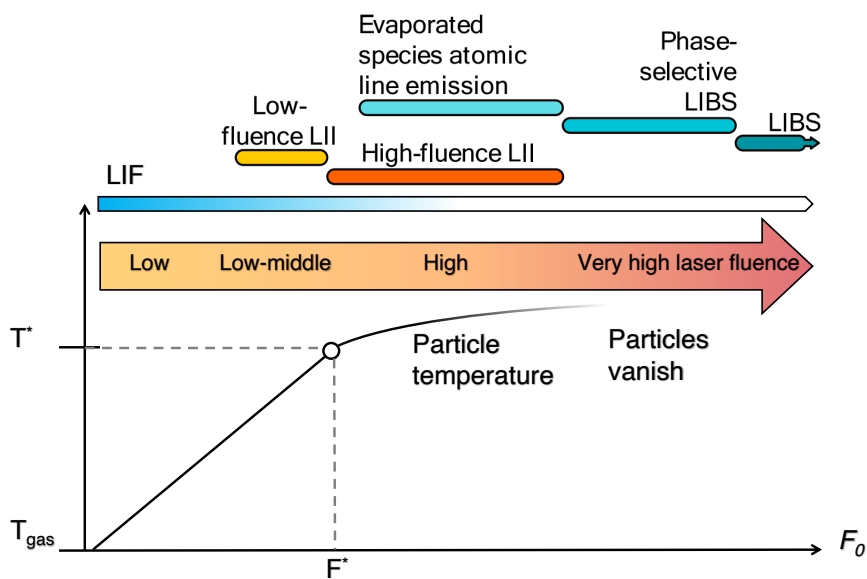


Figure 4.1. Schematic demonstrating the typical progression of the LIF, LII and LIBS signals and particle temperature as a function of the laser fluence, adapted from [12].

4.1 Laser-induced Fluorescence (LIF)

Laser-induced fluorescence (LIF) is a spectroscopic technique that involves using a laser to excite a molecule or atom to a higher energy level, followed by the spontaneous light emission. The sample is irradiated with a laser beam, typically of a specific wavelength that matches the absorption spectrum of the sample. Then the laser fluence to excite an atom or molecule could be only a few mW in case of commercial spectrophotometer. It has been widely used in combustion for detecting specific species and visualizing flow [229]. In material science, a similar process known as photoluminescence (PL) is used to describe the radiative recombination of electron-hole pairs in materials [230]. Although both LIF and PL involve laser-induced emission, they differ in their excitation mechanisms and applications. In combustion, LIF is typically used to probe the properties of gas-phase molecules, while in material science, PL is used to study the optical and electronic properties of materials such as semiconductors and nanoparticles.

A typical fluorescent molecule has several electronic states: a singlet ground state ¹(S_0), singlet excited states (S_n , $n \geq 1$), and triplet excited states (T_n , $n \geq 1$). Numerous vibrational energy levels are associated with each electronic state. This can be summarized with a partial energy-level diagram, also called a Jablonski diagram. The particle energy-level diagram of a typical fluorescent molecule is shown in Fig. 4.2. Many processes are related [231]:

- **Absorption** represents the shift from the ground state to an excited state by absorption of a photon ($S_1 \leftarrow S_0$ or $S_n \leftarrow S_0$), within femtoseconds [232].
- **Fluorescence** corresponds to the radiative relaxation of an excited state towards the fundamental state by emission of a photon (from S_1).
- **Phosphorescence** corresponds to the relaxation of an excited state of different spin multiplicity² from that of the ground state, towards this ground state by emission of a photon (from T_1).
- **Internal conversion** represents a non-radiative relaxation between two electronic states of the same multiplicity ($S_n \rightarrow S_1$ or $S_1 \rightarrow S_0$).
- **Intersystem crossing** corresponds to the transfer of energy in a non-radiative way between two electronic states of different multiplicity ($S_1 \rightarrow T_1$).
- **Vibrational relaxation** represents a transfer of energy between vibrational levels within a same electronic state by intra/intermolecular collision, dissipating energy (heat), occurring within picoseconds or less [232].

¹The ground state is a stationary state of the lowest energy of molecules.

²In quantum chemistry, the multiplicity of an energy level is defined as $2S+1$, where S is the total spin angular momentum. If $S = 1$, states are called singlets [233].

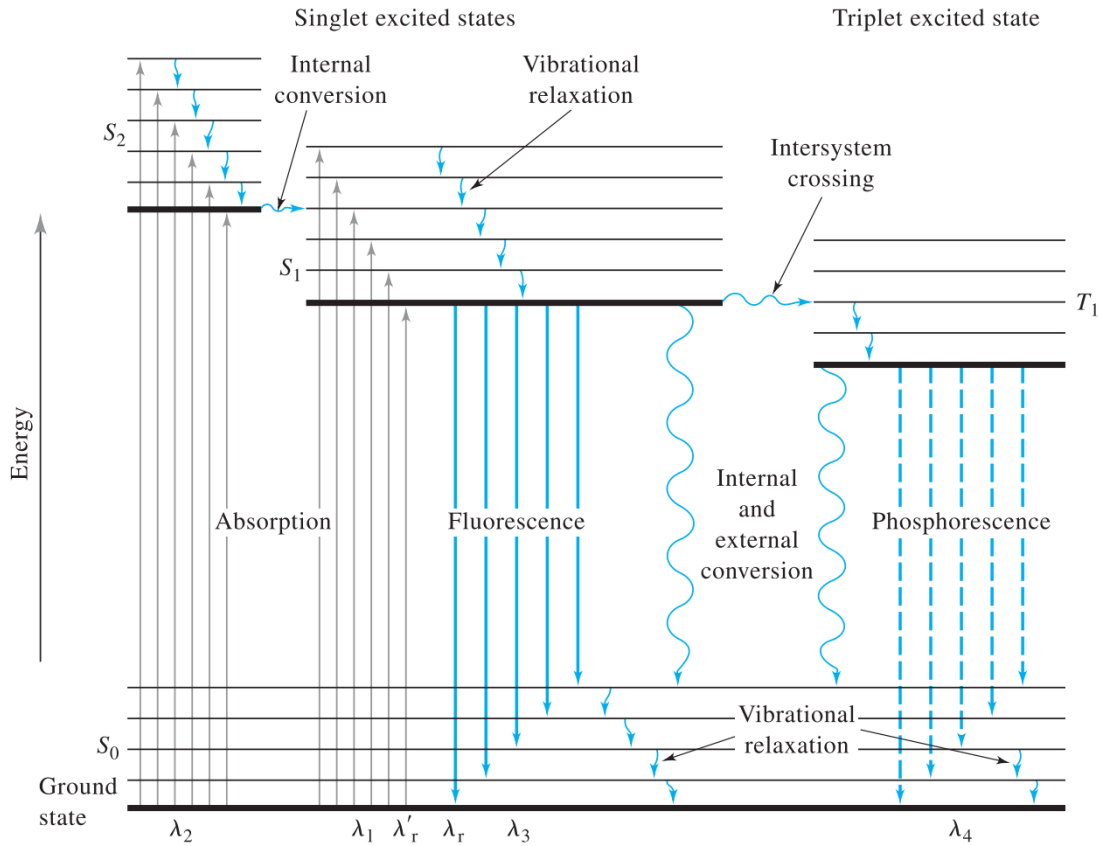


Figure 4.2. Partial energy-level diagram for a fluorescent (photoluminescent) molecule, often called a Jablonski diagram [203].

In fluorescence, incident photons may have enough energy to be absorbed and produce transitions from other inter-nuclear separation distances and vibrational energy levels (Fig. 4.2). This effect gives rise to an absorption spectrum containing multiple peaks [229]. Consequently, during emission, the closely-spaced vibrational energy levels can deliver a wide range of photon energies, leading to emission spectra over a band of wavelengths. Thus, the resulting emission spectra are the sum of transitions with different photon energies. Moreover, nanoscale morphology, crystallinity, and defect chemistry of the material under specific experimental conditions affect each transition with different weights.

Concerning TiO₂, the unique LIF feature is closely related to the photocatalytic performance [232]. There have been persistent efforts for the complete description of the mechanism of LIF emission of TiO₂ nanoparticle [234, 235]. Still, the complex effect of particle property (size, geometry, crystal phase, defect state) and experimental conditions (temperature, excitation laser wavelength, chemical environment, pressure) make interpretation of the LIF emission spectra challenging. This point is briefly discussed in the next section.

4.1.1 Effect of experimental parameters on LIF of TiO₂

Laser wavelength The effect of laser wavelength on the LIF of TiO₂ has been shown by Abazovic et al. [236]. LIF measurement was conducted on synthesized anatase and rutile TiO₂ particles. Excitation was done using a laser photon energy higher than the TiO₂ band-gap energy. Results for the anatase case are presented in Fig. 4.3 for two excitation wavelengths. A broad emission was observed with the presence of well-resolved peaks/shoulders at 426, 442.8, 459.2, 484.3, and 529.8 nm. A larger emission spectrum is found for the shorter excitation wavelength. The same structure of broad emission of LIF was observed with the same location of peaks/shoulders for both rutile and anatase.

Differences in emission spectra are also obtained when considering different laser excitation wavelengths. Results from Wang et al. [237], illustrated in Fig. 4.4, show that temporal evolution of the LIF emission of TiO₂ centered at 820 nm depends on the excitation wavelength (300, 333, 360, 390 nm). A faster decay was detected at a longer laser wavelength excitation. Since shorter wavelengths can produce excited electrons at higher energy levels, alternative relaxation paths might exist before their relaxation down to the conduction band. Therefore, with a shorter excitation wavelength, the resulting LIF signal can show slower decay. In other words, different mechanisms starting from different excitation energies can result in alternative electron relaxation pathways, eventually resulting in different emission spectra.

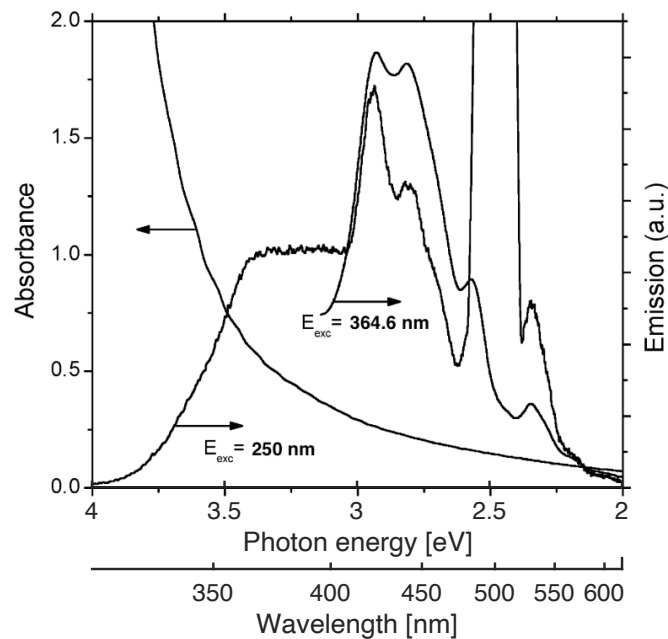


Figure 4.3. Absorption and LIF emission of anatase TiO₂ particles at two excitation wavelengths (250 and 364.6 nm) [236].

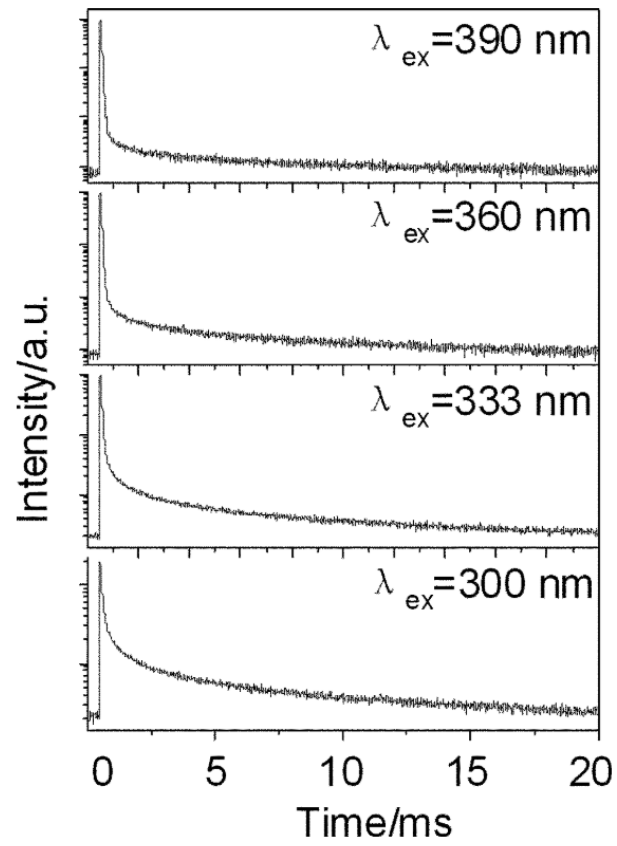


Figure 4.4. Time-resolved LIF spectra of rutile TiO₂ monitored at 820 nm and 77 K. The excitation wavelengths are 300, 333, 360, and 390 nm with a duration of $\sim 2 \mu s$ [237].

Temperature Zhang et al. [238] investigated the temperature dependence of LIF emission spectra of TiO₂ films over a low-temperature range (9–300K). The films were set in an ultra-vacuum cavity, and a close-cycled helium cryostat was used during low-temperature LIF measurement with an excitation of 325 nm laser source with 30 mW power. The obtained LIF spectra are presented in Fig. 4.5. The total LIF spectra are obtained as the sum of five emissions components, illustrated in Fig. 4.5 (b)–(e). The temperature dependence of peak positions, i.e., the emission center, is presented in Fig. 4.5 (f). When increasing temperature, all the bands are shifted towards a higher energy side except for the yellow (2.0 eV) and green (2.2 eV) bands. With increasing temperature, the contribution of each band could be different depending on the origin of its transition. Therefore, the total LIF spectrum from the ensemble of each emission component can show different tendencies depending on the particle electrons/holes states even for the same change in operating condition (e.g., increasing temperature).

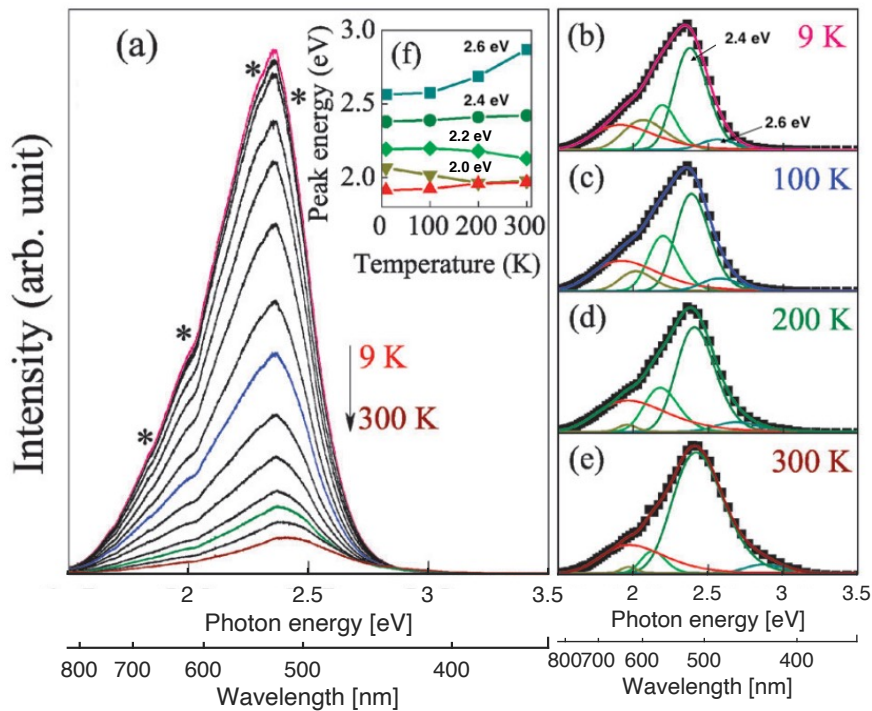


Figure 4.5. (a) Low-temperature LIF emission spectra of pure TiO₂ film in the temperature range of 9–300 K. A five-peak fit of the LIF spectra with the temperature of (b) 9 K, (c) 100 K, (d) 200 K, and (e) 300 K. Note that the inset (f) shows the temperature dependence of the corresponding peak/shoulder positions. Broadening shoulders are indicated by the symbol asterisk (*). Adapted from [238].

Crystalline structure The crystalline structures of TiO₂ can also determine the type of photoluminescence spectra. Generally, during the phase transformation of TiO₂ from anatase to rutile at high temperatures, the specific surface area decreases dramatically due to the geometric structure change [239]. As a result, the anatase and rutile TiO₂ show completely different relaxation processes which results in emission spectra that are distinct [237]: visible luminescence emission for anatase and near-infrared luminescence emission [240] for rutile as illustrated in Fig. 4.6(a). On the other hand, Fig. 4.6(b) shows the LIF spectra of two types of commercial rutile and anatase TiO₂ particles [241]. The different aspects of crystalline structure between Figures 4.6a and b might be because of the difference from particle geometry and surface chemical reactivity under the surrounding environment (ambient air in [240] vs. aqueous solutions in [241]).

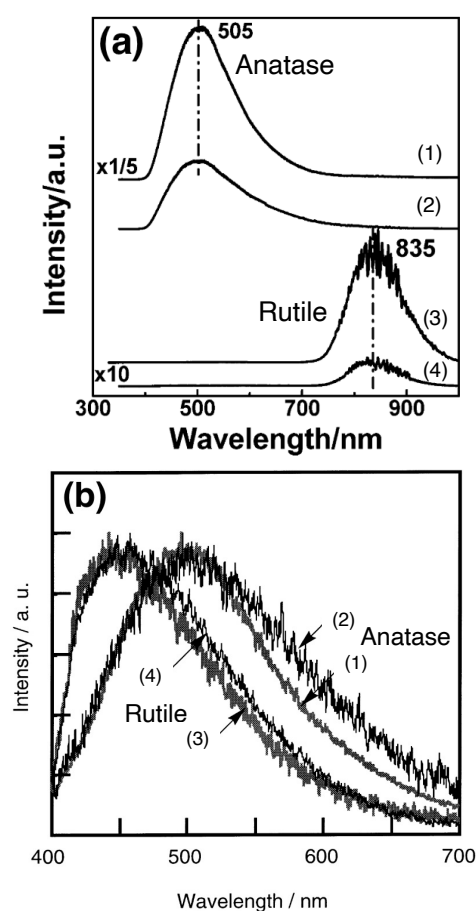


Figure 4.6. LIF spectra of commercial TiO₂ of different crystalline structures. (a) A 325 nm He-Cd laser was used for excitation in an ambient air environment. (1) anatase, (2) Anatase that was calcined at 900 °C for 6 h, (3) anatase that was calcined at 1200 °C for 24 h, and (4) rutile [240]. (b) A 355 nm laser was used for excitation in an aqueous solution. (1) anatase (Merck), (2) anatase (Ishihara Co., ST11), (3) rutile (Ishihara Co., CR-EL), (4) rutile (Toho Titanium Co., NS51) [241].

Particle geometry The LIF emission has also been investigated for different forms of TiO₂ nanomaterials (nanoparticle [236], nanowire [242], nanoribbons [243]). The effect of the particle size on the LIF emission spectra has been shown by Serpone et al. [244]. The absorption and fluorescence spectra of TiO₂ particles are presented in Fig. 4.7. The mean diameter is 2.1 nm for specimen A, 13.3 nm for specimen B, and 26.7 nm for specimen C. Since the excitation conditions were identical ($\lambda_{\text{ex}} = 270$ nm), differences in emission intensities should be originated from the differences in the surface properties of each specimen. The smallest particles (2.1 nm) have the larger density of surface states or defects at which non-radiative recombination predominates [244]. Thus, the overall emission quantum yield decreases with a smaller size when comparing specimens A and B in the same concentration. The number of emitting centers is also different for this geometrical reason. Additional emission centers which are not shown in specimens B and C are observed (414 nm, 444 nm, and 484 nm) for the smallest particles, possibly due to different lattice/surface defects in the particles.

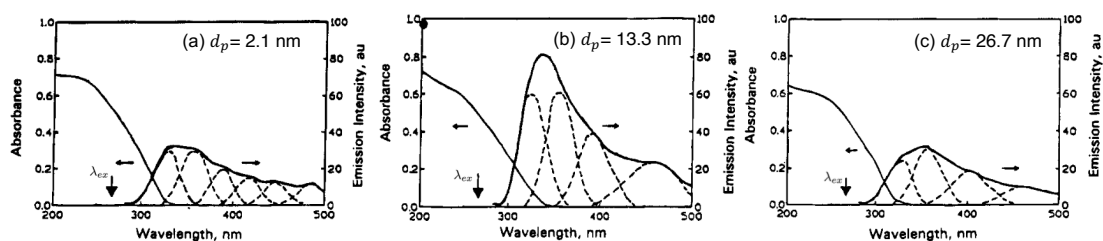


Figure 4.7. Absorption and fluorescence spectra of colloidal TiO₂ particles: (a) specimen A (TiO₂ concentration 0.015 g/L), (b) specimen B (TiO₂ concentration 0.015 g/L), and (c) specimen C (TiO₂ concentration 0.3 g/L). The excitation wavelength at 270 nm [244].

Conclusion

The broad feature of nanoparticle LIF emission spectra is related to the existence of multiple electronic energy levels, each of them can contribute to the final broadband emission spectra [68].

Although not all the mechanisms have been revealed completely, the LIF spectra are closely related not only to the intrinsic structure but also to the surface conditions of the particles in terms of charge carrier³ presence. Each charge carrier pathway is responsible for one transition, and the sum of all the transitions is observed during the LIF measurement. Thus, the emission of LIF on TiO₂ shows wide variation depending not only on the particle properties (size and crystal phase) but also on the experimental conditions (temperature, laser wavelength). Furthermore, the individual effect of each variable is difficult to be estimated since it is often a complex process affected by several experimental parameters simultaneously, including the surrounding environment.

³A charge carrier is a particle that is free to move, carrying an electric charge. Examples are electrons, ions, and holes.

4.2 Laser-induced breakdown spectroscopy (LIBS)

LIBS technique uses a focused laser beam to generate plasma at the surface of a sample in order to ablate material from it. LIBS occurs at very high laser fluence [217]. For high laser fluence, the evaporation of particles decreases the particle size, and atomic line emissions from evaporated species start to be observed.

As the plasma cools and continuum emission (Bremsstrahlung) from the plasma fades, emissions from neutral and ionized species are observed and used to identify and quantify the atomic composition of target molecules [245]. The temporal evolution of each process is schematically illustrated in Fig. 4.8(a). During the lifetime of the plasma (\sim ms), the emission spectrum changes. Figure 4.8(b) shows the emission spectra of the laser-induced plasma after the laser pulse. At the time t_1 (40 to 500 ns from the laser peak [217]), the plasma mainly emits a continuous spectrum from Bremsstrahlung emission and the recombination radiation. At this stage, only small intensity peaks of the atomic and ion lines are visible in overlapped spectra. At the time t_2 (2 to 10 μ s), the plasma is cooled, and the ratio of the peak intensity of the ion/atom line emissions to the continuum background significantly increases. At t_3 (after 10 μ s), the plasma temperature decreases with decreasing emission intensities. Values of t_1 , t_2 , t_3 for the temporal evolution can substantially vary (up to ms [217]) depending on the materials and experimental conditions, including the gas temperature and excitation wavelengths.

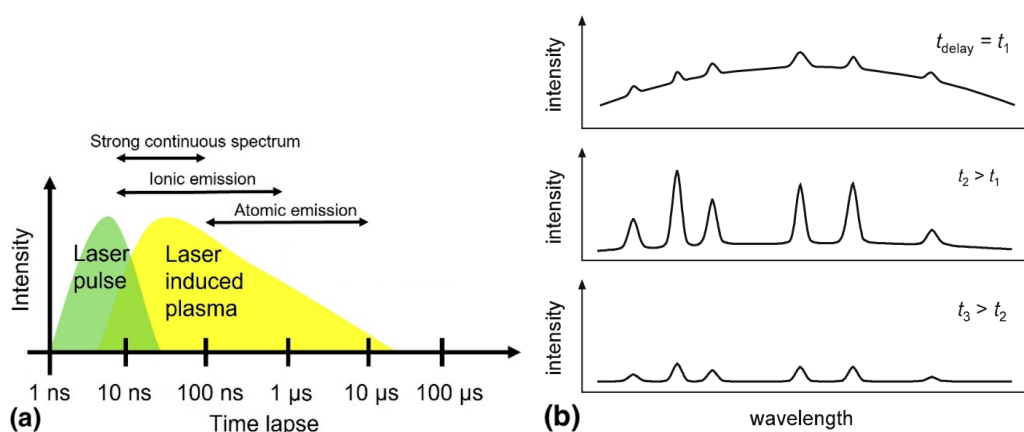


Figure 4.8. (a) Schematic illustration of the temporal variation of laser pulse irradiation and plasma behavior [246], (b) Schematic illustration of the emission spectra of the laser-induced plasma for different time delays with respect to the irradiation of the laser pulse [217].

Concerning TiO₂, LIBS has been used for the characterization of different powders. Some examples are reported in Table 4.1. However, because of its intrusive nature, LIBS is mainly used to determine Ti-content concentration [247, 248, 249, 250, 251]. Conventional LIBS has not been employed for in-situ analysis purposes in flame synthesis because of the strong breakdown process, which wipes away the molecular-level information. Additionally, the high-temperature plasma significantly disturbs the reaction process and synthesis products [95].

Alternatively, a new method using phase-selective (PS) LIBS has been developed for particle characterization [228], which does not create the high perturbation gaseous plasma. In contrast to conventional LIBS, PS-LIBS exhibits a promising prospect of in-situ diagnostics of flame synthesis [252, 253, 254, 255]. The difference in applications between conventional LIBS and PS-LIBS will be described in the following section.

4.2.1 Phase-selective laser-induced breakdown spectroscopy on TiO_2

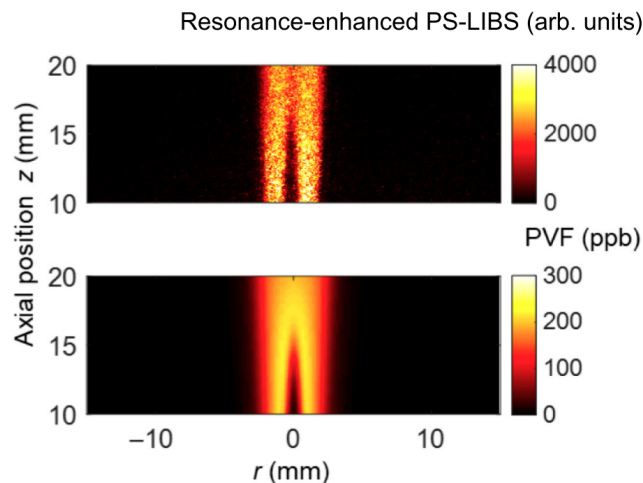


Figure 4.9. Comparison between the two-dimensional resonance-enhanced PS-LIBS snapshots (up) and the simulated particle volume fraction (bottom) in the laminar flame [255].

Phase-selective laser-induced breakdown spectroscopy (PS-LIBS) was developed in a collaboration between Prof. Tse's group (Rutgers University, U.S.A.) and Prof. Li's group (Tsinghua University, China) [228, 256] to investigate the particle formation in TiO_2 nanoparticle synthesis. The principle of this technique is to put the laser fluence lower than the gas breakdown but higher than the evaporation threshold of the nanomaterial. Then, only the nanoparticles in the solid phase dissociate, forming nanoplasmas without any breakdown of the surrounding gas phases. Thus, it is possible to detect specific atomic line emissions from dissociated nanomaterials. The selectivity of low-intensity LIBS could be advantageous for tracking the formation of nanoparticles and measuring the volume fraction of particles during gas-phase synthesis [252]. A lower laser fluence ($1 - 20 \text{ J/cm}^2$ with 10 ns FWHM laser duration in 532 nm) than conventional LIBS ($10-100 \text{ J/cm}^2$ with 10 ns FWHM laser duration in 532 nm) is applied in PS-LIBS, allowing to convert nanoparticles into plasma without affecting the surrounding gas (phase selectivity). The fluence regime at which the phase selectivity ends corresponds to the threshold of gas molecule breakdown, above which the gas phase turns into a plasma (conventional LIBS). The lifetime of PS-LIBS is reported to be shorter (a few tens of nanoseconds [254]) than those of conventional LIBS [257]. This is because there is no gaseous plasma causing long-lasting recombination emission as in LIBS.

The PS-LIBS is applied to determine the chemical composition of the nanoparticle phase from the relative strengths of the atomic emission lines [228]. In the detection of TiO₂, PS-LIBS excites only the Ti atoms in the particle phase, with no breakdown emission occurring for gas molecules including the precursor or surrounding air. Then, using size-dependence of the absorption efficiency for small particles, the saturated fluence level of PS-LIBS (See intensity of atomic spectra of Ti in Fig. 4.11) can be used to estimate the total mass/volume concentration [252]. Zhang et al. [257] measured the nanoparticle volume fraction for TiO₂ nanoparticles generated during flame synthesis based on the relationship between the atomic spectrum intensity and the nanoparticle volume fraction. This study has been extended to the 2D measurement of particle volume fraction in jet-diffusion flame as shown in Fig. 4.9.

Conclusion

The LIBS technique has been used to investigate the elemental chemical composition of various TiO₂ samples. On the contrary, it has been applied seldom for in-situ measurement situations, especially for particle formation in flames due to its intrusive nature.

PS-LIBS, using a laser fluence below gas breakdown, has been introduced. It is based on the emission of nanoplasm from the particle surface. Since it does not completely damage the materials and does not affect the surrounding gas species, it is more suitable for in-situ measurement. PS-LIBS technique has been applied to observe the formation of nanoparticles in flame synthesis. The spectral signals show line emission mainly from the atomic emission of Ti in the case of TiO₂ synthesis [228]. The strong atomic/ionic line emissions of Ti and O are shown in Fig. 4.10. Most Ti/O atomic emissions are distributed below 550 nm. After 600 nm, except for specific lines, there is less population of atomic line emissions. From a temporal point of view, they show a few nanoseconds duration, shorter than the duration of conventional LIBS emission.

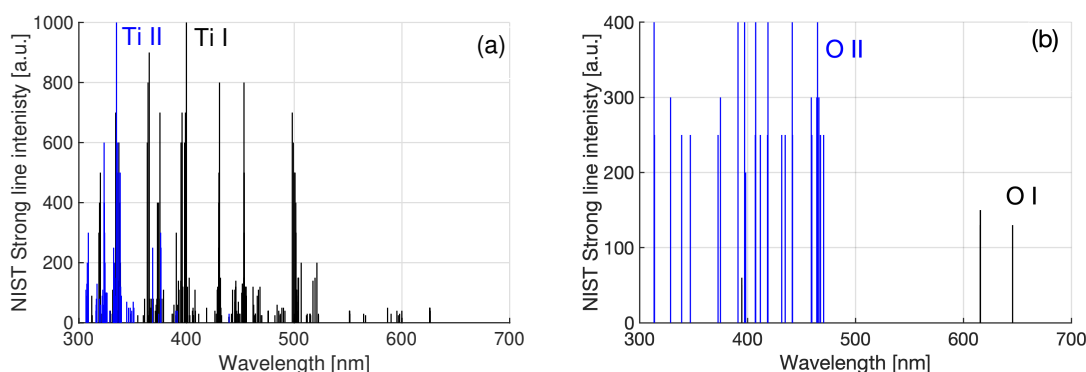


Figure 4.10. (a) Ti atomic emission. Emissions from Ti I are colored in black and emissions from Ti II are colored in blue. (b) O atomic emission. Emissions from O I are colored in black and emissions from O II are colored in blue [258].

Table 4.1 summarizes the various LIBS publications on TiO₂ nanomaterials for different TiO₂ sample preparations and operating fluence regimes with pulse energy. For the same wavelength,

PS-LIBS requires smaller laser fluence than LIBS. Note that Ren et al. [259] reported a relatively low laser fluence regime at the onset of PS-LIBS, where the scattering efficiency (defined as the ratio of the scattering signal intensity to the laser intensity) of clusters is constant before decreasing due to the ablation of particles (Fig. 4.11). Below this laser fluence, laser ablation, which is the necessary condition of PS-LIBS, is incomplete so the atomic emissions from evaporated species can not be detected. In most applications of PS-LIBS, to be in a saturated intensity regime for quantitative measurement, laser fluence over 20 J/cm² at 532 nm is mainly applied.

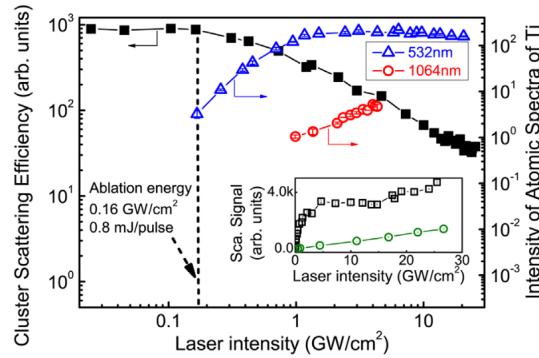


Figure 4.11. Scattering efficiency of TiO₂ clusters with 532 nm laser excitation (black squares) and atomic emission intensity of titanium at 498.17 nm with 532 nm laser (blue triangles) and 1064 nm laser excitation (red circles) at different laser intensities. The inset shows the comparison of scattering signals of clusters (black squares) and gases (green circles) with 532 nm laser excitation [259].

Table 4.1. List of studies of Phase-selective Laser-induced breakdown Spectroscopy (PS-LIBS) and Laser-induced Breakdown Spectroscopy (LIBS) on TiO₂.

	Team	λ_{laser} [nm]	Sample (d_p , T [K])	Operation fluence (mJ/pulse)
	Y.Zhang(2013) [228]	532	stagnation swirl flame: flame-synthesized TiO ₂ (6-8 nm, 1800K)	28 J/cm ² (35 mJ)
	Y.Zhang (2015) [252]	532	Bunsen+ Henchen : flame-synthesized TiO ₂ (15 nm, 1662K)	24 J/cm ² (290 mJ)
	Y.Ren (2015) [259]	532	Bunsen+ Henchen : flame-synthesized TiO ₂ (11 nm, 1550-1750K)	1.6 J/cm ² (minimum ablation)
PS-LIBS		354		24 J/cm ² (30mJ)
	G.Xiong(2016) [254]	532	stagnation swirl flame : flame-synthesized TiO ₂ (10 nm)	24 J/cm ² (30mJ)
		282		(7 mJ)
	G.Xiong(2018) [260]	281	coflow flame-synthesized TiO ₂	6 - 12 J/cm ²
	Y.Ren(2020) [255]	355	laminar and turbulent jet-diffusion flame-synthesized TiO ₂ (29.1 - 30.9 nm)	2 J/cm ²
	Hidalgo (1996) [247]	337	TiO ₂ coating on silicon wafer	8.6 J/cm ²
	Anglos (2001) [249]	1064	Pigment of paint layer	25-56 J/cm ² (2-10mJ)
LIBS	Lebouf (2013) [248]	1064	Degussa P25 20 nm on filter	24 J/cm ² (50mJ)
	Sovago (2013) [250]	1064	5 nm TiO ₂ suspension in water	(10 mJ)
	Menneveux (2015) [251]	1064	sunscreen on aluminum	75 J/cm ² (90mJ)

4.3 Laser-induced incandescence (LII)

The principle of LII is based on heating the particles by laser to reach a high temperature to emit thermal radiation, i.e., incandescence. The amount of the incandescence signal is proportional to the particle volume fraction in the control volume. Furthermore, the decay of the incandescence signal depends on the size distribution of aerosol particles. Using appropriate heat transfer modeling, it is then possible to obtain a size description of the particles.

Although LII has been prominently developed for measuring particle volume fraction, primary particle sizes [10, 11], and other thermophysical properties of carbonaceous particles in flames [261], there exists a growing interest in adapting this technique to non-carbon nanoparticles [262, 263, 22, 15, 23].

Concerning titanium dioxides, after the first attempt by Leipertz et al. [264] in 2003, the group of Zizak et al. [19, 20] has worked intensively on the spectral and temporal aspect of LII emission of TiO₂. Recently, De Iuliis et al. [214, 215] worked on the laser-induced emission (LIE) of flame synthesis of TiO₂ nanoparticles for fluences typical for LII.

Since the LII process is initially developed for soot particles, the adaptation to the inorganic particles, particularly to the TiO₂, may not be straightforward due to different physical and chemical properties. Additionally, the laser-particle interaction can lead to unexpected emissions depending on the experimental conditions such as the previously-discussed LIF and LIBS. Finally, a mixed population of particles with distinct optical properties can be observed, especially when considering hydrocarbons to sustain the pilot flame. In the last case, gaseous carbon atoms excess can lead to the formation of soot or carbon-coated nanoparticles [134, 265]. In this case, the discrimination of the different populations with LII is quite challenging.

Still, the LII has the potential to provide instantaneous 2D quantitative information on TiO₂ characteristics, which is of great interest for the investigation of the synthesis process in turbulent flames. The extension of the LII technique to the investigation of TiO₂ flame synthesis is the core of this research work.

The basics of LII will be presented in Sec. 4.3.1. The procedure for measuring the volume fraction and particle size will be reviewed in Sec. 4.3.2 and 4.3.3, respectively. Then, the challenges of extending LII on non-carbon nanoparticles, particularly on TiO₂, will be described in Sec. 4.3.4.

4.3.1 Basics on LII

Laser-induced incandescence occurs when the particles are heated to high temperatures so that they emit thermal irradiation. The LII signal can be described by introducing the Planck's law, where the blackbody intensity $I_b(\lambda, T(t))$ of a body for wavelength λ at absolute temperature $T(t)$ of a body is then given by [266]:

$$I_b(\lambda, T(t)) = \frac{2hc^2}{\lambda^5} \left[\exp\left(\frac{hc}{\lambda k_B T(t)}\right) - 1 \right]^{-1} \quad (4.1)$$

with h is the Planck constant, c the speed of light in a vacuum, k_B the Boltzmann constant. $I_b(\lambda, T(t))$ is in unit $W/(m^3 \cdot sr)$, which is the emissive power per unit area, per unit solid

angle, per unit wavelength.

The contribution of one nanoparticle to the detected signal is given by [W]:

$$S_{\text{LII}}(\lambda, T(t)) = C_{\text{abs},\lambda} I_b(\lambda, T_p(t)) \Delta\Omega_{\text{det}} = Q_{\text{abs},\lambda} \frac{\pi d_p^2}{4} I_{\lambda,b}(T_p) \Delta\Omega_{\text{det}} \quad (4.2)$$

where $C_{\text{abs},\lambda}$ is the absorption cross-section, $Q_{\text{abs},\lambda}$ is the absorption efficiency, $\Delta\Omega_{\text{det}}$ is the solid angle subtended by the detector as viewed by the nanoparticle, and $\frac{\pi d_p^2}{4}$ is the physical cross-sectional area of the particle.

When the nanoparticle size is sufficiently smaller than the wavelength of light, where the dimensionless size parameter $x = \frac{\pi d_p}{\lambda} \ll 1$, and phase shift criterion $x = \pi d_p / \lambda \cdot |m_\lambda| \ll 1$, the Rayleigh regime is verified and the absorption efficiency and cross section read as:

$$Q_{\text{abs},\lambda} = 4x \cdot E(m_\lambda) = \frac{4\pi d_p E(m_\lambda)}{\lambda} \quad (4.3)$$

$$C_{\text{abs},\lambda} = \frac{\pi^2 d_p^3}{\lambda} E(m_\lambda) \quad (4.4)$$

where m_λ is the complex index of refraction and $E(m_\lambda)$ is the refractive index function for absorption properties of the particle (Eq. B.1).

Finally, the incandescent light emitted from a single spherical nanoparticle with diameter d_p at a wavelength λ at temperature T , integrated over all solid angles (4π) can be written as:

$$S_{\text{LII}}(\lambda, T(t)) = \frac{8\pi^3 d_p^3 h c^2 E(m_\lambda)}{\lambda^6} \left[\exp\left(\frac{hc}{\lambda k_B T(t)}\right) - 1 \right]^{-1}. \quad (4.5)$$

Therefore, the incandescent signal S_{LII} increases with particle temperature, which increases with laser fluence as illustrated in Fig. 4.12. For low to moderate laser fluence regimes, the peak signal increases linearly with fluence until the peak temperature approaches the sublimation/boiling temperature of particles. Then, there is a "plateau region" where further temperature change is achieved by increasing the laser fluence due to the phase change to gas. Beyond this plateau regime, irradiation under the high laser fluence regime results in atomic line emission of evaporated species (PS-LIBS regime). In the high laser fluence region, the particles can be vaporized at the surface and then have a smaller particle diameter, which affects the temporal decay rate of the emissions (in Fig. 4.1).

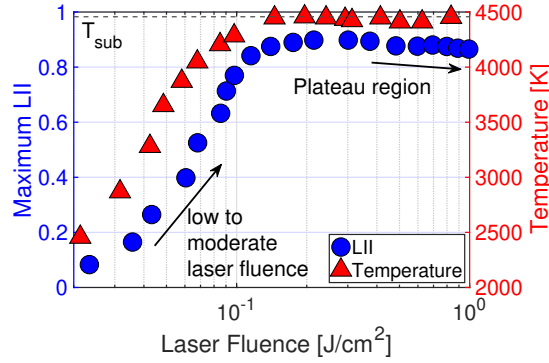


Figure 4.12. Typical fluence dependence of the maximum LII (left) and temperature (right) of soot particles generated in ethylene/air laminar diffusion flame. LII signal is recorded at 681.8 nm and the laser wavelength of 532 nm was used [267].

4.3.2 LII signal and volume fraction

Assuming that the spatial fluence distribution across the laser beam profile is uniform and that all particles are identical, all particles in the LII probe volume will be heated up to the same temperature T_p . Under these assumptions, the LII signal emitted by an ensemble of spherical particles N_p in the probe volume having the same diameter d_p under Rayleigh regime is expressed by:

$$S_{\text{LII}}(\lambda, T_p(t)) = \frac{8\pi^3 d_p^3 hc^2 E(m_\lambda)}{\lambda^6} \left[\exp\left(\frac{hc}{\lambda k_B T_p(t)}\right) - 1 \right]^{-1} N_p. \quad (4.6)$$

The LII signal depends on the particle number density in the control volume (N_p , unit: particles/m³) and the cubic particle diameter (d_p^3). The particle volume fraction (f_v) is defined as the volume occupied by particles per unit volume:

$$f_v = \frac{N_p \pi d_p^3}{6}. \quad (4.7)$$

Then Eq.(4.6) can be written as :

$$S_{\text{LII}}(\lambda, T_p(t)) = \frac{48\pi^2 hc^2 E(m_\lambda)}{\lambda^6} \left[\exp\left(\frac{hc}{\lambda k_B T_p(t)}\right) - 1 \right]^{-1} f_v \quad (4.8)$$

meaning that the LII signal is proportional to the particle volume fraction.

Until now, the particles have been considered to have monodispersed distribution with a sphere geometry. However, in nanoparticle flame synthesis, each formation step (nucleation, surface growth, aggregation/agglomeration, sintering) has an effect on the size distribution and morphology of particles. The generated particles are mostly polydispersed and fractal-like agglomerates (Chap. 2).

The RDG-PFA (Rayleigh-Debye-Gans Polydisperse Fractal Aggregate) [174] theory states that primary particles in an aggregate absorb light volumetrically and independently on the aggregate

nature, i.e., as if they are isolated particles [175]. This theory is applicable to the aggregates whose primary particles are in the Rayleigh regime. If the aggregates are within the RDG-PFA limit, large and small particles are heated to the same final temperature [268]. Therefore, when considering one aggregate is constituted of n_{pp} primary particles of identical diameter d_{pp} , the LII signal reads as:

$$S_{LII}(\lambda, T_p(t)) = \frac{8\pi^2 hc^2 E(m_\lambda)}{\lambda^6} \left[\exp\left(\frac{hc}{\lambda k_B T_p(t)}\right) - 1 \right]^{-1} n_{pp} \pi d_{pp}^3. \quad (4.9)$$

The polydispersity of the primary particles diameter in one aggregate can be accounted for by introducing the distribution functions of diameter $p(d_{pp})$ of primary particles. By considering a population of primary particles with number density N , the final expression for the LII signal is:

$$\begin{aligned} & S_{LII}(\lambda, T_p(t)) \\ &= N \int_0^\infty p(d_{pp}) \frac{8\pi^2 hc^2 E(m_\lambda)}{\lambda^6} \left[\exp\left(\frac{hc}{\lambda k_B T_p(t)}\right) - 1 \right]^{-1} \pi d_{pp}^3 dd_{pp} \\ &= \frac{48\pi^2 hc^2 E(m_\lambda)}{\lambda^6} \left[\exp\left(\frac{hc}{\lambda k_B T_p(t)}\right) - 1 \right]^{-1} f_v \end{aligned} \quad (4.10)$$

with

$$f_v = N \frac{\pi}{6} \int_0^\infty p(d_{pp}) d_{pp}^3 dd_{pp}. \quad (4.11)$$

Effective particle temperature

Concerning the particle temperature, since the distribution of particle diameter and size of aggregate in the measurement volume as well as the laser fluence are not uniform, the measured temperature has to be treated as an "effective temperature". The effective temperature is a weighted average of temperature from the different size distributions of nanoparticles, generally biased toward the hottest particles [269]. The weighting of nanoparticle size distribution is highly non-linear and relatively sensitive to nanoparticle size. Then, the decay of the effective temperature is also closely related to the size distribution of the particles and their morphology, including fractal dimensions [270, 271].

To describe the effective particle temperature T_{eff} , which corresponds to the average temperature of the polydispersed distribution of primary particle and aggregate sizes, the Eq.(4.10) can be expressed as :

$$S_{LII}(\lambda, T_{eff}(t)) = E(m_\lambda) \frac{48\pi^2 hc^2}{\lambda^6} \left[\exp\left(\frac{hc}{\lambda k_B T_{eff}(t)}\right) - 1 \right]^{-1} f_v \quad (4.12)$$

Information on T_{eff} can be obtained by different techniques. In the following, two main techniques will be presented: two-color pyrometry and spectral fitting of Planck's law.

Two-color optical pyrometry Two-color LII technique is based on the simultaneous detection of the temporal evolution of the LII signal (Eq.(4.12)) at two different wavelengths. The detected signals $I_{\text{SLII},\lambda}$ read as :

$$I_{\text{SLII},\lambda_1}(T_{\text{eff}}(t)) = \theta_{\lambda_1} E(m_{\lambda_1}) \frac{48\pi^2 hc^2}{\lambda_1^6} \left[\exp\left(\frac{hc}{\lambda_1 k_B T_{\text{eff}}(t)}\right) - 1 \right]^{-1} f_v \quad (4.13)$$

$$I_{\text{SLII},\lambda_2}(T_{\text{eff}}(t)) = \theta_{\lambda_2} E(m_{\lambda_2}) \frac{48\pi^2 hc^2}{\lambda_2^6} \left[\exp\left(\frac{hc}{\lambda_2 k_B T_{\text{eff}}(t)}\right) - 1 \right]^{-1} f_v \quad (4.14)$$

where θ_{λ_i} is the detector efficiency at λ_i (including PMT sensitivity and bandpass filter sensitivity [267]). Using the Wien's approximation, the signal ratio R_{12} between wavelengths λ_1 and λ_2 can be written as :

$$R_{12} = \frac{I_{\text{SLII},\lambda_1}(T_{\text{eff}}(t))}{I_{\text{SLII},\lambda_2}(T_{\text{eff}}(t))} = C \frac{E(m_{\lambda_1})}{E(m_{\lambda_2})} \left(\frac{\lambda_2}{\lambda_1}\right)^6 \exp\left[\frac{hc}{k_B T_{\text{eff}}(t)} \left(\frac{1}{\lambda_2} - \frac{1}{\lambda_1}\right)\right] \quad (4.15)$$

where $C = \frac{\theta_{\lambda_1}}{\theta_{\lambda_2}}$ is a constant corresponding to the detection efficiency at λ_1 and λ_2 . Therefore, the ratio of measured LII signals at two wavelengths depends on the (effective) time-dependent temperatures:

$$T_{\text{eff}} = \frac{hc}{k_B} \left(\frac{1}{\lambda_2} - \frac{1}{\lambda_1}\right) \cdot \left[\ln \left(C^{-1} \frac{E(m_{\lambda_2})}{E(m_{\lambda_1})} \left(\frac{\lambda_1}{\lambda_2}\right)^6 R_{12} \right) \right]^{-1}. \quad (4.16)$$

From this equation, it can be deduced that the knowledge of the absolute value of $E(m_\lambda)$ is not required. However, the ratio $\frac{E(m_{\lambda_2})}{E(m_{\lambda_1})}$ needs to be known. Assuming that $E(m_\lambda)$ values is not dependent on λ , as commonly done for the case of soot particles [25], Eq.(4.16) simplifies as :

$$T_{\text{eff}} = \frac{hc}{k_B} \left(\frac{1}{\lambda_2} - \frac{1}{\lambda_1}\right) \cdot \left[\ln \left(C^{-1} \left(\frac{\lambda_1}{\lambda_2}\right)^6 R_{12} \right) \right]^{-1} \quad (4.17)$$

This technique has already been used by Lehre et al. [18] to investigate nano-scaled metal oxide particle synthesis in a laser vaporization reactor. However, the accuracy of this technique in the detection of particle temperature is strongly related to the knowledge of $E(m_\lambda)$ as a function of λ for the materials under consideration.

Spectral fitting of Planck's law This technique consists in inferring the temperature by fitting detected spectrally-resolved LII emission $I_{\text{SLII},\lambda}(T_{\text{eff}}(t))$ to the Planck's curve [267, 272]. It is indeed possible to rewrite Eq.(4.12) to identify the dependence of the different terms on T_{eff} and λ :

$$\begin{aligned} I_{\text{SLII},\lambda}(T_{\text{eff}}(t)) &= 24\pi f_v \frac{E(m_\lambda)}{\lambda} v_\lambda I_b(\lambda, T_{\text{eff}}(t)) \\ &= K_1 \cdot g(\lambda) \cdot I_b^d(\lambda, T_{\text{eff}}(t)) \end{aligned} \quad (4.18)$$

where $K_1 = 24\pi f_v$ does not depend on λ , while $g(\lambda) = \frac{E(m_\lambda)}{\lambda}$ depends only on λ and $I_b^d(\lambda, T_{\text{eff}}(t)) = v_\lambda I_b(\lambda, T_{\text{eff}}(t))$ depends on both λ and T_{eff} corresponds to the black body emission at temperature T_{eff} . Apparent black-body radiation spectral emittance I_b^d can be calibrated using a tungsten lamp with known emissivity (v_λ is the calibration function related to the optical devices for detection system) as done in the following.

It should be noticed that the spectral information of the $I_{\text{SLII},\lambda}$ does not depend on f_v (treated as constant K_1 in Eq. (4.18)), so that this quantity does not need to be known to identify T_{eff} . On the contrary, the knowledge of $E(m_\lambda)$ as a function of λ is required.

To conclude, information on $E(m_\lambda)$ as a function of λ is essential to obtain T_{eff} . The absolute value of the absorption function is needed to successively quantify the volume fraction from Eq.(4.12). For soot particles, the absorption function is often considered constant, with values between 0.1 and 0.4. On the contrary, for some metal oxide particles the absorption function is not well-known and cannot be assumed as constant. Thus, it could be a critical issue for using LII to characterize inorganic particle production in flames, as discussed in Sec. 4.3.4.

4.3.3 Information on particle size distribution

The LII signal decay has a complex evolution that depends on the particles (or aggregates) size distribution, the morphology of the aggregate fractal dimension, and the particle temperature .

Previous studies have shown the effect of particle geometry on LII signal and temperature decay in terms of primary particle size d_{pp} [273, 274, 275], monodisperse/polydispersed distribution $p(d_{\text{pp}})$ [270, 276], the distribution of the number of primary particles in one aggregate $p(n_{\text{pp}})$ [273, 271], and fractal dimension D_f [270, 277]. The particle size distribution can be inferred by comparing the measured LII signal decay and simulated LII modeling. This methodology requires an LII model which considers heat transfer processes during the LII process. The details can be found in Appendix B. The LII modeling of the unsteady energy and mass conservation equations is numerically resolved to determine the temporal evolution of the effective particle temperature. Then, the difference between experimentally-observed and modeled data is minimized using the least-squares method. The parameters minimizing the residual between the data and its modeled equivalent determine the particle size distribution (or other quantity of interest).

This post-processing procedure is not trivial. On one side, in the LII modeling, some variables are not explicitly known. Typical examples are the thermal accommodation coefficient and ab-

sorption function. These variables can be derived from other techniques like molecular dynamics for thermal accommodation coefficient [278], or line-of-sight attenuation (LOSA) for absorption function [24]. On the other side, since different particle distributions can result in the same signal decay, this problem is mathematically ill-posed [276] in terms of particle size distribution. Therefore, the process of obtaining the precise size distribution can be highly dependent on the prior knowledge of certain parameters as well as information about the aggregation state of the system [279].

4.3.4 Challenges of laser-induced incandescence on TiO₂

The generalization of the LII technique to non-soot particles is challenging. At first sight, one might think that engineered nanoparticles have a more known composition with well-defined morphologies (e.g., isolated spherical nanoparticles) than heterogeneous polydispersed soot aggregates with various chemical compositions. However, when considering flame synthesis, they can also have non-spherical geometry [280]. In addition, the differences in optical, physical, and chemical properties from conventional carbonaceous particles (Table 4.2) result in additional difficulties in applying the LII techniques. For instance, there have been several trials to conduct LII on flame-synthesized TiO₂ nanoparticles [264, 19, 20, 214, 215]. Still, according to the present state of knowledge, no study has succeeded in recovering the volume fraction and particle size distribution from the detected LIE emission of TiO₂. A recent review paper by Sipkens et al. [12] summarized the difficulties in non-soot LII. This section will review the challenging points of adapting LII especially for TiO₂, by relying on the comparison with carbonaceous particles and on the results of pioneering works.

Table 4.2. Properties of carbon black and TiO₂ nanoparticles.

Property	Carbon Black	TiO ₂ (Rutile)
Melting temperature [K]	3823 [281]	2128 [282]
Boiling temperature [K]	4473 [281]	2773 - 3273 [283]
$E(m_\lambda)$ at 355 nm *	0.195 [25]- 0.372 [284]	0.0131[285] - 0.0155[286]
$E(m_\lambda)$ for VIS *	nearly constant	varying (Fig. 4.13)

* Note the values are measured at room temperature and will be considerably different at elevated temperatures.

1) Low absorption function $E(m_\lambda)$

Performing LII on TiO₂ supposes that the particles absorb laser radiation. For a spherical particle in the Rayleigh regime, where the particle diameter d_p is much smaller than laser wavelength λ_{ex} , the rate of laser absorption can be expressed as :

$$\dot{Q}_{abs} = \frac{\pi^2 d_p^3}{\lambda_{ex}} E(m_{\lambda_{ex}}) F q(t) \quad (4.19)$$

where F is the laser fluence (unit: J/cm^2) and $q(t)$ is the profile of laser. The absorption function $E(m_\lambda)$ translates the ability to absorb laser radiation. $E(m_\lambda)$ is a function of the refractive index m at a wavelength λ .

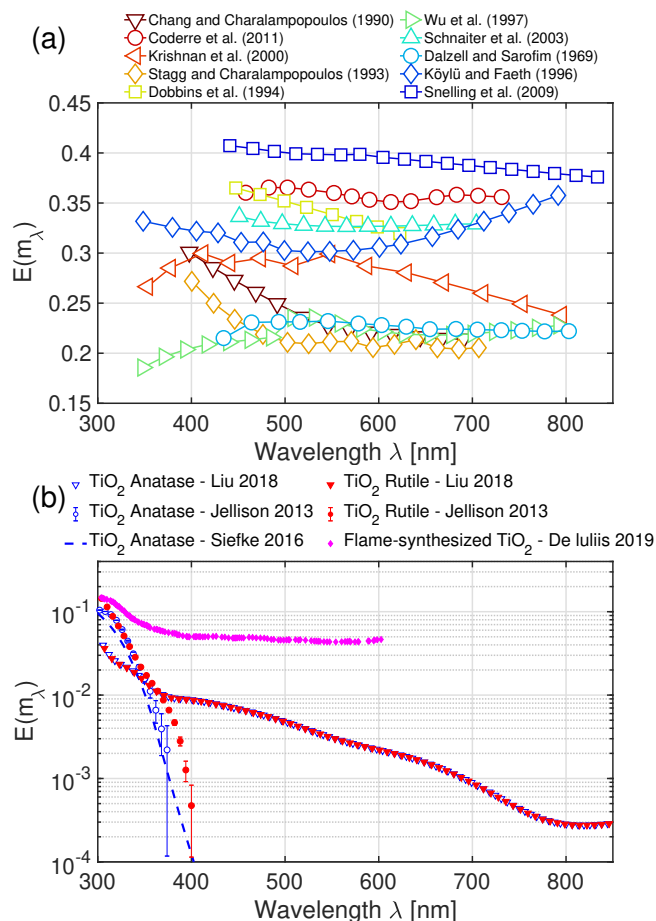


Figure 4.13. Absorption function $E(m_\lambda)$ of (a) carbonaceous particles [287, 288, 289, 290, 291, 292, 293, 294, 295, 296] and (b) TiO_2 nanoparticles (in log scale) [285, 286, 297, 214]. Liu et al. [148] synthesized nanofilms by mist chemical vapor deposition using TTIP and annealing to transform anatase to rutile. Jellison et al. [286] generated TiO_2 nanofilms by RF magnetron sputter deposition. Siefke et al. [297] used atomic layer deposition with TTIP at a deposition temperature of 100°C to create nanofilms. De Iuliis et al. [214] measured the extinction coefficient (ex-situ) for flame-synthesized nanoparticles

Figure 4.13 displays the absorption function $E(m_\lambda)$ from various sources of literature of TiO_2 [285, 286, 297, 214] and carbonaceous particles (e.g., soot) [287, 288, 289, 290, 291, 292, 293, 294, 295, 296] for comparison [298]. $E(m_\lambda)$ can vary depending on the particle morphology, maturity [299, 300], and chemical composition (e.g., H/C ratio [301]) for soot particles. The

values of $E(m_\lambda)$ for soot are generally comprised between 0.18 and 0.42 with an excitation wavelength of 1064 nm and are commonly assumed to be constant [302], or slightly wavelength dependent [287, 303]. The variability indicates the level of uncertainty present in the values documented in the literature [298].

The main challenge in applying LII to flame-synthesized TiO₂ particles, as well as other flame-synthesized particles, is related to the specific optical properties. Fig. 4.13(b) illustrates the values of $E(m_\lambda)$ for TiO₂ on a logarithmic scale. However, the $E(m_\lambda)$ of TiO₂ varies significantly across studies, depending on the synthesis process, and all reported values are remarkably small, a few orders of magnitude smaller than those of carbonaceous particles. While TiO₂ has better absorption in the UV part, it decreases significantly in the visible range, except for De Juiis et al. [214] (flame-synthesized TiO₂) where it remains nearly constant. This tendency highlights two main pieces of information. First, to improve heat-up efficiency, it is recommended to heat TiO₂ particles using a UV laser, which is challenging in flame due to potential interferences with gaseous species fluorescence [304]. Second, the laser incandescence signal emitted in the visible range for an equivalent volume fraction of TiO₂ particles will be weaker by a few orders of magnitude compared to soot particles.

2) Interference with other parasitic laser-induced emissions

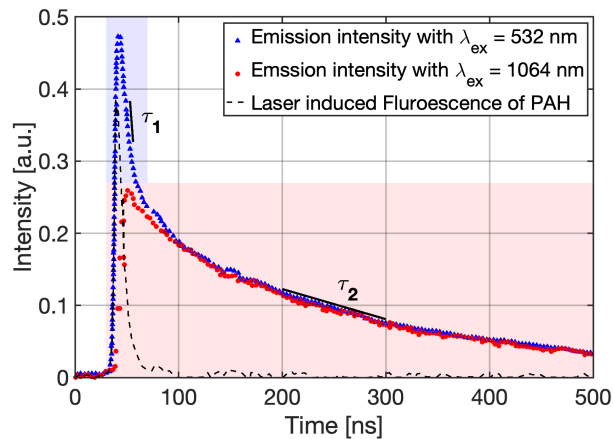


Figure 4.14. Temporal profiles of laser-induced emission of soot particles in the methane diffusion flame, adapted from [305]. Blue triangles represent the total laser-induced emission from soot particles using a 532 nm laser. The red round points indicate the laser-induced incandescence signal from soot particles using a 1064 nm laser. The black dotted line shows the subtracted part between blue and red points, signifying the LIF part from the PAH species of the flame.

The possible overlap of other laser-induced emissions such as LIF and LIBS makes it even more challenging to distinguish the nature of the detected signal. This interference of other laser-induced emissions can also exist in LII on sooting flames. Figure 4.14 shows the temporal profile of LII intensity in the diffusion methane flame at 30 mm height above the burner for two excitation laser wavelengths and laser fluences. The temporal profile at 1064 nm (pulse energy:

0.49 mJ, red round) was adjusted to fit the 532 nm (pulse energy: 0.245 mJ, blue triangle) using well-adjusted laser energies. During prompt LII emission (up to 50 ns), a short parasitic interference signal can be observed when considering the emission induced by a laser at 532 nm. This parasitic signal is attributed to laser-induced fluorescence (LIF) signal from PAHs [306]. The PAHs fluorescence can be extracted by subtracting the 1064 and 532 nm signals (black dotted line). This LIF emission creates a severe change in slope from τ_1 in the first interval (identified by the blue zone in Fig. 4.14) and τ_2 for longer times (red zone in Fig. 4.14). In general, a drastic change in the slope of the signal temporal evolution indicates the presence of parasitic signals.

The UV excitation can cause other LIEs that may contaminate the LII signal of TiO₂ during the measurement. It is, therefore, important to properly characterize the nature of the LIE. For example, careful attention should be given when using prompt LII emission to evaluate peak temperature. The interference may also cause discrepancies between modeled and measured LII signals [307]. Possible sources of interference in LII measurement reported in the literature [19, 13] are: short-lived photo-luminescence of TiO₂ by laser photon absorption (=LIF), emission of molecular bands from fragments or combustion products (e.g., C₂ swan band), excited-state emission from the ambient gas, emission from vaporized or dissociated species from the heated nanoparticle that become electronically excited (=LIBS), chemiluminescence from recombining vaporized products and plasmon resonances.

When the LII measurements are conducted in non-reactive ambient conditions, there will be no combustion related products. Therefore, interferences with combustion-products are absent. But when considering TiO₂ flame synthesis, the contribution from combustion products may not be negligible. Similarly, chemiluminescence is not expected to occur when considering a non-reactive inert gas environment, but it can be observed when considering the flame. Excited ambient gas species emissions can be generally accounted for via the background subtraction process. Plasmon resonances typically happen at the surface of metal nanoparticles [308] and have not been observed in literature for metal oxides TiO₂ without doping the metallic layer. Generally, the LIF and PS-LIBS from TiO₂ nanoparticles are expected to be a major source of interference in laser-induced incandescence of TiO₂ measurement, as discussed by De Iuliis et al. [214]. Note that the appearance of PS-LIBS from TiO₂ can be controlled with laser fluence.

The perturbation from non-incandescent laser-induced emission (LIE) has been investigated temporally [267, 305, 307, 261, 309] and spectrally [310, 214]. The LII signal is expected to have a longer lifetime than fluorescence emission or LIBS atomic emissions because of different signal decay mechanisms (thermal/ incandescence-based mechanism vs. electronic mechanism) [13, 311, 304, 312]. Consequently, many studies use delayed detection to avoid LIF signal emission for LII measurement of soot particles with UV-VIS excitation wavelength [310, 306, 313, 305]. Alternatively, they use the IR range excitation wavelength not to excite the fluorescent species in flame emissions [268], which may not be suitable for TiO₂ nanoparticles due to their low absorption in near IR regime (Fig. 4.13(b) and [314]).

3) Phase change from low melting point

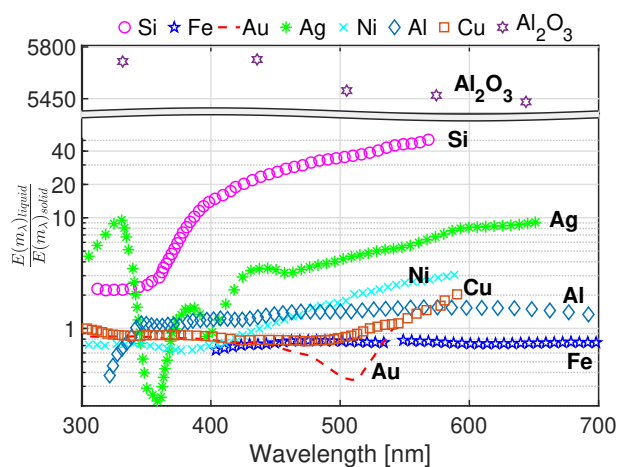


Figure 4.15. Ratio of liquid and solid phase $E(m_\lambda)$. Si and Fe from [12]; solid Au, Ag, and Ni from [12] and liquid Au, Ag and Ni from [26]; Al, Cu from [26]; Al₂O₃ from [315].

Additional complexity for applying LII to non-soot nanoparticles comes from the lower melting point of non-carbonaceous particles compared to that of soot so that the particles can experience multiple phase changes during the LII process. Specifically, the laser irradiation during LII can melt the particle into a liquid so the LII process can happen in both states. In addition, TiO₂ could also be in the liquid phase before laser irradiation due to the high flame temperature. Liquid-state LII has been investigated in various liquid-state metals and metalloids [316, 227, 16]. The main difficulty is linked to the fact that phase change can cause changes in optical properties. For example, solid silicon is a semiconductor whose absorption spectrum is related to the band-gap energy [317], but liquid silicon behaves like a metal whose optical properties can be described with Drude theory [318]. Figure 4.15 shows the ratio of the liquid to the solid phase of $E(m_\lambda)$ as a function of the wavelength for several metal particles as well as Al₂O₃⁴. One can note that Ni, Au, Cu, Al, and Fe have spectrally different absorption functions when they are in a liquid state, the ratio fluctuating close to 1. Ag, Si, and Al₂O₃ have a much higher absorption function in a liquid state. In terms of LII, the higher absorption function in the liquid state can make the particles absorb the laser better, resulting in high temperature following vaporization. The significant difference in optical properties of solid and liquid nanoparticles increases the complexity of the interpretation of the LII signal.

To date, there is no information available on the optical properties of molten TiO₂ in the literature. One possible method to estimate the refractive index of ceramics is the Drude-Lorentz

⁴While there are clear indications of significant differences in the absorption coefficient values between the melt and the crystal near the melting point, suggesting a sudden rise in the absorption coefficient during melting, it is worth mentioning that not all researchers studying the absorption coefficient of molten alumina share this perspective [319]. In most investigations, it is generally accepted that the sudden alteration is caused by the γ -phase-like coordination present in liquid Al₂O₃ [319].

dispersion theory. This theory has been used to describe the dielectric response of the electrons in metals, which exhibit strong dependence on the behavior of their free electrons in the UV/Vis/NIR absorption range [29]. For semiconductors, the Lorenz oscillator model has been applied to explain the optical response of TiO₂ layers [320, 321]. Optical characterization of TiO₂ has been based on the Tauc-Lorentz model using spectroscopic ellipsometry measurements [322, 323, 324]. However, these models require information on certain parameters that need to be determined through ellipsometry experiments [325]. This approach has been used for liquid silicon and germanium during melting induced by pulsed laser [326], but not for liquid TiO₂.

Applicability of Rayleigh approximation It is important to verify the applicability of the Rayleigh approximation for TiO₂ nanoparticles. The first size parameter criterion ($x = \frac{\pi d_p}{\lambda} \ll 1$) is well satisfied with $d_p = 28$ nm and $\lambda_{laser} = 355$ nm. However, the second phase shift criterion ($x = \pi d_p / \lambda \cdot |m_\lambda| \ll 1$) requires more attention. For solid TiO₂, it is certainly satisfied due to the small refractive index of TiO₂ in the visible range. For liquid TiO₂, however, this is less certain because its refractive index may differ considerably from that of the solid phase. If the refractive index for liquid TiO₂ is not small enough to satisfy the Rayleigh approximation, changes induced by laser to the particle morphology may influence the spectroscopic cross-section of the particles. This issue is well-described for metal nanoparticles in [327].

4) Mixed particle populations

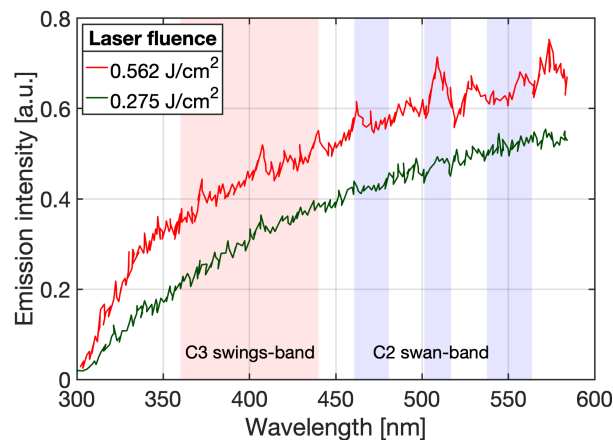


Figure 4.16. Laser-induced light emission under different laser fluences at HAB = 2 cm in TiO₂ nanoparticle flame spray synthesis at prompt detection timing, adapted from [215]. C₂ and C₃ bands from [312].

In the flame synthesis of nanoparticles, the simultaneous presence of particles with different characteristics can be observed. For example, De Iuliis et al. [215] conducted LII on TiO₂ nanoparticles produced in a flame environment with a 1064 nm laser. For this, the liquid precursor (TTIP) was dissolved in ethanol, and its combustion was assisted by a premixed methane-air

flame. In the spectral emission represented in Fig. 4.16, the C₂ Swan band and C₃ Swing band from the excited carbon species [312] are detected for high laser fluence regime. These bands indicate the presence of carbon species in the flame synthesis of TiO₂. The quantitative characterization of f_v of TiO₂ from the LII signal is challenging when particle populations of different natures coexist. In specific, the distribution of particles can include multiple particle populations like (1) carbon-coated TiO₂, (2) carbon-coated TiO₂ together with soot, or (3) pure TiO₂ and soot particles, depending on the local flame environment [265, 134, 35]. Therefore, it can be extremely difficult to assess for sure if the LII signal comes from pure TiO₂ particles or carbonaceous (soot or carbon-coated) nanoparticles.

4.4 Conclusion

Laser diagnostics are getting more attention in the flame synthesis of nanoparticles. Among them, LII can provide the capacity to characterize the particle diameter and volume fraction in an in-situ approach in the flame synthesis of nanoparticles. The adaptation of LII from conventional soot particles to non-soot metal oxide nanoparticles can raise issues related to unfavorable optical properties, the existence of laser-induced interference emission during the measurement, and the possible phase change during the LII process. To the authors' knowledge, studies applying LII on TiO₂ until now have been done under the risk of carbon trace in signals from the hydrocarbon fuel or carbon-containing precursors [19, 20, 214, 215] with high flame temperature over the melting point of TiO₂, leading to uncertainty about the origin of the incandescent signal. The short reviews on LIF and PS-LIBS emissions reminded first that parasitic signals with a short lifetime are expected to be found, and second that LIE of TiO₂ nanoparticles have to be carefully analyzed to correctly characterize the LII nature of the observed signals. Therefore, the next chapter aims to verify the feasibility of laser-induced incandescence measurements on pure TiO₂ nanoparticles aerosol in a non-reactive environment.

Chapter 5

Characterization of the LIE of TiO₂ nanoparticles in a non-reactive environment

The short review of Chap. 4 about the use of the LII technique to flame-synthesized TiO₂ nanoparticles highlights the importance of working with high-purity TiO₂ nanoparticles. Additionally, De Iuliis et al. [214] showed that the nature of laser-induced emission (LIE) has to be carefully analyzed since parasitic signals can be observed in the prompt emission spectra in both low and high fluence regimes. In this pioneering work [214], the LIE was characterized on flame-synthesized TiO₂, i.e., possibly containing carbon trace, that was precedently deposited on a sampling filter, which can introduce parasitic LIE signals. The core of the present chapter is a comprehensive characterization of the LIE at the prompt and delayed acquisition of high-purity TiO₂ nanoparticles (99.9995 %) to be sure of the absence of carbon materials in a well-controlled environment that has expected to have a negligible contribution to LIE signal. For this, an aerosol made of commercial high-purity TiO₂ nanoparticles produced via the sol-gel process is transported by a nitrogen flow in an optical cell at room temperature. This permits avoiding the risk of 1) melting from the local environment, i.e., to guarantee of solid state prior to the laser interaction, 2) interferences from carbon-related species during the measurements 3) parasitic signal from gaseous species characterizing flame environment. The effect of laser fluence and delay time with respect to the signal peak is investigated and compared to well-known carbon black nanoparticles LIE acquired in the same condition.

The spectral and temporal evolution of the signals are explored under different laser excitation and detection schemes to interpret the LIE of TiO₂ nanoparticles. The feasibility of LII on pure TiO₂ aerosol is then demonstrated. This chapter is organized as follows. First, the scientific strategy to investigate the nature of LIE is presented in Sec. 5.1. Then, the experimental setup is described in Sec. 5.2. Finally, experimental results are discussed in Sec. 5.3.

5.1 Strategy to analyze LIE

Three different types of laser-induced emissions from TiO₂ nanoparticles are investigated here: Laser-Induced Fluorescence (LIF), Phase-selective Laser-induced breakdown spectroscopy (PS-LIBS), and Laser-Induced Incandescence (LII). Conventional LIBS is not concerned since the fluence regime used in this work is lower than the air breakdown threshold ($\sim 100 \text{ J/cm}^2$ at 355 nm [218]). As a confirmation, no visible spark was observed during our measurements. The three considered LIEs can simultaneously occur during the laser excitation as illustrated in Fig. 5.1, which displays the schematic of the fluence range of LIE with their emission duration and the corresponding particles phase (solid, liquid, and gas). Since various LIEs of TiO₂ nanoparticles have different characteristic times and occur under different fluence regimes as summarized in Table 5.1, it is possible to characterize the nature of the detected signal by examining the impact of laser fluence and temporal characteristics of the spectral emission of TiO₂.

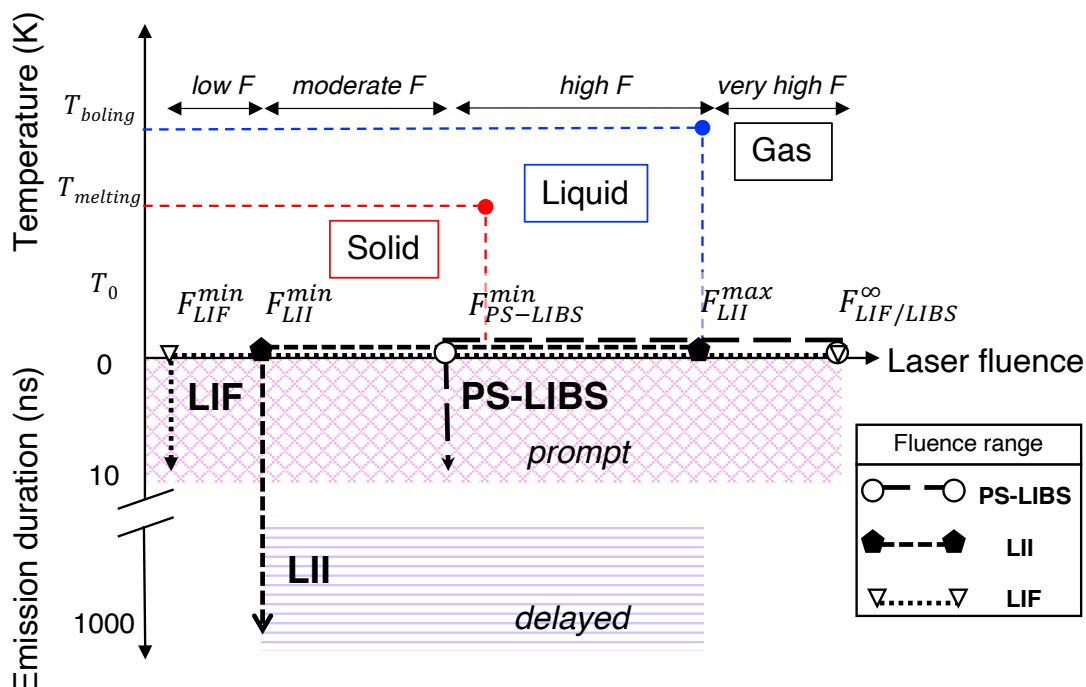


Figure 5.1. Schematic of the particle phase information related to the temperature (top) and to the LIE characteristic emission duration (bottom) as a function of the typical fluence range of different LIE signals.

First, general characteristics of LIE will be presented in Sec. 5.3.1 to clarify the retained strategy. Then, LIE at prompt will be investigated in Sec. 5.3.2. Specifically, only TiO₂ LIF is expected to occur when working at low laser fluence regimes where LII and PS-LIBS are not expected to occur, as indicated in Fig. 5.1. Then, by increasing the laser fluence, the TiO₂ particle temperature is expected to rise, and different spectral features of TiO₂ fluorescence could

Table 5.1. Characteristics of the laser-induced emissions of TiO₂ nanoparticles in terms of operating fluence range, and characteristics time (at 1 atm)

Laser wavelength	LIF	PS-LIBS	LIBS	LII
UV	continuous wave (~mW)	0.4 - 32 J/cm ² at 355 nm [254]	-	0.0007 - 0.05 J/cm ² (filter) 0.08 -0.15 J/cm ² (flame) at 266 nm [214]
Fluence range				
532 nm	-	1.6-56 J/cm ² [253, 259, 254]	-	-
1064 nm	-	10 - 45 J/cm ² [259]	24 - 75 J/cm ² [248, 251]	0.01-0.56 J/cm ² [215]
Characteristic time	ps to 10 ns [307]	10 ns [228]	300 ns - ms [217]	10 ² -10 ³ ns

be induced [238]. From moderate to high laser fluence regimes, the LIF, PS-LIBS, and LII of the TiO₂ nanoparticles could occur simultaneously with different intensities making the signal analysis very challenging in these regimes. Finally, a delay in the signal detection will be introduced in Sec. 5.3.3 so that LIF and PS-LIBS emission signals which are characterized by a short (tens of ns) lifetime are expected not to be found. Thus, under different laser fluence regimes, the time-resolved behavior of delayed TiO₂ emission spectra will be investigated based on LII theory to demonstrate its LII nature.

5.1.1 LII theory

To verify the LII nature of the LIE, the theoretical evolution of the signal in Sec 5.3.3 will be verified following 3 points:

- The spectral emission will be analyzed as a function of temperature. To illustrate this, the spectra calculated from Eq.(4.2) are shown in Fig. 5.2 for different particle temperatures by assuming that $E(m_{\lambda_{em}})$ and d_p are not dependent on temperature, i.e., no change of the particle (solid/liquid/gas) state. $E(m_{\lambda_{em}})$ is also assumed to be constant between 400 - 700 nm. Under these assumptions, the peak location of the spectrum shifts towards a longer wavelength (red-shifted) with decreasing temperature or towards shorter wavelengths (blue-shifted) with increasing temperature, i.e., the spectrum follows Wien's displacement law. It should be remembered that this thermal shift is valid only if $E(m_{\lambda_{em}})$ is invariant with particle temperature. Therefore, if the particles undergo a physical phase change (a change in radiative properties with temperature in the solid phase or from liquid to solid) during their cooling, all along this manuscript, these assertions may be questionable due to the low melting temperature for TiO₂ ($T_{melting}=2128$ K [282]). A variation of the absorption function may be expected due to the phase change, as illustrated in Fig. 4.15.

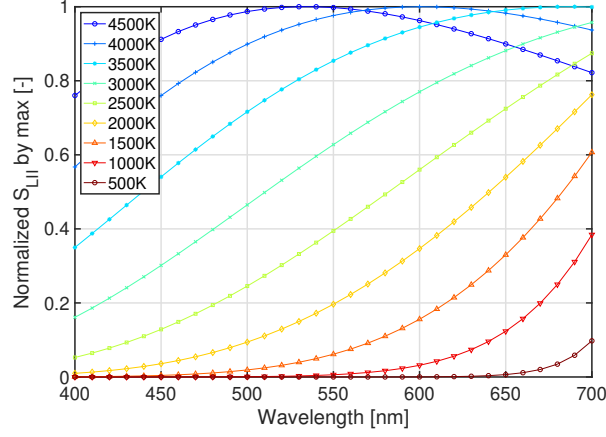


Figure 5.2. Effect of the temperature on LII emission spectra $S_{LII}(\lambda_{em}, T_p(t))$, normalized by maximum value between 400-700 nm.

- The decay characteristic time under different detection wavelengths will be investigated to confirm the incandescence nature among other interference emissions through temporal signals in Sec. 5.3.3. LII signal $S_{LII}(\lambda_{em}, T_p(t))$ is a function of emission wavelength λ_{em} (Eq. (4.2)). If $d_p(t)$ ¹ and $E(m_{\lambda_{em}})$ are assumed constant during the LII decay, by putting a natural log on both sides of Eq. (4.2), it can be obtained that:

$$\ln(S_{LII}(\lambda_{em}, T_p(t))) = \ln C - \ln \left(\exp \left(\frac{hc}{\lambda_{em} k_B T_p(t)} \right) - 1 \right) \quad (5.1)$$

with $C = 8\pi^3 d_p^3 hc^2 E(m_{\lambda_{em}}) \lambda_{em}^{-6}$. Considering constant C during the time duration $[t_i, t_j]$, a decay characteristic time τ can then be defined as:

$$\begin{aligned} \tau &= \frac{t_i - t_j}{\ln(S_{LII}(t_i)) - \ln(S_{LII}(t_j))} \\ &= \frac{t_i - t_j}{\ln \left(\exp \left(\frac{hc}{\lambda_{em} k_B T_p(t_j)} \right) - 1 \right) - \ln \left(\exp \left(\frac{hc}{\lambda_{em} k_B T_p(t_i)} \right) - 1 \right)} \end{aligned} \quad (5.2)$$

Since $\frac{hc}{\lambda_{em} k_B T_p(t)} \gg 1$, the Wien's approximation can be applied:

$$\exp \left(\frac{hc}{\lambda_{em} k_B T_p(t_i)} \right) - 1 \approx \exp \left(\frac{hc}{\lambda_{em} k_B T_p(t_i)} \right)$$

so that:

$$\tau = \frac{k_B \lambda_{em}}{hc} (t_i - t_j) \left(\frac{1}{T_p(t_j)} - \frac{1}{T_p(t_i)} \right)^{-1}. \quad (5.3)$$

¹ $d_p(t)$ constant means that sublimation is negligible during the duration of the LII process.

It can be noted that the decay characteristic time τ is linearly proportional to the emission wavelength λ_{em} for the same temperature decay: $\tau \propto \lambda_{em}$. This relationship is valid only for LII, meaning that if it is verified, interference signals like fluorescence or atomic emission are negligible. τ is classically used to provide information on particle diameter even if, in reality, it is a function of the temperature of the particle and not of the diameter. Still, assuming that all particles attain the same temperature for a given fluence, the decay characteristic time will be inversely proportional to the particle diameter.

If the primary particle diameters follow a lognormal distribution, the count mean diameter d_{cmd} and the geometric standard deviation σ_g can both be used to create simulated LII signal decay profiles. In such a case, the lognormal distribution can be represented by combining the d_{cmd} and the geometric standard deviation σ_g as described in Eq. 5.4. Subsequently, the TiRe-LII signal produced by polydisperse particles is a combination of decaying functions (df) for various size classes (one particle size class between d_p and dd_p), with each function weighted by its corresponding probability [328]. To simplify matters, the present study assumes a monodisperse distribution within the probe volume.

$$df = \frac{1}{\sqrt{2\pi}d_p \ln\sigma_g} \exp\left[-\frac{(\ln d_p - \ln d_{cmd})^2}{2(\ln\sigma_g)^2}\right] dd_p \quad (5.4)$$

- From Eq.(5.1), it is possible to derive the quantity ΔT^{-1} :

$$\Delta T^{-1}(t) = \frac{1}{T_p(t_0)} - \frac{1}{T_p(t)} = \ln\left[\frac{S_{LII}(\lambda_{em}, T_p(t))}{S_{LII}(\lambda_{em}, T_p(t_0))}\right] \left(\frac{hc}{\lambda_{em}k_B}\right)^{-1} \quad (5.5)$$

This quantity depends only on the particle temperature evolution from its prompt value, i.e., at time t_0 . This means that it is not dependent on the detection wavelength, implying the same evolution has to be calculated when using the signal if it has an LII-nature no matter which emission wavelengths are considered:

$$\begin{aligned} \ln\left[\frac{S_{LII}(\lambda_{em,i}, T_p(t))}{S_{LII}(\lambda_{em,i}, T_p(t_0))}\right] \left(\frac{hc}{\lambda_{em,i}k_B}\right)^{-1} \\ = \ln\left[\frac{S_{LII}(\lambda_{em,j}, T_p(t))}{S_{LII}(\lambda_{em,j}, T_p(t_0))}\right] \left(\frac{hc}{\lambda_{em,j}k_B}\right)^{-1}, \forall \lambda_{em,i}, \lambda_{em,j}. \end{aligned} \quad (5.6)$$

The temporal estimation of $\Delta T^{-1}(t)$ will be calculated from PMT signals at two different λ_{em} in Sec. 5.3.3. If identical, the LII nature of the signal at λ_{em} will be confirmed at least for the two considered wavelengths.

In the following, carbon black will serve as a reference case for typical LII behavior and will be compared to the TiO₂ LIE observed in similar operating conditions.

5.2 Experimental set-up

The experimental set-up considered in this work consists of three parts, as illustrated in Fig. 5.3: particles dispersion, laser setting, and signal detection.

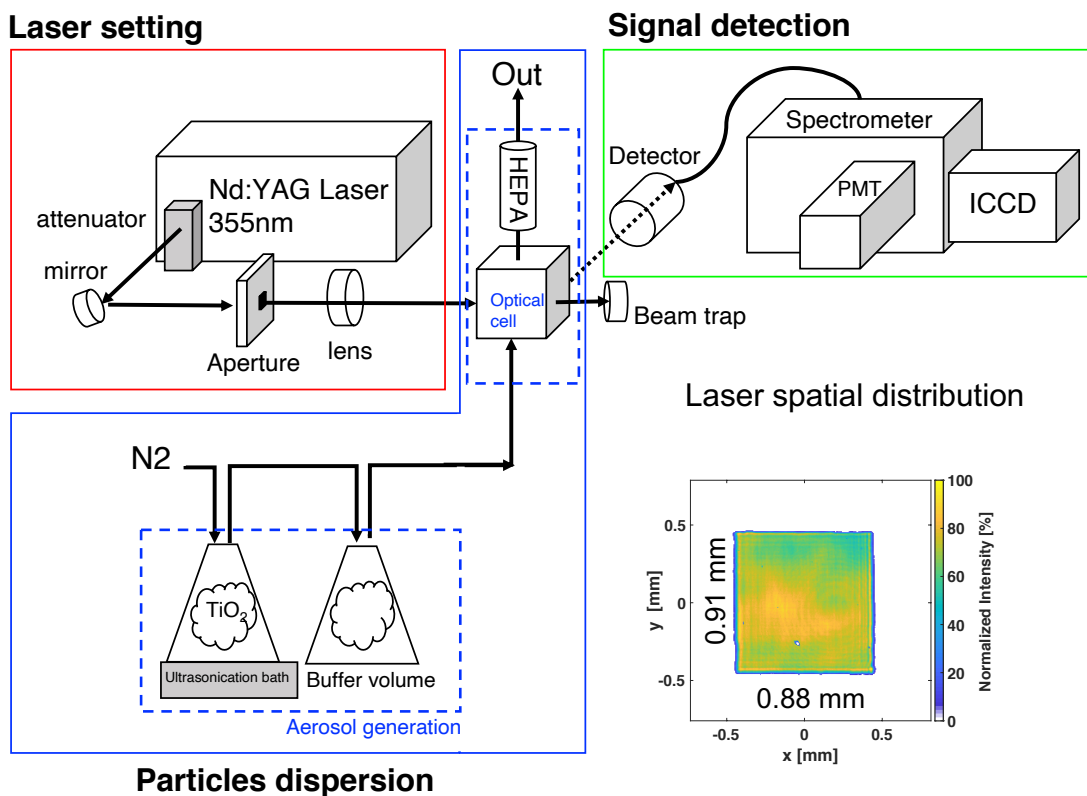


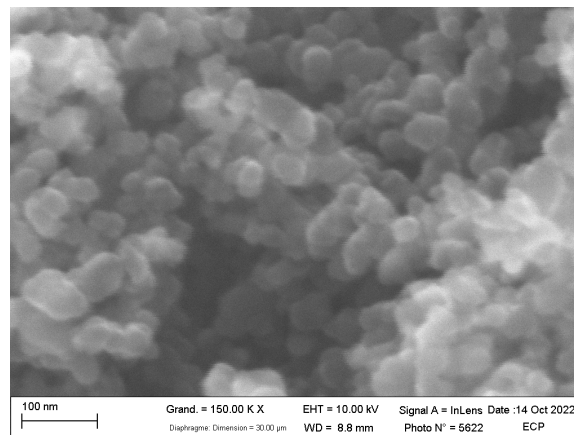
Figure 5.3. Schematic presentation of the experimental set-up developed to investigate the laser-induced emission from TiO₂ nanoparticle-laden aerosol using a pulse YAG laser at 355 nm with a top-hat spatial profile (bottom-right). The laser profile is captured in 500 individual shots, and the resulting images are averaged to create a top-hat image.

5.2.1 Particle dispersion

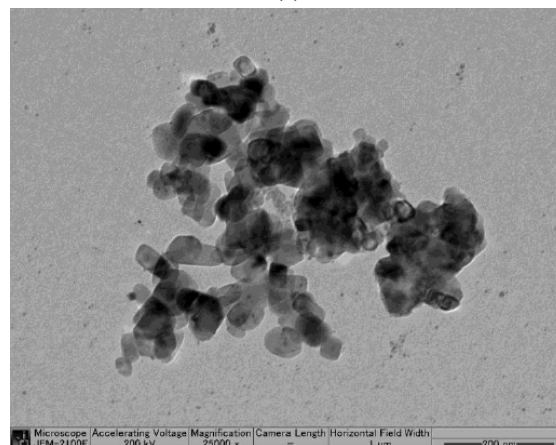
A nanoparticle-laden aerosol is prepared using commercially available particles of carbon black (nanografi, NG04EO0709, mean primary particle diameter $d_{pp} = 20$ nm, spherical) or of TiO₂ (nanografi, Rutile (NG04SO3507), mean primary particle diameter $d_{pp} = 28$ nm, purity 99.995+%, produced by sol-gel method). Microscopic images are illustrated in Fig. 5.4. Averaged primary particle sizes analyzed from the microscopy images are $d_{pp, \text{carbon}} = 30 \pm 4$ nm, $d_{pp, \text{TiO}_2} = 31 \pm 5$ nm. The polydispersity of the target particles remains constant during the measurement, despite being small.

Nanoparticles are transported in a non-reactive environment with N₂ flow (16.67 slm, 9.8 m/s) in a first flask (1L) placed inside an ultrasonic water bath. Ultrasonication is employed to break

apart the agglomerates of the powder [329]. The solid-gas mixture passes through another buffer flask (1L) to have a homogeneous distribution. Then, the nanoparticle aerosol is dispersed in an optical cell. The optical cell is composed of two 1-inch opposite windows (UVFS, Thorlabs WG41010) for the laser path and a 2-inch window (UVFS, Thorlabs WG42012) for the detection system. Particles are evacuated through the top hood equipped with a HEPA filter.



(a)



(b)

Figure 5.4. Microscopy image of commercial nanoparticles used in this study. (a) SEM image of carbon black nanoparticle. (b) TEM image of TiO₂ nanoparticles (provided by nanografi).

Since the dispersion rate of the particles is decreasing over time, the particles inside the first flask are reloaded after each series of measurements with $m_g = 200$ mg of particles, allowing repeatable experimental conditions. When changing the particle's nature (TiO₂ or carbon black), all the equipment components in contact with particles are completely changed to prevent any intervention of particles from previous measurements.

5.2.2 Laser setting

An Nd:YAG laser beam (Quantel, Q-smart 850) with a repetition rate of 10 Hz is used for the LII measurement. Operation wavelength was tested for three different harmonics - fundamental (1064 nm), second (532 nm), and third (355 nm)- on both carbon black and TiO₂ by adding harmonic generation modules to the laser head. The laser fluence is controlled using an attenuator consisting of a half-wave plate and two polarizers.

The beam presents a top-hat energy distribution of $0.88 \times 0.91 \text{ mm}^2$, represented in the bottom-right in Fig. 5.3 and also as a histogram in Fig. 5.5 that is monitored with a beam profiler (Gentec Beamage). The top-hat shape laser is then 1:1 relay-imaged at the centerline of the optical cell.

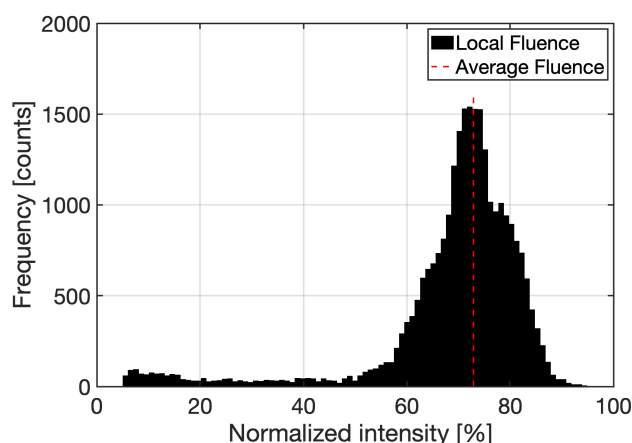


Figure 5.5. Histogram of laser fluence viewed by the detection optics across the laser beam.

5.2.3 Signal detection

The detection system comprises a telescope comprised of two achromatic lenses ($f_1 = 10 \text{ cm}$ and $f_2 = 20 \text{ cm}$). A magnification factor of 2 is used to collect the induced signal at 90° of the laser beam direction. Two notch filters (355 and 532 nm) were used to suppress the laser harmonic signal. For this reason, the emission spectra between 525 nm and 540 nm have been excluded for all the following results. This telescopic collector is connected to the spectrometer entrance (Princeton Instruments, HRS-500, grating groove density of 150 groove/mm) through a multimode optical fiber (Thorlabs, FG365UEC) with a core diameter of $365 \mu\text{m}$. The probe volume is 0.58 mm^3 .

One exit of the spectrometer is connected to an intensified charge-coupled device (ICCD) camera (Princeton Instruments, PI-MAX 4 1024EMB) to measure the spectral emission with a gate width of 20 ns. The temporal behavior of emission spectra is measured at different acquisition gate delay times ($\tau_d = 0 - 500 \text{ ns}$ from the peak signal). The detection system is calibrated using a tungsten filament lamp for signal intensity and a mercury lamp for wavelength. The calibration function is illustrated in Fig. 5.6. The acquisition parameters are adapted to ensure the best signal-to-noise (S/N) ratio and to prevent saturation of the device. The intensity level is then rescaled to be treated on the same scale. The spectra displayed in this work are averaged

over 5000 single shots.

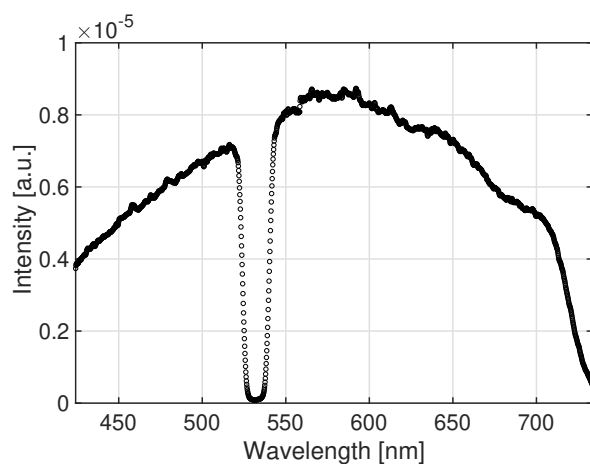


Figure 5.6. Calibration function for spectral detection via spectrometer.

The time-resolved laser-induced emission was measured using a photomultiplier that detects visible light (PMT, HAMAMATSU, R2257), which is connected to the second exit slit of the spectrometer. Signals were measured at four different wavelengths (450, 570, 640, and 710 nm for carbon black, and 450, 550, 650, and 710 nm for TiO₂) with a detection bandwidth of 20 nm FWHM. PMT signals were recorded at 10 Hz using an oscilloscope (Lecroy WaveSurfer 434 with a 350 MHz bandwidth and 2 GS/s sampling rate). As the particle dispersion rate decreases, the signal intensity also decreases, and so does the S/N. For this reason, only the PMT signals with the similar S/N are kept, then normalized by their maximum intensity, and averaged over 6000 single shots.

5.3 Results and discussion

The general spectral and temporal characteristics of LIE will first be discussed in Sec. 5.3.1. Then, the nature of prompt emission spectra will be discussed in low and high laser fluence regimes in Sec. 5.3.2. Finally, the LII nature of delayed signal will be verified to demonstrate the feasibility of the LII technique for high-purity TiO₂ nanoparticles in Sec. 5.3.3. All TiO₂ measurements will be compared with those of carbon black particles as a representative LII behavior under laser irradiation.

5.3.1 General characteristics and comparison with carbon black

The first step of this work consisted of testing three laser wavelengths (1064 nm, 532 nm, and 355 nm) to measure the LIE of pure TiO₂ and to compare the results to those obtained for carbon black in similar conditions (Table 5.2). For carbon black, a significant level of signals from LIE was detected for all excitation wavelengths. On the contrary, for pure TiO₂ it was not possible to detect enough signal with the considered detection system when working at 532 nm and 1064 nm. This is likely to be due to the fact that the absorption function $E(m_{\lambda_{em}})$ of pure TiO₂ above the UV range is very low compared to the carbonaceous particles (Fig 4.13). Therefore, only the 355 nm laser wavelength is used in the following to study the LIE of pure TiO₂ and carbon black particles.

Table 5.2. Detectable LIE signals with our detection system for different laser wavelengths for carbon black and pure TiO₂ nanoparticles.

Wavelengths	1064 nm	532 nm	355 nm
Carbon black	YES	YES	YES
TiO ₂	NO	NO	YES

5.3.1.1 Spectral analysis

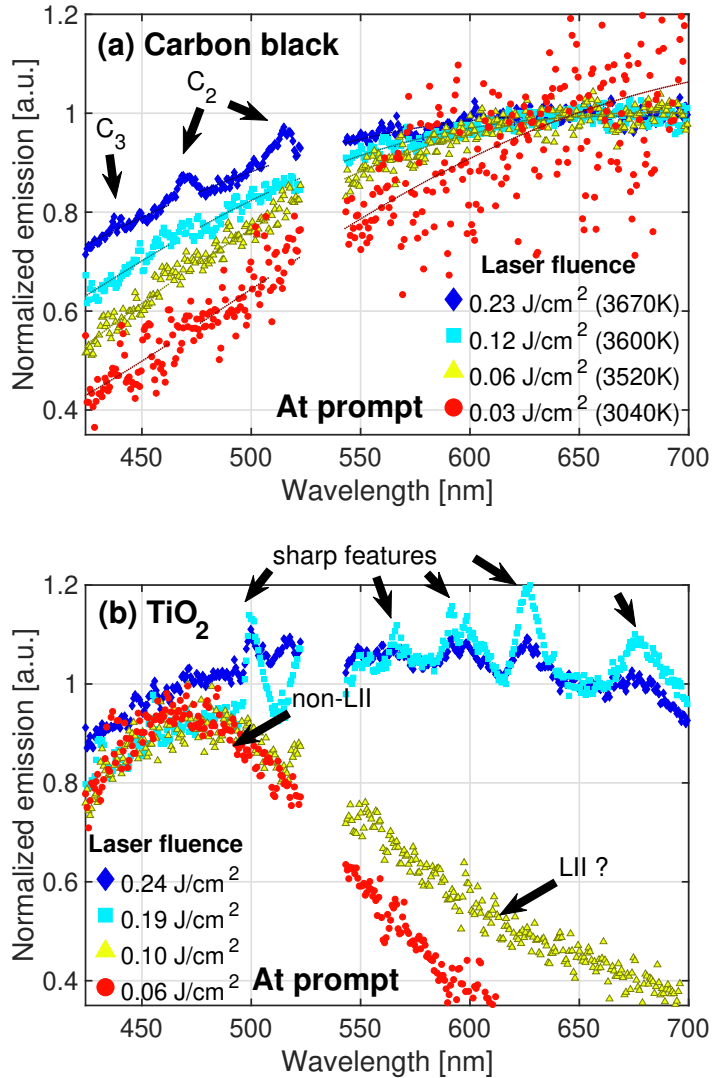


Figure 5.7. Effect of laser fluence F on laser-induced emission spectra at prompt for (a) carbon black and (b) TiO₂ nanoparticles. The temperature in the legend for carbon black particles is obtained from the spectrum fitting of the Planck function. Spectra are normalized by the value at 650 nm, except for the case of TiO₂ $F = 0.06 \text{ J/cm}^2$ and $F = 0.10 \text{ J/cm}^2$, whose normalization is based on the maximum value at 470 nm for visualization purpose.

Figure 5.7 shows the spectra under different laser fluences in prompt measurements. The equivalent temperature T_{eq} is obtained for carbon black by fitting the spectrum into Planck's law (Eq.(4.2)) while considering $E(m_{\lambda_{\text{em}}})$ constant. The obtained T_{eq} value is reported in the legend

of Fig. 5.7(a). The equivalent temperature for TiO₂ is not calculated because of the large variation of the spectral form of absorption function in the visible range (Fig. 4.13). Due to these high uncertainties in $E(m_{\lambda_{em}})$, it is unreliable to apply the fitting to extract the temperature information from spectra of Fig. 5.7(b).

Concerning carbon black, the laser fluence of $F = 0.03 \text{ J/cm}^2$ is the minimum fluence to obtain a detectable level of LII signal with our detection system. Still, the S/N is not high enough to allow accurate signal characterization. The case of $F = 0.03 \text{ J/cm}^2$ will then not be considered in the following.

For all the considered fluences, the LIE signals exhibit continuous spectra in the visible wavelength range with low intensity towards shorter wavelengths. When increasing the laser fluence, the curve moves towards shorter wavelengths. This blue shift indicates increased particle temperatures, as confirmed by the T_{eq} value. This trend follows Wien's displacement law, confirming the expected LII nature of the LIE signals for carbon black particles. By looking at the values of T_{eq} , it is found that the temperature increases with fluence for $F < 0.12 \text{ J/cm}^2$, whereas it does not considerably change between 0.12 and 0.23 J/cm^2 while approaching the particle sublimation temperature.

Additionally, for the highest fluence ($F = 0.23 \text{ J/cm}^2$), the presence of C₂ LIF signals (at approximately 468 and 516 nm) and of some C₃ bands (at approximately 437 nm) are clearly noticed. This indicates the presence of a sublimation of soot particles. All these results are coherent with literature [330, 331, 332]. Especially when considering LII of soot particles produced in a premixed methane/air flame with a 355 nm laser, a laser fluence level of approximately 0.07 J/cm^2 is enough to reach the "plateau" region [330]. In the present case, it might be possible that sublimation occurs for fluence values as small as $F = 0.06 \text{ J/cm}^2$, but its effect on particle diameter is expected to be negligible since neither C₂ nor C₃ bands are observed.

The prompt emission spectra of pure TiO₂ particles show, on the contrary, a clearly different tendency as a function of laser fluence. At low fluence ($F = 0.06 \text{ J/cm}^2$), a relatively narrow continuous spectrum centered at 470 nm is observed. This signal does not seem to correspond to LII emission that is expected to cover the whole visible range. For $F = 0.1 \text{ J/cm}^2$, the spectrum covers a wider region, reaching the longest wavelengths (550-700 nm). As the laser fluence increases ($F = 0.19$ and 0.24 J/cm^2), the emission presents a continuous broadband spectrum in the visible range overlapped with sharp features. Compared to the broadband emission, these peaks are less significant at $F = 0.24 \text{ J/cm}^2$ than at $F = 0.19 \text{ J/cm}^2$, possibly indicating that the relative contribution of the broadband spectrum to the total emission is likely to increase with laser fluence. As the interpretation of the prompt LIE of pure TiO₂ particles is not straightforward, a deep characterization in terms of LIF, PS-LIBS, and LII emissions will be detailed in Sec. 5.3.2.

5.3.1.2 Temporal evolution

Before analyzing the temporal evolution of LIE, it is important to note that the temporal profile is closely related to the particle size distribution [221]. In this study, particles of the constant size distribution (narrowly polydisperse but assumed to be monodisperse for the sake of simplicity) are expected to be distributed in the optical cell during the measurement. However, in flame synthesis, an evolving polydisperse population along the flame height is typically found. It is worth noting that the particle diameter may decrease with time in cases of sublimation, such as in high laser fluence regimes [333]

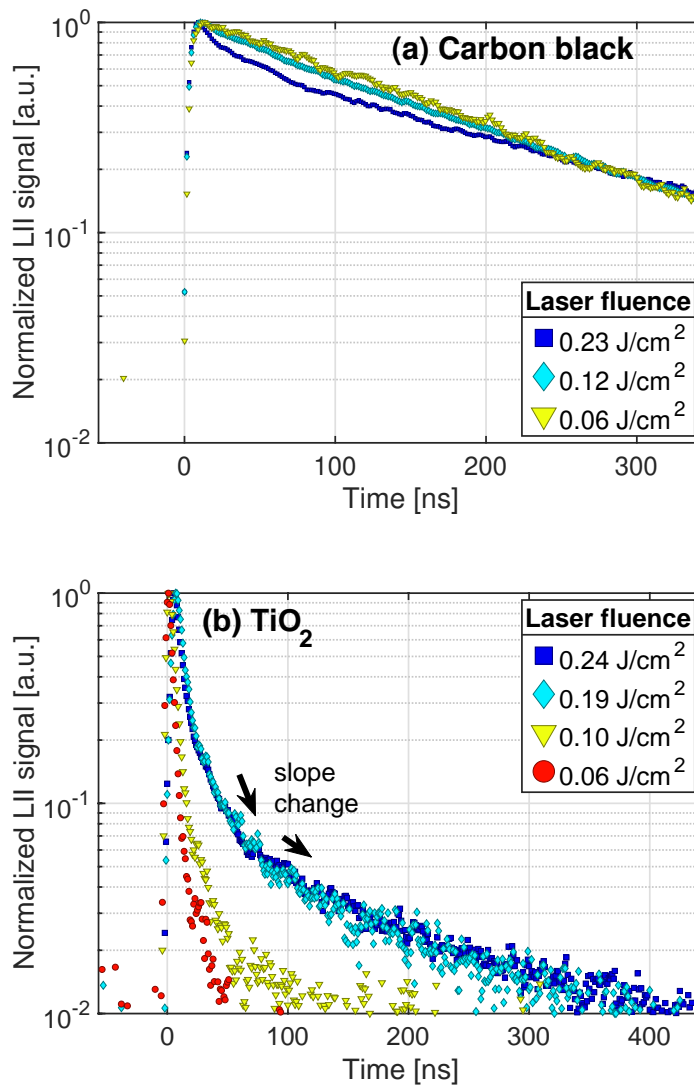


Figure 5.8. Temporal evolution of laser-induced emission of (a) carbon black and (b) TiO₂ nanoparticles at 450 ± 10 nm detection wavelength. Each profile is normalized by its maximum value.

The temporal evolution of the signals emitted at 450 nm for carbon black and TiO₂ under different fluences are presented in Fig. 5.8. For carbon black, the decay rates are relatively linear (in log scale) without significant slope change for all fluences except for $F = 0.23 \text{ J/cm}^2$. Since the particle temperatures for $F = 0.06$ and 0.12 J/cm^2 are pretty similar, the decay rates are nearly the same in Fig. 5.8(a). At $F = 0.23 \text{ J/cm}^2$, the high fluence induces sublimation of the particles, resulting in excited emissions from vaporized species and decreasing the particle diameter. Consequently, the LII signal has a rapid decay close to the prompt and presents a slope change of around 50 ns.

For pure TiO₂ particles, at low laser fluence ($F \leq 0.1 \text{ J/cm}^2$), a short-lifetime signal is detected at 450 nm. Together with previous spectral analysis, this possibly indicates that the LII component, known to be characterized by a long decay time, is not observed at this fluence because the particle temperature is not high enough to emit a detectable LII signal. The lifetime $t_{\text{non-LII}}$ of this signal is estimated to be $\approx 100 \text{ ns}$ (FWHM around 10 ns, tail of temporal profile rests until 60 ns). At higher fluences ($F \geq 0.19 \text{ J/cm}^2$), a slope change is observed near $t_{\text{non-LII}}$, indicating the presence of multiple signals: some short, some long. The short non-LII contributions are predominant over the first $t_{\text{non-LII}}$ and present a significant slope. The long ones dominate the second period of the emission.

Comparing $F = 0.19$ and $F = 0.24 \text{ J/cm}^2$ for $t \geq t_{\text{non-LII}}$, the decay rate is nearly identical, meaning that the origin of the delayed LIE is quite similar for these two fluences. Once again, if the interpretation of temporal emission from soot particles is well established in the literature [268], temporal LIE from TiO₂ requires a more extensive analysis, which will be performed in the next section by examining the prompt and delayed acquisition time.

5.3.2 Characterization of prompt LIE from TiO₂

In the previous section, we observed that the behavior of prompt spectra emitted by carbon black is in agreement with the literature trends [334]. On the contrary, LIE from high-purity TiO₂ still needs to be characterized. In this section, we will discuss the nature of the non-LII component of the LIE from TiO₂ by examining the results at the prompt as a function of the laser fluence. As seen previously, in the low laser fluence regime, TiO₂ nanoparticles present a narrow emission centered at 470 nm with a short lifetime $< 100 \text{ ns}$. At low fluence, PS-LIBS is not expected, and LII is usually a signal covering the whole visible spectrum lasting over hundreds of nanoseconds. Therefore, the emission observed at low laser fluences is most likely to be LIF. To confirm this conclusion, the TiO₂ spectra emission for a low laser fluence ($F = 0.06 \text{ J/cm}^2$) is reminded in Fig. 5.9. The spectrum obtained here for TiO₂ rutile nanoparticles is quite similar to LIF emission spectra found in the literature, even for different crystal phases [335, 243]. As an example, the spectra in low laser fluence regimes from Paul et al. [335] for anatase nanorods and Santara et al. [243] for TiO₂(B) nanoribbons are added to Fig. 5.9 in green and in red, respectively. Each curve can be interpreted as the sum of the gaussian fit sub-band emissions illustrated with thin dashed/dotted lines in Fig. 5.9. These observations leads to conclude that the prompt LIE of pure TiO₂ is dominated by its fluorescence in the low fluence laser regime excited at 355 nm.

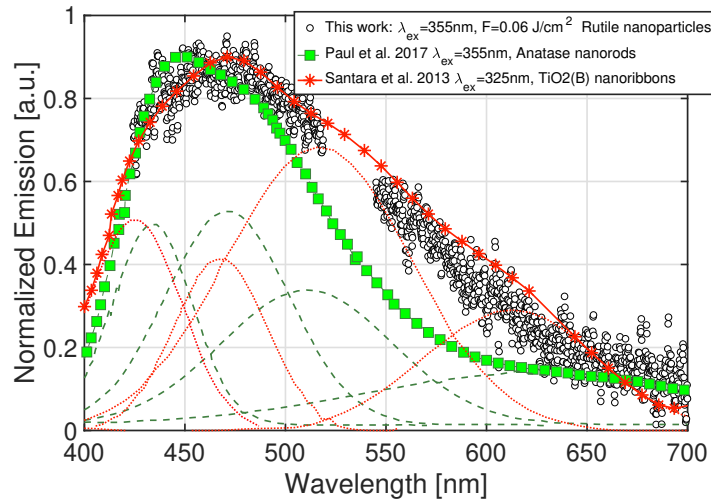


Figure 5.9. Emission spectra of TiO₂ nanoparticles at prompt under laser fluence $F = 0.06 \text{ J/cm}^2$ (black round points). The LIF emission spectra (square and start symbol) are from gaussian fitted spectra (green dashed line from Paul et al. [335], red dotted lines from Santara et al. [243]).

When increasing the laser fluence ($F = 0.10 \text{ J/cm}^2$), a wider spectrum (Fig. 5.7(b)) is emitted with a lifetime longer than $t_{\text{non-LIF}}$ as seen in Fig. 5.8(b). This seems to indicate the presence of a second signal in addition to LIF, whose contribution to the total LIE is not significant enough to be characterized.

At higher fluences ($F \geq 0.19 \text{ J/cm}^2$), the nature of multiple emissions can be investigated by looking at the prompt emission spectra of TiO₂ nanoparticles in Fig. 5.10. A broadband emission in the visible range is observed together with the presence of pronounced peak emissions, whose origins are unknown. The nature of peak emissions is first analyzed. One might think it corresponds to the atomic emission from laser breakdown (LIBS) of TiO₂. However, the energy level is still lower than the typical LIBS [248]. Therefore, two possibilities can be considered to interpret these signals: LIF and/or PS-LIBS emissions.

To consider the first option, deconvoluted gaussian band emissions from various literature works are illustrated together with the emission spectra of TiO₂ in Fig. 5.10(a). Only the center of each gaussian band with the standard deviation $\pm\sigma$ range is shown for a clear view. The sub-bands from the literature cover almost all the distinct feature ranges over the spectrum. Therefore, the LIE can be the result of these different LIF contributions. As laser fluence increases, the positions of the sub-band peaks could potentially remain the same while becoming sharper until attaining a line distribution [236]. This could be the first route to explain the edged features of the emission spectra of TiO₂ for high laser fluences.

Alternatively, it is possible to consider the distinct features as atomic emissions of PS-LIBS. Although the laser fluence used in this experiment is lower than the minimum PS-LIBS range reported in the literature (0.4 J/cm^2 at 355 nm in [254]), it is possible that single-photon absorption causes atomic emission, following the mechanism proposed by [259] for PS-LIBS of flame-synthesized TiO₂. To explore this possibility, Ti and O atomic emissions from NIST are

overlapped in blue and in red, respectively, to the emission spectrum of TiO₂ in Fig. 5.10(b). The peak locations match well with the Ti and O atomic emissions. The broadened line emission can be explained by the presence of multiple species with different excitation levels (ion charge) and relative intensities (Ti I, Ti II, Ti III, Ti IV..., O I, O II...), as can be observed in the NIST database.

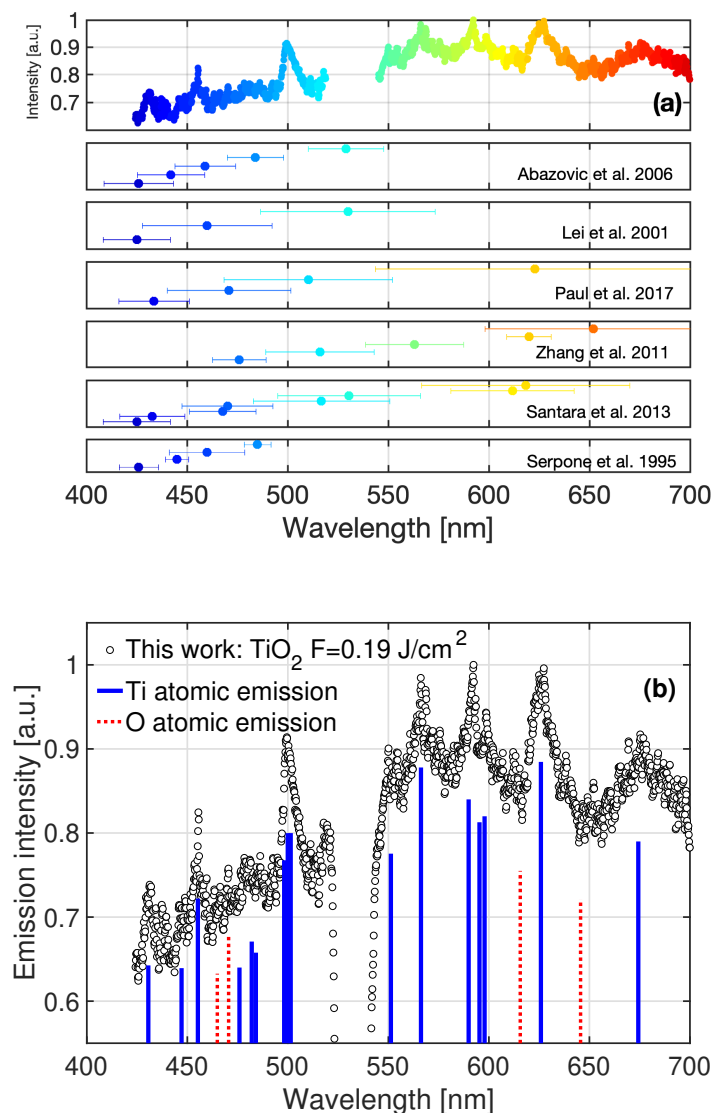


Figure 5.10. Normalized emission spectra of TiO₂ for $F = 0.19 \text{ J/cm}^2$ with (a) gaussian fit of band emission of LIF from literature [236, 244, 243, 238, 335, 336] and (b) Ti and O atomic emissions from NIST [258] corresponding to peak location of emission spectra. The intensities of each transition are adapted for a clear view with the curve, not expressing the relative intensities.

The current results suggest that in a high laser fluence regime, LIF and/or PS-LIBS of pure TiO₂ occur at prompt. These emissions are expected to occur over a short period of time, corresponds to the short lifetime discussed in Sec. 5.3.1.2 (Fig. 5.8(b)). On the contrary, the broadband emission covers the whole visible spectrum, and it corresponds to the long-lasting contribution of the total LIE in Fig. 5.8(b). These pieces of evidence seem to indicate that this broadband emission corresponds to LII. To confirm it, laser-induced emissions at delayed acquisition times are investigated in the following section.

5.3.3 LII nature of delayed LIE from TiO₂

As discussed previously, LIF and/or PS-LIBS of pure TiO₂ nanoparticles are observed on the emission at prompt. Since they present a short characteristic decay time, it is possible to investigate the nature of the long-lasting broadband contribution by looking at the delayed LIE of TiO₂. The trend as a function of gate delay and emission wavelength is compared with the theoretical behavior for LII described at Sec. 5.1.1 and with reference results from carbon black.

First, Fig. 5.11 shows the laser-induced emission spectra of carbon black and pure rutile TiO₂ particles for three fluences by considering various acquisition delays (over 20 ns) from the prompt timing, i.e., the signal peak. The emission spectra of carbon black show a red-shift for increasing time delay for all laser fluences. The red-shift observed in the emission spectra is indicative of a temperature decrease, which is supported by the calculated equivalent temperature values in agreement with LII theory.

Concerning TiO₂ nanoparticles, for the lowest fluence ($F = 0.06 \text{ J/cm}^2$), the signal-to-noise ratio is not sufficiently high to obtain an exploitable spectrum for an acquisition delay as small as 20 ns. When looking at a higher laser fluence ($F = 0.1 \text{ J/cm}^2$), a continuous broadband emission, which is the typical characteristic of the LII signal, is measured with a low S/N ratio. This seems to indicate that at this fluence the incandescence signal starts to contribute to the whole spectrum over fluorescent emissions at prompt (Fig. 5.7(b)).

For the highest laser fluence ($F = 0.24 \text{ J/cm}^2$), the spectrum presents incandescence trends as a function of the acquisition delay: the spectrum shifts towards longer wavelengths with time delay. This indicates that temperature decreases during the signal decay due to the particles cooling, confirming the black-body-like tendency for pure TiO₂. Note that at 20 ns and 40 ns, there might exist certain contributions from the emission of LIF or PS-LIBS as deduced from temporal signal evolution at Fig. 5.8(b), still the overall spectra accompanied with further delayed spectra show the consistent red-shift particle with cooling. A very similar trend is observed for $F = 0.19 \text{ J/cm}^2$ (not shown). The discussed incandescent features appear only under high fluence conditions when working with TiO₂. This is probably due to the low absorption function $E(m_\lambda)$ for pure TiO₂ compared to soot particles: higher energy is needed to heat the particles high enough to emit detectable thermal radiation compared to carbon black case.

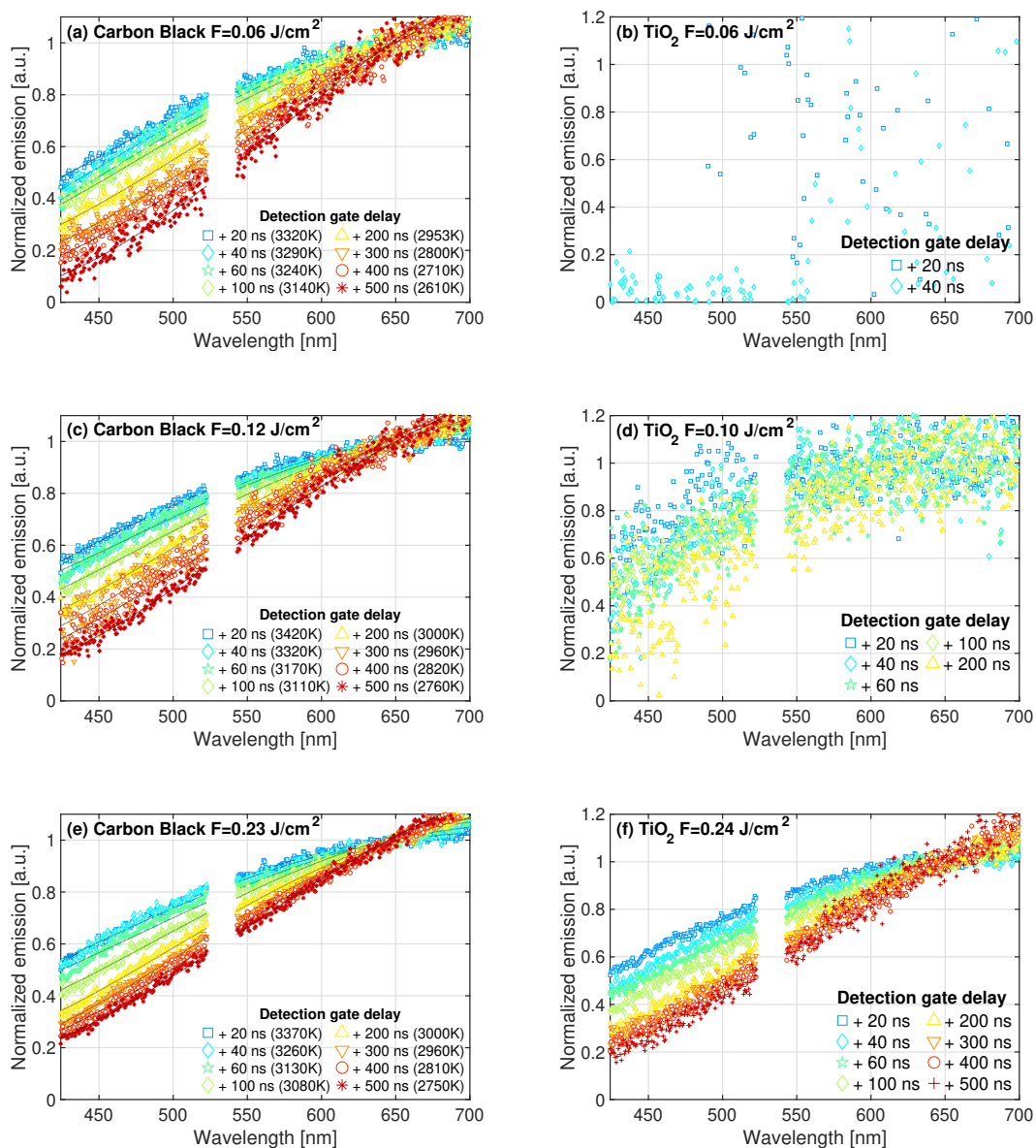


Figure 5.11. Effect of gate delay (gate width = 20 ns) on emission spectra of laser-induced emissions of (a,c,e) carbon black nanoparticles and (b,d,f) rutile TiO_2 nanoparticles. The temperature given inside the legend for carbon black particles is from spectrum fitting. Spectra are normalized with the value of the spectrum at 650 nm.

To confirm it, the temporal evolutions of LIE emissions at four wavelengths are considered for various laser fluences characterized by a significant S/N ratio. Only the temporal signals after 100 ns from peak signal are considered to completely avoid non-LII contribution and normalized at 100 ns delayed timing to compare the temporal decay. Figures 5.12 and 5.13 show the normalized temporal evolution of signal for three different fluences for carbon black and two different fluences for TiO₂ for different detection wavelengths. The same tendency for carbon black has been observed for $F = 0.06 \text{ J/cm}^2$ and $F = 0.12 \text{ J/cm}^2$ for the 4 considered wavelengths since the particles reach relatively close temperatures, as deduced for Fig. 5.11. That might signify that we have reached the beginning of plateau regime. On the other side, the case of $F = 0.23 \text{ J/cm}^2$ showed differences since the particles now are under sublimation, being far from the plateau zone in the fluence curve as previously discussed. In the case of TiO₂ curves exhibit the same decay tendency for all fluences and wavelengths.

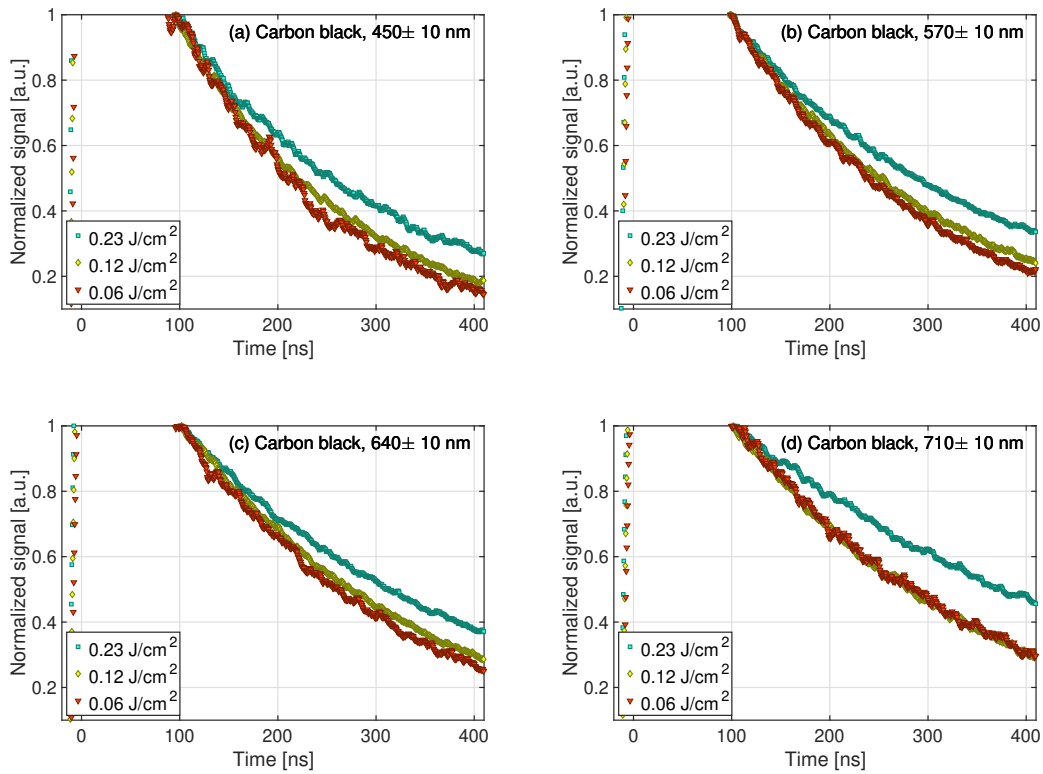


Figure 5.12. Normalized temporal evolution of carbon black nanoparticles at different laser fluences at detection wavelengths of (a) $450 \pm 10 \text{ nm}$, (b) $570 \pm 10 \text{ nm}$, (c) $640 \pm 10 \text{ nm}$ and (d) $710 \pm 10 \text{ nm}$. All profiles are normalized with the value of the signal at 100 ns.

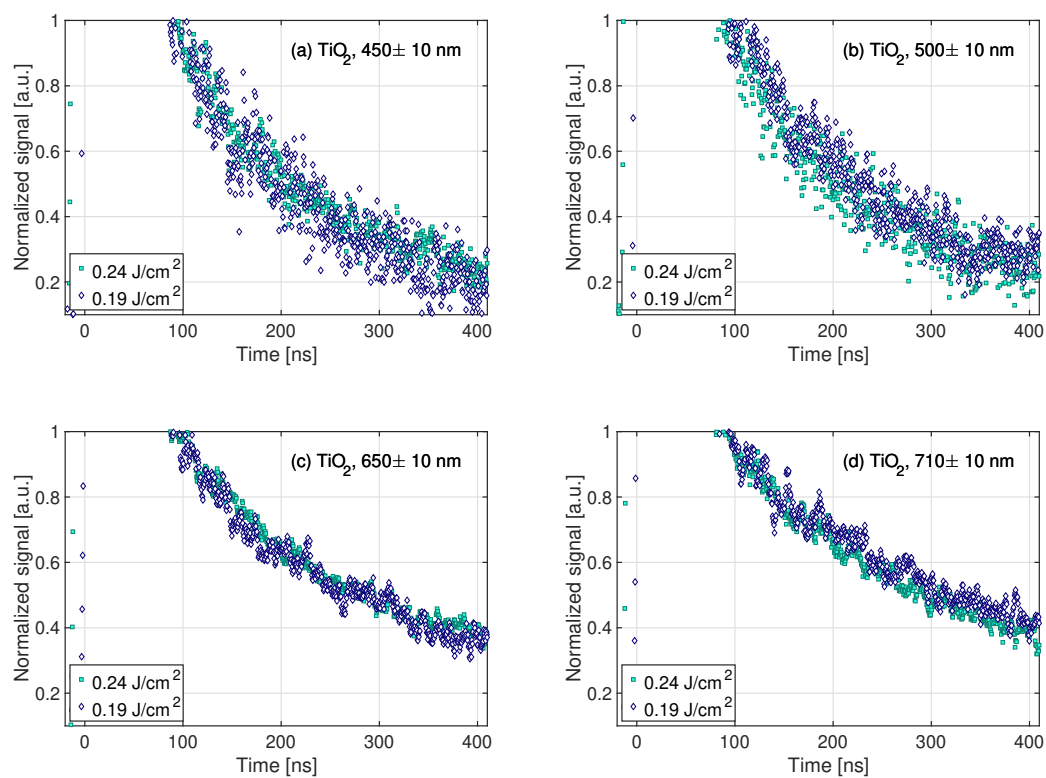


Figure 5.13. Normalized temporal evolution of high-purity TiO_2 nanoparticles at different laser fluences at detection wavelengths of (a) 450 ± 10 , (b) 550 ± 10 , (c) 650 ± 10 and (d) $710 \pm 10 \text{ nm}$. All profiles are normalized with the value of the signal at 100 ns.

To validate the LII nature of the delayed LIE, the decay characteristic time τ is calculated using Eq. (5.2) by fitting the LIE signals between 100 and 400 ns after the peak signal by using a log function. Results are shown in Figs. 5.14(a) and 5.14(b) for carbon black and TiO₂, respectively. Here, the fluence values before the evident vaporization regime (at the beginning of the plateau curves) are considered, i.e., $F = 0.12 \text{ J/cm}^2$ et $F = 0.19 \text{ J/cm}^2$ for carbon black and high-purity TiO₂, respectively. For other laser fluences, the same linear tendencies have been observed (not shown).

Concerning carbon black nanoparticles, the decay characteristic time τ increases with the wavelength in accordance with Eq. (5.3), which has been derived for LII signals assuming a constant primary particle diameter d_p . Similarly, for pure TiO₂ nanoparticles, the decay characteristic time τ values are linearly proportional to the emission wavelength, confirming the LII nature of the delayed LIE as derived from the LII theory of Sec. 5.1.1.

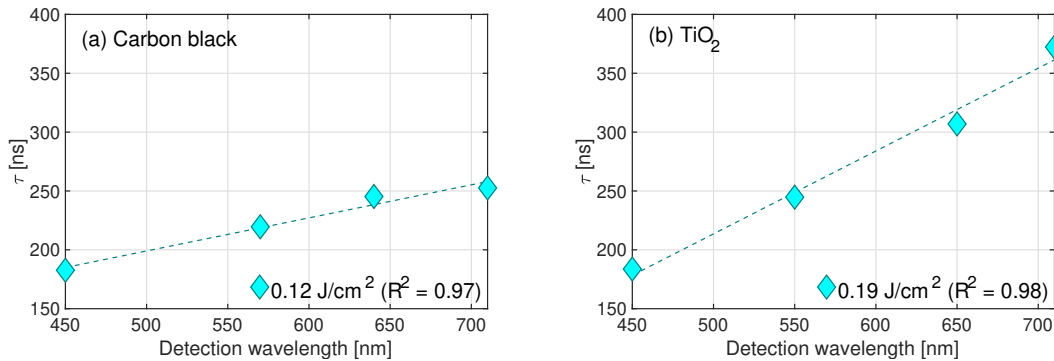


Figure 5.14. Decay characteristic times of LIE signal for (a) carbon black and (b) TiO₂ as a function of detection wavelength. The R^2 value inside the legend represents the coefficient of determination for the fitting procedure. The dotted lines are the results of the linear fitting.

Finally, the temporal evolution of quantity ΔT^{-1} defined in Eq. (5.5) is illustrated in Fig. 5.15 for different fluences from the temporal profile starting at $t_0 = 100 \text{ ns}$ from prompt. In the case of carbon black, the ΔT^{-1} for $\lambda_{em} = 640$ and 710 nm are identical, confirming the incandescent nature of signal for all signal durations for fluences of 0.06 and 0.12 J/cm^2 . Once again, discrepancies are observed for the highest fluence ($F = 0.23 \text{ J/cm}^2$), where sublimation is suspected. The evolution of ΔT^{-1} of TiO₂ of high purity in an inert environment is illustrated in Fig. 5.16. The evolution of ΔT^{-1} at $\lambda_{em} = 650 \text{ nm}$ and $\lambda_{em} = 710 \text{ nm}$ shows the same decreasing tendency than carbon black for the two fluences values. Therefore, the LII behavior of pure TiO₂ is demonstrated at least for the signals at these wavelengths.

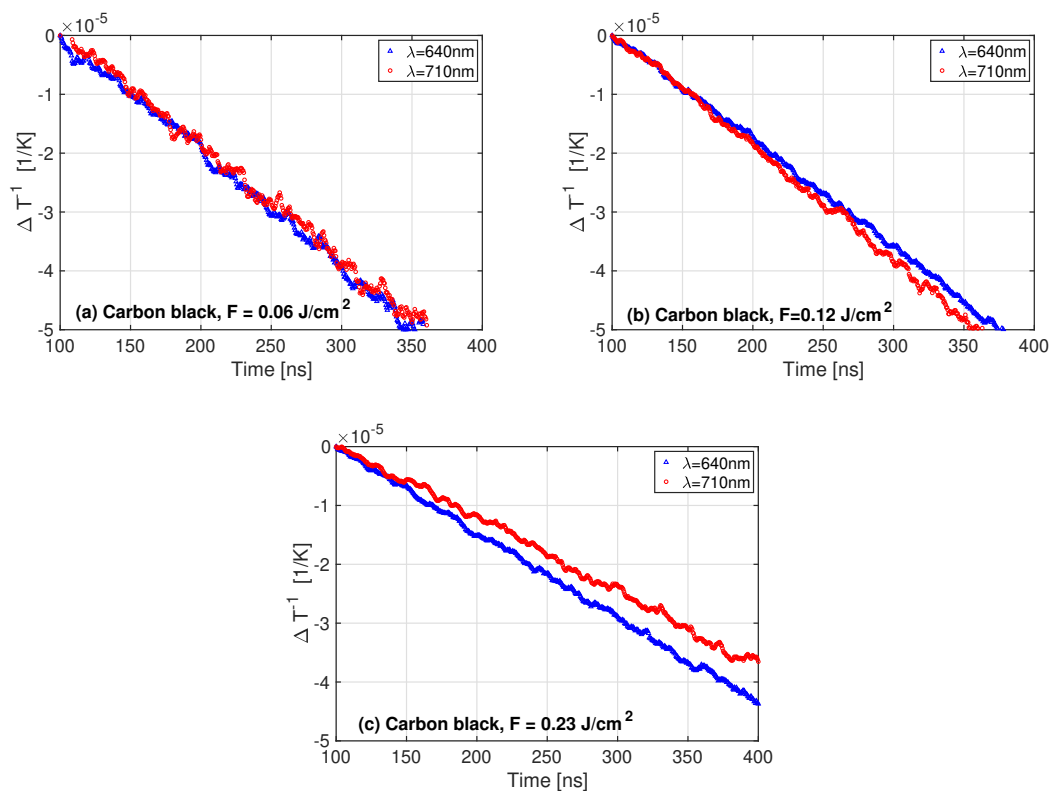


Figure 5.15. Time evolution of ΔT^{-1} of carbon black nanoparticles LIE for three laser fluences at (a) $F = 0.06$, (b) $F = 0.12$ and (c) $F = 0.23 \text{ J/cm}^2$.

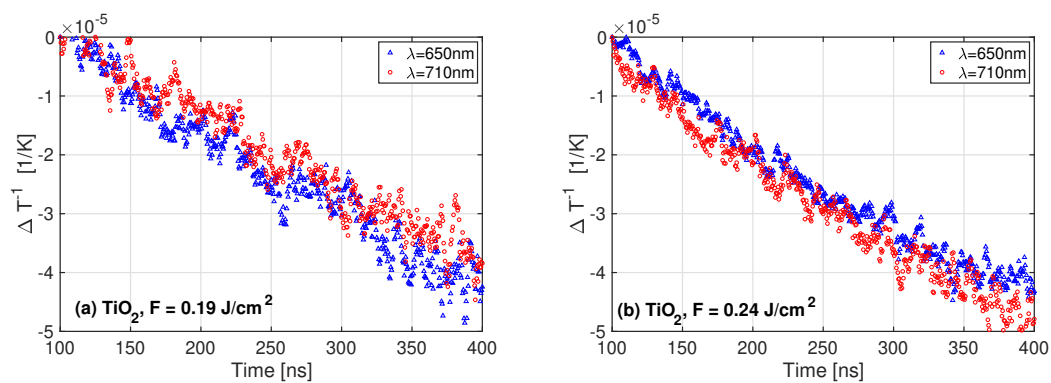


Figure 5.16. Time evolution of ΔT^{-1} of pure TiO_2 nanoparticles LIE for three laser fluences at (a) $F = 0.19$ and (b) $F = 0.24 \text{ J/cm}^2$.

5.4 Conclusion

In this chapter, the LIE of pure TiO₂ nanoparticles has been characterized in a well-controlled non-reactive environment. Spectral and temporal behavior of LIE on pure TiO₂ were investigated based on the LII theory and the behavior of conventional LII of carbon black nanoparticles.

At prompt timing, non-LII emissions were detected. At a low fluence regime, the emission spectra of pure TiO₂ resemble the literature on LIF with a minor differences from the difference in particle fabrication/experiments parameters. At a high fluence regime, sharp emission features superimposed to broadband emission spectra were detected. The distinct features can be interpreted as accentuated LIF emissions or PS-LIBS atomic line emissions. In a temporally resolved signal, those interferences disappear after 100 ns with an apparent change of decaying slope. Based on the temporal information, delayed emission spectra of pure TiO₂ were shown to have red-shifted signals with time evolution. In the temporal profile, the linear relationship between the decay characteristic time τ and the detection wavelength, and the identical evolution of ΔT^{-1} at different detection wavelengths have been proven based on LII theory.

The feasibility of LII on pure TiO₂ has been demonstrated in a non-reactive environment. Nevertheless, the coexistence of non-LII emissions should be carefully considered in the in-situ LII measurement of particle flame synthesis. Then, the same procedure to identify the LII contribution has to be applied in TiO₂ in flame synthesis and further LII emission interpretation. The characterization of LIE in TiO₂ generated by flame will be presented in the next chapter.

Chapter 6

Characterization of the LIE of TiO₂ nanoparticles in a reactive environment

The feasibility of LII of highly pure TiO₂ nanoparticles in a non-reactive environment has been demonstrated in Chap. 5 by characterizing the LIE at prompt and delayed timings. Here, the feasibility is investigated by looking at flame-synthesized TiO₂ in a reactive environment. Specifically, TiO₂ particles produced in a laminar coflow H₂/Ar/TTIP flame are investigated in this chapter. Hydrogen has been chosen to minimize the carbon contents of the generated particles and reduce as much as possible the presence of solid carbon in the detected signal.

The experimental set-up for the flame synthesis of nanoparticles is presented in Sec. 6.1. The general spectral and temporal aspects of LIE of flame synthesis of TiO₂ will be characterized to check their LII signal feasibility in Sec. 6.2.1. Then, the nature of prompt emissions spectra will be discussed for low and high laser fluence regimes in Sec. 6.2.2. The feasibility of LII on flame-synthesized TiO₂ nanoparticles will be discussed in Sec. 6.2.3. Further discussion and conclusion comparing two systems of Chap. 5 and Chap. 6 will follow in Sec. 6.3.

6.1 Experimental set-up

The same set-up for the laser excitation (Sec. 5.2.2), temporal and spectral signal detection (Sec. 5.2.3) are utilized for LIE measurement as in Chap. 5. Therefore, elements exclusively developed for the TiO₂ production with a laminar pre-vaporized flame will be discussed.

6.1.1 Yale diffusion burner (YDB)

The Yale diffusion burner (YDB) [337] allows the stabilization of a coflow diffusion flame. The system has been originally developed at Yale University to study steady [338] and time-varying [339] flames. It has been shared with many laboratories worldwide and has abundant experimental/numerical literature for various operating conditions [340, 341, 342, 343]. In this research work, the YDB design is chosen to synthesize TiO₂ nanoparticles in flame while rethinking the injection and the pre-vaporization system. The schematic illustration is shown in Fig. 6.1. The burner consists of a center fuel tube (inner diameter $D_i = 3.9$ mm) surrounded by air coflow

(inner diameter $D_o = 76$ mm). The housing is filled with glass beads (diameter: 3 mm) to homogeneously distribute the airflow. The honeycomb structure on the top of the housing defines the exit velocity profile of air coflow. The detailed information on the burner can be found in [337].

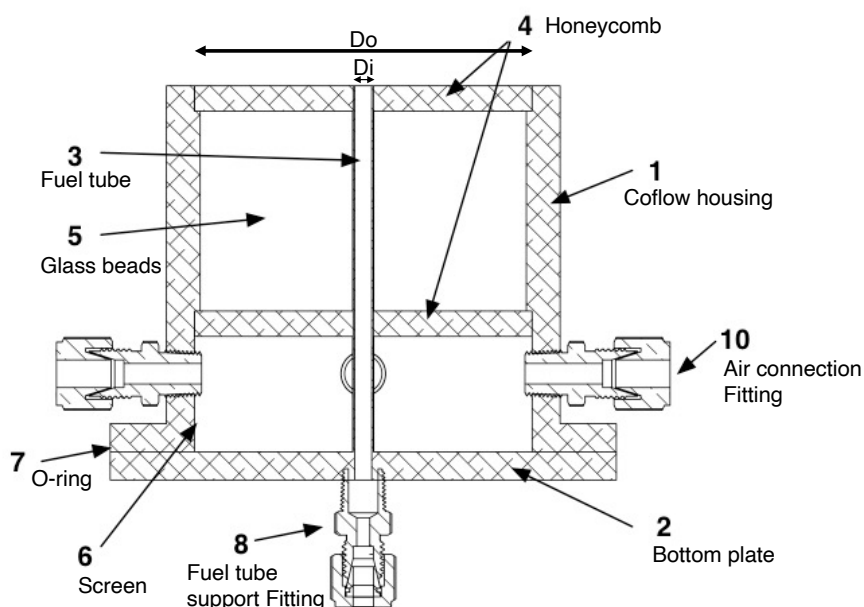


Figure 6.1. Schematic of the burner configuration, D_i is the inner tube diameter, D_o is the coflow diameter [337].

In this study, H₂ is selected as fuel to minimize the trace of the carbon species, as done in [134]. The fuel is diluted by Ar in the fuel tube to increase the stability of the flame. The total inflow velocity is at 1.51 m/s at ambient temperature. H₂O contents in gases are also strictly controlled for hydrogen (<0.5 ppm) and argon (<0.5 ppm) to minimize hydrolysis during the pre-vaporization of the precursor. The coflow keeps relatively strong (0.4 m/s at ambient temperature) to avoid flame fluctuation at the flame tail.

6.1.2 Pre-vaporization system

Liquid injection

The schematic illustration for the liquid injection system is shown in Fig. 6.2(a). In this study, a commercial Coriolis mass flowmeter is used to guarantee a stable low flow rate injection. Titanium isopropoxide Ti(OCH(CH₃)₂)₄ (TTIP, Sigma Aldrich (Merck), purity $\geq 97.0\%$) was selected as the precursor to generate TiO₂ nanoparticles. The liquid is conserved in a pressurized vessel by 6 bar of N₂. Then, it is filtered with a 15-micron pore-size particulate filter (Swagelok, SS-6TF-MM-15) before entering the Coriolis flowmeter (Bronkhorst, MINI CORIFLOW, ML120V21-BAD-11-0-S). The Coriolis flowmeter controls the injection rate in a steady and stable way for a small amount of precursor (0.5 g/h). This precursor line joins the fuel

(H_2 and Ar mixture), whose temperature is controlled to be hot enough to vaporize the liquid precursors immediately after joining the line.

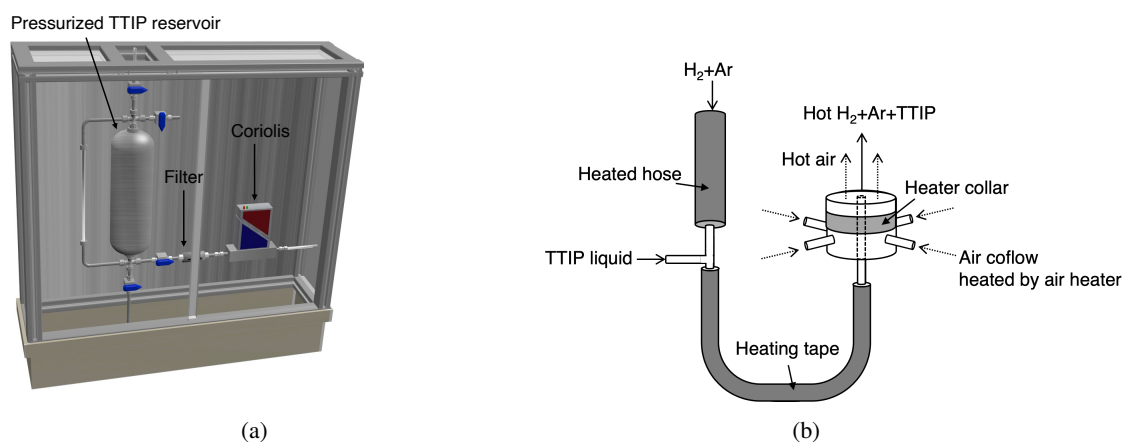


Figure 6.2. (a) Injection system of liquid precursor. (b) Schematic of the vaporization system.

Vaporization system

The liquid precursor is pre-vaporized, and the ensemble of the system is maintained at a high temperature to avoid condensation of precursor vapor. The schematic illustration of the burner heating system is shown in Fig. 6.2(b). The input fuel gas is heated by a heated hose (Thermocoax, isopad IHH-ST2A/ST2D, 200W) over $80\text{ }^\circ\text{C}$ before joining the injected liquid TTIP line. Then a flexible stainless steel tube (1 m long) transports the mixture of gas and vaporized precursor into the fuel tube of the burner. The flexible tube is heated by glass silk heating tape (Thermocoax, isopad IT-S20, 330W), maintaining $130\text{ }^\circ\text{C}$ to control heating power to completely evaporate the liquid precursor before reaching at the center fuel tube of the burner.

The burner is also heated by a heater collar (Vulcanic, COLLIERS MICA BLINDES, 450W) which maintains the burner temperature at $150\text{ }^\circ\text{C}$. The air coflow is heated by an air heater (Leister, LE MINI SENSOR, 800W) up to $180\text{ }^\circ\text{C}$ surrounding the inner fuel tube. Finally, at the exit of the burner, the temperature keeps $100\text{ }^\circ\text{C}$ for the fuel exit in the middle and around $142\text{ }^\circ\text{C}$ for the coflow air exit. K-type thermocouples are utilized to measure the temperatures with a T-connector in the transporting line. It took around 40 minutes to be thermally stable without fluctuation from the liquid injection.

6.1.3 Flame configuration

The selected flame is a laminar Ar-diluted H_2 diffusion flame, surrounded by coflowing air. The operation conditions for the flame synthesis of TiO_2 nanoparticles are described in Table 6.1. The molar fractions are $X_{\text{H}_2}=0.9773$, $X_{\text{Ar}}=0.0221$, $X_{\text{TTIP}}=0.0007$, corresponding to the mass fractions of $Y_{\text{H}_2}=0.646$, $Y_{\text{Ar}}=0.291$, $Y_{\text{TTIP}}=0.063$, so the hydrogen takes most of the mixture in volume. Assuming that all the TTIP is converted into TiO_2 , the production rate would be 0.14 g/h .

Flame	Fuel				Coflow	
	\dot{m}_{H_2}	\dot{m}_{Ar}	\dot{m}_{TTIP}	T_F	\dot{m}_{air}	T_C
H ₂ -TTIP flame	5.1 g/h	2.3 g/h	0.5 g/h	380 K	7759 g/h	412 K

Table 6.1. Operating conditions for the preheated hydrogen and precursor (TTIP) coflow flame. The inflow velocity is 1.9 m/s, and the coflow velocity is 0.55 m/s in high-temperature conditions.

Typical H₂ flames with and without TTIP are presented in Fig. 6.3. The flame length is about 4 cm, with a pale blue color upstream (HAB < 10 mm) and a reddish color downstream (HAB > 20 mm). The blue color corresponds to the long-wavelength side of the OH* peak (from 412 nm to 510 nm), constituted of distinct finer spectral features superimposed on a broadband continuum [344]. The red color is due to the emission from excited H₂O [345] in the wavelength range from 600 to about 900 nm.

After injecting the precursor TTIP in the hydrogen flame, a strong luminous cylindrical zone is observed as schematically illustrated in Fig. 6.3(c). The diameter of this zone (~ 4.5 mm) is close to the inner size of the center fuel tube (~ 3.9 mm). Its color changes from orange (HAB 10-20 mm) to white (HAB 20-50 mm) followed by a blue tail (HAB > 60 mm), denoting the presence of TiO₂ nanoparticles. After being deposited in the filter, the produced particles exhibit a bright white color. The central luminescent cylindrical zone is surrounded by the flame with much weaker luminescence, similar to the hydrogen flame without TTIP of Fig. 6.3(a). For the characterization of LIE of flame-synthesized TiO₂, the point at HAB = 45 mm in the centerline in the white region is selected.

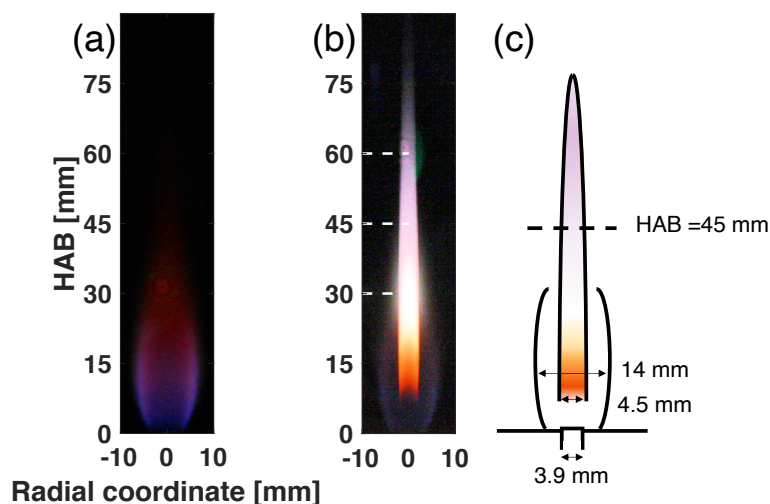


Figure 6.3. Picture of targeting diffusion coflow argon-diluted hydrogen flames before (a) and after (b) injecting TTIP precursor. The camera exposition is adapted for better visualization for each figure. (c) Schematic illustration of H₂/Ar/TTIP flame.

Nucleation of TiO₂ To describe the conversion from gaseous TTIP to solid TiO₂ particles, hydrolysis and thermal decomposition pathways are commonly described. Globally, they read as:

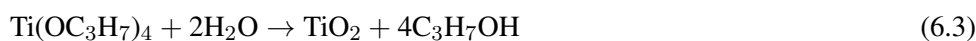
- (1) **Thermal decomposition** The first-order rate expression of the thermal decomposition of TTIP vapor is given as [120]:



Using the measurement of propene (C₃H₆) gas concentration via gas chromatograph, the effective first-order rate constant and its temperature dependence are estimated :

$$k = 3.96 \times 10^5 \exp(-8479.7/T), \text{ s}^{-1} \quad (6.2)$$

- (2) **Hydrolysis** The global formation of TiO₂ from the TTIP reaction with H₂O is expressed in [346]:



with a first-order rate constant given by $k = 3 \times 10^{15} \exp(-1013.9/T(\text{K})), \text{ s}^{-1}$.

In addition to these global mechanisms, detailed mechanisms have been investigated including various molecule bond breakage [347, 348, 349, 350]. However, the TTIP conversion mechanisms remain an open question due to the difficulty of experimentally measuring each intermediate species during the thermal decomposition and hydrolysis process in a high-temperature environment [350].

Several intermediate species like Ti(OH)₄ could appear in both reaction processes. Certain hydrocarbon species (C₃H₆, C₃H₆O, C₃H₇OH, and many other species) could be released during the breakage of chemical bonds during the reaction. The thermal decomposition can be favored in the post-flame region (after passing the flame front where combustion takes place) and is highly sensitive to the temperature [95].

Most studies reported that the fast hydrolysis reaction rate dominates the formation of TiO₂ based on TTIP precursor in flame reactors in the presence of H₂O [351, 352]. This tendency is then more critical for hydrogen-based flame, which results in H₂O as the main combustion product, as investigated in this study. Due to a low activation energy barrier ¹, hydrolysis can start in the pre-heat zone, upstream of the flame reaction zone [352].

6.2 Results

In this section, the LIE of flame-generated TiO₂ will be discussed in terms of spectral and temporal characteristics in Sec. 6.2.1. Then, the prompt emissions spectra will be investigated in terms of their origin of emissions in both low and high laser fluence regimes in Sec. 6.2.2. Finally, the feasibility of the LII technique for flame-generated TiO₂ will be demonstrated through the LII nature of the signal in Sec. 6.2.3.

¹Minimum amount of energy that must be provided for compounds to result in a chemical reaction.

6.2.1 General characteristics

Laser-induced emission in flames under the same laser fluence is not expected to be identical to the results of the non-reactive experiment in Chap. 5 for the main reason that the initial temperature for the LII process is much higher (around 1800-2000 K) than the optical cell case (300K). Indeed, the high flame temperature can lead to (1) higher LII emission from a higher particle temperature, or/and (2) a change of optical property from solid to liquid phase change since the melting point is at 2128 K [282], (3) a change of thermo-physical property of nanoparticles (i.e., heat capacity) together with (4) crystalline structure change [353].

In nanoparticle flame synthesis, the particle characteristics may vary with the flame height and the residence time. First, the particle size could be different. Second, the use of TTIP precursor containing C-atoms may potentially lead to the generation of solid particles with a carbon content that varies with HAB. Indeed, even if H₂ is the main fuel, to this day, there is no experimental proof that highly pure TiO₂ nanoparticles are produced in our system. The point regarding the contribution of carbon contents to the LIE signal will be discussed in Sec. 6.3.

6.2.1.1 Spectral emission

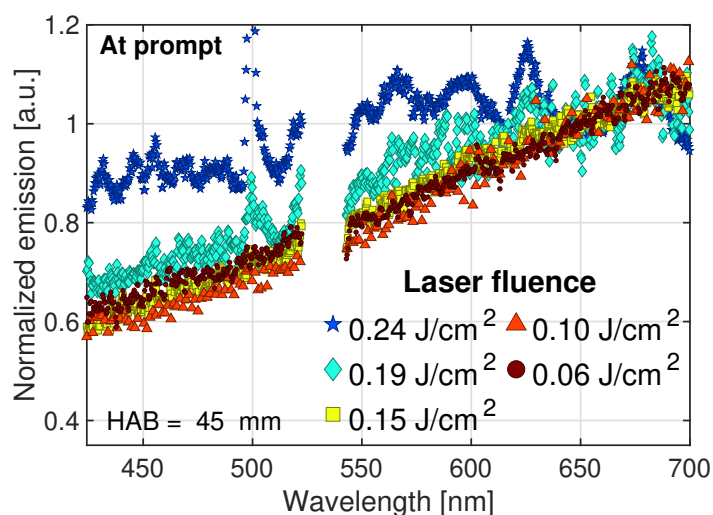


Figure 6.4. Effect of laser fluence on laser-induced emission spectra of TiO₂ nanoparticles at HAB = 45 mm. Measurements are done at prompt, i.e., at peak signal. Spectra are normalized with the value of 650 nm for each curve with different fluence.

The emission spectra of TiO₂ nanoparticles in flame synthesis under different laser fluences at prompt are shown in Fig. 6.4. At low laser fluence regimes (from $F = 0.06$ to $F = 0.15$ J/cm²), the LIE signals show continuous spectra in the visible wavelength range with high intensity at longer wavelengths. The dynamics between them are not strong, so the curves nearly overlap each other. For higher laser fluence regimes ($F = 0.19$ J/cm² and $F = 0.24$ J/cm²), sharp emission features overlapping with broadband emission spectra are detected, indicating the presence

of LIE signals resulting from multiple natures of signals.

6.2.1.2 Temporal emissions

The temporal profiles of the emission at 500 nm from TiO₂ nanoparticles at various fluences are presented in Fig. 6.5. At low laser fluence ($F \leq 0.1 \text{ J/cm}^2$), the decay rates exhibit a gradual slope change that is relatively linear in log scale. As the fluence increases, the decay rates become more rapid (smaller τ), indicating a rise in particle temperature due to laser irradiation. At fluences of 0.15 and 0.19 J/cm², the two signals appear similar, possibly indicating the approach of the plateau region. Then, at $F = 0.24 \text{ J/cm}^2$, a sudden change in the temporal emission occurs, indicating the presence of signals from multiple sources. This brutal change clearly shows the presence of signals from multiple sources. The dominant component of the emission during the first 65 ns is the short non-LII part with a lifetime of $t_{\text{non-LII}}$, which has a FWHM of approximately 10 ns. This short duration signals suggest that non-LII components are present during this duration. At the same time, the presence of waviness in this section may suggest the existence of multiple non-LII signals with distinct durations. The second long signal after 65 ns, which persists for over 400 ns, is likely to originate from a different emission source than the first short non-LII part.

The difference between the two parts of signals is more pronounced than in the non-reactive case discussed in the previous chapter (see Fig. 5.8(b)). This is because the initial short signal is much stronger than the subsequent long signal than those of non-reactive case, and the normalization process, which involves dividing by the maximum value, accentuates the change in decay mode.

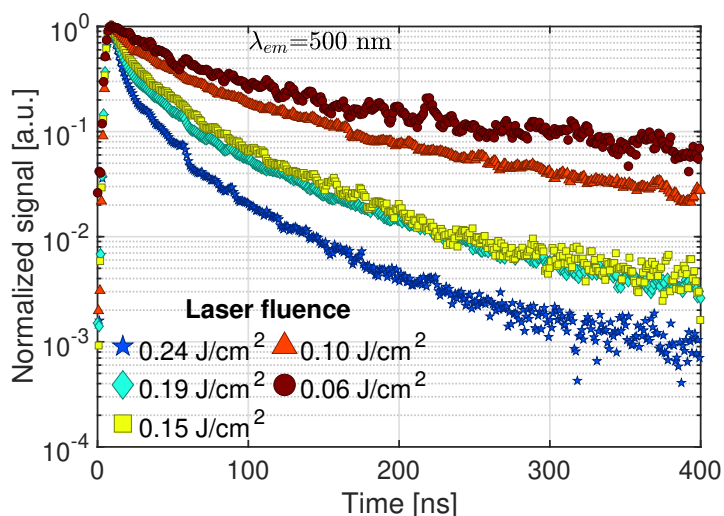


Figure 6.5. Temporal evolution of laser-induced emission of flame-synthesized TiO₂ nanoparticles at HAB= 45 mm, detected at $500 \pm 10 \text{ nm}$. Each signal is normalized by its maximum value.

The brutal change of temporal evolution is closely related to the emission wavelength. To illustrate this point, the temporal evolution of LIE signals at two detection wavelengths (450 and 710nm) are shown in Fig. 6.5 for low and high fluences. As shown in Fig. 6.6(b), at high

fluences, the two-mode decay is more noticeable in detection wavelength 450 nm than 710 nm. This might be because most of the emission centers of the LIF and/or PS-LIBS of TiO₂ are more distributed in the UV range and below 550 nm as described in Sec. 4.1 and Sec. 4.2. In terms of overall signal detection, there may be a greater chance of dominance of LIF or PS-LIBS emission than LII emission in a blue-green visible wavelength range (below 550 nm). These features are less pronounced in low laser fluence regimes, as observed in Fig. 6.6(a) for both detection wavelengths.

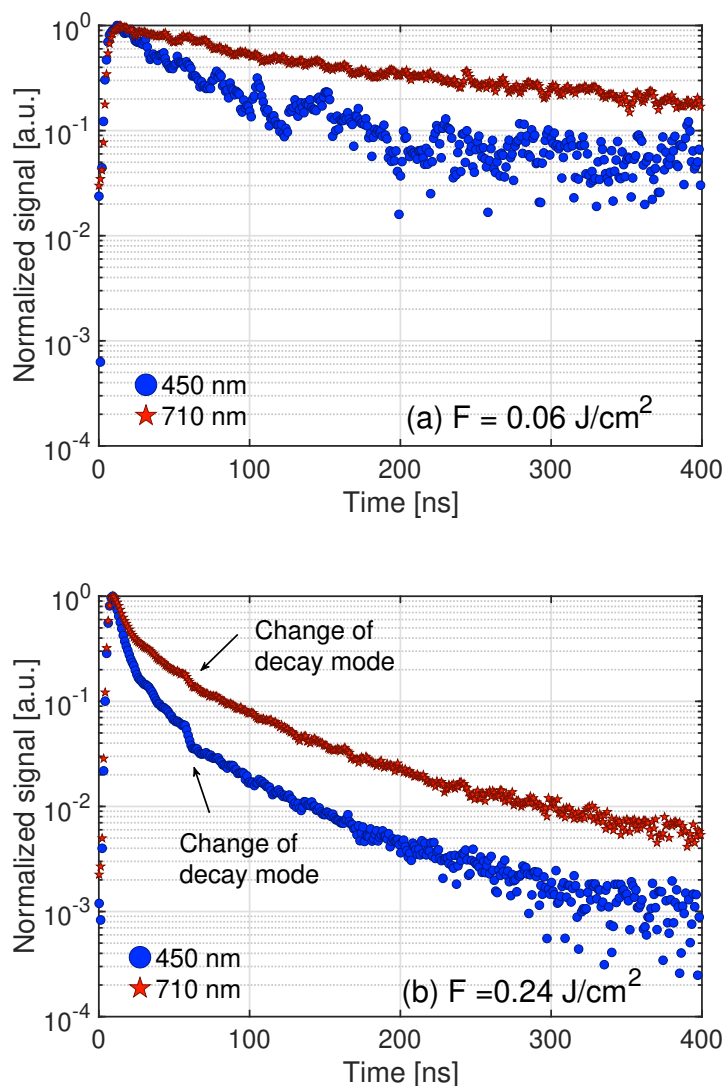


Figure 6.6. Temporal evolution of laser-induced emission of flame-synthesized TiO₂ nanoparticles at (a) $F = 0.06 \text{ J/cm}^2$ and (b) $F = 0.24 \text{ J/cm}^2$ detected at $450 \pm 10 \text{ nm}$ and $710 \pm 10 \text{ nm}$. Each graph is normalized by its maximum value. The change of decay mode is expressed with arrows.

6.2.2 Characterization of prompt LIE from flame-generated TiO₂

To investigate the nature of prompt LIE from flame-synthesized TiO₂, the LIE spectra at prompt are reminded in Fig. 6.7. At low fluence, continuous emission spectra are observed at prompt as shown in Fig. 6.7. However, it is not possible to assume whether it is purely a contribution from LII or whether it can include LIF emission as in the case of pure TiO₂ nanoparticles presented in the previous chapter since no measurements at even lower fluence regimes are available. In this section, the origin of the pronounced peak emissions in the high-fluence regime $F = 0.24$ J/cm² will be investigated by comparing the prompt emission spectra of flame-generated TiO₂ nanoparticles with the possible sources of non-LII emissions.

It should be noticed that the hydrogen flame includes carbon species from the TTIP precursor (C₁₂H₂₈O₄Ti). Therefore, there might be possible to detect laser-induced emission from the carbon species, especially in a high laser fluence regime with UV range excitation [354]. The same analysis, as shown in Fig. 4.16, can facilitate the comparison between our emission spectra and possible carbon LIF emission bands. The emission spectrum of flame-generated TiO₂ nanoparticles at the prompt is overlapped with the typical region of C₂ and C₃ bands in Fig. 6.7. There is little risk of detecting the emission from the C₂ Swan bands since none of the sharp features can be attributed to each band range. On the other hand, the emission band of C₃ Swing bands, whose center is located at 400 nm [355], could include the features centered at 431 nm of TiO₂. Still, the nature of entire sharp features over 450 nm is unknown. As in the analysis of non-reactive LIE of TiO₂, two more possibilities can be considered: LIF and/or PS-LIBS emissions.

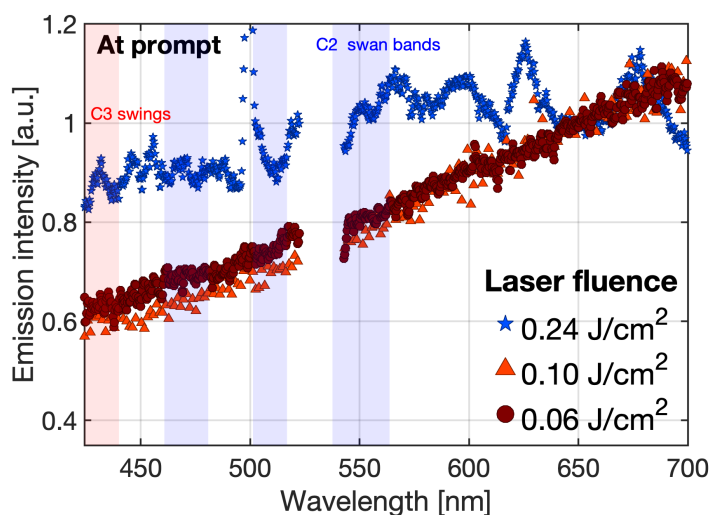
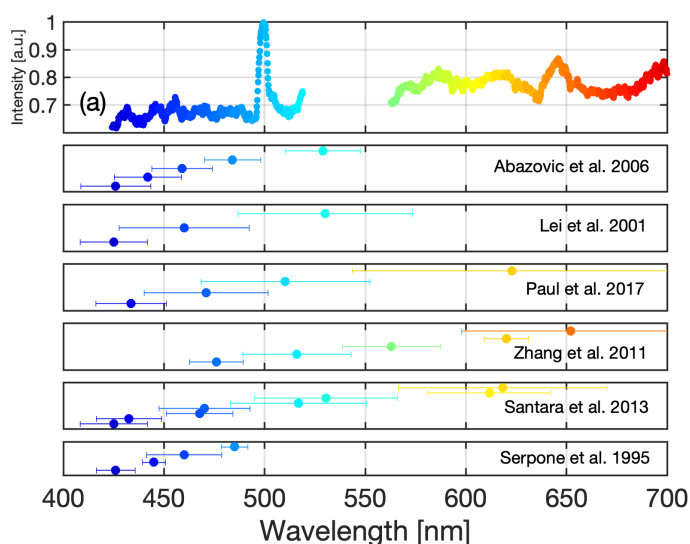


Figure 6.7. Emission spectrum of flame-generated TiO₂ at prompt under laser fluence $F = 0.24$ J/cm², normalized by the value of 650 nm of each curve. The C₂ and C₃ bands are from [356].

The deconvoluted gaussian sub-band LIF emission from various literature works are displayed with the emission spectrum of flame-generated TiO₂ in Fig. 6.8(a). As in Fig. 5.10(a), only the center of each gaussian band with the standard deviation $\pm\sigma$ range is shown. Almost all the distinct features of the spectrum can be covered by the sub-bands from the literature. With high laser fluence, the LIF sub-band peaks can become narrower [236], keeping the same position. Therefore, the LIF of TiO₂ could be the source of the sharp features of the spectrum.

On the other hand, the atomic emissions caused by PS-LIBS could also be considered as the source of sharp features. The laser fluence in this study is lower than the PS-LIBS range in the literature, yet the single-photon absorption mechanism may cause atomic emissions, especially enhanced in a high temperature environment in flames [357]. The possible atomic lines (Ti, O) are illustrated in the emission spectrum of flame-generated TiO₂ nanoparticles in Fig. 6.8(b). The location of each peak has a good accordance with the Ti and O atomic emissions from the NIST database. For that reason, PS-LIBS could also be a candidate to explain the multi-peak LIE emission in flame synthesized TiO₂ nanoparticles at prompt.

In conclusion, in a high laser fluence regime, (1) LIF of TiO₂ and/or (2) atomic emissions from PS-LIBS of TiO₂ could coexist in LIE on TiO₂ in flame synthesis at prompt whereas LIF from carbon species seems unlikely for the particles considered in this work. These emissions have relatively short characteristics times. Therefore, LIE at delayed acquisition will be characterized in the following to confirm the LII nature of the long-lasting signal.



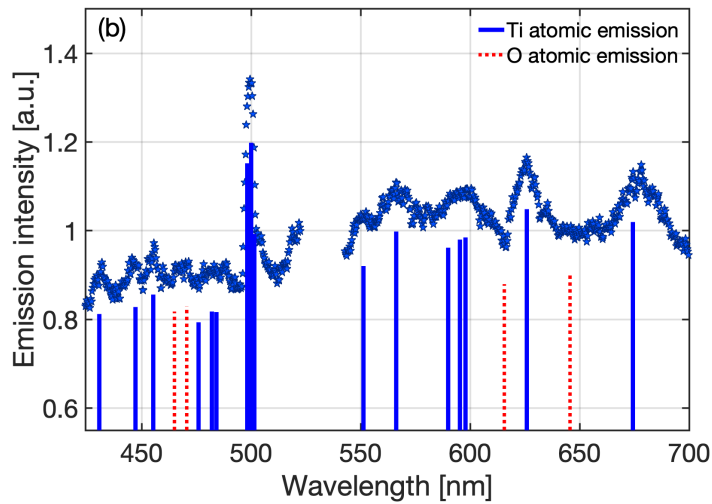


Figure 6.8. Normalized emission spectra of flame-generated TiO₂ nanoparticles at prompt under laser fluence of $F = 0.24 \text{ J/cm}^2$ with (a) Gaussian fit of sub-band emissions (peak location μ and $\pm\sigma$) of the LIF from literature [236, 336, 335, 238, 243, 244] and (b) Ti and O atomic emission from NIST [258] corresponding to peak location of emission spectra. The intensities of each transition are adapted for a clear view with curve, not expressing the relative intensities. The curves are normalized by its value at 650 nm.

6.2.3 LII nature of delayed LIE from flame-generated TiO₂ nanoparticles

The interference of signal from LIF or PS-LIBS can be avoided by delaying the detection timing. Then, the origin of the second long part of LIE of TiO₂ nanoparticles can be investigated by looking at delayed emission. Based on the spectral/temporal emission information under different laser fluence regimes, the moderate fluence $F = 0.15 \text{ J/cm}^2$ was selected. The evolutions of LIE spectra of flame-generated TiO₂ nanoparticles are shown in Fig. 6.9. No sharp emission features are detected, and the long-lasting signal is assured with enough intensity. The red-shift of the emission spectra of flame-generated TiO₂ nanoparticles for increasing time delay is observed. This demonstrates the decrease in temperature during the signal decay. The black-body-like tendency of flame-generated TiO₂ nanoparticles is demonstrated for flame synthesis of TiO₂.

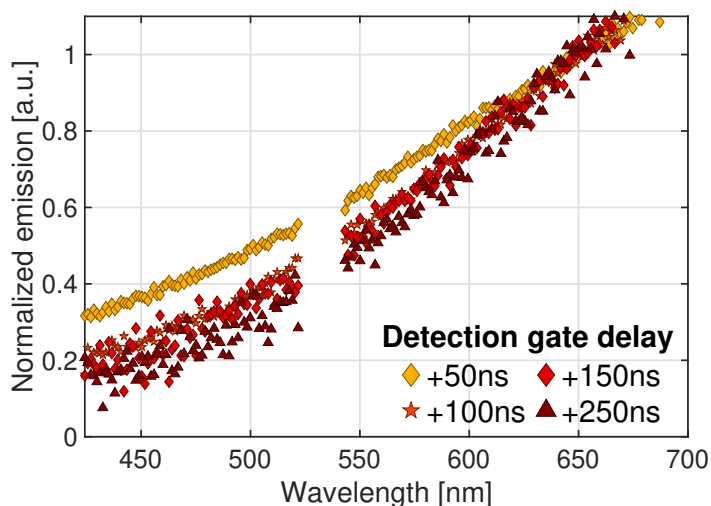


Figure 6.9. Effect of gate delay (gate width = 20 ns) on emission spectra of laser-induced emission of TiO₂ particles in flame synthesis at HAB = 45 mm. Laser fluence $F = 0.15 \text{ J/cm}^2$ was applied. Spectra are normalized with the value of each curve at 650 nm.

The temporal evolutions of the LIE are again considered to confirm the LII behavior. The normalized time evolution of the signal at 100 ns for different fluences is shown in Fig. 6.10. In this long delay, only the LII contributions remain significant. The cases of $F = 0.06$ and 0.1 J/cm^2 showed that we are slowly approaching the plateau region. The diminution of the decay dynamic is observed between 0.15 , 0.19 , and 0.24 J/cm^2 for detection wavelengths at 650 nm and 710 nm, having relatively close temperatures under the same particle diameter. The close dynamic indicates that we are close to the plateau regime for these fluence ranges. This behavior was not detected in LIE on pure TiO₂ in a non-reactive environment. The temporal profile at 450 nm and 500 nm are not considered here, since the emission could be mainly dominated by LIF of TiO₂ for signal interpretation.

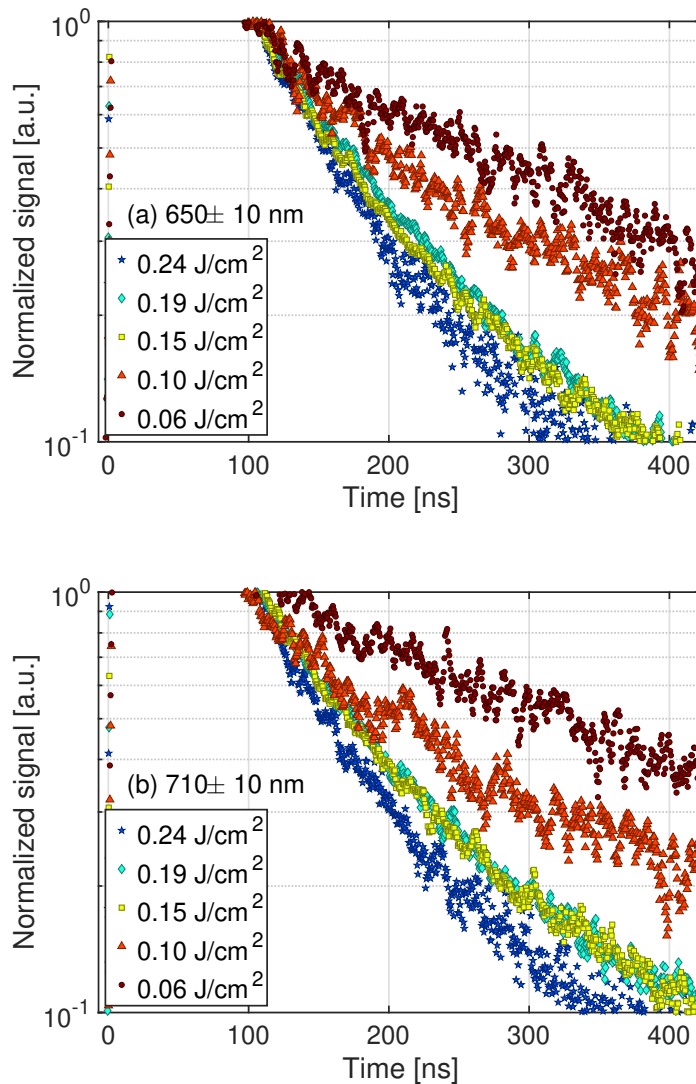


Figure 6.10. Normalized time evolution of flame-generated TiO₂ nanoparticles at HAB=45mm at different laser fluences at a detection wavelength of (a) 650 ± 10 nm and (b) 710 ± 10 nm. All graphs are normalized with the value of each curve at 100 ns. The reverse tendency between $F = 0.15$ J/cm² and 0.19 J/cm² in (b) is from the normalization process.

The decay characteristic time τ is calculated using Eq. (5.2) for temporal profiles of LIE for different laser fluences. With enough delay over $t \sim 100$ ns after the peak signal timing, the non-LII contribution of the signal can be avoided (Fig. 6.11). The linear correlation between detection wavelength and decay characteristic time τ is clearly identified for different laser fluences, confirming the LII-like nature of the delayed LIE. The linear relationship was conducted mainly with the detection wavelengths where enough S/N is assured. The same tendency is

confirmed for other laser fluences.

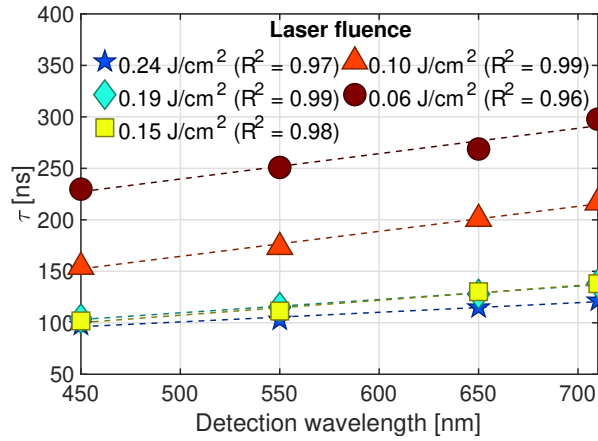


Figure 6.11. Decay characteristic time τ of LIE signal at HAB = 45 mm at $F = 0.15 \text{ J/cm}^2$. To determine τ , the LIE signals between 100 ns - 400 ns after the peak signal have been fitted using a log function. The R^2 value inside the legend represents the coefficient of determination for the fitting procedure. The dashed lines are the results of the linear fitting.

The ΔT^{-1} decays on flame synthesized TiO₂ are shown in Fig. 6.12 at $F = 0.15 \text{ J/cm}^2$. It should be noticed that at these two wavelengths, parasitic signal contribution at the prompt is negligible so it is possible to investigate ΔT^{-1} even close to the prompt. The time evolutions of ΔT^{-1} at $\lambda_{em} = 650 \text{ nm}$ and at $\lambda_{em} = 710 \text{ nm}$ show identical decay, so it confirms the LII nature for these wavelengths even close to prompt.

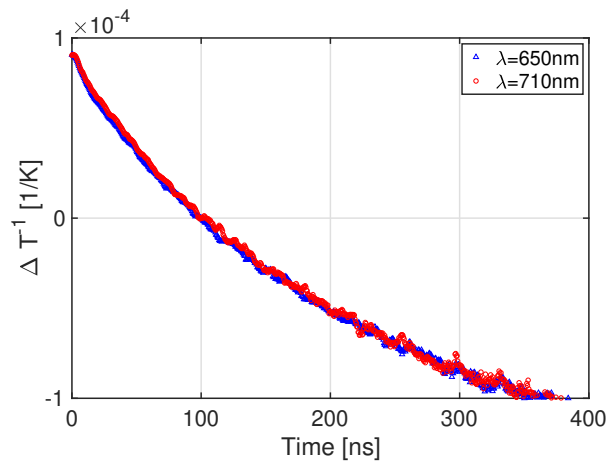


Figure 6.12. Evolution of ΔT^{-1} with of flame-synthesized TiO₂ nanoparticles LIE for two wavelengths for $F = 0.15 \text{ J/cm}^2$ at HAB = 45mm.

6.3 Discussion and conclusion

In Chapter 5 and 6, the LIE of high-purity TiO₂ in a non-reactive optical cell and flame-synthesized TiO₂ was studied. In both cases, we have demonstrated that LII on TiO₂ is feasible. However, similarities and differences are identified:

- (1) The prompt emission at different fluences is shown in Fig. 6.14. In low laser fluence regimes ($F = 0.06$ and 0.10 J/cm^2), only the LIF spectra are observed in non-reactive ambient temperature LIE on pure TiO₂, whereas in LIE on flame-synthesized TiO₂ nanoparticles, the continuous spectra emission are observed. This may be due to the difference in ambient temperature. At high ambient temperatures, less energy is needed to reach the incandescent temperature. Also, the change of optical property and higher heat capacity of TiO₂ with temperature [353] could enhance the absorption rate (Eq.(B.7)). Thus, detectable incandescence could be achieved easier than in a cold environment, especially in visible range wavelength.

On the other hand, this can be due to the strong emission from the flame synthesis of TiO₂ that has high luminosity (Fig. 6.13). The UV-ranged emission probably originates from the relatively high absorption function of TiO₂ in UV wavelength (Fig. 4.13(b)), and the continuous part to the longer wavelength could be attributed to the emission of H₂O. The detailed analysis is beyond the scope of this research work, however, this flame background luminosity could be so strong that it is not possible to observe the LIF of TiO₂ as in the non-reactive case with our current detection equipment.

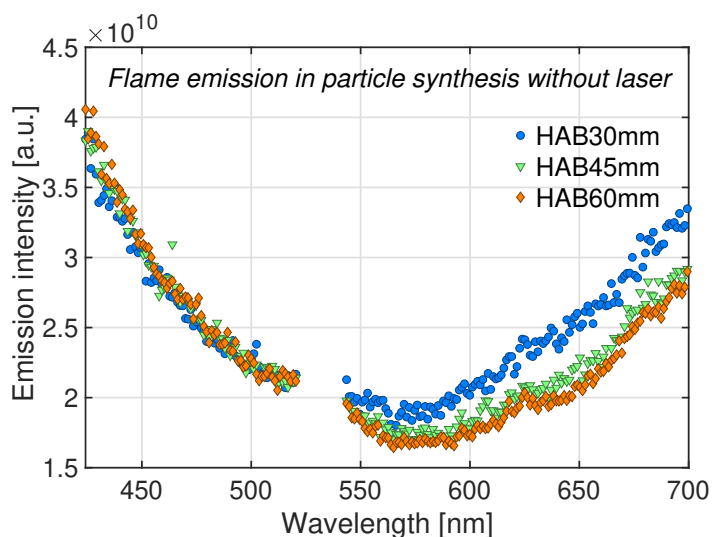


Figure 6.13. Flame emission intensity as a function of wavelength at different heights above the burner.

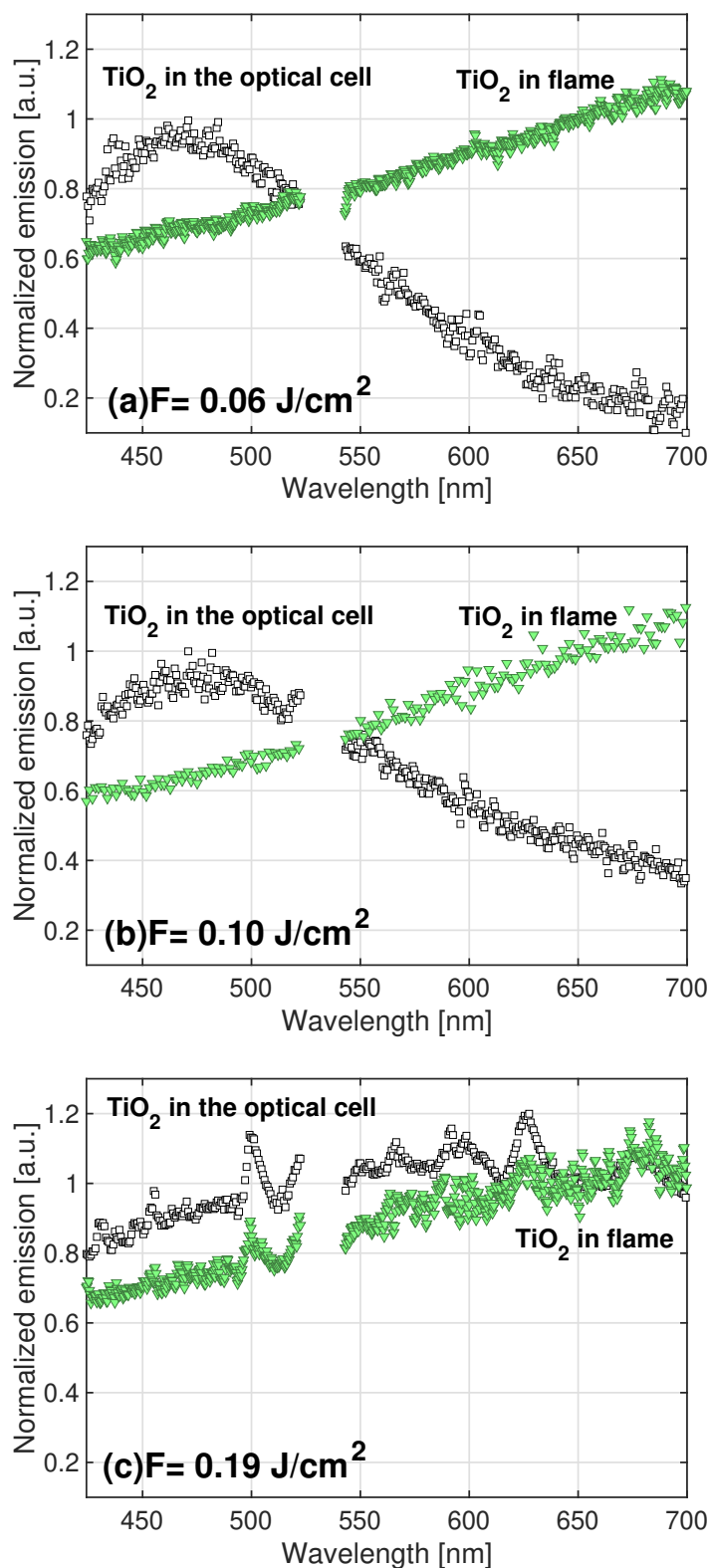
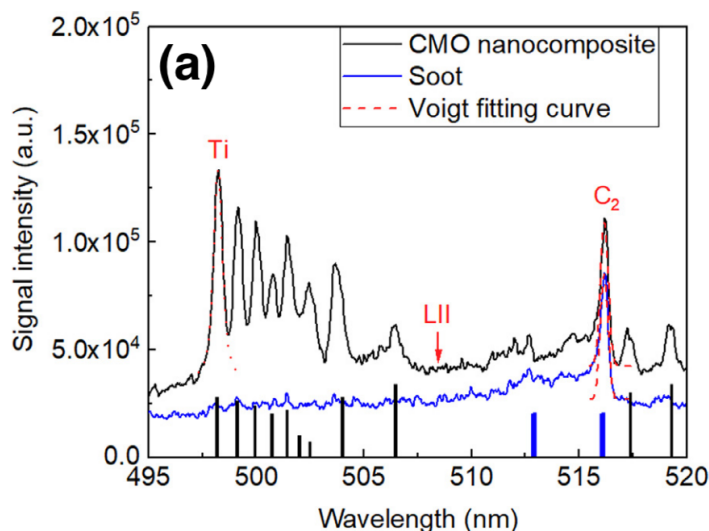


Figure 6.14. Emission spectra of TiO₂ nanoparticles from the optical cell (non-reactive, white square) and flames (reactive, at HAB= 45mm, green triangle symbol) at prompt under laser fluences of (a) 0.06 J/cm², (b) 0.10 J/cm², (c) 0.19 J/cm².

(2) At a strong laser fluence regime ($F = 0.19 \text{ J/cm}^2$), sharp line emissions are observed in both cases, which may result from the LIF and/or PS-LIBS signals of TiO₂ nanoparticles (Fig. 6.14(c)). Ren et al. [265] synthesized carbon-metal-oxide (CMO) nanocomposites in a counterflow burner fueled by C₂H₄. The PS-LIBS spectroscopy (pulse energy: 18.9 mJ/pulse) of these carbon-coated TiO₂ nanoparticles and soot particles are shown in Fig. 6.15(a). The spectrum from soot particles (blue line) presents C₂ emission at 516 nm superposed to a broadband emission from LII. The emission spectra of carbon-coated TiO₂ nanoparticles (black line) show both the line features from Ti atoms (near 500 nm) and the C₂ emission from the carbonaceous component (near 516 nm), revealing the presence of carbon materials on TiO₂ particles. Thus, it can be concluded that the emission contains information on the composition of nanoparticles.

The prompt emission spectra of carbon black, pure TiO₂, and flame-generated TiO₂ at the maximum fluence in our study are shown in Fig. 6.15(b). All emission spectra show apparent sharp emission features at high laser fluence due to the excited species of the vaporized particles overlapping with a continuous curve. The spectral features of C₂ near 516 nm are first confirmed in the emission spectra of carbon black nanoparticles in our study, accompanied by the feature near 468 nm (blue line, Fig. 6.15(b)). The flame-generated TiO₂ in our study (green line, Fig. 6.15(b)) does not show any of the characteristics of C₂ in its emission spectra. Instead, they correspond well to the Ti emission near 500 nm of the work of Ren et al. (Fig. 6.15(a)), albeit with a much lower spectral resolution. Moreover, the spectral features of flame-generated TiO₂ (green line) and those of the high-purity TiO₂ (black line) in Fig. 6.15(b) are very close. Thus, it can be inferred that there is much less trace of carbon in the TiO₂ nanoparticles generated by H₂ flame compared to those generated by C₂H₄ flame in the study of Ren et al. [265].



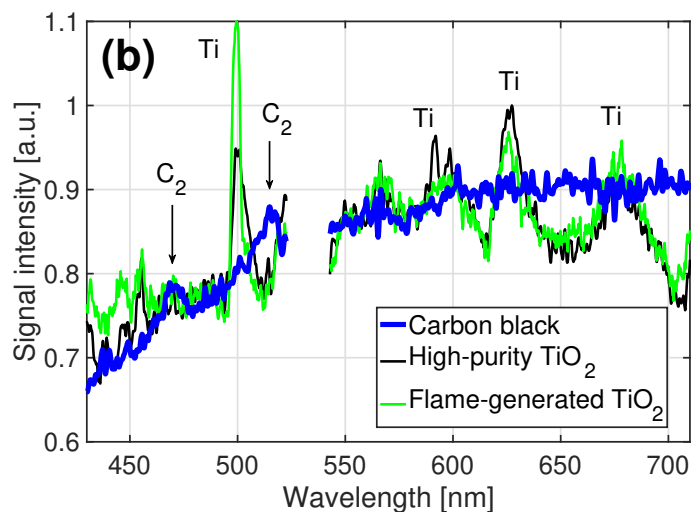


Figure 6.15. (a) PS-LIBS spectra of carbon-metal oxide (CMO) nanocomposites (black line) and pure soot particles (blue line) are shown, along with the Voigt fitting curves (red dotted lines) for Ti atomic emission (NIST database, represented as black columns) and C₂ Swan band [265]. (b) The emission spectra from the current study are displayed for carbon black nanoparticles in the optical cell (blue line), high-purity TiO₂ nanoparticles in the optical cell (black line), and flames-synthesized TiO₂ nanoparticles (at HAB= 45mm, green line) at prompt under a laser fluence of 0.24 J/cm².

Possible causes of such differences could be the absence of carbon atoms in the H₂ fuel. As clearly shown in the produced carbon-metal oxide nanoparticles in counterflow flame [265], there are more carbon coatings with increasing C₂H₄ fuel mass fractions (both proven by TEM image and by C₂ swan band signal intensity), especially on the fuel side. Note that for verification of the particle composition, additional analyses such as energy-filtered TEM or XRD are required.

- (3) These parasitic signals from non-LII contributions have a duration of FWHM 10 ns which completely disappear 65 ns after the peak signal. Therefore, at least 50 ns of the delay in acquisition timing for a high S/N ratio, or 100 ns delay in acquisition timing to be free of interference should be applied to analyze LII contributions. The spectral emissions in the delayed acquisition time of two TiO₂ configurations are compared in Fig. 6.16. For the non-reactive case, the laser fluence $F = 0.19 \text{ J/cm}^2$ is chosen. For the reactive case, the laser fluence at $F = 0.15 \text{ J/cm}^2$ is selected for comparison, as they are both considered close to the plateau region in the fluence curve. Therefore, they are expected to have both reached the boiling temperature at prompt under laser irradiation. Then, the difference in spectral emission at the same delay time from the laser peak could be interpreted as (1) the effects of the different emission functions $E(m_\lambda)$ of each particle or (2) the difference in particle morphology and structure as a result of the different generation process, i.e., sol-gel vs. flame synthesis.

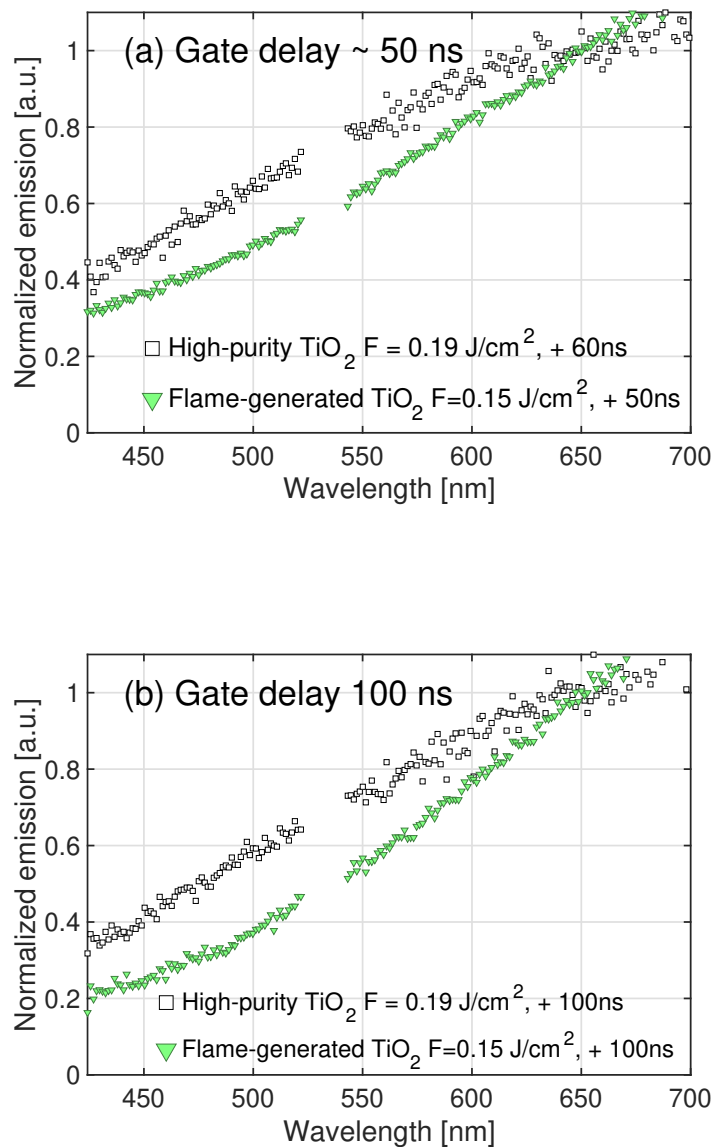


Figure 6.16. Comparison of emission spectra between high-purity TiO_2 and flame-generated TiO_2 nanoparticles. Emission spectra of TiO_2 nanoparticles from the optical cell (non-reactive, white square) and flames (reactive, at $\text{HAB} = 45$ mm, green triangle symbol) have been shown with delayed acquisition time at (a) around 50 ns (60 ns for the high-purity TiO_2 case) and (b) 100 ns, under laser fluence of 0.19 J/cm^2 for non-reactive case and 0.15 J/cm^2 for the reactive case. Both spectra are normalized by the value of each curve at 650 nm.

- (4) The identical evolution of ΔT^{-1} at 650 nm and 710 nm in Fig. 6.17 for both reactive and non-reactive cases indicates that the signals at both wavelengths come from the LII contribution, even from $t = 0$ ns. Indeed, at these wavelengths, the spectral features from the emission of LIF and/or PS-LIBS from TiO_2 are known to be less present (Chap. 4). The

LIF emissions of carbonaceous species are in fact more pronounced below 600 nm [304], which makes it possible to avoid intervention in this range of detection wavelengths. The difference in ratio between decay characteristic time and detection wavelength τ/λ_{em} of two systems could come from the difference in ambient temperature, and particle geometry, especially the particle diameter. For the following, these two detection wavelengths will mainly be treated as LII emission components.

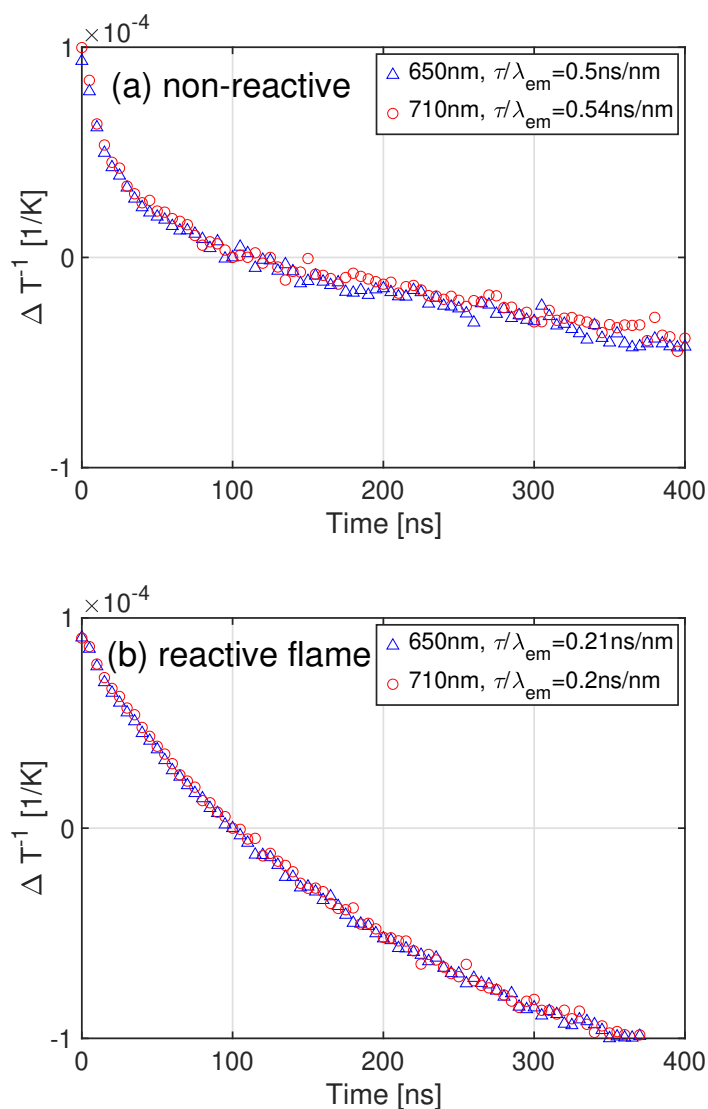


Figure 6.17. The evolution of ΔT^{-1} at 650 nm and 710 nm of (a) TiO_2 nanoparticles from the optical cell (non-reactive) and (b) flame (reactive); laser fluence of 0.19 J/cm^2 for the non-reactive case and 0.15 J/cm^2 for the reactive case. The value of τ/λ_{em} is written inside the legend.

In this chapter, the LIE on TiO₂ in flame synthesis was characterized under different laser fluence regimes and acquisition delay times. The action of carbon is minimized by hydrogen for particle synthesis. Non-LII emissions contributions appear during the LII measurement in flame synthesis. In the prompt, especially in high laser fluence regimes, sharp line emissions are detected. This could be the contribution of LIF or PS-LIBS, whose duration is relatively shorter than LII.

Then, in the delayed acquisition time, spectral emissions are verified again for their LII nature with a spectral shift to a longer wavelength with cooling. Moreover, the decay characteristic time as a function of the detection wavelength shows linear evolution according to the LII theory. The LII component in the LIE emission has been verified for flame-synthesized TiO₂ nanoparticles for all wavelengths for sufficiently delayed gate times (~ 100 ns) and for $\lambda_{em} = 650$ and 710 nm even at prompt. However, the interpretation of LII emission to obtain particle volume fraction and particle size distribution is not straightforward. In fact, information on the optical properties and particle temperature T_p are needed to obtain quantitative soot volume fraction values (Eq.(4.8)). In the last part of this manuscript, a post-processing approach is proposed to obtain information on the absorption function $E(m_\lambda)$, necessary for quantification of f_v . The feasibility is demonstrated by looking at both carbon black and TiO₂ measurements. Based on this approach, the evolution of $E(m_\lambda)$ and f_v in the laminar flame will finally be discussed in the last chapter.

Part III

Towards quantitative characterization of TiO₂ production in flames based on LII measurements

Chapter 7

Methodology for quantifying spectral properties of absorption function

$$E(m_\lambda)$$

Information on the absorption function $E(m_\lambda)$ is essential not only to quantify nanoparticles volume fraction from LII measurements but also to characterize the optical properties of the final nanomaterials. Even though the absorption function $E(m_\lambda)$ is often assumed to be spectrally constant in the visible and near infrared when considering mature soot particles [302, 358], this assumption may not be valid for TiO_2 nanoparticles. As already shown in Fig. 4.13(b), $E(m_\lambda)$ values for TiO_2 strongly vary with λ , and its spectral characteristic may depend on the nanoparticles production method. In this chapter, a new method to derive the spectral information of the absorption function $E(m_\lambda)$ is presented using LII measurements. First, a technique to determine the spectral dependence of $E(m_\lambda)$ is proposed in Sec. 7.1. Then, an estimation of the range of absolute values of $E(m_\lambda)$ is provided in Sec. 7.2.

It should be mentioned that the experimental database was originally planned for measurements to demonstrate LII feasibility in the previous part of the manuscript. Therefore, it is far from being optimized for measuring $E(m_{\lambda_{\text{laser}}})$. Nevertheless, we will exploit the available measurements to prove the feasibility of the strategy proposed for the estimation of $E(m_{\lambda_{\text{laser}}})$. This estimation is an essential step for quantifying normalized volume fraction from the LII signal, as discussed in Chap. 8.

7.1 Determining the spectral form of $E(m_\lambda)$

By reminding the theory of LII and of two-color optical pyrometry already presented in Sec. 4.3.2, the ratio of the signal at two wavelengths may be rewritten as (Eq. (4.15)):

$$R_{12} = \frac{I_{\text{SLII},\lambda_1}(t)}{I_{\text{SLII},\lambda_2}(t)} = C \frac{E(m_{\lambda_1})}{E(m_{\lambda_2})} \left(\frac{\lambda_2}{\lambda_1}\right)^6 \exp\left[\frac{hc}{k_B T_{\text{eff}}(t)} \left(\frac{1}{\lambda_2} - \frac{1}{\lambda_1}\right)\right]$$

where $C = \frac{\theta_{\lambda_1}}{\theta_{\lambda_2}}$ is a constant considering the detection efficiency at λ_1 and λ_2 . It is then possible to calculate the evolution $\varepsilon^*(\lambda, t)$ of the absorption function normalized by the value at a reference wavelength λ_{ref} at time t :

$$\varepsilon^*(\lambda, t) = \frac{E(m_\lambda, t)}{E(m_{\lambda_{\text{ref}}}, t)} = \exp \left(\ln \left(\frac{I_{\text{SLII}}(\lambda, t)}{I_{\text{SLII}}(\lambda_{\text{ref}}, t)} \right) + 6 \ln(\lambda/\lambda_{\text{ref}}) + \frac{B \left(\frac{1}{\lambda} - \frac{1}{\lambda_{\text{ref}}} \right)}{T_{\text{eff}}(t)} \right) \quad (7.1)$$

with $I_{\text{SLII}}(\lambda)$ is the LII emission signal at wavelength λ already corrected by the detection efficiency at λ , $B = hc/k_B$ and $\lambda_{\text{ref}} = 650$ nm. This requires the knowledge of the effective particle temperature T_{eff} . However, information on $E(m_\lambda)$ is needed to determine T_{eff} with two-color pyrometry via Eq. (4.16):

$$T_{\text{eff}}(t) = B \left(\frac{1}{\lambda_2} - \frac{1}{\lambda_1} \right) \cdot \left[\ln \left(C^{-1} \frac{E(m_{\lambda_2})}{E(m_{\lambda_1})} \left(\frac{\lambda_1}{\lambda_2} \right)^6 R_{12} \right) \right]^{-1}$$

Therefore, the system cannot be closed without assuming a constant spectral behavior of $E(m_\lambda)$. In order to circumvent this problem, we propose here to identify a range of possible values of particle temperature $T_{\text{eff}} \in [T_{\text{min}}, T_{\text{max}}]$ and successively calculate the correspondent $\varepsilon^*(\lambda)$. To calculate the range of possible values of T_{eff} , we proceed as following:

1. Assume that $E(m_\lambda)$ is constant over a small wavelength range $\Delta\lambda$:

$$E(m_\lambda) \approx E(m_{\lambda+\Delta\lambda}). \quad (7.2)$$

This condition is less restrictive than assuming a constant $E(m_\lambda)$ for the overall spectral range and is verified for $\Delta\lambda \rightarrow 0$. One expects to reduce the impact of this assumption by considering small $\Delta\lambda$ (in the following $\Delta\lambda = 2$ nm).

2. For a given λ and time t , the effective temperature is estimated via:

$$T_{\text{eff}}^\lambda(t) \approx \frac{\left(\frac{1}{\lambda+\Delta\lambda} - \frac{1}{\lambda} \right) B}{\ln \left(\frac{I_{\text{SLII}}(\lambda, t)}{I_{\text{SLII}}(\lambda+\Delta\lambda, t)} \right) + 6 \ln \left(\frac{\lambda}{\lambda+\Delta\lambda} \right)} \quad (7.3)$$

using spectral information measured by the spectrometer.

3. In order to account for the uncertainties related to the choice of the value of λ for a given time t , T_{eff}^λ is calculated over a range of $\lambda \in [\lambda^{\text{min}}, \lambda^{\text{max}}]$. The minimum and maximum values of T_{eff}^λ , namely T_{min} and T_{max} , will then provide the range of possible effective temperatures:

$$T_{\text{eff}} \in [T_{\text{min}}, T_{\text{max}}]. \quad (7.4)$$

The extreme values T_{min} and T_{max} will depend on the values retained for λ^{min} , λ^{max} , and $\Delta\lambda$ as well as the postprocessing procedure used to obtain $I_{\text{SLII}}(\lambda)$ and $I_{\text{SLII}}(\lambda + \Delta\lambda)$ from the spectral emission. Still, this approach allows accounting for the uncertainties in

the estimation of T_{eff} , which are hidden when using the classical estimation $T_{\text{eff}}^{\text{const}}$, i.e. by assuming a constant $E(m_\lambda)$ over the whole λ range: $E(m_{\lambda_{\text{min}}}) = E(m_{\lambda_{\text{max}}})$.

In the following, $\lambda \in [650, 710]$ nm will be considered since the LII nature is most evident at these wavelengths for TiO_2 nanoparticles with enough S/N ratio, as concluded in Part II.

Once the range of possible T_{eff} is known, the region of possible $\varepsilon^*(\lambda)$ is obtained from the minimum and maximum temperature values using the spectral information from the spectrometer via Eq. (7.1). Additionally, $\varepsilon^*(\lambda)$ is also calculated for the sublimation (or boiling) temperature to identify the profile of $E(m_\lambda)$ we assumed to have reached the 'plateau' region.

For this procedure based on LII theory, it is important to choose only the LII contributions of the LIE emission. Therefore, one should consider laser fluences which can result in enough S/N for the LII part without sublimation (or boiling) of particles and delayed acquisition times to avoid any signals from interference. Since Eq. (7.2) is sensitive to noise, the post-processing procedure should be carefully considered.

7.1.1 Post-processing procedure

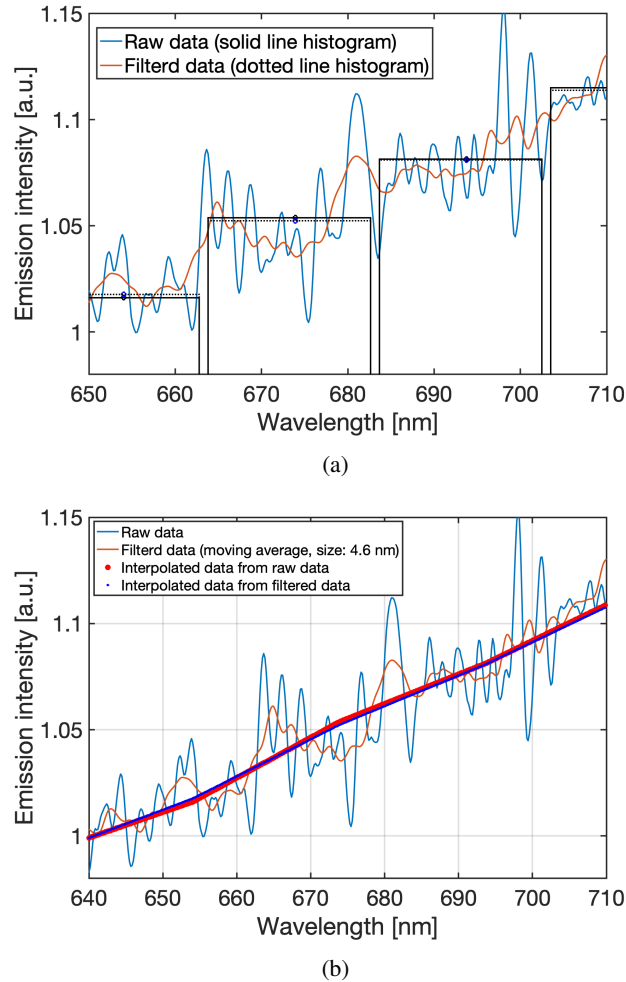
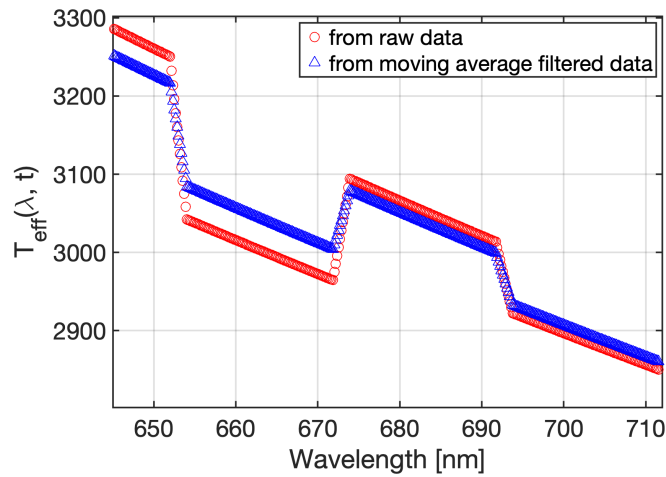


Figure 7.1. Post-processing method to apply two-color pyrometry from spectral information: (a) Calculation of averaged values of emission spectra for each 20 nm and (b) linear fitting of selected data. Data correspond to LIE from carbon black nanoparticles at $F = 0.06 \text{ J/cm}^2$ and a delay of 100 ns from laser excitation (blue line). The effect of data filtering (orange line) is illustrated.

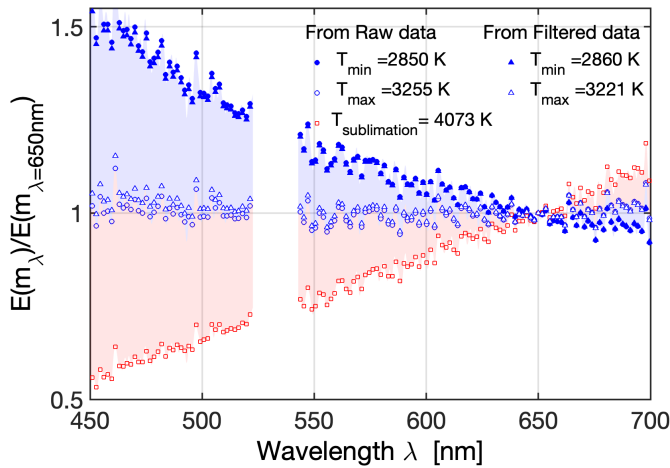
In this section, the post-processing procedure will be illustrated for the emission spectra of carbon black nanoparticles under $F = 0.06 \text{ J/cm}^2$ at a delay of $t = 100 \text{ ns}$ (Fig. 7.1):

1. Emission spectrum between 650 nm and 710 nm is considered. Averaged values (calculated by the area under the curve divided by the window size) in the range are selected every 20 nm (window size) as illustrated in Fig. 7.1(a).
2. The averaged values are linearly interpolated in Fig. 7.1(b).
3. The effective temperature is calculated via Eq. (7.3) with $\Delta\lambda = 2 \text{ nm}$ as in Fig. 7.2(a). Discontinuities are observed due to the linear reconstruction. In order to reduce such disconti-

nities, it is possible to filter the spectrum data as illustrated in Fig. 7.1(a). It is observed that the discontinuities for the derived effective temperature are reduced as shown in Fig. 7.2(a). However, since we are interested in the estimation of the maximum and minimum temperatures, we prefer in the following to consider results from raw data not to impose any graphical assumption during the post-treatment. The use of post-processing filters such as LOESS [359] can enhance this process as well.



(a)



(b)

Figure 7.2. Post-processing method to calculate the possible range of $\varepsilon^*(\lambda)$: (a) Estimation of possible effective temperature values from Eq. (7.3) and (b) corresponding $\varepsilon^*(\lambda)$ region (blue zone) extended to sublimation temperature (red zone). Both results from the raw and filtered spectra are shown. Data correspond to LIE from carbon black nanoparticles at $F = 0.06 \text{ J/cm}^2$ and a delay of 100 ns from the peak.

In this case, T_{\max} is 3255 K, and T_{\min} is 2850 K as shown in Fig. 7.2(a). From these two values, $\varepsilon^*(\lambda, t)$ is obtained via Eq. (7.1). The range of possible $\varepsilon^*(\lambda, t)$ is visualized in blue in Fig. 7.2(b). The $\varepsilon^*(\lambda, t)$ obtained with the sublimation temperature is also shown to limit the estimation range. Results are illustrated by a red zone in Fig. 7.2(b). Although we may use the term "sublimation temperature" for convenience, it should be noted that there is no true "sublimation temperature" for LII process, as sublimation is a non-equilibrium process [360]. Rather, the term refers to the temperature at which particle evaporation becomes observable.

Effect of $\Delta\lambda$

The values of T_{\max} and T_{\min} may depend on the size of $\Delta\lambda$. The emission of carbon black at $F = 0.06 \text{ J/cm}^2$ is again used as an example at gate delay of $t = 100 \text{ ns}$. Results for different $\Delta\lambda$ on the maximum and minimum $T_{\text{eff}}(\lambda)$ are shown in Fig. 7.3. As expected, the temperature range converges when considering a small value of $\Delta\lambda$. In the following, a value of $\Delta\lambda = 2 \text{ nm}$ is retained.

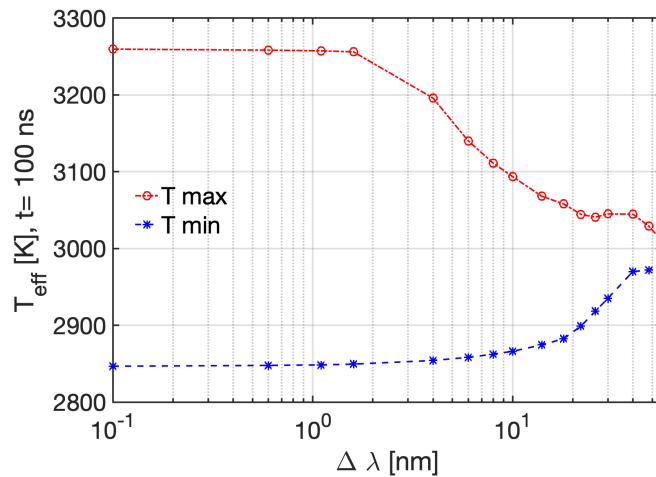


Figure 7.3. Effect of $\Delta\lambda$ on the estimation of maximum and minimum effective temperatures. Data correspond to LIE from carbon black nanoparticles at $F = 0.06 \text{ J/cm}^2$ and a delay of 100 ns from the peak (blue line).

7.1.2 Results

The resulting spectral shape of $E(m_\lambda)$ for carbon black, high-purity TiO_2 and flame-synthesized TiO_2 nanoparticles are presented.

7.1.2.1 Feasibility on carbon black particles in non-reactive environment

The validation of the methodology to obtain the spectral shape of the absorption function is demonstrated by analyzing carbon black nanoparticles with varying fluence and acquisition delay times. Literature databases are available for this purpose. To illustrate the possible effects of fluence and acquisition delay time on estimating $\varepsilon^*(\lambda)$, we analyze the results at three different fluences and four acquisition delay times. The evolution of $\varepsilon^*(\lambda)$ for carbon black is shown in Figs. 7.4, 7.5 and 7.6 for $F = 0.06, 0.12, \text{ and } 0.23 \text{ J/cm}^2$, respectively. The blue region represents the zone between T_{\min} and T_{\max} (the corresponding temperatures are indicated inside the legend), while the red zone indicates the values between T_{\max} and $T_{\text{sublimation}}$.

For $F = 0.06 \text{ J/cm}^2$ (Fig. 7.4), the LIE of carbon black includes only the contribution of LII. Thus, it is possible to consider the results for acquisition delay times between 0 and 200 ns from the peak. It can be observed that the blue areas look alike for the four acquisition delay times, following the same trend as the $\varepsilon^*(\lambda)$ of Yon et al. [261] for diesel and diester soot. It is worth noting that even though we have assumed that $E(m_\lambda)$ is constant for a small $\Delta\lambda$, the spectral form of $E(m_\lambda)$ is not constant for the entire range of the wavelength spectrum. This assumption is less restrictive than imposing a constant $E(m_\lambda)$ for all visible ranges once the emission level with enough S/N ratio is assured. The fact that the blue areas do not depend on time evolution shows the robustness of the proposed technique. On the other hand, the red area shows a different behavior. At the prompt, it retrieves the literature values (Chang et al. [287], Faeth and Koylu [361], and Krishnan et al. [362]). For delayed timing, the red area becomes larger. This is not surprising since the acquisition delay time increases the cooling of the particles. As a consequence, the assumption of sublimation temperature becomes increasingly invalid, and $\varepsilon^*(\lambda)$ deviates further from the literature results. Overall, the form of $E(m_\lambda)$ strongly depends on the effective temperature T_{eff} . The variability found in the literature for $\varepsilon^*(\lambda)$ could be due to various factors. One reason is that the $E(m_\lambda)$ function is inferred from a variety of measurement techniques, which can lead to differences in results. Additionally, $E(m_\lambda)$ can vary depending on the origin and morphology of particles. This point has been discussed in previous studies such as [288, 363].

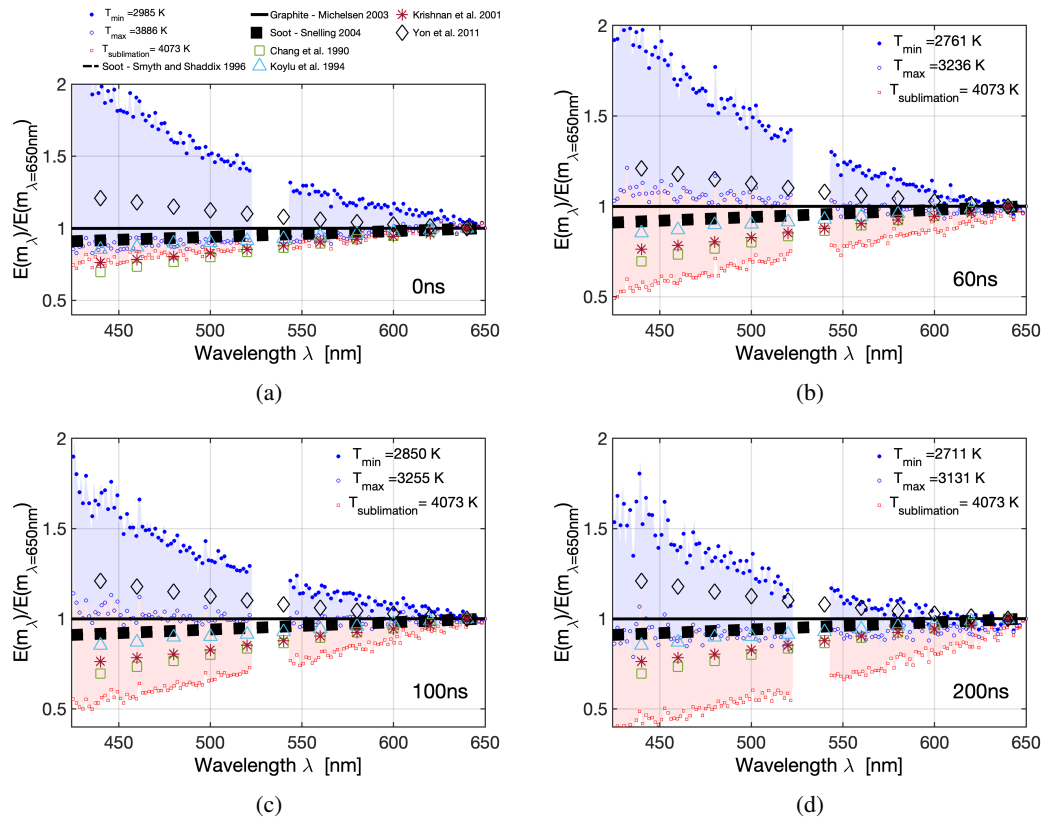


Figure 7.4. $\varepsilon^*(\lambda, t)$ for carbon black nanoparticles using LIE at $F = 0.06 \text{ J/cm}^2$ and different acquisition delay times: (a) 0, (b) 60, (c) 100, (d) 200 ns. Values of T_{\min} and T_{\max} are shown in the legend. The values $\varepsilon^*(\lambda)$ found in the literature are also presented [364, 25, 303, 287, 361, 362, 261].

When considering higher fluences ($F = 0.12 \text{ J/cm}^2$ in Fig. 7.5 and $F = 0.23 \text{ J/cm}^2$ in Fig. 7.6), sublimation and non-LII emission signals were observed in Chap. 5. Therefore, the component at the prompt should not be considered for the estimation of $\varepsilon^*(\lambda)$, again emphasizing that one should use only the signals from the LII contribution, i.e., for acquisition delay times higher than $t_{\text{non-LII}} \approx 100 \text{ ns}$. All cases recover the experimental data even if for higher fluences a wider range of possible $\varepsilon^*(\lambda)$ is observed. In conclusion, the method works reasonably for carbon black nanoparticles. In the next section, the same method will be applied for pure TiO_2 nanoparticles.

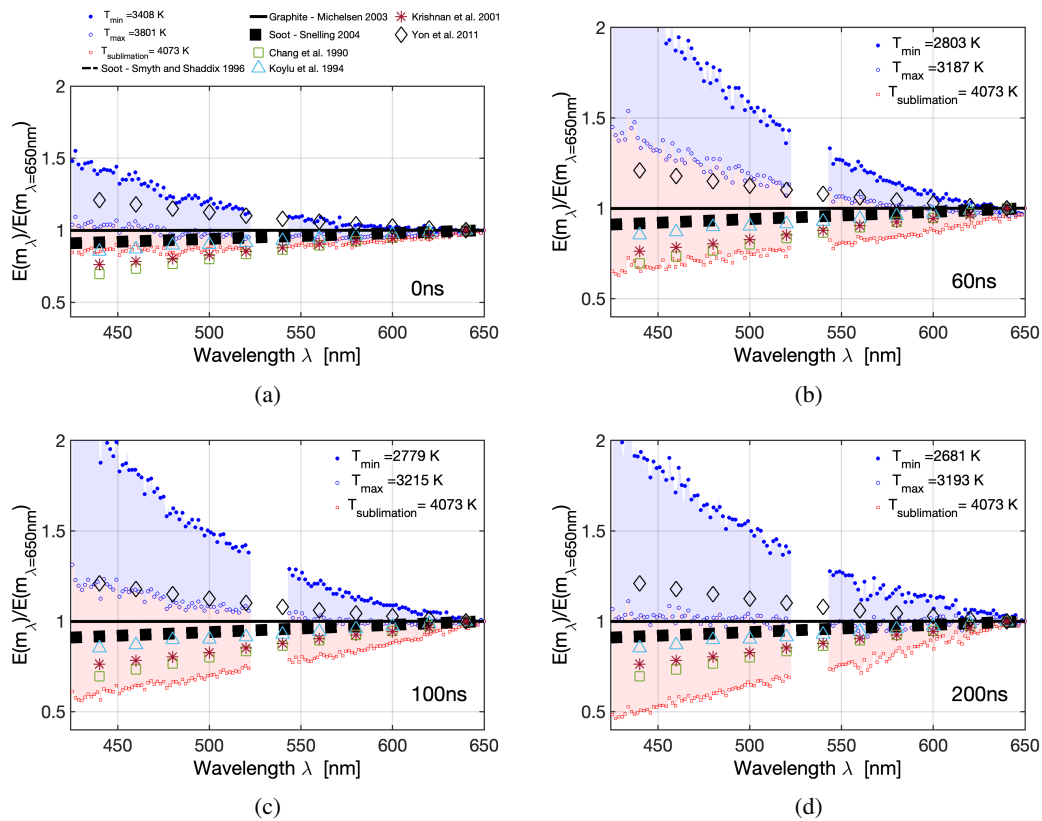


Figure 7.5. $\varepsilon^*(\lambda, t)$ for carbon black nanoparticles using LIE at $F = 0.12 \text{ J/cm}^2$ and different acquisition delay times: (a) 0, (b) 60, (c) 100, (d) 200 ns. Values of T_{\min} and T_{\max} are shown in the legend. The values $\varepsilon^*(\lambda)$ found in the literature are also presented [364, 25, 303, 287, 361, 362, 261].

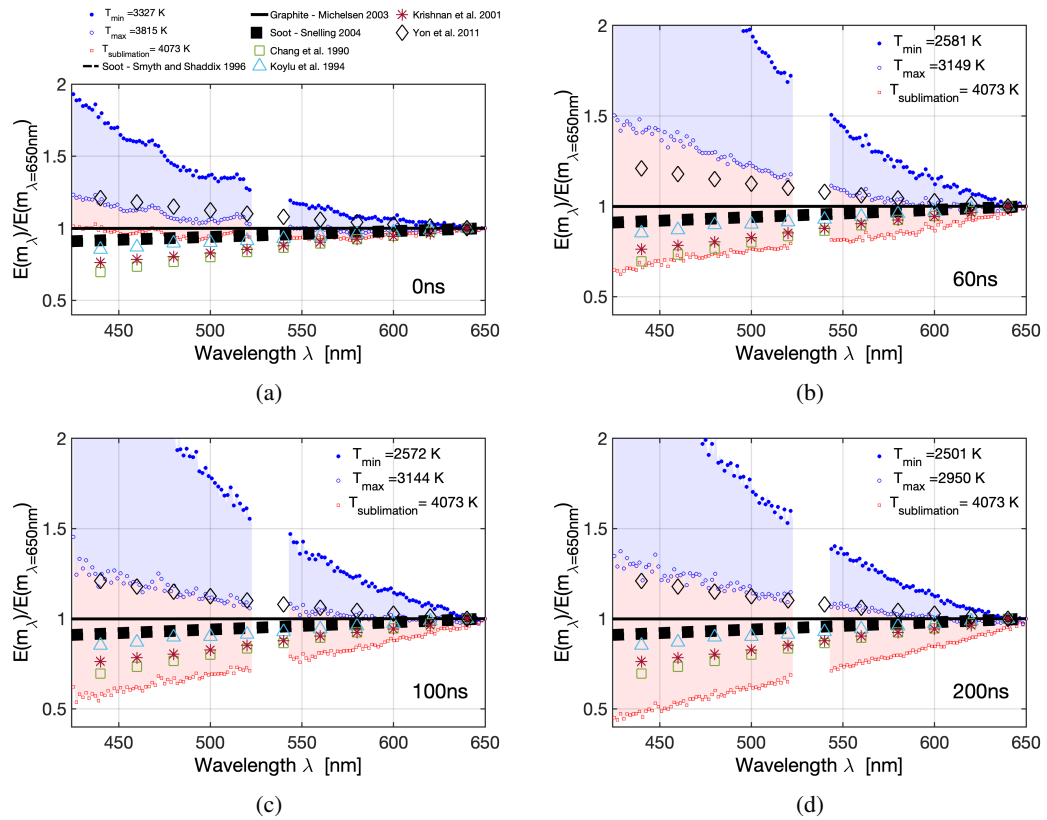


Figure 7.6. $\varepsilon^*(\lambda, t)$ for carbon black nanoparticles using LIE at $F = 0.23 \text{ J/cm}^2$ and different acquisition delay times: (a) 0, (b) 60, (c) 100, (d) 200 ns. Values of T_{\min} and T_{\max} are shown in the legend. The values $\varepsilon^*(\lambda)$ found in the literature are also presented [364, 25, 303, 287, 361, 362, 261].

7.1.2.2 Application to TiO₂ nanoparticles in non-reactive environment

The results for TiO₂ are first considered at $F = 0.19 \text{ J/cm}^2$ (Fig. 7.7) for four different acquisition delay times. At prompt (Fig. 7.7(a)), due to the presence of emission from non-LII contributions, sharp peaks are observed. Therefore, prompt results should not be considered for the estimation of $\varepsilon^*(\lambda, t)$. Only results for 60, 100, and 200 ns are considered. For 60 ns after the peak signal, a small part of the LIF/PS-LIBS emission could exist. The $\varepsilon^*(\lambda)$ calculated using the LIE signals after an acquisition delay of $t_{\text{non-LII}} \approx 100 \text{ ns}$ is therefore more reliable. When increasing the delay time, the blue region is not drastically modified, whereas the red zone increases since the estimated temperatures are farther and farther from the boiling temperature.

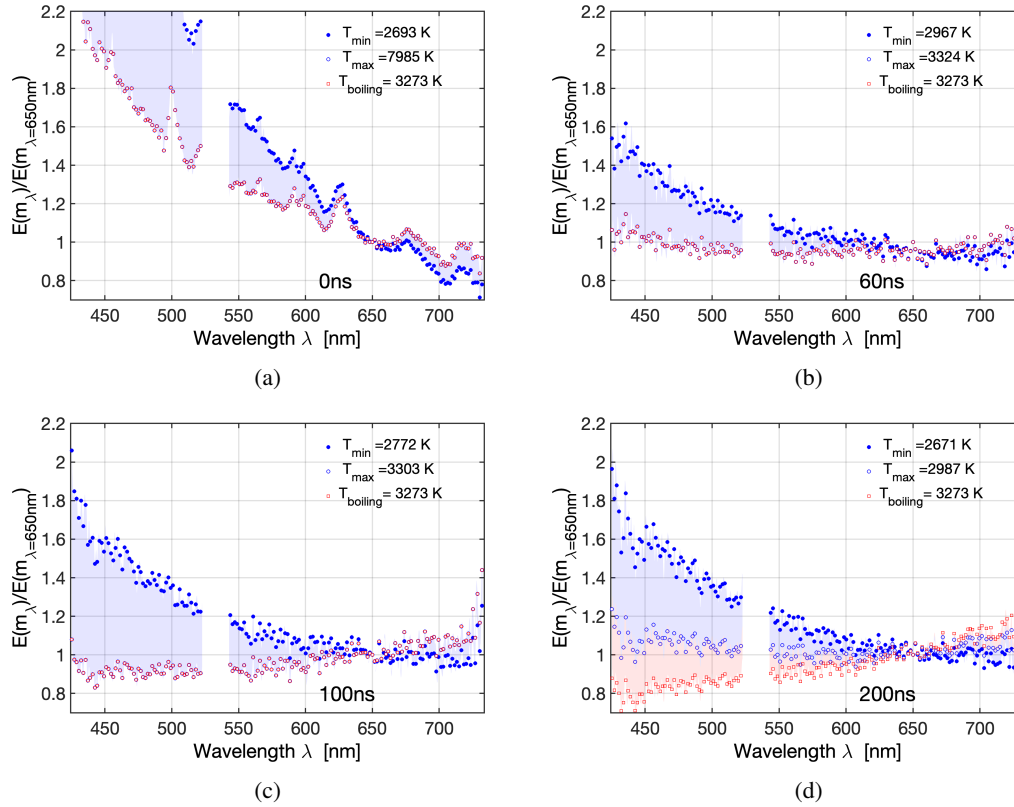


Figure 7.7. $\varepsilon^*(\lambda, t)$ for high-purity TiO₂ nanoparticles using LIE at $F = 0.19 \text{ J/cm}^2$ and different acquisition delay times: (a) 0, (b) 60, (c) 100, (d) 200 ns. Values of T_{min} and T_{max} are shown in the legend. T_{min} is bigger than melting point of TiO₂ (2128 K [282]) so estimated $\varepsilon^*(\lambda, t)$ are for liquid state particles.

For $F = 0.24 \text{ J/cm}^2$ (Fig. 7.8), the high fluence results in particle vaporization, which affects the emission spectra. At prompt, the calculated effective temperature is higher than the boiling temperature of TiO₂. As expected from the results presented in Chap. 5, the data for this fluence should not be considered since they probably correspond to the 'plateau' region, where vaporization is potentially not negligible. In addition, the 'plateau' regime of the fluence curve

should be carefully treated for TiO_2 nanoparticles since it can be accompanied by the phase change to liquid during the increase of laser fluence. At the same time, it is also possible to occur an additional phase change into gas due to high laser fluence.

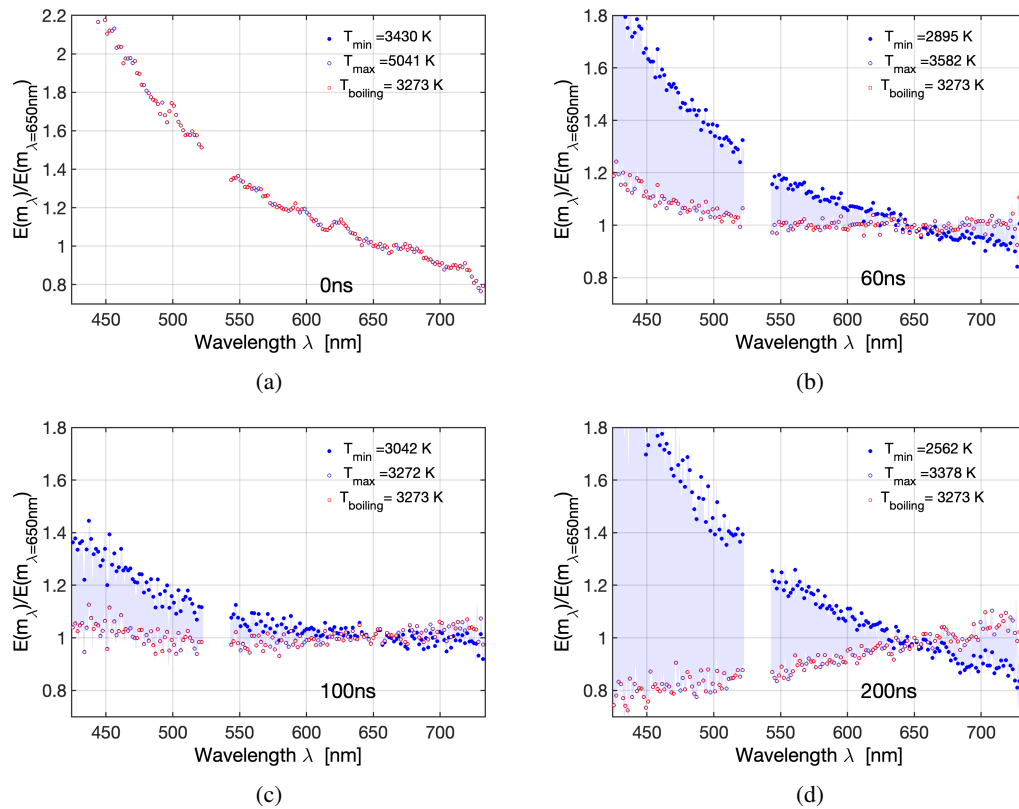


Figure 7.8. $\varepsilon^*(\lambda, t)$ for high-purity TiO_2 nanoparticles using LIE at $F = 0.24 \text{ J/cm}^2$ and different acquisition delay times: (a) 0, (b) 60, (c) 100, (d) 200 ns. Values of T_{\min} and T_{\max} are shown in the legend. T_{\min} is bigger than melting point of TiO_2 (2128 K [282]) so estimated $\varepsilon^*(\lambda, t)$ are for liquid state particles.

From the application of the technique to TiO_2 nanoparticles in non-reactive condition, it is essential to consider the following:

- Time delayed spectra where no parasitic signals can occur;
- Laser fluences for which particle sublimation is negligible.

Therefore, data obtained for $F = 0.19 \text{ J/cm}^2$ at 100 ns are retained. Using values of $\varepsilon^*(\lambda)$, the spectral evolution of $E(m_\lambda)$ normalized at 451 nm is shown in Fig. 7.9 and compared with available experimental data. The estimation of normalized $E(m_\lambda)$ covers the absorption function of De Iuliis et al. [214]. Our estimation shows a slower decrease than that of Liu et al. [285]. The possible range of identified $E(m_\lambda)$ profile looks reasonable since it is between the literature data. Still, one should consider that sampled nanoparticle phases are different since the mostly liquid state is expected here due to laser irradiation, whereas particles were solid-

state in the literature works relying on different experimental diagnostics. Thus, the different phases could be the origin of distinctive features. In the following, the approach is applied to the investigation of TiO_2 nanoparticles in flame synthesis.

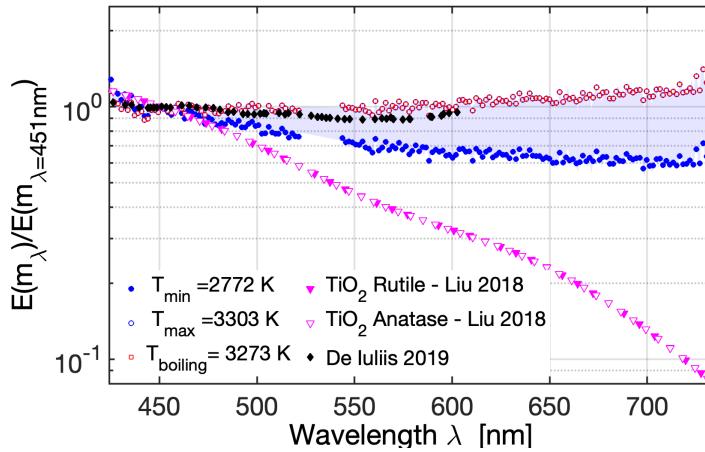


Figure 7.9. $E(m_\lambda)$ normalized at 451 nm for high-purity TiO_2 nanoparticles from LIE at $F = 0.19 \text{ J/cm}^2$ and 100 ns from prompt. Results are compared to literature data [285, 214]. T_{\min} is bigger than melting point of TiO_2 so it should be in liquid state.

7.1.2.3 Application to flame-synthesized TiO_2 nanoparticles

As done for the other experimental database, the shape of the absorption function is calculated for $F = 0.15 \text{ J/cm}^2$ at different acquisition delay times (0, 50, 100, 150, and 250 ns from the peak). Results are illustrated in Fig. 7.10. At prompt, the parasitic emission signals exist so that it is not recommended to take them into account in the calculation. The blue zones do not change significantly with time evolution over 50 and 100 ns. For longer acquisition time ($t=150 \text{ ns}$ and 250 ns), a similar trend is observed but results do not have good enough S/N and it is preferred not to consider them. Unfortunately, the available experimental data for flame-synthesized TiO_2 is quite limited. However, analogous to the conclusion on black carbon and high-purity TiO_2 nanoparticles, $\varepsilon^*(\lambda)$ from the LIE spectrum at $F = 0.15 \text{ J/cm}^2$ and 100 ns from prompt is used to show the spectral evolution of $E(m_\lambda)$ normalized to 451 nm in Fig. 7.11.

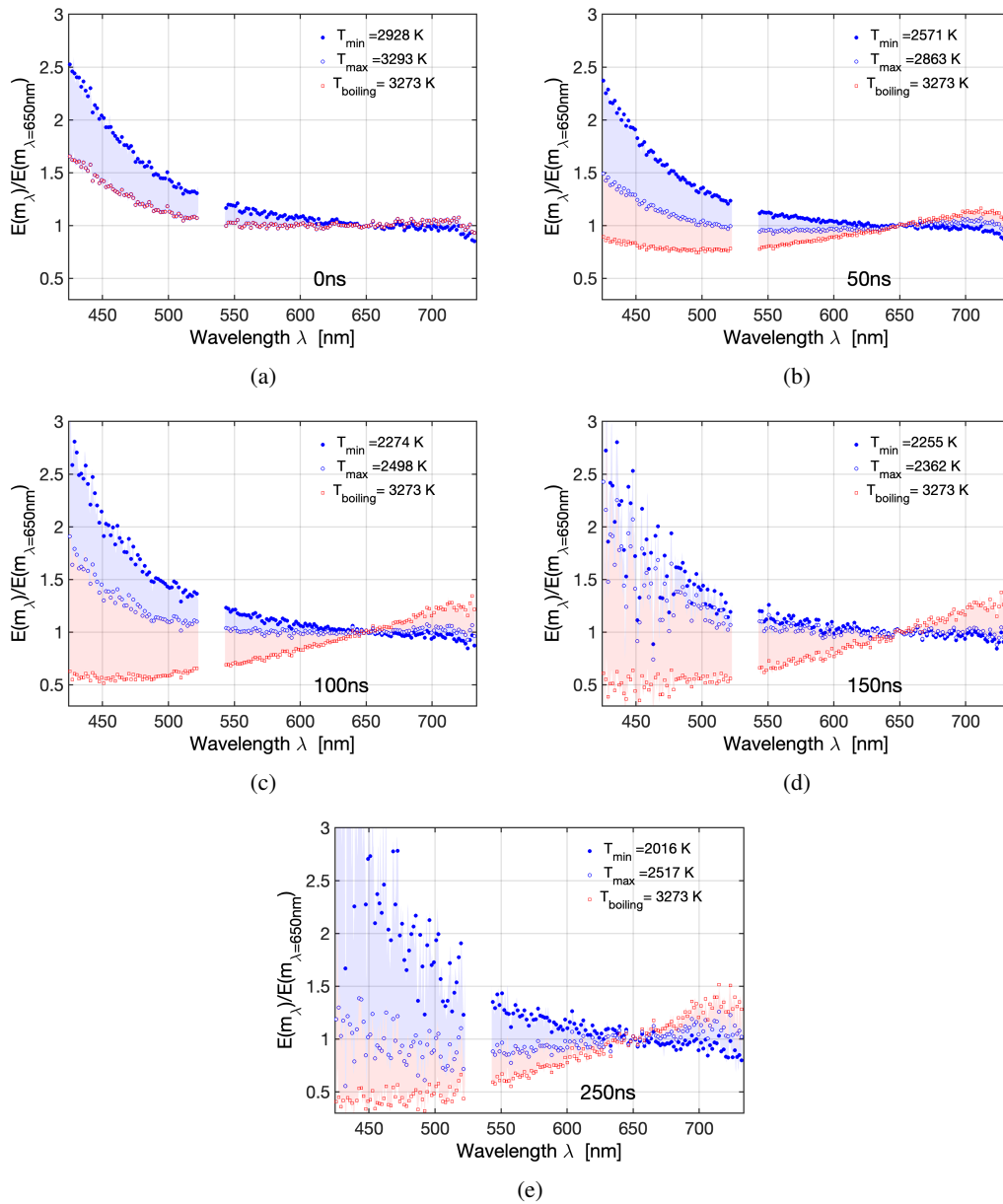


Figure 7.10. $\varepsilon^*(\lambda, t)$ for flame-synthesized TiO_2 nanoparticles using LIE at $F = 0.15 \text{ J/cm}^2$ and different acquisition delay times: (a) 0, (b) 50, (c) 100, (d) 150 and (e) 250 ns. Values of T_{\min} and T_{\max} are shown in the legend. T_{\min} is bigger than melting point of TiO_2 (2128 K [282]) so estimated $\varepsilon^*(\lambda, t)$ are for liquid state particles.

Compared to the carbon black case, there is a significant change in the dynamics of $E(m_\lambda)$ in the target spectral range, demonstrating that this strategy is able to capture highly variable $E(m_\lambda)$ functions. Our estimated (blue) zone is located between the values of Liu et al. [285] and De Iuliis et al. [214]. Still, the spectral dependence could originate from the change of nanoparticle phases (solid \rightarrow liquid), therefore, further studies of particle phases during the LII process are needed to elucidate the origin of this strong dynamic of $E(m_\lambda)$ of flame-synthesized TiO_2 nanoparticles.

Even if the measurements performed in this work were not designed to measure $E(m_\lambda)$, it has been possible to obtain an estimation of its possible spectral evolution. This information will be used in the Chap. 8 to study the spatial evolution of the nanoparticles volume fraction f_v via Eq.(4.12). Before this, in the next section, we propose a strategy to estimate the absolute value of $E(m_\lambda)$ once the spectral evolution is known.

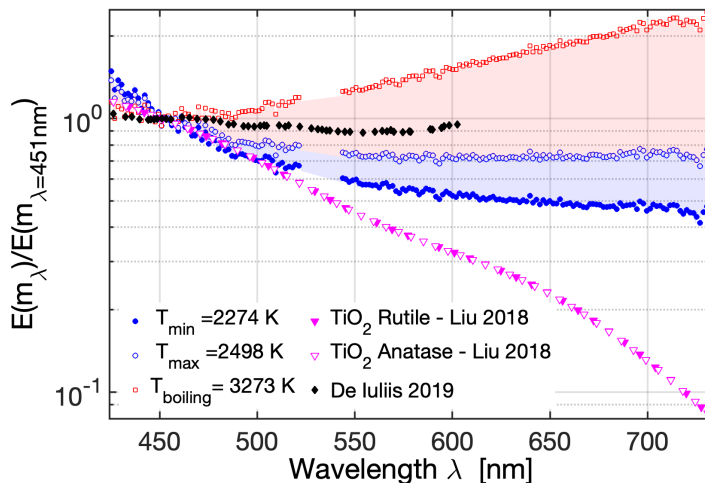


Figure 7.11. $E(m_\lambda)$ normalized at 451 nm for flame-synthesized TiO_2 nanoparticles from LIE at $F = 0.15 \text{ J/cm}^2$ and 100 ns from prompt. Results are compared to literature data of solid TiO_2 [285, 214]. T_{\min} is bigger than melting point of TiO_2 so it should be in liquid state.

7.2 Derivation of the absolute value of $E(m_\lambda)$

The previous section showed how to derive $\varepsilon^*(\lambda)$, i.e., the spectral dependence of $E(m_\lambda)$. Here, the absolute values of $E(m_\lambda)$ are provided with the following strategy:

1. The value of $E(m_{\lambda_{\text{laser}}})$ at the laser excitation wavelength λ_{laser} is calculated. For a fluence low enough to avoid sublimation, i.e., when a linear relationship between laser fluence and temperature can be found [365, 366, 367, 368], thermal losses due to radiation and conduction occurring during the laser pulse can be considered negligible at prompt. Only the absorption terms of the heat transfer equation are concerned in terms of the energy equation (Eq. (B.5)). In addition, both internal energy and absorption are volumetric for small particles under Rayleigh approximation, so the dependence on particle size can be neglected. Under these assumptions, the $E(m_{\lambda_{\text{laser}}})$ can be calculated as :

$$E(m_{\lambda_{\text{laser}}}) = \rho c_p \frac{\lambda_{\text{laser}} T_{\text{eff}}^0 - T_{\text{gas}}}{6\pi F} \quad (7.5)$$

where ρ and c_p are the density and the heat capacity of particles which vary with the temperature of the particles, respectively, T_{gas} is ambient gas temperature, T_{eff}^0 is particle temperature at prompt, and F is laser fluence.

Various research groups, including Eremin's and Daun's [369, 370], have utilized the presented calorimetry method (Eq. (7.5)) to determine the absolute value of $E(m_{\lambda_{\text{laser}}})$ and investigate the properties of different types of nanoparticles. However, it is important to note that the application of Eq. (7.5) is subject to simplifying assumptions that may introduce errors into the results. Factors such as changes in the material's density and specific heat during laser heating, as well as changes in its optical properties, could significantly impact the inferred value of $E(m_{\lambda_{\text{laser}}})$. Additionally, if the particles are not in the Rayleigh regime, they will heat to different peak temperatures, as demonstrated in the literature [327]. Furthermore, it is crucial to take into account the change in sensible energy during the process of particle melting. The most significant factor to consider is the modification in $E(m_{\lambda_{\text{laser}}})$ as the particles undergo a phase transition from solid to liquid, which may also vary with the temperature. Therefore, it is crucial to exercise caution and carefully consider these factors when employing this approach. The validation of this method for $E(m_{\lambda_{\text{laser}}})$ estimation is beyond the scope of this thesis, but the validity of the assumptions used for this method can be found in [366].

2. The value of $E(m_\lambda)$ for a given λ is then calculated from $\varepsilon^*(\lambda)$:

$$E(m_\lambda) = \frac{E(m_\lambda)}{E(m_{\lambda_{\text{ref}}})} \frac{E(m_{\lambda_{\text{ref}}})}{E(m_{\lambda_{\text{laser}}})} E(m_{\lambda_{\text{laser}}}) = \frac{\varepsilon^*(\lambda)}{\varepsilon^*(\lambda_{\text{laser}})} E(m_{\lambda_{\text{laser}}}) \quad (7.6)$$

with $\lambda_{\text{laser}}=355$ nm and $\lambda_{\text{ref}}=650$ nm to minimize the effect of interference emission in normalization.

In the following, to validate the post-processing procedure, the $E(m_\lambda)$ is calculated for carbon black particles. Then the procedure is applied to high-purity as well as flame-synthesized TiO₂ nanoparticles. For each database, two different cases are tested:

- Assuming spectrally constant $E(m_\lambda)$, i.e., $\varepsilon^*(\lambda) = 1$. Results are presented in Sec. 7.2.1.

- Considering spectrally non-constant $E(m_\lambda)$, i.e., using the $\varepsilon^*(\lambda)$ obtained in the previous section. Results are presented in Sec. 7.2.2.

For all cases, the gaseous temperature will be considered equal to 300K for the non-reactive conditions and assumed equal to 1900 K under reactive conditions, which is the typical temperature of hydrogen diffusion flame [371].

7.2.1 Assuming spectrally-constant $E(m)$

In this section, the experimental database is analyzed by assuming a spectrally-constant value of the absorption function $E(m_\lambda) = E(m)$. As explained previously, in order to obtain a good estimate of $E(m_{\lambda_{\text{laser}}})$, the measurements should be performed at a laser fluence for which a linear relationship between temperature and fluence is observed. The validity of this assumption is evaluated here by estimating the effective temperature as a function of laser fluence at different acquisition times.

First, carbon black measurements are considered to validate the post-processing procedure. In Fig. 7.12(a), the effective particle temperature has been obtained as a function of laser fluence considering spectral LIE at $t=0, 60$ and 100 ns using the two-color pyrometry strategy explained in Sec. 7.1. Between $F = 0.06$ and 0.12 J/cm², the temperature increases with laser fluence. For $F = 0.23$ J/cm², the temperature increases when considering prompt, but it is lower compared to smaller fluences for $t=60$ and 100 ns. Such behavior is not surprising since we have already shown in Chap. 5 that sublimation is not negligible for this fluence so results may be affected by sublimation. The linear regime of the fluence curve could not be clearly demonstrated since the trend for other fluences has not been verified. However, the smallest fluence ($F = 0.06$ J/cm²) seems not to reach the 'plateau', and it will be considered to calculate $E(m_{\lambda_{\text{laser}}})$ from Eq. (7.5). As largely discussed in Part II, to ensure exclusion of parasitic signals and accurate consideration of only LII spectral contributions, it is necessary to take into account information regarding delayed times. Thus, it is important to evaluate the effect of such a delayed acquisition on the estimated $E(m_{\lambda_{\text{laser}}})$ values. For this, $E(m_{\lambda_{\text{laser}}})$ is here calculated using Eq. (7.5) by considering the effective particle temperature $T_{\text{eff}}(t)$ obtained from delayed LIE measurements and not necessarily the prompt effective temperature T_{eff}^0 , results are illustrated in Fig. 7.12(b). The effective temperature is expected to decrease with time. Between 60 and 100 ns, temperature decay becomes smoother and the estimation of the decreasing trend can be affected by the low S/N ratio of signals. It should be reminded that from Eq. (7.5), the correct estimation of $E(m_{\lambda_{\text{laser}}})$ corresponds to T_{eff}^0 since the cooling effect can only be neglected during the LII process at prompt times. Therefore, results at Fig. 7.12(b) do not indicate that $E(m_{\lambda_{\text{laser}}})$ evolves with time. On the contrary, this figure illustrates the errors in the estimation of $E(m_{\lambda_{\text{laser}}})$ when effective temperature $T_{\text{eff}}(t)$ at delayed times is considered instead that T_{eff}^0 . In other words, the evolution shows the validity of assuming negligible thermal losses for delayed time, with an error under 10 % with the averaged value represented in the black dashed line (0.333).

On the one side, to avoid parasitic signals, results at prompt could not always be applied, and delayed measurements should be preferred. On the other side, considering delayed measurements may induce a bias on the estimation of $E(m_{\lambda_{\text{laser}}})$ since the cooling process is no longer negligible. In the case of the studied carbon black nanoparticles, and for the given fluence and wavelengths, it appeared that there were no parasitic signals detected during the prompt phase.

Therefore, the value of $E(m_{\lambda_{\text{laser}}}) = 0.35$ was maintained for these carbon black nanoparticles. Considering results at $t = 60$ and 100 ns, the value of 0.32 is obtained for $E(m_{\lambda_{\text{laser}}})$. These values are in good agreement with results from literature [358].

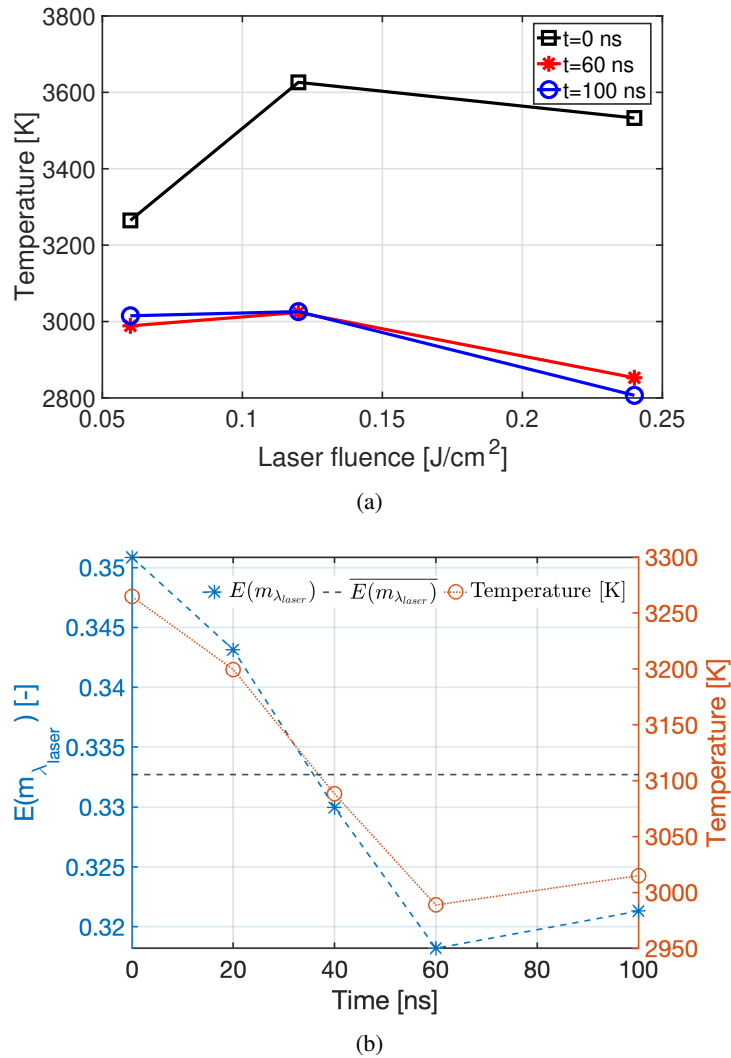


Figure 7.12. (a) Effective temperature as a function of laser fluence from LIE of carbon black nanoparticles at three acquisition times ($t=0$ ns, 60 ns, and 100 ns). The observed reduction at $F = 0.23$ J/cm² appears to be due to the sublimation effect. (b) Estimation of $E(m_{\lambda_{\text{laser}}})$ when using the effective temperature calculated at a given time t from LIE of carbon black nanoparticles for $F = 0.06$ J/cm², where the plateau regime does not seem to be reached yet. The blue dashed lines are for the $E(m_{\lambda_{\text{laser}}})$ obtained at each instant (left axis), black dashed line is the average for all instants (left axis), and the red dotted line for the temperature considered for the calculation (right axis).

The same post-processing is now applied to the available measurements for high-purity TiO_2 nanoparticles under non-reactive conditions. Results are available only for two fluences: 0.19 and 0.24 J/cm^2 . The particle temperatures at $t = 0, 60,$ and 100 ns are illustrated in Fig. 7.13(a). Temporal data at 650 nm and 710 nm have been used to deduce the evolution of the particle temperature.

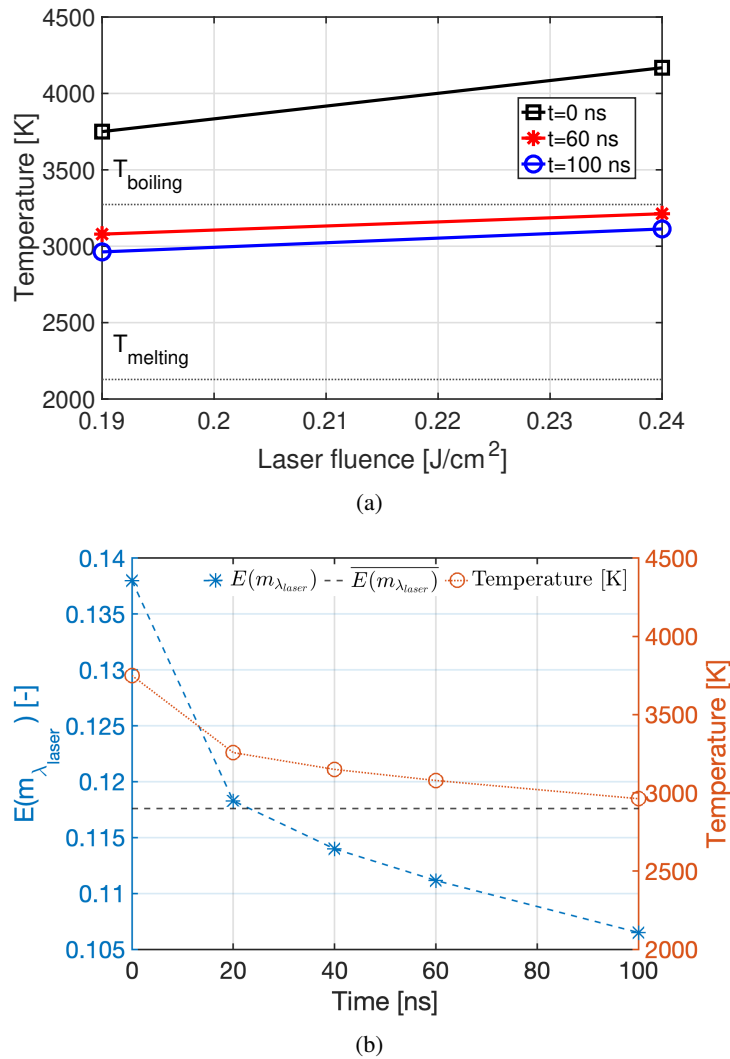


Figure 7.13. (a) Effective temperature as a function of laser fluence obtained from LIE of high-purity TiO_2 nanoparticles at three acquisition times ($t=0$ ns, 60 ns, and 100 ns). (b) Estimation of $E(m_{\lambda_{\text{laser}}})$ when using the effective temperature calculated at time t from LIE of high-purity TiO_2 nanoparticles for $F = 0.19 \text{ J}/\text{cm}^2$. The blue dashed lines represent the $E(m_{\lambda_{\text{laser}}})$ obtained at each instant (left axis), the black dashed line represents the average for all instants (left axis), and the red dotted line represents the temperature used for the calculation (right axis). Since the effective temperature is higher than the melting point of TiO_2 , $E(m_{\lambda_{\text{laser}}})$ is for liquid state particles.

It is important to note that when using LIE at the prompt, there may be parasitic LIF/PS-LIBS signals present, but they can be considered negligible at wavelengths of 650 nm and 710 nm. However, the calculated temperatures exceed the vaporization (boiling) temperature ($T=3273$ K) for both fluences, which could indicate errors resulting from assuming a constant $E(m_\lambda)$ as a function of λ . Alternatively, it is possible that the particles are in the process of vaporization. For all instances and fluence values considered, the temperature of the particles is higher than the melting temperature. Although the temperature of the particles may slightly increase with laser fluence, the results suggest that vaporization occurs at $F = 0.24$ J/cm². Therefore, the smallest laser fluence ($F = 0.19$ J/cm²) is used to calculate $E(m_{\lambda_{\text{laser}}})$ in Fig. 7.13(b). At this fluence, $E(m_{\lambda_{\text{laser}}}) \approx 0.1$, but it is important to note that this value may be underestimated if $F = 0.19$ J/cm² already falls within the regime of particle vaporization. The value of $\frac{E(m_{\lambda_{\text{laser}}})}{E(m_{\lambda_{\text{laser}}})}$ decreases over time, but the deviation is around $\pm 20\%$ with an averaged value of $E(m_{\lambda_{\text{laser}}})$. This low value of $E(m_{\lambda_{\text{laser}}})$ potentially supports the use of the Rayleigh approximation.

Finally, results for TiO₂ nanoparticles in the flame are considered. Only prompt measurements are available for different laser fluences in Fig. 7.14. The effective particle temperature is shown in Fig. 7.14(a). It should be noted that at prompt, the LIE may present parasitic signals so caution has been paid to analyze these results even if negligible effects are deduced for 650 and 710 nm.

Similar to our conclusions in Chap. 6, it seems that at $F = 0.15$ J/cm² the vaporization has not yet fully occurred, supposing no phase change during the increase of laser fluence. Therefore, available results for this fluence at different detection times are used to calculate the effective particle temperature and the corresponding $E(m_{\lambda_{\text{laser}}})$ in Fig. 7.14(b). When considering prompt measurements, $E(m_{\lambda_{\text{laser}}}) = 0.06$ is obtained. When considering delayed acquisitions, $E(m_{\lambda_{\text{laser}}}) \approx 0.025$ is found. The order of magnitude is quite reasonable compared to results in the literature (0.01 from Jellison et al. [286]).

Doubts may arise concerning the capability of a TiO₂ particle to absorb enough energy to emit a detectable signal due to even low absorption at low fluence ($F = 0.15$ J/cm², compared to high laser fluence of $F = 0.19$ J/cm² in non-reactive case). This can be attributed to the high temperature environment in flames as discussed in Sec. 6.3, which promotes the emission of LII signal despite the limited absorption of energy. Nevertheless, further investigations are necessary to comprehensively understand the absorption mechanism of TiO₂, although it exceeds the scope of this study.

Once again, it is important to remember that the values of $E(m_{\lambda_{\text{laser}}})$ obtained in this section by assuming a constant $E(m_\lambda)$ as a function of λ . Since such an assumption may be too restrictive on the basis of the results of the previous section, the case of a spectral variable $E(m_\lambda)$ will be considered in the following.

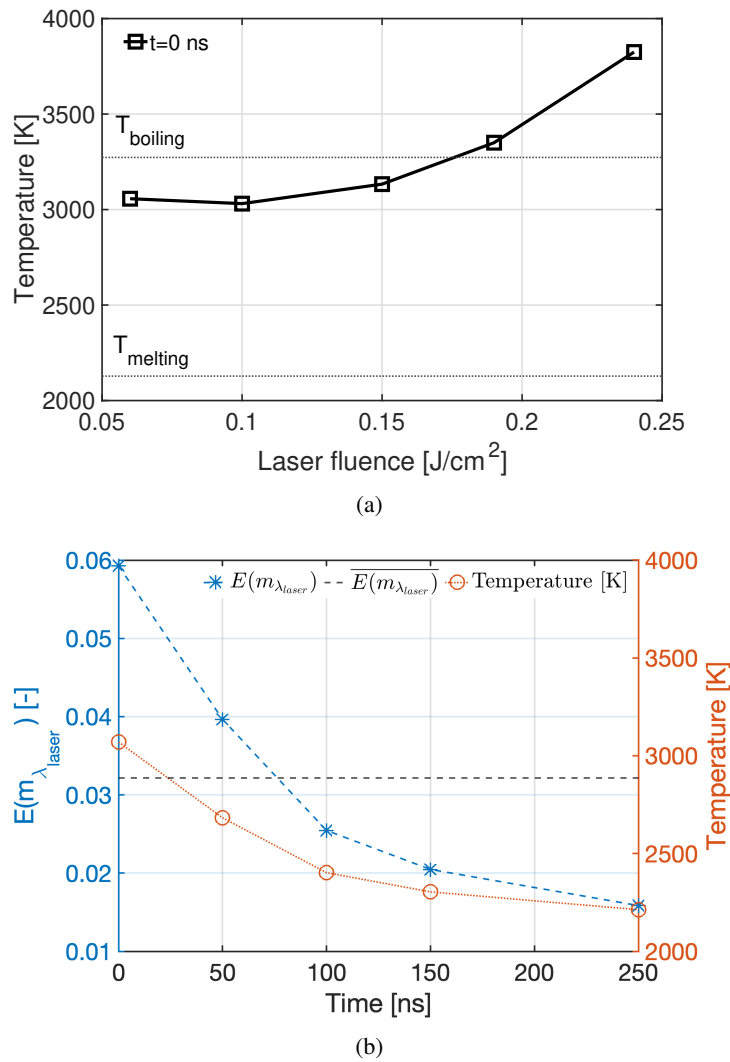


Figure 7.14. (a) Effective temperature as a function of laser fluence from LIE of flame-synthesized TiO_2 nanoparticles at prompt (HAB = 45 mm). (b) Estimation of $E(m_{\lambda_{laser}})$ when using the effective temperature calculated at a given time t from LIE of flame-synthesized TiO_2 nanoparticles for $F = 0.15 J/cm^2$ (HAB = 45 mm). The blue dashed line corresponds to $E(m_{\lambda_{laser}})$ obtained at each instant (left axis), black dashed line is the average for all instants (left axis), and the red dotted line corresponds to the temperature used for the calculation (right axis). Since the effective temperature is higher than the melting point of TiO_2 , the obtained $E(m_{\lambda_{laser}})$ is expected to correspond to liquid state particles.

7.2.2 Assuming spectrally-variable $E(m_\lambda)$

In this section, $E(m_\lambda)$ is obtained considering a spectral dependency of $E(m_\lambda)$ by following a two-step procedure.

At the first step, $E(m_{\lambda_{laser}})$ is calculated via Eq. (7.5) using T_{min} and T_{max} values obtained at Sec.

7.1.1. Results are summarized in Table 7.1. For the three kinds of particles considered in this work (carbon black, high-purity TiO₂, flame-synthesized TiO₂), the values obtained in Sec. 7.2.1 assuming constant $E(m)$ are also shown in the right column. The values from the estimated temperature using our method (T_{\min} , T_{\max} columns) are close to the values from assuming constant $E(m)$ (constant $E(m)$ column). Values for high-purity TiO₂ nanoparticles are almost a third of those found for carbon black particles. For flame-synthesized TiO₂ nanoparticles, the estimated $E(m_{\lambda_{\text{laser}}})$ is even smaller. In general, results at different gate delays do not change significantly, but the estimated temperature ranges are all above the melting point. However, results obtained at $t = 0$ and 60 ns may be influenced by the presence of parasitic signals or sublimation effects. Therefore, only results at 100 ns will be considered in the following analysis. As a consequence, it is possible that the estimated value of $E(m_{\lambda_{\text{laser}}})$ is underestimated.

Table 7.1. T_{\min} and T_{\max} and corresponding $E(m)$ at 355 nm ($= E(m_{\lambda_{\text{laser}}})$) at three acquisition delay times for carbon black, high-purity TiO₂ and flame-generated TiO₂ nanoparticles. When the maximum estimated temperature is higher than the sublimation (or boiling) temperature, the sublimation (or boiling) temperature was selected for the calculation.

	Fluence	time		T_{\min}	T_{\max}	constant $E(m)$
Carbon black	$F = 0.06 \text{ J/cm}^2$	0 ns	T [K]	2985	3886	3300
			$E(m)$	0.3177	0.4244	0.35
		60 ns	T [K]	2761	3236	2990
			$E(m)$	0.2912	0.3475	0.319
		100 ns	T [K]	2850	3255	3010
			$E(m)$	0.3018	0.3496	0.321
High-purity TiO ₂	$F = 0.19 \text{ J/cm}^2$	0 ns	T [K]	2693	3273 (7985)	3781
			$E(m)$	0.0956	0.1189	0.1392
		60 ns	T [K]	2967	3273(3324)	3062
			$E(m)$	0.1066	0.1189	0.115
		100 ns	T [K]	2772	3303	2886
			$E(m)$	0.0988	0.1189	0.1034
Flame-synthesized TiO ₂ (HAB =45 mm)	$F = 0.15 \text{ J/cm}^2$	0 ns	T	2928	3293	3133
			$E(m)$	0.052	0.069	0.062
		50 ns	T [K]	2571	2863	2706
			$E(m)$	0.0339	0.048	0.0408
		100 ns	T [K]	2274	2498	2435
			$E(m)$	0.018	0.03	0.025

At the second step, $E(m_\lambda)$ is calculated from Eq. (7.6) once $\varepsilon^*(\lambda_{\text{laser}})$ is given. Unfortunately, this quantity is not known since our acquisition system is not able to detect signal at the excitation wavelength $\lambda_{\text{laser}}=355$ nm. In the following, to face this problem, the absorption function will be calculated from:

$$E(m_\lambda) = \frac{E(m_\lambda)}{E(m_{\lambda_{\text{ref}}})} \frac{E(m_{\lambda_{\text{ref}}})}{E(m_{\lambda_{450}})} \frac{E(m_{\lambda_{450}})}{E(m_{\lambda_{\text{laser}}})} E(m_{\lambda_{\text{laser}}}) = \frac{\varepsilon^*(\lambda)}{\varepsilon^*(\lambda_{450})} \frac{E(m_{\lambda_{450}})}{E(m_{\lambda_{\text{laser}}})} E(m_{\lambda_{\text{laser}}}) \quad (7.7)$$

The ratio $\frac{E(m_{\lambda_{450}})}{E(m_{\lambda_{\text{laser}}})}$ is estimated with two different methods:

Linear extrapolation Here, a linear extrapolation is considered to evaluate $\frac{E(m_{\lambda_{450}})}{E(m_{\lambda_{\text{laser}}})}$ using the signal from the spectrum at $\lambda = 431$ and 500 nm:

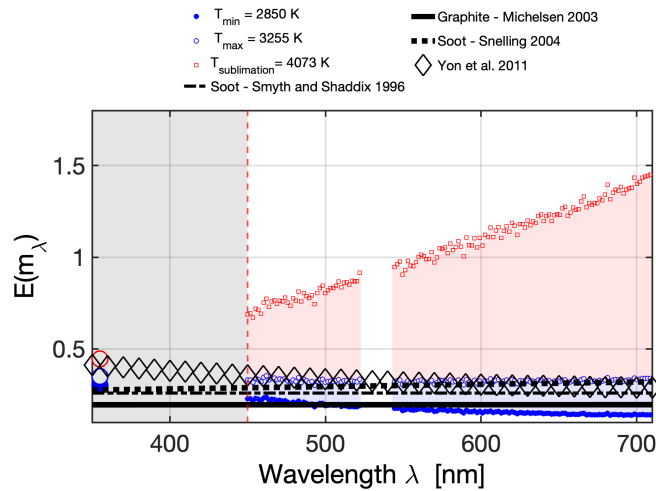
$$\frac{E(m_{\lambda_{450}})}{E(m_{\lambda_{\text{laser}}})} = 1 + \frac{m_{431,500}}{E(m_{\lambda_{\text{laser}}})} (450 - \lambda_{\text{laser}}) \quad (7.8)$$

with:

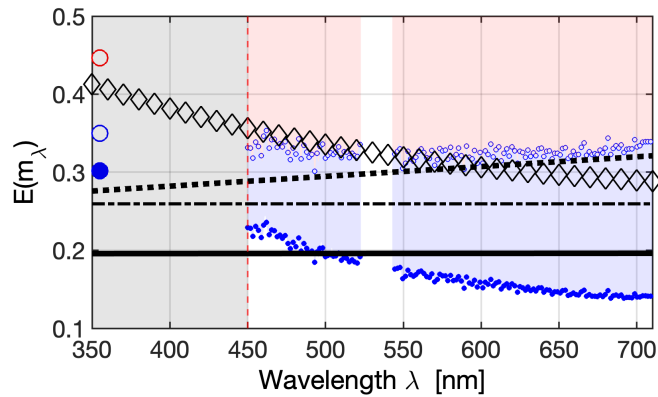
$$m_{431,500} = \overline{\nabla \varepsilon^*(\lambda)}, \quad \lambda \in [431, 500] \quad (7.9)$$

where ∇ is gradient, $\varepsilon^*(\lambda) = \frac{E(m_\lambda)}{E(m_{\lambda_{\text{ref}}})}$.

The absolute value of $E(m_\lambda)$ for the carbon black particle is shown in Fig. 7.15. The estimated blue zone retrieves well the results from literature [364, 25, 303].



(a)



(b) Zoom

Figure 7.15. (a) $E(m_\lambda)$ for carbon black nanoparticles from LIE at $F = 0.06 \text{ J/cm}^2$ and 100 ns from prompt. Results are compared to literature data [364, 25, 303]. A linear extrapolation is considered between $E(m_{\lambda_{\text{laser}}})$ and $E(m_{\lambda_{450}})$. (b) Zoom between 0.1 - 0.5.

The estimated $E(m_\lambda)$ for high purity TiO_2 nanoparticles is shown in Fig. 7.16 in log scale. The estimated values of $E(m_\lambda)$ are much smaller than that of carbon particles, but they are higher than the results from literature for TiO_2 . Indeed, the possible region approaches results found in De Iuliis [214], which are the highest among different values found in the literature.

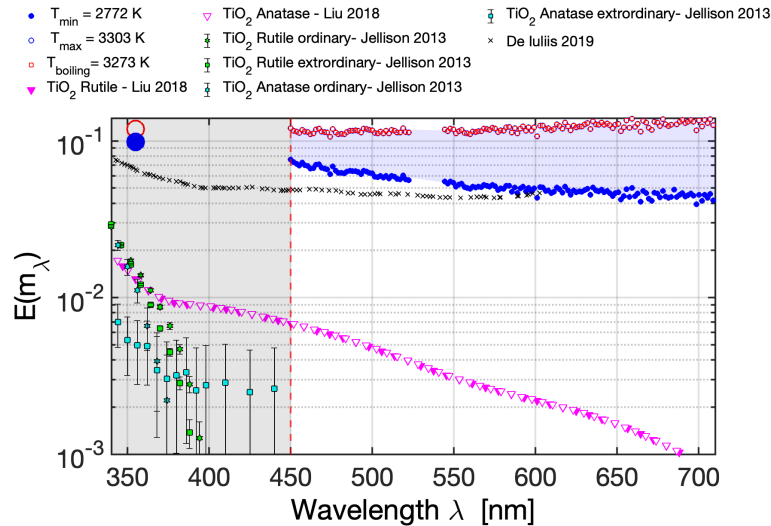


Figure 7.16. $E(m_\lambda)$ for high-purity TiO_2 nanoparticles from LIE at $F = 0.19 \text{ J/cm}^2$ and 100 ns from prompt. Results are compared to literature data [285, 286, 214]. A linear extrapolation is considered between $E(m_{\lambda_{\text{laser}}})$ and $E(m_{\lambda_{450}})$. Since the effective temperature is higher than the melting point of TiO_2 , our $E(m_\lambda)$ corresponds to liquid state.

The results on $E(m_\lambda)$ for flame-generated TiO_2 nanoparticles are presented in Fig. 7.17 in log scale. For this case, the blue zone of possible $E(m_\lambda)$ is located between the experimental data of De Iullis et al. [214] and Liu et al. [285]; the values obtained can therefore be considered a reasonable level of estimation. However, once again, our estimation is based on the liquid-state nanoparticles and the corresponding discrepancy should be carefully considered. By looking at the red zone, it is possible to conclude that the results strongly depend on the estimated value of the effective temperature and that a correct quantification of this variable is needed.

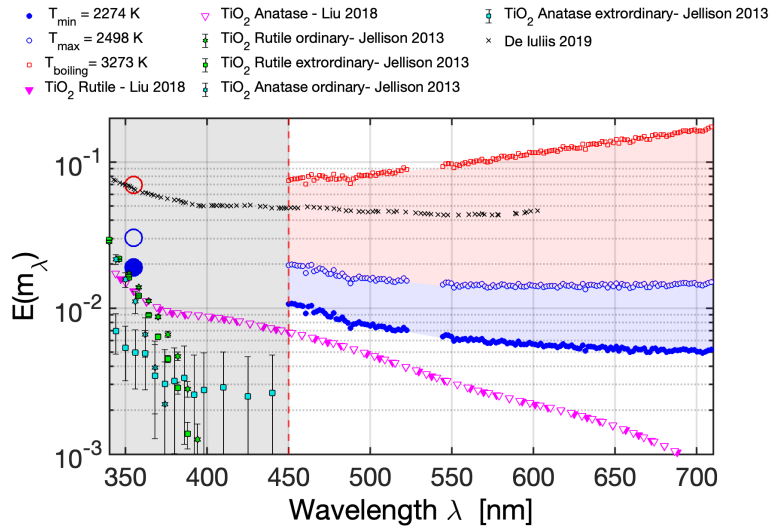


Figure 7.17. $E(m_\lambda)$ for flame-synthesized TiO_2 nanoparticles from LIE at $F = 0.15 \text{ J/cm}^2$, delayed at 100 ns from prompt. Results are compared to literature data for solid TiO_2 [285, 286, 214]. A linear extrapolation is considered between $E(m_{\lambda_{\text{laser}}})$ and $E(m_{\lambda_{450}})$. Since the effective temperature is higher than the melting point of TiO_2 , our $E(m_\lambda)$ corresponds to liquid state.

However, here a linear behavior of $E(m_\lambda)$ has been assumed between 350 and 450 nm. Looking at the literature data, it is observed that the absorption function for TiO_2 is usually not linearly proportional to the wavelength when considering λ between 350 and 450 nm. In the following, a different reconstruction is then considered for $\frac{E(m_{\lambda_{450}})}{E(m_{\lambda_{\text{laser}}})}$.

Based on the literature A different estimation for quantity $\frac{E(m_{\lambda_{450}})}{E(m_{\lambda_{\text{laser}}})}$ is proposed here by extracting it from experimental values for three different experimental databases: 0.7396 for De Iullis [214], 0.4707 for Jellison [286] and 0.52 for Liu [285]. The estimated $E(m_\lambda)$ for high purity TiO_2 nanoparticles taking the $\frac{E(m_{\lambda_{450}})}{E(m_{\lambda_{\text{laser}}})}$ from literature are shown in Fig. 7.18(a, c, e) (left column). In all cases, quite high values are obtained compared to the literature. When using the estimation of $\frac{E(m_{\lambda_{450}})}{E(m_{\lambda_{\text{laser}}})}$ from the data due to Liu et al. [285] and Jellison et al. [286], the blue region recovers the results obtained by De Iullis [214].

Results for flame-generated TiO_2 nanoparticles are visualized in Fig. 7.18(b, d, f) (right column). The absorption function of TiO_2 is smaller than the carbon black nanoparticles for both high-purity sol-gel TiO_2 and flame-synthesized TiO_2 . The developed strategy seems to provide a reasonable estimation of $E(m_\lambda)$ for TiO_2 nanoparticles, needed for the quantification of the LII signal in terms of nanoparticles volume fraction.

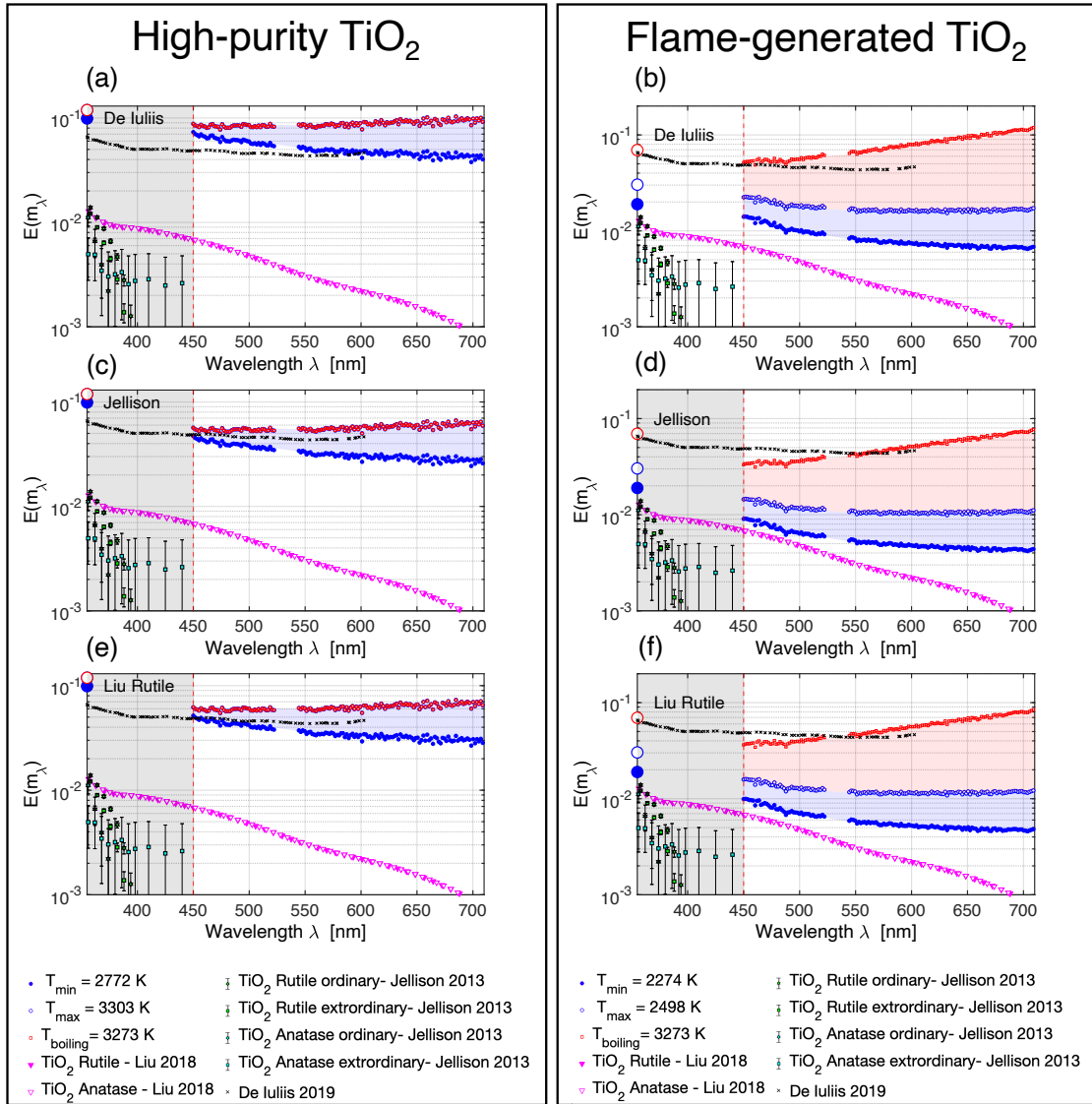


Figure 7.18. (a), (c), (e) $E(m_\lambda)$ of high-purity TiO_2 nanoparticles from LIE at $F = 0.19 \text{ J/cm}^2$ and 100 ns from prompt. (b), (d), (f) $E(m_\lambda)$ of flame-synthesized TiO_2 nanoparticles from LIE at $F = 0.15 \text{ J/cm}^2$ and 100 ns from prompt. Results are compared to literature data [285, 286, 214].

The quantity $\frac{E(m_{\lambda_{450}})}{E(m_{\lambda_{\text{laser}}})}$ is extrapolated from available experimental data from De Iuliis et al. [214] (a, b), Jellison et al. [286] (c,d), and Liu et al. [285] (e,f).

7.3 Conclusion

In this chapter, a new method for deriving the evolution of the absorption function $E(m_\lambda)$ is presented, based on the spectral emission of LII of nanoparticles. The assumption that $E(m_\lambda) \approx E(m_{\lambda+\Delta\lambda})$ allows for an initial estimate of possible effective temperature values, from which the spectral shape of $E(m_\lambda)$ can be derived.

A strategy to estimate the absolute value of $E(m_\lambda)$ is then provided. First, the $E(m_{\lambda_{\text{laser}}})$ at the laser excitation is calculated, assuming that the contributions of conduction and radiation processes to the particle temperature at prompt are negligible. In order to avoid parasitic signals, delayed LIE spectra are considered, as these spurious signals can affect the estimation of the particle temperature at prompt, and consequently underestimate $E(m_{\lambda_{\text{laser}}})$. The absolute value of $E(m_\lambda)$ is then calculated from information on the spectral dependence of $E(m_\lambda)$.

Despite some uncertainties that have been discussed, the method used to estimate $E(m_\lambda)$ provides a reasonable initial estimate that is consistent with existing literature results for carbon black and TiO_2 nanoparticles. It is noteworthy that the flame-synthesized TiO_2 nanoparticles exhibit a considerably lower $E(m_\lambda)$ than their high-purity TiO_2 counterparts. This difference could be attributed to differences in the synthesis processes (sol-gel vs. flame-synthesis), leading to variations in crystal phase and impurities originating from the carbonaceous matter in the precursor. Obtaining laser-induced incandescence (LII) signals in a non-reactive cell is more challenging than in a flame, as it necessitates a higher energy input to raise the particle temperature to a measurable level. Consequently, caution should be exercised while comparing results obtained using these two systems. If the particles in two systems exhibit identical optical properties, the dependence of the LII process on ambient temperature and particle size becomes more significant.

In future work, it would be beneficial to design the LII system to cover the same spectral range of laser excitation and detection, in order to avoid extrapolation that might lead to errors. While this was not possible with the TiO_2 nanoparticles used in this study, as their absorption is preferred in the short wavelength UV range, future research should consider visible range excitation within the spectral range for detection.

In this study, the boiling/sublimation temperature is considered the maximum temperature that particles can reach during the LII process due to laser heating. However, it is important to note that the peak nanoparticle temperature may exceed the bulk material's boiling/sublimation temperature due to superheating. This occurs because the laser pulse occurs over a much shorter timescale than that of boiling/sublimation, causing energy to accumulate in the nanoparticle, resulting in superheating. Depending on the laser pulse duration, this can lead to a superheat of several hundred Kelvin. It is crucial to consider this phenomenon in future work to capture the phase change due to laser irradiation using an in-situ method as shown in [372].

At the same time, one should note that this potential liquid-phase nanoparticles could cause the nanoparticles to be outside the Rayleigh/RDG-FA regime, making the accuracy of $E(m_\lambda)$ questionable and rendering the particle emission cross-section sensitive to the geometry as well, as discussed in Sec. 4.3.4. Therefore, further investigation into the liquid-state nanoparticles during the LII process is necessary to obtain more precise results.

Nevertheless, the feasibility of the approach has been shown, and results from flame-generated

TiO₂ nanoparticles will be considered in the next chapter to propose the first preliminary characterization of TiO₂ production in the YDB burner.

Chapter 8

On the dependence of absorption function $E(m_\lambda)$ and effective temperature T_{eff} in analyzing TiO_2 nanoparticles volume fraction in flame synthesis

Although it is common to interpret the LII intensity directly as nanoparticle volume fraction [373, 374], the volume fraction f_v is actually given by:

$$f_v = \eta_{\text{CAL}} S_{\text{LII}}(\lambda_{\text{em}}, T_{\text{eff}}) E(m_{\lambda_{\text{em}}})^{-1} \left(\frac{48\pi^2 hc^2}{\lambda_{\text{em}}^6} \right)^{-1} \left[\exp \left(\frac{hc}{\lambda_{\text{em}} k_B T_{\text{eff}}} \right) - 1 \right]. \quad (8.1)$$

Therefore, f_v is a function of the LII signal S_{LII} , of the irradiated particles temperature T_{eff} , the emission wavelength λ_{em} , and the absorption function $E(m_\lambda)$. η_{CAL} is a calibration factor that accounts for the effects of laser sheet thickness, detector gain, and other geometrical and spectral factors of the detection system [375]. Therefore, information on T_{eff} as well as $E(m_{\lambda_{\text{em}}})$ have to be known at each spatial position of the flame to correctly calculate the spatial evolution of f_v from the LII signal. The spatial evolution of the normalized volume fraction f_v^* can be obtained as:

$$f_v^*(z) = \frac{f_v(z)}{f_v(z_0)} = \frac{S_{\text{LII}}(\lambda_{\text{em}}, T_{\text{eff}}(z)) E(m_{\lambda_{\text{em}}}, z_0)}{S_{\text{LII}}(\lambda_{\text{em}}, T_{\text{eff}}(z_0)) E(m_{\lambda_{\text{em}}}, z)} \frac{\left[\exp \left(\frac{hc}{\lambda_{\text{em}} k_B T_{\text{eff}}(z)} \right) - 1 \right]}{\left[\exp \left(\frac{hc}{\lambda_{\text{em}} k_B T_{\text{eff}}(z_0)} \right) - 1 \right]} \quad (8.2)$$

where volume fraction $f_v(z)$ at position z (flame height direction = HAB) has been normalized with volume fraction $f_v(z_0)$ at position z_0 . In this work, the calibration process was not conducted, therefore, experimental measurements can be post-processed to obtain information on f_v^* in the following. For this, a numerical simulation of the flame has also been performed to provide complementary information on the gaseous phase. The experimental set-up for the 2D

measurement will be discussed in Sec. 8.1.1, and the numerical set-up in Sec. 8.1.2. Then, three different cases will be considered:

1. Spatially-uniform effective temperature and absorption function (Sec. 8.2).
2. Spatially-uniform absorption function but spatially non-uniform effective temperature (Sec. 8.3).
3. Spatially non-uniform effective temperature and spatially non-uniform absorption function (Sec. 8.4).

In the following, the spatial evolution of f_v^* is provided along the flame centerline and compared to numerical results to provide a first qualitative comparison between experiments and simulation of TiO_2 nanoparticle production in a laminar coflow Yale diffusion TTIP/ Ar/H_2 flame.

8.1 Set-up

8.1.1 Experimental set-up for 2D spatial distribution

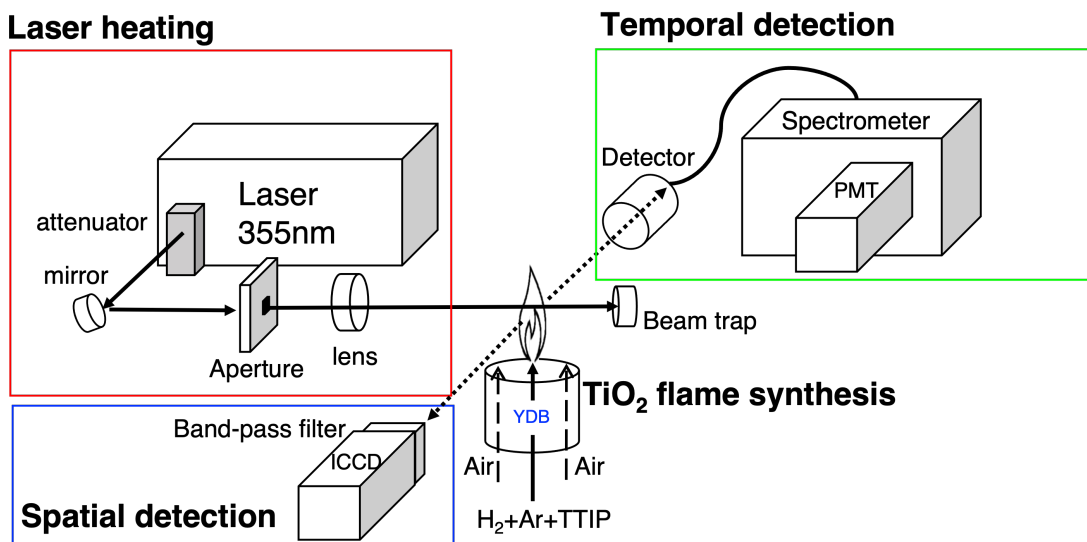


Figure 8.1. Schematic of the LII set-up for TiO_2 nanoparticles in flame synthesis. The excitation and temporal detection parts are identical to those presented in Part II. An additional ICCD camera is used to obtain spatial distribution information.

Figure 8.1 presents the experimental setup used in Chapters 6 and 7, which has been modified to include an intensified camera (Princeton Instruments, PI-MAX 4, 1024i) equipped with a bandpass filter centered at $640 \text{ nm} \pm 7 \text{ nm}$ (Edmund optics, 86995). The camera is placed at the opposite side of the telescope detector and is used to study the spatial distribution of the laser-induced emission (LIE). In contrast to the previous setup, the spectrometer is used here only for temporal detection via photomultiplier (PMT, HAMAMATSU, R2257), with the center wavelength being changed through the grating drive system of the spectrometer. As a result, spectral information is no longer available.

The height of the burner is controlled by a hydraulic crank with an accuracy of 0.01 mm using attached vernier calipers. Laser-induced emission signals are recorded at a two-dimensional grid with a width of 8 mm and a height of 1 mm, covering the homogeneous laser top-hat (height 0.9 mm in Fig. 5.3). The detection timing is synchronized with the laser peak, and measurements are taken at prompt, 50, 100, and 150 ns after the peak signal with gate width of 20 ns. Measurements at different flame heights (every 2 mm) are performed by moving the burner holder in the z-direction (HAB). Signal intensity at $\text{HAB} < 10 \text{ mm}$ was too low to be properly detected.

Simultaneously with the camera acquisition, the temporal profile at $640 \pm 10 \text{ nm}$ is recorded via the PMT. Additional temporal profiles are collected at $\text{HAB} = 30, 45, \text{ and } 60 \text{ mm}$ for two wavelengths ($650 \pm 10 \text{ nm}$ and $710 \pm 10 \text{ nm}$). The background signal with flame emission is measured without a laser pulse and then subtracted for each measurement. The burner operating condition is described in Sec. 6.1.3. A target laser fluence of $F = 0.15 \text{ J/cm}^2$ is selected to avoid evident vaporization (with sharp features from PS-LIBS emission) during the LII process (Chap. 6), while maintaining a relatively high signal-to-noise ratio.

Consistency between PMT and camera To confirm the temporal and spectral consistency of the two detection devices, the results from the camera and PMT are compared at $\lambda_{\text{em}} = 640 \text{ nm}$ detection wavelength at the flame centerline for three HABs at different time delays. The comparison is shown in Fig. 8.2. The temporal signals are first integrated for the same gate duration (20 ns) and then normalized by the maximum signal. For the camera, the signal intensities of all pixels of the equivalent detection volume are summed. The overall trend in the normalized signals is in good agreement between the two detection devices.

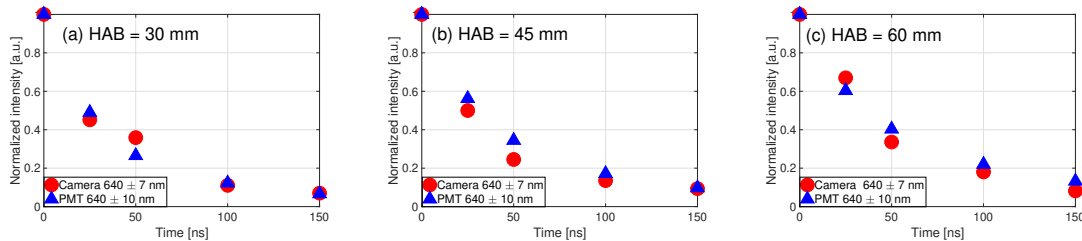


Figure 8.2. Comparison between data from two different detection devices for $\lambda_{\text{em}} = 640 \text{ nm}$: camera (spatial, red round symbol) and PMT (temporal, blue triangle symbol). Measurements were done along the flame centerline at three flame heights.

Variability of results The variability of PMT and camera data is shown in Fig. 8.3 along the flame centerline based on 2 and 7 different measurement campaigns, respectively. The observed significant variability is likely due to the unsteady production of TiO_2 in the flame, indicating the need to improve the experimental burner and injection system in the future. Despite this variability, the intensity and spatial evolution of the signal are reproducible, with a standard deviation of approximately 30 % for PMT and 20 % for the camera. The standard deviation is calculated based on the peak values for temporal detection (PMT) and spatial average of target volume for spatial detection (camera) of all measurements taken for each set of single shots.

To investigate the spatial evolution of the LII signal along the centerline, the average of these curves is considered. It is worth noting that the signal voltage obtained from PMT in Fig. 8.3a is 5 to 10 times lower than the conventional signal level of carbon black nanoparticles detected with the same equipment (see Chap. 5), highlighting the low S/N ratio in the measurement of flame-synthesized TiO_2 nanoparticles.

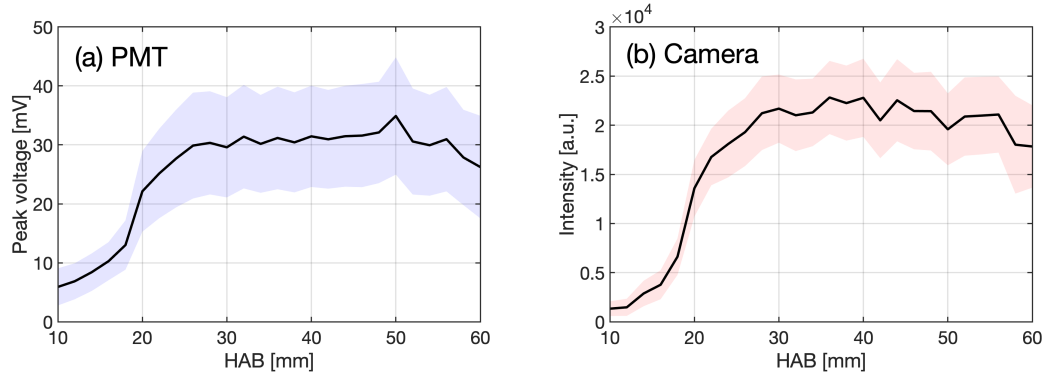


Figure 8.3. Variability of LII signal intensity from (a) 7 sets of PMT and (b) 2 sets of camera measurements at prompt along the flame centerline. Standard deviations (σ) of each measurement are represented in colored area, the averaged values are represented in black lines.

LII nature of flame-synthesized TiO_2 nanoparticles LIE Before analyzing the emission, the incandescence nature of LIE signals is checked for three HABs. As done in Chap. 5 and 6, the temporal evolution of ΔT^{-1} is plotted for two wavelengths (650 and 710 nm) in Fig. 8.4. These wavelength values were retained from the analysis at Chap. 6, since they were proven to be only slightly affected by parasitic signals even at prompt. Since the signals are superposed, the incandescent nature of the signal for 650 and 710 nm is confirmed. Therefore, these two wavelengths will be used in the following section to estimate the effective particle temperature since they present less risk of contamination by spurious signals from LIF and/or PS-LIBS.

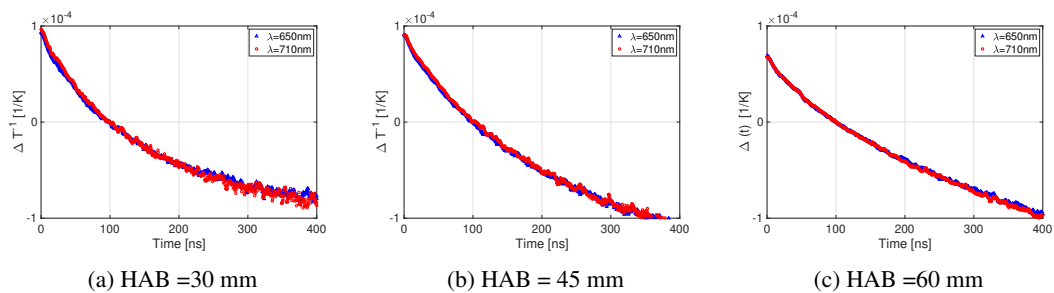


Figure 8.4. Evolution of ΔT^{-1} under laser fluence at $F = 0.15 \text{ J/cm}^2$ of flame-generated TiO_2 nanoparticles for two wavelengths at (a) HAB = 30 mm, (b) HAB = 45 mm, (c) HAB = 60 mm.

Flame brightness The natural emission of particle synthesizing flame is depicted in Fig. 8.5, showing the flame brightness (without laser) as evaluated by summing the RGB intensity of the image captured using a CANON camera along the centerline (left image, red dashed line), while the intensity is presented in the right image. It can be observed that the brightness increases abstractly until $\text{HAB} = 30$ mm, followed by a gradual decline. The flame emissions arise from different sources, including thermal emission from hot particles and electronically excited species, as well as H_2O recombination vibrations and OH radicals to some extent, as discussed in [376]. The abrupt increase in brightness may be attributed to the change of particle state, and it is plausible to consider a clear demarcation in emitted intensity due to varying optical properties when particles undergo melting and solidification, as demonstrated in the case of Al_2O_3 [319]. Hence, for future work, it is imperative to study the development of TiO_2 's optical properties during the melting and/or solidification process.

In principle, for particles in the Rayleigh limit, the intensity should depend on the particle volume fraction, regardless of size. However, the validity of this assumption along the flame height is questionable due to not only the phase change but also certain particle growth mechanisms such as aggregation, sintering, coalescence, or agglomeration, which are detailed in Chap. 2. Future investigations will be needed to determine the specific point at which particles grow to a size that exhibits radiative properties typical of TiO_2 , or whether they exhibit entirely unanticipated behavior.

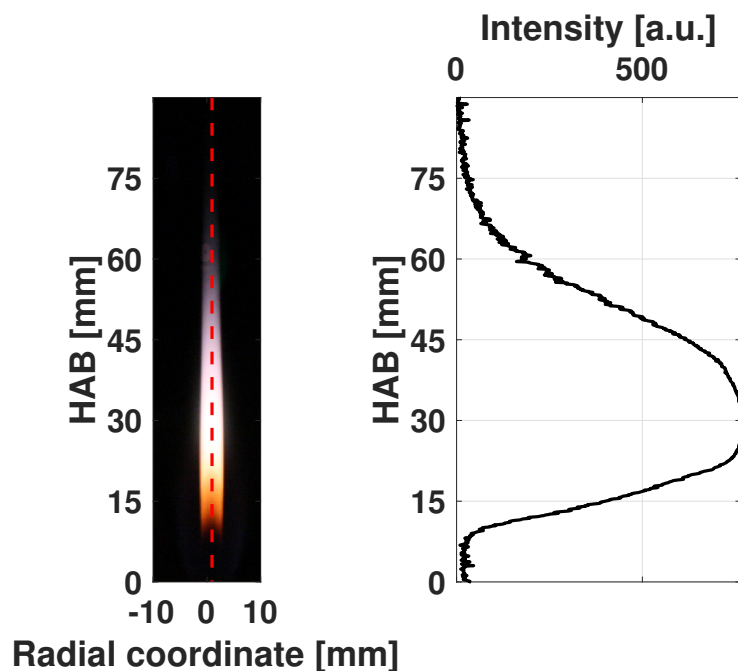
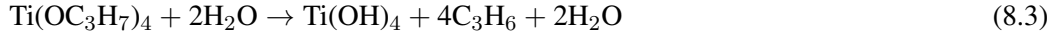


Figure 8.5. Intensity of flame brightness (right) at the centerline along the flame height (left).

8.1.2 Numerical simulation

Numerical simulation will be used to investigate the production of TiO_2 nanoparticles in the same flame configuration. The coflow hydrogen flame in the YDB burner has been simulated using the LaminarSMOKE solver [377] by considering an axial plane ($0 < r < 38$ mm and $-2.5 < z < 120$ mm) imposing axis-symmetric. The gas phase is described using the Syngas mechanism developed by the CRECK team [378]. It accounts for 21 species and 62 reactions. To this, a global reaction for the conversion of TTIP into $\text{Ti}(\text{OH})_4$ has been added:



The reaction parameters correspond to a newly developed model [351]. $\text{Ti}(\text{OH})_4$ is considered to be the precursor for the first TiO_2 nuclei. Nucleation is modeled as the result of the collision of two $\text{Ti}(\text{OH})_4$ nuclei [142]. For TiO_2 nanoparticles, only nucleation, coagulation, and sintering processes are considered. TiO_2 solid phase is accounted with a monodisperse three-equation model [379], based on the transport of mass fraction, number density, and total surface. Descriptions for coagulation and sintering models can be found in [380] and [381], respectively. Thermophoresis is taken into account using the thermophoresis velocity $v_T = -C_{\text{th}} \frac{\nu}{T} \nabla T$ with $C_{\text{th}} = 0.554$ [382] and the diffusivity is calculated using the collision diameter [380].

The grid accounts for 14000 cells, mainly concentrated in the flame zone (spatial resolution is approximately 0.18 mm) using a double stretching factor along the axis and in the radial direction. The boundary conditions replicate the experimental operating conditions (see Table 6.1).

A qualitative comparison of the flame structure is presented in Fig. 8.6. On the first column from the left, the flame luminosity (a) is shown. On the right side, the results of numerical simulation include the volume fraction of TiO_2 , the mass fraction of OH (b), the temperature field (c), and the mean primary particle diameter (d). The outer reaction zone represented with OH mass fraction shows a good agreement with colorless hydrogen flame in the experiment (Fig. 8.7). The maximum volume fraction of TiO_2 nanoparticles in the numerical simulation corresponds to the highest luminosity of the experimental flame. In the following, the point z_0 (in Eq. (8.2)) corresponds to the centerline of the flame at $\text{HAB} \approx 30$ mm, will be used to normalize the volume fraction signal. One should note that the maximum luminosity appearing in the experimental result includes the effect of both the volume fraction and the local flame temperature. This possibly explains why a non-zero volume fraction is predicted numerically for $\text{HAB} > 75$ mm, whereas no luminosity is experimentally observed for such heights where temperature decreases. As can be seen from Fig. 8.6(d), the primary particle diameter grows with flame height as a result of condensation and aggregation to occur due to collisions.

Based on the temperature readings shown in Fig. 8.6, it can be inferred that the TiO_2 particles may have turned into a liquid state at some point during the flame. It is worth noting that the melting point of nanomaterials can be significantly lower than that of bulk material due to their increased surface energy [383, 384]. As a result, changes in the absorption and emission properties of the particles in the flame may occur abruptly due to the phase change, even without the use of a laser. To gain more knowledge about the spectroscopic characteristics of molten TiO_2 , a LOSA measurement similar to those conducted in previous studies [23, 372] would provide valuable insights.

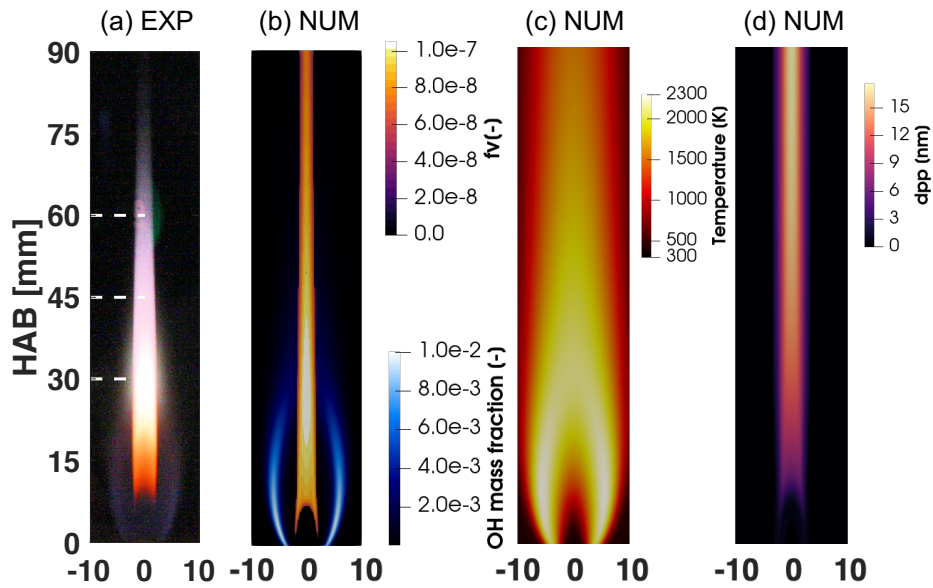


Figure 8.6. Comparison between flame luminosity obtained with a CANON camera (a) and numerical simulation (b,c,d). For the result of simulation, the volume fraction of TiO_2 is expressed in a yellow-red color bar, with the mass fraction of OH expressed in blue color in (b), temperature (c), and size of primary particle (d) are also shown.

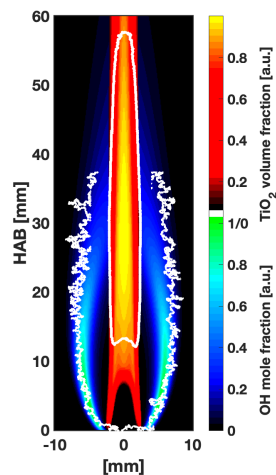


Figure 8.7. Comparison between experimental flame luminosity outline (white line for luminous cylindrical zone and surrounding transparent flame) and numerical OH mole fraction (blue colormap) and TiO_2 volume fraction (red-yellow colormap). The boundary of the experimental flame luminosity is taken from 30 % of the highest intensity for the middle cylindrical zone. For the colorless surrounding part, the image has been split into RGB colormap and only the blue component has been considered for defining the boundary. Numerical values are normalized by each maximum value.

8.2 Spatially-constant effective temperature and $E(m_{\lambda_{\text{em}}})$

In this section, we consider the simplest case to extract information on f_v^* from Eq. (8.2) by assuming a spatially-constant effective temperature ($T_{\text{eff}}(z) = T_{\text{eff}}(z_0) = T_{\text{eff}}$) and spatially-constant absorption function ($E(m_{\lambda_{\text{em}}}, z) = E(m_{\lambda_{\text{em}}}, z_0) = E(m_{\lambda_{\text{em}}})$). The normalized volume fraction f_v^* then reads as:

$$f_v^*(z) = \frac{f_v(z)}{f_v(z_0)} = \frac{S_{LII}(\lambda_{\text{em}}, T_{\text{eff}}(z))}{S_{LII}(\lambda_{\text{em}}, T_{\text{eff}}(z_0))}. \quad (8.4)$$

In this case, the post-processing of the LIE signals to obtain f_v^* is quite straightforward since they could be considered as directly proportional to f_v^* , once it has been verified that the signal only accounts for LII.

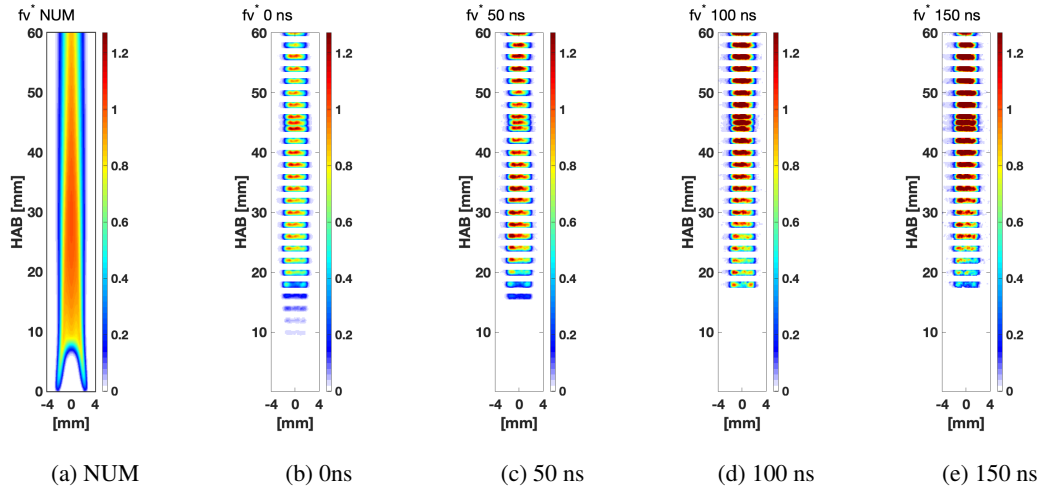


Figure 8.8. Spatial distribution of f_v^* from (a) numerical simulation, from LIE signals (b-e) assuming spatially-uniform absorption function and effective temperature. Measurements at (b) prompt and delayed time at (c) 50, (d) 100 and (e) 150 ns are considered for Eq. (8.4).

The experimental 2D spatial distribution of f_v^* along the flame height are shown in Fig. 8.8 by considering LIE signals at different time delays (0, 50, 100, and 150 ns). The laser arrives from the left side (-4 mm) of the image, showing the effect of attenuation on the right side (higher signal on the left side). The field of f_v^* of numerical simulation is added on the left (Fig. 8.8(a)). Two different fronts of f_v^* are observed close to the injection and join at about $\text{HAB} \approx 10$ mm. In the experimental results, the maximum value is localized at the flame wings for $\text{HAB} < 18$ mm. For higher HABs, almost homogeneous f_v^* is observed both in experimental and numerical results. At prompt, the f_v^* increases gradually, and the same trend is shown for the 50 ns delayed case. For time-delayed acquisition ($t > 50$ ns), the f_v^* strongly increases at higher flame heights ($\text{HAB} > 30$ mm).

Figure 8.9 shows the evolution of f_v^* along the flame centerline obtained from LIE signals at different time delays. The f_v^* profiles are quite different, indicating that different spatial evolution of volume fraction will be obtained depending on the considered signal. Specifically,

by increasing the time delay, the peak position shifts farther downstream. On the one side, it has been largely discussed in the previous chapter that prompt LIE can be affected by parasitic signals (LIF and PS-LIBS). On the other side, the contribution to the LII signal from the small particles is neglected when increasing the time delay [385]. As the cooling of big particles is slower than for small particles, the incandescence emitted by the large nanoparticles dominates over incandescence from the smaller nanoparticles when considering delayed signals. As seen from the numerical results (see Fig. 8.6d), the primary particle diameter is expected to increase with HAB. Thus, the LII signal is expected to last longer at higher heights, possibly explaining the shift of the peak position towards higher heights for delayed acquisition. Therefore, the interpretation of the signal should be carefully considered: at prompt, it is possible to have interference from the non-LII components (LIF, PS-LIBS) of laser-induced emissions of TiO_2 , whereas for delayed detection times, the information of small particles can disappear. Still, at detection wavelength near 640 nm, few LIF features (Chap. 4) are observed for TiO_2 nanoparticles, and the emission spectrum at prompt does not show sharp PS-LIBS emissions for all flame heights at fluence $F = 0.15 \text{ J/cm}^2$ (see Fig. D.1 in Appendix D). Thus, it could be more reasonable to assume a particle size distribution inside the control volume as polydispersed. Since the f_v^* curves clearly change between 0 and 100 ns, we will consider the following results at prompt and at 100 ns to illustrate the possible variability of the data.

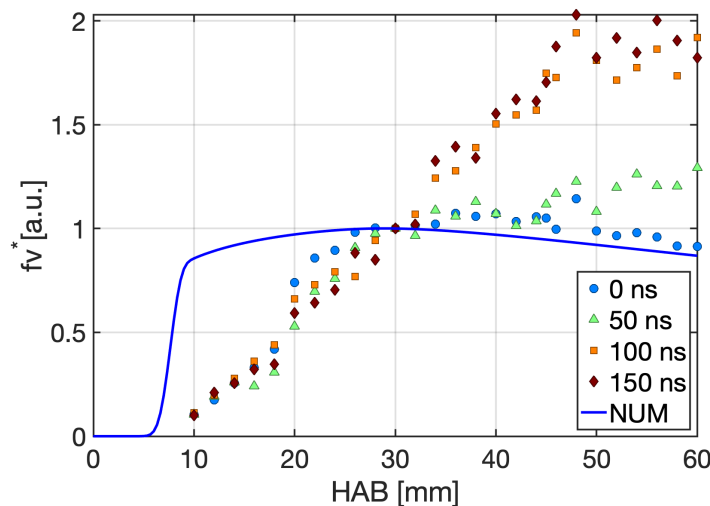


Figure 8.9. Evolution of f_v^* along the flame centerline based on S_{LII} signals at 0, 50, 100 and 150 ns. The numerical simulation result is also shown.

The f_v^* from TiO_2 volume fraction from the numerical simulation is also added to Fig. 8.9 as a blue line. The simulated profile is shifted close to the burner compared to the f_v^* profile from the experimental measurements. This seems to indicate that TiO_2 are produced too quickly in the numerical simulation. Or, it could be under a detectable incandescence signal with our experimental equipment [386]. However, before concluding, it is essential to verify the effect of the spatial evolution of the effective temperature and of the absorption function on f_v^* .

8.3 Spatially-constant $E(m_{\lambda_{\text{em}}})$ and non-uniform effective temperature

In this section, we consider an intermediate case by assuming spatially-constant absorption function ($E(m_{\lambda_{\text{em}}}, z) = E(m_{\lambda_{\text{em}}}, z_0) = E(m_{\lambda_{\text{em}}})$) but a non-uniform effective temperature ($T_{\text{eff}}(z) \neq T_{\text{eff}}(z_0)$). The normalized volume fraction then reads as:

$$f_v^*(z) = \frac{f_v(z)}{f_v(z_0)} = \frac{S_{LII}(\lambda_{\text{em}}, T_{\text{eff}}(z)) \left[\exp\left(\frac{hc}{\lambda_{\text{em}} k_B T_{\text{eff}}(z)}\right) - 1 \right]}{S_{LII}(\lambda_{\text{em}}, T_{\text{eff}}(z_0)) \left[\exp\left(\frac{hc}{\lambda_{\text{em}} k_B T_{\text{eff}}(z_0)}\right) - 1 \right]} \quad (8.5)$$

The effective temperature $T_{\text{eff}}(z)$ has then to be estimated. As already discussed in Chap. 4, $T_{\text{eff}}(z)$ can be calculated using the two-pyrometry approach (Eq. 4.16):

$$T_{\text{eff}}(z) = \frac{hc}{k_B} \left(\frac{1}{\lambda_{\text{ref}}} - \frac{1}{\lambda} \right) \cdot \left[\ln \left(C^{-1} \frac{E(m_{\lambda_{\text{ref}}})}{E(m_\lambda)} \left(\frac{\lambda}{\lambda_{\text{ref}}} \right)^6 \frac{S_{LII}(\lambda, T_{\text{eff}}(z))}{S_{LII}(\lambda_{\text{ref}}, T_{\text{eff}}(z))} \right) \right]^{-1} \quad (8.6)$$

once the LII signal is known at two wavelengths λ and λ_{ref} as well as the ratio $\varepsilon^*(\lambda) = E(m_\lambda)/E(m_{\lambda_{\text{ref}}})$. Most often, when considering soot particles, the absorption function is considered independent from the wavelength $E(m_\lambda) = E(m_{\lambda_{\text{em}}}) = E(m_{\lambda_{\text{laser}}}) = E(m)$, i.e., $\varepsilon^*(\lambda) = 1$. In this case, no knowledge of the spectral dependence of $E(m_\lambda)$ is required to calculate T_{eff} in Eq. (4.17). However, when available, information on $\varepsilon^*(\lambda)$ should be applied.

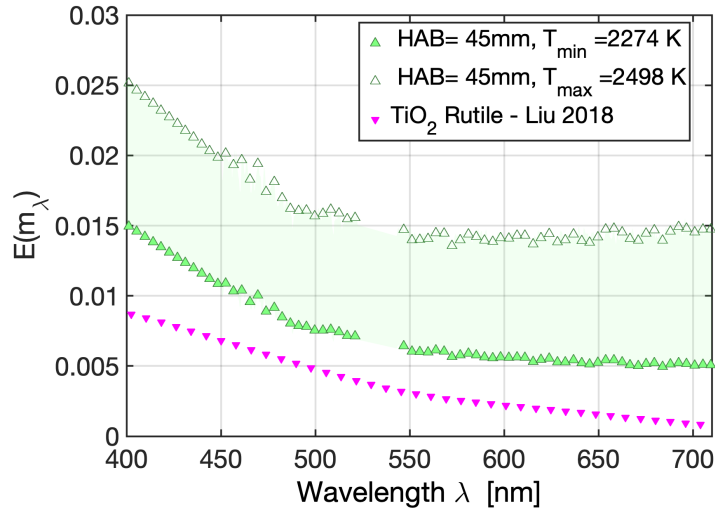


Figure 8.10. Estimated $E(m_\lambda)$ range for TiO_2 nanoparticles produced in the YDB burner. Results have been obtained in Chap. 7 using the LII spectra at HAB=45 mm under $F = 0.15 \text{ J/cm}^2$ at $t = 100 \text{ ns}$. Literature results from Liu et al. [285] are added for comparison. Note that our results are possible for liquid state nanoparticles and those of Liu et al. [285] come from solid films.

In the following, we will consider both $\varepsilon^*(\lambda) = 1$ and $\varepsilon^*(\lambda) \neq 1$ cases. For $\varepsilon^*(\lambda) \neq 1$, the absorption function $E(m_\lambda)$ obtained in Chap. 7 using the LII spectra at HAB=45 mm under

$F = 0.15 \text{ J/cm}^2$ at $t=100 \text{ ns}$ is retained here. The target $E(m_\lambda)$ is shown in Fig. 8.10, together with results from Liu et al. [285]. Note that our results are based on the liquid state nanoparticles and the results Liu et al. [285] are based on the TiO_2 film.

8.3.1 Spatial evolution of effective temperature

The effective temperature is calculated here for three HABs using the two-color pyrometry technique. For this, information from PMT at HAB= 30, 45, and 60 mm at two detection wavelengths ($\lambda = 650 \text{ nm}$ and 710 nm) are used. First, $\varepsilon^*(\lambda)=1$ case is considered, i.e., $E(m_{710 \text{ nm}})/E(m_{650 \text{ nm}})=1$ (Eq.(4.17)). The corresponding effective temperature at prompt and 100 ns is listed in Table 8.1 by considering the signals at prompt or 100 ns after the peak signal. Second, the case of $\varepsilon^*(\lambda) \neq 1$, i.e., the value of $E(m_\lambda)$ depends on λ , is considered (Eq. (8.6)). For this, the spectral dependence of $\varepsilon^*(\lambda)$ obtained in Chap. 7 is considered. Specifically, the two extreme values for $E(m_{710 \text{ nm}})/E(m_{650 \text{ nm}})$ (Table 8.1) are considered to calculate the effective temperature at both prompt and 100 ns.

Table 8.1. Effective temperature of the flame-generated TiO_2 nanoparticles at three flame heights (HAB = 30, 45, 60 mm) calculated with the two-color pyrometry at 650 nm and 710 nm. Four different values of $\frac{E(m_{710 \text{ nm}})}{E(m_{650 \text{ nm}})}$ are considered corresponding to: constant $E(m)$, minimum and maximum $E(m_\lambda)$ function obtained in Chap. 7, $E(m_\lambda)$ from Liu et al. [285]. The temperatures at prompt and at 100 ns are calculated using prompt and time-delayed LIE signals.

	$\frac{E(m_{710 \text{ nm}})}{E(m_{650 \text{ nm}})}$	T_{eff} [K], at $t=0 \text{ ns}$			Ref.
		HAB = 30 mm	HAB = 45 mm	HAB = 60 mm	
$\varepsilon^*(\lambda) = 1$	1	3006	3157	3091	Eq.(4.17)
$\varepsilon^*(\lambda) \neq 1 \text{ min}$	0.9304	2693	2814	2762	Chap. 7
$\varepsilon^*(\lambda) \neq 1 \text{ max}$	1.0015	3013	3165	3099	Chap. 7
$\varepsilon^*(\lambda) \neq 1 \text{ Liu et al.}$	0.4986	1419	1451	1437	[285]

	$\frac{E(m_{710 \text{ nm}})}{E(m_{650 \text{ nm}})}$	T_{eff} [K], at $t=100 \text{ ns}$			Ref.
		HAB = 30 mm	HAB = 45 mm	HAB = 60 mm	
$\varepsilon^*(\lambda) = 1$	1	2461	2405	2490	Eq.(4.17)
$\varepsilon^*(\lambda) \neq 1 \text{ min}$	0.9304	2248	2200	2271	Chap. 7
$\varepsilon^*(\lambda) \neq 1 \text{ max}$	1.0015	2466	2409	2495	Chap. 7
$\varepsilon^*(\lambda) \neq 1 \text{ Liu et al.}$	0.4986	1284	1269	1292	[285]

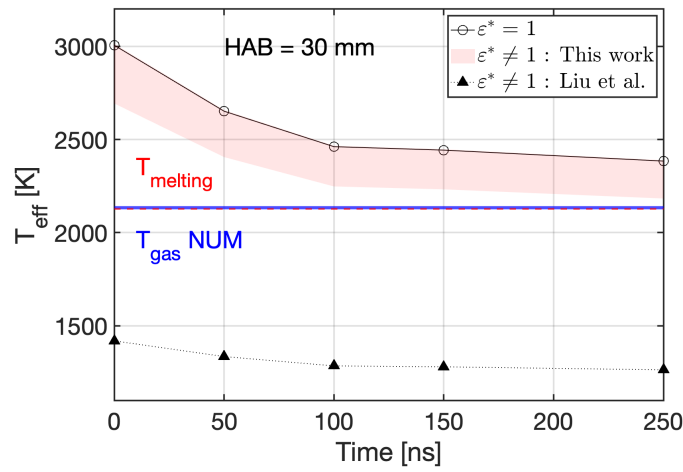
At prompt, the temperature at HAB = 45 mm is the highest for all $\varepsilon^*(\lambda)$ assumptions. For

$\varepsilon^*(\lambda)=1$, the effective temperatures are around 3000 K for all heights. Then, for $\varepsilon^*(\lambda) \neq 1$ case, one of the extreme values is close to 1, so that the effective temperature is close to results for $\varepsilon^*(\lambda)=1$. For the other value ($\varepsilon^*(\lambda) \approx 0.93$), smaller effective temperatures are obtained. From signals at 100 ns, the general trend is the same as at $t = 0$ ns, but the lowest temperature is found at HAB =45 mm, whereas the highest temperature is found at HAB =60 mm for all $\varepsilon^*(\lambda)$ cases. Temperature values using the absorption function from Liu et al. ($\varepsilon^*(\lambda) \approx 0.5$) are also reported in Table 8.1. In this case, the temperature values are quite small (< 1500 K).

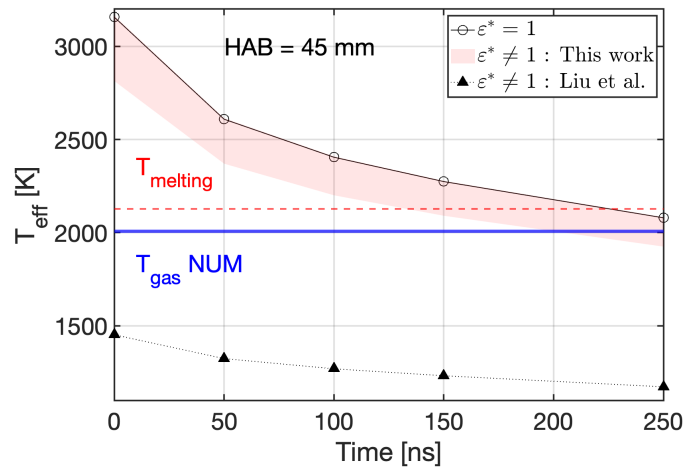
The temporal evolution of the effective temperature is shown in Fig. 8.11 for three HABs. The black round void corresponds to the $\varepsilon^*(\lambda) = 1$ case, the reddish zone corresponds to the $\varepsilon^*(\lambda) \neq 1$ case. The black triangle corresponds to the effective temperature using the absorption function from Liu et al. [285]. The red line indicates the melting point of TiO_2 , and the blue line shows the gas temperature of the flame estimated from the numerical simulation. As expected, the effective particle temperature decreases with the time approaching slowly the gas temperature obtained from numerical results, confirming once again the LII nature of the signal.

When utilizing the results on $\varepsilon^*(\lambda)$ from the preceding chapter, it is important to note that the effective temperature is higher than the melting point of TiO_2 nanoparticles (2128 K), at least for $t < 200$ ns. Additionally, as mentioned previously, the melting temperature of nanoparticles may be reduced by several hundred degrees relative to the bulk temperature due to their increased surface energy [383, 384]. This suggests that the LII process is likely occurring on liquid-state particles.

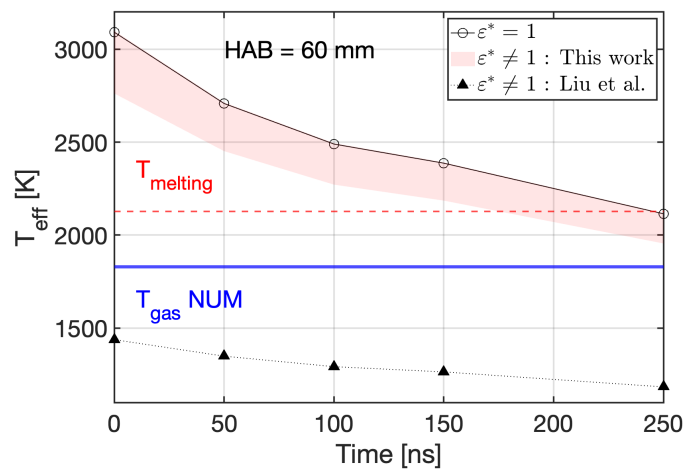
The effective temperature estimated using results from Liu et al. [285] is smaller than the gaseous temperature obtained from the numerical results. Thus, using the absorption function from Liu et al. [285] leads to incoherent results since particles subjected to laser heating are expected to have a temperature higher than the gas temperature. This seems to be additional support the ε^* function derived in the previous chapter as well as the need of measuring $E(m_\lambda)$ function in each configuration since results may strongly vary depending on the particle properties, which strongly depends on the environment conditions particles have experienced during their production.



(a)



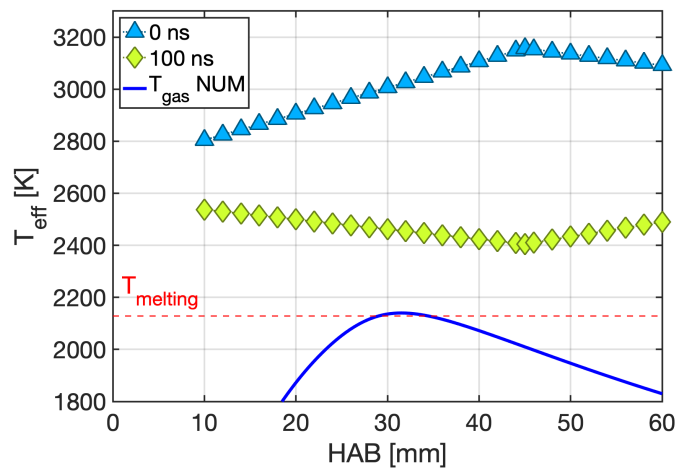
(b)



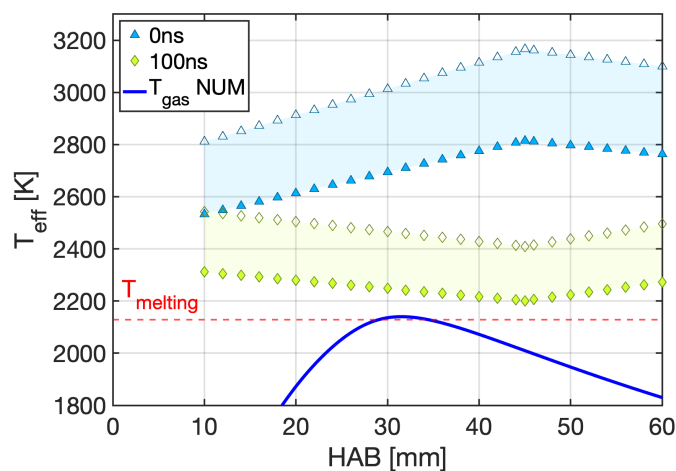
(c)

Figure 8.11. Effective particle temperature obtained by two-color pyrometry at 650 and 710 nm under $F = 0.15 \text{ J/cm}^2$ at different acquisition timing: (a) at HAB = 30 mm, (b) at HAB = 45 mm, and (c) HAB = 60 mm. Round black symbols are for $\epsilon^*(\lambda) = 1$. The red area corresponds to $\epsilon^*(\lambda) \neq 1$. The absorption function of Liu et al. [285] is shown in black triangle symbols.

In order to obtain information on the effective temperature along the whole flame centerline, the effective temperatures are linearly interpolated from the three known heights (HAB=30, 45, 60 mm). The interpolated temperatures for cases $\varepsilon^*(\lambda) = 1$ and $\varepsilon^*(\lambda) \neq 1$ at 0 and 100 ns are shown in Fig. 8.12. These effective temperatures will be used to calculate f_v^* from Eq. (8.5) in the following. Results using $\varepsilon^*(\lambda)$ from Liu et al. [285] are not considered since they lead to inconsistent temperature values. The gas temperature profile from the numerical results is added to Fig. 8.12. Along the centerline, the gas temperature is slightly over the melting point of TiO_2 at HAB =30 mm. At this height, the particles could already be in liquid form before the laser irradiation for the LII process, showing distinct optical properties. For the other HABs, the gas temperature is lower than the particle melting point, so the particles are likely to be in a solid state. However, since they are not too far from the particle melting point, it is possible that a phase change occurs during the laser heating. Further analysis of the phase change during the LII process is out of the scope of this research work. Still, knowing the initial gas temperature plays an important role in analyzing LII emission based on the physical state of particles.



(a) $\varepsilon^*(\lambda) = 1$



(b) $\varepsilon^*(\lambda) \neq 1$

Figure 8.12. Evolution of temperature along the flame centerline when assuming (a) $\varepsilon^*(\lambda) = 1$ and (b) $\varepsilon^*(\lambda) \neq 1$.

8.3.2 Spatial evolution of f_v^*

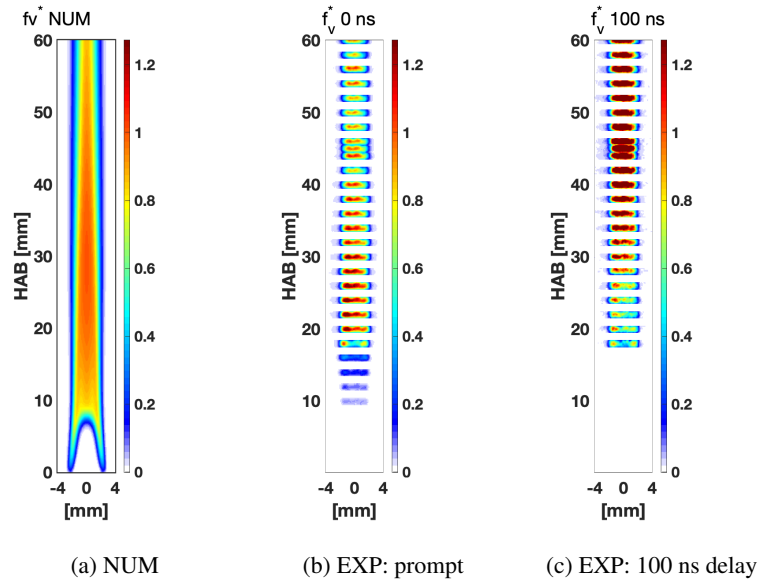
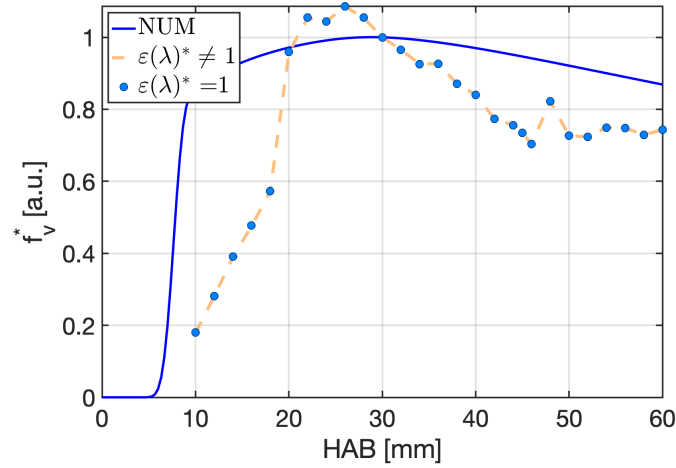


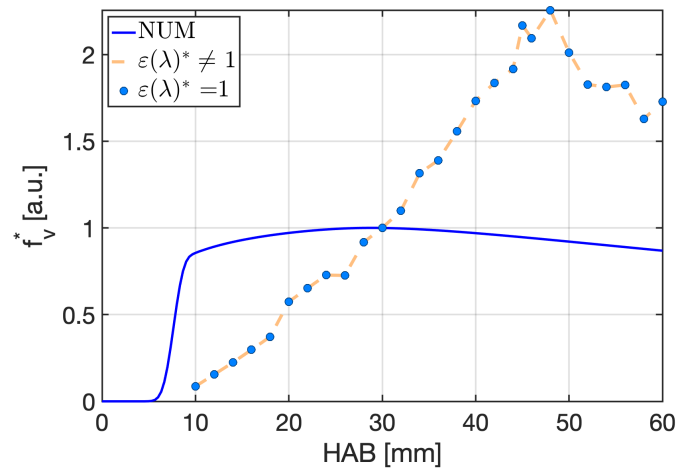
Figure 8.13. Spatial distribution of f_v^* obtained using numerical simulation (a) and LIE signals assuming a spatially uniform absorption function and non-uniform effective temperature from measurements at (b) prompt and (c) 100 ns delay time. Eq. (8.5) was used to calculate f_v^* in all cases.

Figure 8.13 shows the 2D distribution of f_v^* , which assumes a spatially-constant absorption function and non-uniform effective temperature (upper limit in Fig. 8.12(b)). In addition, Fig. 8.13(a) presents the numerical distribution of TiO_2 nanoparticles for comparison. In the experimental results, the prompt f_v^* (Fig. 8.13(b)) initially increases rapidly up to a HAB of approximately 25 mm, followed by a decrease. However, when considering LIE signals at 100 ns (Fig. 8.13(c)), the volume fraction continues to increase for HAB values greater than 30 mm. The same trend is observed in the centerline f_v^* of the flame (Fig. 8.14). It is important to note that only the T_{eff} values are affected by the assumption made on the $E(m_\lambda)$ shape (i.e., $\varepsilon^*(\lambda) = 1$ or $\varepsilon^*(\lambda) \neq 1$), while the f_v^* profiles remain consistent across the flame. However, a change in the volume fraction with time is clearly observed in Fig. 8.14. At prompt, the maximum value of f_v^* is observed near $\text{HAB} = 25$ mm, decreasing for higher flame heights, which is similar to the numerical estimation of the gas temperature shown in Fig. 8.12. For a 100 ns delay, the volume fraction continues to increase with flame height, reaching a maximum near $\text{HAB} = 45$ mm before slightly decreasing up to $\text{HAB} = 60$ mm. Discrepancies between prompt and 100 ns results may be due to the presence of parasitic signals at prompt (or short delay time) or underestimation of LII signals for small particles at 100 ns. For future work, it could be interesting to look at LII signals at different/longer delay times where non-LII contributions should be negligible. Under these conditions, taking into account the particle size distribution (especially for small particles), exploring the trend of f_v^* with HAB and at different delay times might be worth investigating. The volume fraction of TiO_2 along the flame centerline from the numerical simulation (blue lines

in Fig. 8.14) indicates a rapid increase below $\text{HAB} = 10$ mm and a gradual decrease at higher flame zones ($\text{HAB} > 30$ mm). However, the simulations appear to show a faster production rate compared to the experimental results.



(a) 0 ns



(b) 100 ns

Figure 8.14. Evolution of f_v^* along the centerline of the flame height is calculated from S_{LIE} at 0 ns (a) and 100 ns (b), considering $\varepsilon^*(\lambda) = 1$ and $\varepsilon^*(\lambda) \neq 1$. Non-uniform temperature is also considered. The numerical simulation results are also shown in blue line.

8.4 Non-uniform $E(m_{\lambda_{\text{em}}})$ and non-uniform effective temperature

In this section, we consider the final case by considering a spatially non-uniform ($E(m_{\lambda_{\text{em}}}, z) \neq E(m_{\lambda_{\text{em}}}, z_0)$) and a spatially non-uniform effective temperature ($T_{\text{eff}}(z) \neq T_{\text{eff}}(z_0)$). The normalized volume fraction then reads as:

$$f_v^*(z) = \frac{f_v(z)}{f_v(z_0)} = \frac{S_{LII}(\lambda_{\text{em}}, T_{\text{eff}}(z)) E(m_{\lambda_{\text{em}}}, z_0)}{S_{LII}(\lambda_{\text{em}}, T_{\text{eff}}(z_0)) E(m_{\lambda_{\text{em}}}, z)} \frac{\left[\exp\left(\frac{hc}{\lambda_{\text{em}} k_B T_{\text{eff}}(z)}\right) - 1 \right]}{\left[\exp\left(\frac{hc}{\lambda_{\text{em}} k_B T_{\text{eff}}(z_0)}\right) - 1 \right]}. \quad (8.7)$$

Since the experimental database was not originally created to go so far in the analysis of the nanoparticle production in the YDB flame, we dispose of LII spectra only at HAB = 45 mm. Therefore, it is not possible to calculate $E(m_{\lambda_{\text{em}}}, z)$ at the different position for the case of $\varepsilon^*(\lambda) \neq 1$. Thus, in this section, we will consider only case $\varepsilon^*(\lambda) = 1$. However, as observed in the previous section, results on the spatial evolution of f_v^* are expected not to be strongly affected by this assumption, at least for this specific flame configuration.

In the following, results on the effective temperature $T_{\text{eff}}(z)$ for $\varepsilon^*(\lambda) = 1$ obtained in the previous section and listed in Table 8.1 are considered.

8.4.1 Spatially non-uniform absorption function

To evaluate the spatial evolution of volume fraction from the LII signal, the value of $E(m_{\lambda_{\text{em}}})$ at the emission wavelength should be first estimated. As already mentioned, here we consider $\varepsilon^*(\lambda) = 1$, meaning that $E(m_{\lambda_{\text{em}}}, z) = E(m_\lambda, z) = E(m, z)$. For this, Eq. (7.5) can be used once the particle effective temperature and gaseous temperature are known:

$$E(m, z) = E(m_{\lambda_{\text{laser}}}, z) = \rho(z) c_p(z) \frac{\lambda_{\text{laser}} T_{\text{eff}}^0(z) - T_{\text{gas}}(z)}{6\pi F} \quad (8.8)$$

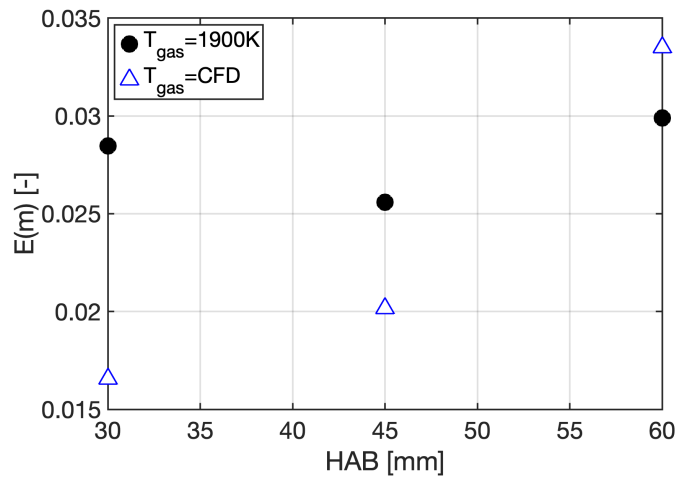
where ρ is the density of particles, c_p is the heat capacity of particles, T_{gas} is the gas temperature, T_{eff}^0 is particle temperature at prompt, and F is laser fluence.

For this, the gas temperature T_{gas} has to be known. In this work, we evaluate $E(m)$ from two T_{gas} estimations:

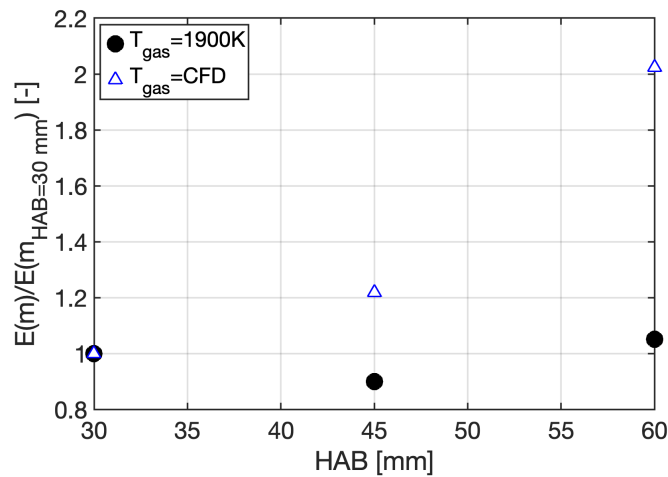
1. As done in Chap 7, T_{gas} does not depend on the HAB and is equal to 1900 K ($T_{\text{eff}}^0(z) = T_{\text{gas}}(z) = 1900$ K).
2. T_{gas} is obtained from the numerical simulation ($T_{\text{gas}}(z) = T_{\text{CFD}}(z)$).

Results for $E(m_\lambda, z)$ are shown in Fig. 8.15 considering the effective temperature obtained from signals at prompt and 100 ns and reminded in Table 8.1. $\rho(z) c_p(z)$ are considered as constant for z and the values are from [353]. For the case $T_{\text{gas}} = 1900$ K (black symbols), the calculated value of $E(m_\lambda)$ shows the same trend as temperature so that a non-monotonic evolution of $E(m_\lambda)$ is observed when increasing HABs. When considering a more realistic estimation of T_{gas} using results from the numerical simulation, a monotonic evolution of $E(m)$ is found with HABs (blue symbols).

Specifically, the value of $E(m)$ increases with the HABs, in analogy with literature trends in the case of soot particles. In the case of soot particles, their maturity related to the optical properties



(a)



(b)

Figure 8.15. Estimated absorption function $E(m, z)$ at different flame heights from the effective temperature obtained in Fig. 8.11 for $\varepsilon^* = 1$. Black symbols are obtained assuming a gas temperature of 1900 K, and blue symbols correspond to gas temperature from numerical simulation. Full and void symbols are obtained from LIE signals at 100 ns. (a) $E(m, z)$ value and (b) $E(m, z)/E(m, z_0)$ normalized value with the value at $\text{HAB} = 30$ mm.

evolves with the flame height in coflow type diffusion flame [387]. The newly formed soot particles undergo the high-temperature environment during the characteristic residence time to become graphite-like crystallites [388]. Thus, the value of the absorption function increases with flame height [300]. In the case of TiO_2 , the crystal phase change from anatase to rutile along the flame height has been reported [20]. The change of surface crystalline feature along the flame height might be interpreted in analogy with soot particles, resulting in the increase of the absorption function. From $\text{HAB} = 30$ mm to $\text{HAB} = 60$ mm, $E(m_\lambda)$ value is almost doubled.

To confirm such a hypothesis, ex-situ measurements such as XRD analysis (Chap. 3) should be performed to analyze the particles crystalline structure. Even if these measurements would be of great value, they are out of the scope of this work. Alternatively, as discussed in Sec. 4.3.4 and Sec. 8.1.2 regarding the optical properties of liquid-phase particles, the variations in phase (from solid to liquid) along the flame height can explain this observation. Changes in temperature along the height of the flame can cause the solidification and melting of materials, resulting in the evolution of $E(m)$ in relation to the HAB.

8.4.2 Spatial evolution of f_v^*

Once $E(m, z)/E(m, z_0)$ and the effective temperature $T_{\text{eff}}(z)/T_{\text{eff}}(z_0)$ are known, the normalized volume fraction f_v^* can be estimated from the LII signal. The values of $E(m, z)/E(m, z_0)$ and of $T_{\text{eff}}(z)/T_{\text{eff}}(z_0)$ between HAB = 30, 45, and 60 mm are linearly interpolated. The value below HAB = 30 mm is estimated by linear extrapolation down to HAB = 10 mm. Only the case $T_{\text{gas}}(z) = T_{\text{CFD}}(z)$ is retained.

The 2-D normalized volume fractions considering non-uniform effective temperature $T_{\text{eff}}(z)$ and non-uniform $E(m, z)$ along the flame height from the signal at prompt and at 100 ns are presented in Figs. 8.16(b) and 8.16(c), respectively. The normalized TiO_2 volume fraction of the numerical simulation is shown for comparison in Fig. 8.16(a).

At prompt, the highest f_v^* values are observed between HAB = 20 mm and 30 mm. Then, for higher flame heights, the intensity decreases. When considering the delayed signal, the obtained volume fraction f_v^* shows a maximum volume fraction at HAB = 45 mm.

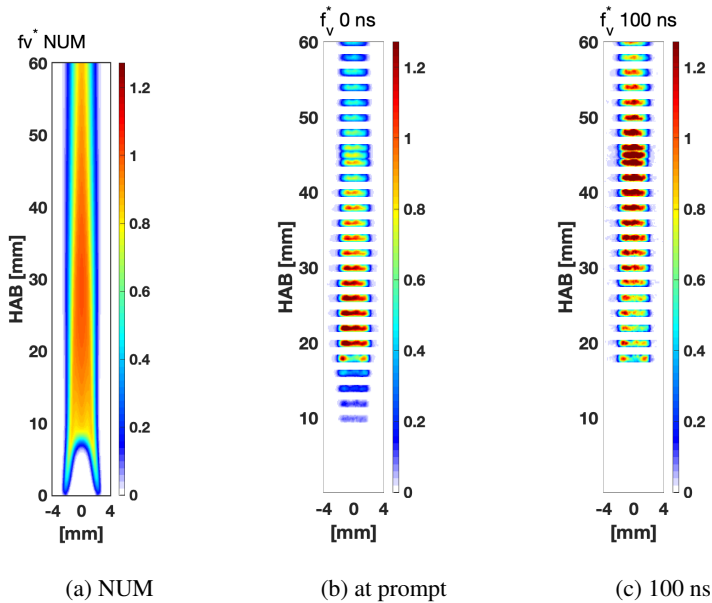


Figure 8.16. Spatial distribution of f_v^* in the case of non-uniform absorption function and non-uniform effective temperature (with $\epsilon(\lambda) = 1$). (a) numerical simulation. f_v^* from measurements at (a) prompt and (c) delayed time at 100 ns.

Figure 8.17 shows the f_v^* evolution along the centerline using signals at prompt (a) and delayed (b) acquisition time. Numerical results are also added. When looking at results at prompt, a maximum of f_v^* is observed at approximately HAB=25 mm. For delayed signal, the peak position is found downstream at HAB=45 mm (Fig. 8.17(b)). Compared to the numerical profiles, results at prompt seem to indicate that TiO_2 volume fraction is too quickly produced by the numerical simulation with a too stiff initial increase of f_v^* .

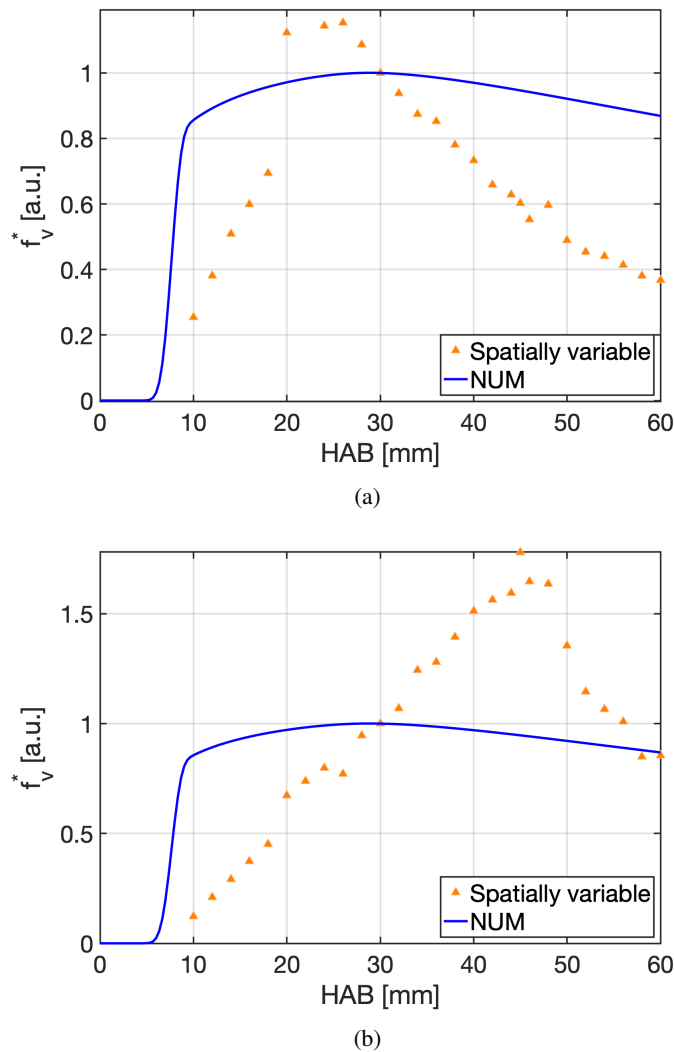


Figure 8.17. Normalized volume fraction at the centerline of flame synthesis derived with spatially variable $E(m)$ (a) at prompt and (b) 100 ns after.

8.5 Conclusion

In this chapter, the spatial distribution of volume fraction of flame-generated TiO_2 nanoparticles is investigated via LII diagnostics using different assumptions on the particle effective temperature and absorption function. Results along the flame centerline are summarized in Fig. 8.18 and compared with numerical results. The non-uniform absorption function and non-uniform effective temperature considered for calculation are shown in Fig. 8.19. As shown previously, the absorption function $E(m_\lambda)$ increases its dynamic about twice between $\text{HAB} = 30$ mm and $\text{HAB} = 60$ mm, the effective temperature reaches its maximum at $\text{HAB} = 45$ mm, then decreases towards $\text{HAB} = 60$ mm.

When estimating f_v^* , on one hand, emission at prompt (Fig. 8.18(a)) may be affected by parasitic signals and may not solely account for LII. On the other side, when considering emission delayed of 100 ns (Fig. 8.18(b)), the LII signal is mainly governed by the emission of the biggest particles/bigger aggregates. Then, it is sure that the particle distribution is considered as poly-dispersed from the significant difference between prompt and 100 ns delayed results. Thus, f_v^* may possibly be underestimated, especially at small HABs where particles are expected to be small. It is, therefore, quite difficult to identify the adequate strategy, i.e., the most appropriate f_v^* profile. However, based on the conclusions in Chap. 6, the LIE signal at 640 nm seems not to be largely affected by the parasitic signals, so the results at prompt can be considered as a starting point to investigate TiO_2 nanoparticles production in the YDB burner and to evaluate the accuracy of the numerical model. By looking at the results in Fig. 8.18(a), the spatial evolution of the effective temperature and the absorption function has an impact on f_v^* profile. In this work, various assumptions have been made to address this issue, and information only at three collection points was available. This may be a possible explanation for the discontinuity observed near $\text{HAB} = 20$ mm, as only limited information was available at three collection points..

The obtained f_v^* profile should be considered with caution to evaluate the validity of the model. Overall, all the obtained results seem to point out that the numerical simulation presents a too-stiff production of TiO_2 , localized too close to the burner injection. At the same time, the fact that the signal levels were 5 to 10 times smaller than those of the carbonaceous particles (Chap.5) reminds that the overall S/N ratio is not high enough, limiting the detection sensitivity for the spatial distribution of nanoparticle production. Still, it is the first time that the volume fraction of numerical simulation is compared with normalized volume fraction obtained from the LII on TiO_2 nanoparticles. This kind of comparison has a tendency to generate large uncertainties even in the case of well-established soot [365].

In general, it can be concluded that the developed YDB burner is an interesting experimental configuration for the characterization of TiO_2 production in laminar flames and for the development and validation of numerical models. For this, the LII technique is a promising technique for the characterization of the absorption function and volume fraction. This chapter shows its high potential, but extensive work to obtain an accurate quantitative estimation of f_v is still needed.

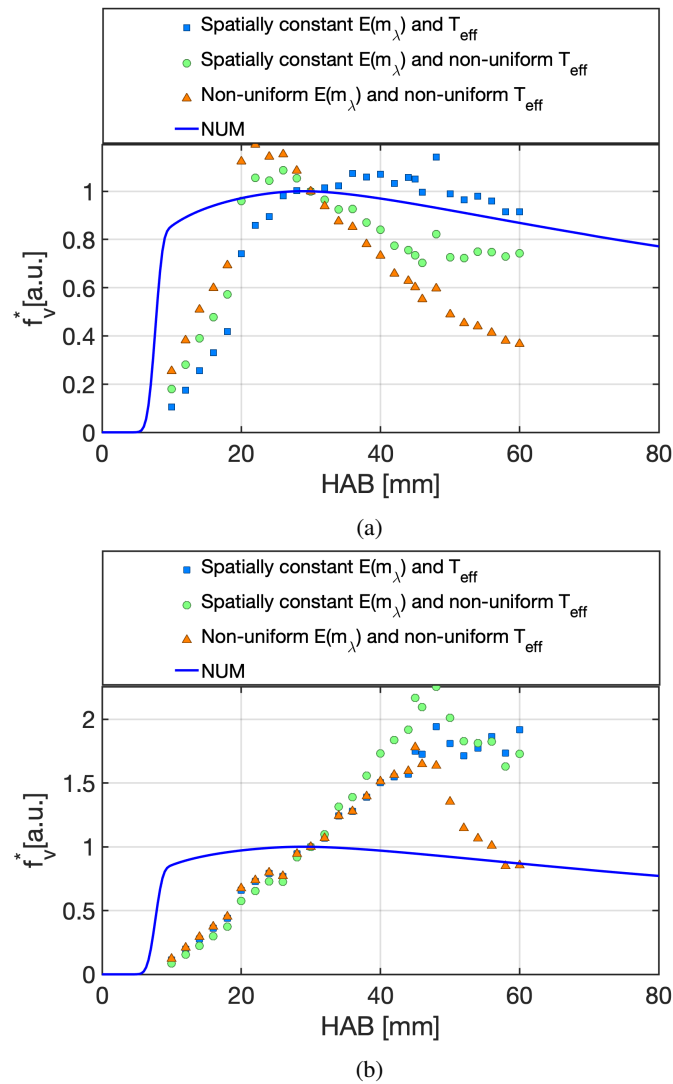


Figure 8.18. Normalized volume fraction f_v^* at the centerline of flame synthesis derived with considered strategies: spectrally constant $E(m_{\lambda_{\text{em}}})$ and T_{eff} , spectrally constant $E(m_{\lambda_{\text{em}}})$ and non-uniform T_{eff} , non-uniform $E(m_{\lambda_{\text{em}}})$ and T_{eff} and numerical simulation at prompt (a) and delayed (100 ns) (b) case.

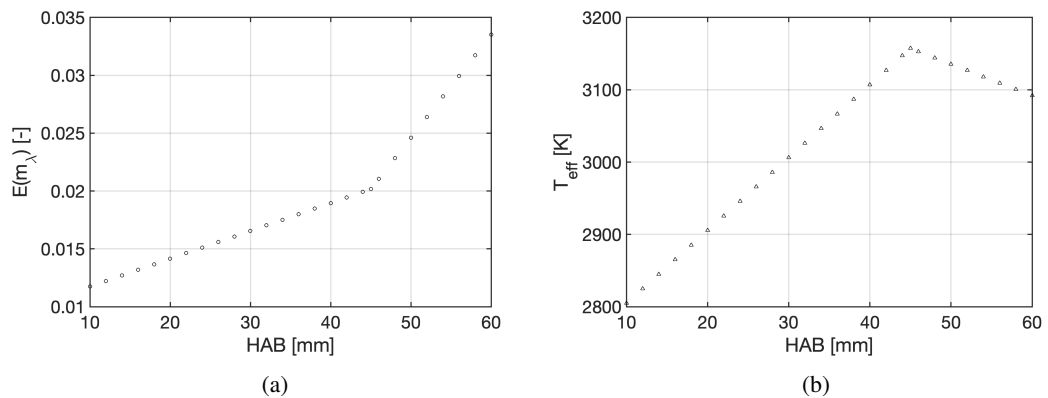


Figure 8.19. (a) Absorption function and (b) effective temperature at prompt used for non-uniform $E(m_\lambda)$ and non-uniform T_{eff} case. The values are interpolated between 30 and 60 mm.

Conclusion

Titanium dioxide (TiO_2) is one of the most commonly used nanomaterials due to its increasing interest on its unique semiconductor properties in high-end applications. To meet the needs for advanced characteristics, flame spray synthesis has been investigated to generate materials outside the thermodynamic stability limits [389], thanks to its high-temperature gradient with a short residence time. These local conditions play an important role in determining the properties of the generated particles during their formation. Consequently, particle formation and growth in flame synthesis should be understood. The physical processes can be monitored by in-situ diagnostics providing a spatial description of the particle formation. The laser-induced incandescence (LII) technique can characterize the particle volume fraction (f_v) in flames in a quasi-non-intrusive manner. If applicable to TiO_2 nanoparticles, it will provide new information on the synthesis process of metal oxides in spray flames. Although this technique has been established for soot particles [10, 11], its application to non-soot nanomaterials [12] is challenging. This study investigated the laser-induced emission of TiO_2 nanoparticles to verify whether the LII technique could be employed to characterize their volume fraction distribution in flame synthesis.

In the present work, the detailed spectral and temporal behavior of pure TiO_2 nanoparticles are investigated. First, commercially available high-purity TiO_2 nanoparticles have been considered in a non-reactive inert environment working with pure TiO_2 nanoparticles assures that the LIE signal originates from TiO_2 and not from carbon materials from combustion products. In addition, considering a non-reactive inert environment, nanoparticles are dispersed via N_2 gas flow with the help of an ultrasonic bath. The aerosol passes through the optical cell, where a top-hat 355 nm laser irradiates the particles. Then, the spectral and temporal information are detected by a spectrometer and photomultiplier tube perpendicular to the laser direction. The methodology to verify the LII nature includes the investigation under different laser fluences, detection delay gates, and detection wavelengths to identify the LII contributions in laser-induced emission (LIE) of TiO_2 . Carbon black nanoparticles are considered in parallel to provide reference behavior. The emissions of carbon black particles show a blue-shift with increasing laser fluence and exhibiting a long characteristic lifetime (more than 500 ns) in line with the expected LII trend. A red shift for delayed acquisition, i.e., during particle cooling, is observed additionally confirming the LII-like nature of the emitted signal. C_2 band emission is observed for high laser fluences from the vaporized species.

The spectral emission of TiO_2 nanoparticles shows a different nature when varying laser fluence. At low laser fluence regimes, short emissions centered near 470 nm are observed, which

could be interpreted as TiO₂ LIF from various transitions inside the molecule. Then, for higher laser fluences, they show sharp features overlapping with continuous emissions whose temporal decay shows multiple modes. By analyzing the different distributions of the Gaussian fit of Laser-Induced Fluorescence (LIF) of TiO₂, it is possible to propose that the distinct sharp features arise from the LIF of TiO₂ nanoparticles. This phenomenon can alternatively be explained as Phase-Selective Laser-Induced Breakdown Spectroscopy (PS-LIBS) of TiO₂, based on the atomic emissions of Ti and O. Further investigation is required to characterize these non-LII components. Then, delayed LIE of TiO₂ is investigated to verify the LII behavior. The emission spectra of TiO₂ nanoparticles show a red shift during particle cooling as a function of delay time, indicating its LII nature. The LII nature of the delayed signal has also been shown by considering the linear tendency of decay characteristic time with emission wavelength for TiO₂ nanoparticles. The difference in the reverse of temperature, ΔT^{-1} , also confirms that the LII nature of the temporal emission at 650 and 710 nm for TiO₂ nanoparticles.

The next step is to study nanoparticles generated in flame synthesis. TiO₂ nanoparticles are generated in an argon-diluted hydrogen/air diffusion flame to limit the addition of carbon species in the fuel. The classical Yale Diffusion Burner has been modified with a heating system to vaporize the liquid TTIP precursor before injecting it in flames. The same protocol used for high-purity TiO₂ has been applied to confirm the LII nature of LIE for flame-synthesized TiO₂. The spectral emissions at prompt show non-LII components in LIEs. The delayed emission spectra show a red-shift during the cooling process. The evolution of ΔT^{-1} shows consistency between detection wavelengths of 650 and 710 nm, confirming LII for these two wavelengths. In comparison with pure TiO₂, the same conclusion is obtained for the description of flame synthesis in a reactive environment. The emission spectrum shows a different characteristics when comparing pure TiO₂ and flame synthesis, possibly indicating different optical properties. Then, a first step for the utilization of the LII signal to characterize the nanoparticle property is introduced. First, a new method has been proposed to infer the spectral shape of the absorption function. This strategy based on an estimation of the possible range of particles temperature by assuming a constant $E(m_\lambda)$ over a small wavelength interval has been applied to the LII signal from carbon black, retrieving the literature results well. Then, the same methodology is applied to TiO₂ nanoparticles in non-reactive and reactive cases. The shape of $E(m_\lambda)$ differs in the two cases, possibly due to different optical properties because particles are produced with totally different processes. Then, a strategy to estimate $E(m_\lambda)$ absolute values is presented. Once again, different results are obtained for the two types of TiO₂. Still, they are quite in line with the literature data.

A strategy to evaluate the spatial evolution of nanoparticles volume fraction f_v along the flame centerline is provided. For this, spatial variability of the particle effective temperature T_{eff} and the absorption function $E(m_\lambda)$ should be accounted for. Normalized TiO₂ nanoparticles volume fraction f_v^* is obtained by taking them into consideration simultaneously or not. It has been observed that the spatial evolution of T_{eff} and $E(m_\lambda)$ can largely affect the estimation of f_v^* . At the same time, it has been observed that state-of-the-art simulations predict a too fast production of TiO₂. More optimized experimental work is still required if the volume fraction f_v has to be quantitatively measured.

This work shows that it is possible to apply LII on flame-synthesized TiO₂ nanoparticles, but

with more cautions than conventional soot nanoparticles in particle characterization. The choice of laser fluence and acquisition timing must be carefully considered due to the possible existence of prompt interference from laser-induced interferences. Then, another adjustment should be considered to compensate for the small particle contributions, which could be underestimated in the delayed detection system.

With the objective of verifying the feasibility of adapting the LII technique to TiO_2 nanoparticles, both pure and flame-generated TiO_2 nanoparticles have successfully shown the potential of particle characterization via the LII process. Particle volume fractions through LII were not fully evaluated here, but several expected difficulties are pointed out to provide directions for future works.

- Choice of excitation wavelength: To fully utilize the proposed method for the estimation of the absorption function in Chap. 7, the excitation wavelength should be in the detection wavelength range so that there is no need for an additional extrapolation. A complete description of the optical property will help further quantitative measurement of volume fraction.
- Choice of detection wavelength: In this study, the spectrometer is limited to the visible range, so only wavelengths of 650 - 710 nm could be used for the analysis avoiding non-LII contribution of TiO_2 LIE. With a more extended detection range, it might be possible to choose a more appropriate detection wavelength that completely avoids all the non-LII components whose distributions are relatively concentrated in the UV-visible range. Then, the prompt emission can be used for volume fraction analysis.
- Complete spectral and temporal measurements for all spatial evolutions: In this study, only three flame heights ($HAB = 30, 45, 60$ mm) have been chosen for temporal measurements, where whitish particles are observed by the naked eye. Results from these three points were then extrapolated to match with the spatial measurement for all flame heights in the volume fraction measurement in Chap.8. Then, it would be more proper to conduct all spectral and temporal measurements for each spatial measurement without extrapolation. The complete description of spectral and temporal detection for all flame heights can provide proper T_{eff} and $E(m_\lambda)$ and further volume fraction estimation.
- Calibration and the absorption function $E(m_\lambda)$: To obtain quantitative volume fraction, the calibration process is essential. Auto-compensating LII [375] could have been explored but the broad estimation of absolute absorption function would result in significant uncertainties over volume fraction. Then, other calibration methods such as light extinction [390], cavity ring-down spectroscopy extinction (CRDE) technique [391] also require the information of absorption function. Therefore, the importance of the absolute value of the absorption function $E(m_\lambda)$ of materials is again highlighted. The ellipsometry technique has been broadly used for measuring the refractive index of various materials [286]. However, its ex-situ measurement nature does not guarantee the instantaneous optical property during the LII process after laser irradiation. Thus, further investigation is needed to obtain in-situ optical properties in high-temperature environments. For example, complementary diagnostics like in-situ line-of-sight attenuation (LOSA) measurements have been used for retrieving the absorption function of gas-borne silicon [23, 16, 372], copper [16] and liquid germanium [24]. After regulating these issues, quantitative comparison

with numerical simulation could provide a fruitful indication to deeply understand the formation process and control the particle property in flames to fulfill the demands for producing advanced materials.

- Comparison between experimental flame luminosity and numerical simulation results: In this study, the flame luminosity profile taken from the camera is directly compared with the OH mole fraction profile and TiO₂ nanoparticles volume fraction. However, this comparison should be treated carefully because they are not based on the same quantities (experimental flame luminosity on the one side, numerically calculated mole fraction, and volume fraction on the other side). As pointed out in [392], a direct comparison between the experimental signals and the numerically synthesized signals can then be performed (forward method) to validate the numerical models. For this work, the numerical results of species concentration and temperature can be utilized for synthesizing the emission spectrum in the visible range with the help of the theoretical spectrum of each species. Then the validation of numerical models can be strengthened with less post-processing and/or assumptions to the experimental signal, which could increase the uncertainty.

Most of the discussion treated in this thesis could be applied to other metal oxides nanomaterials, especially SiO₂, whose physicochemical property is similar to TiO₂ and the flame spray combustion systems, could bring potential benefit [393]. The LII on SiO₂ has been studied [17], but its application for measuring the volume fraction or particle size distribution has not yet been fully discovered. Verifying the nature of LIE will be an indispensable step to expand LII measurements to those new particles. The unknown optical properties in the synthesis environment could be estimated based on the strategy proposed in the thesis for further quantitative analysis of volume fraction.

Appendix A

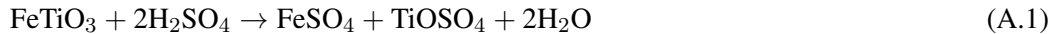
Industrial manufacturing process of TiO_2

The detailed sulfate and chloride processes are summarized based on the description in [3].

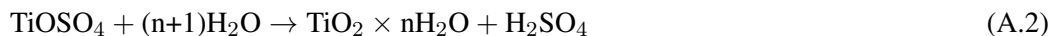
A.1 Sulfate process

The sulfate process is a batch process that uses sulfuric acid to extract titanium dioxide from Ilmenite or titanium slag.

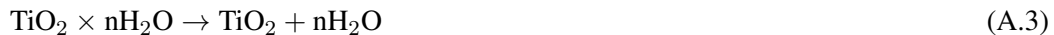
Ilmenite (FeTiO_3) or titanium slag is reacted with sulfuric acid (H_2SO_4).



The waste product iron(II) sulfate (FeSO_4) is removed. As it is insoluble at low temperatures, the solution is cooled to around 15°C , and FeSO_4 crystallizes, which can then be removed by filtration. The remaining aqueous digestion products are heated to around 110°C in order to hydrolyze the titanium oxygen sulfate (TiOSO_4).



The hydrolysis stage of the process produces sulfuric acid H_2SO_4 waste and a precipitate gel containing hydrated titanium dioxide $\text{TiO}_2 \times n\text{H}_2\text{O}$. In the final stage, the hydrated titanium dioxide is heated in large rotary kilns to remove the water (at temperatures between $200\text{-}300^\circ\text{C}$) and produce crystals of anatase or rutile.



A.2 Chloride process

Titanium ore (which contains at least 70% rutile) is transformed at high temperatures into titanium tetrachloride vapor TiCl_4 using chlorine and coke.



Liquid TiCl₄ is distilled off. It is then converted back into TiO₂ in a pure oxygen flame with the help of toluene or in plasma (with AlCl₃) at temperatures of 1200 - 1700 °C. The majority of applied chlorine is recovered and recycled.



The product can be subjected to a calcination process at high temperature to change the crystal phase.

Appendix B

LII modeling process

B.1 Important parameters in LII model

Refractive index $E(m_\lambda)$ is the absorption function of complex refractive index m_λ , defined as:

$$E(m_\lambda) = -Im \left[\frac{m_\lambda^2 - 1}{m_\lambda^2 + 2} \right] \quad (\text{B.1})$$

where the refractive index $m_\lambda = n_\lambda - ik_\lambda$ is an important wavelength-dependent optical property for LII mechanisms. n_λ describes the scattering characteristic (opacity) and k_λ accounts for the light-absorbing capacity of the particle [394].

Thermal accommodation coefficient α_T The accommodation coefficient α_T describes the exchange movement of gas molecules with a surface during surface-scattering by vibrational, rotational, and translational forms of energy [268]. It is a ratio of the actual average energy transfer to the maximum energy transfer allowed by the second law of thermodynamics. Despite its importance in the calculated conductive cooling rate and particle sizing by LII, many uncertainties are still associated with calculating the thermal accommodation coefficient. There have been a few trials to measure directly this coefficient value [395]. The thermal accommodation coefficient is mostly inferred from pulsed-LII-temporal profiles with the LII model. Recently, molecular dynamics have been actively employed to obtain the thermal accommodation coefficient [278]. For mature soot, the value of 0.23 - 0.37 is commonly adapted [333].

Equivalent sphere diameter d_{eff} In the case of mono-dispersed particle distribution, the number of primary particles in aggregates is $N_p=1$. For poly-dispersed particle distribution, $N_p>1$, it is possible to define an equivalent sphere diameter d_{eff} [396] based on a fractal-like approach. This definition accounts for the shielding effect, i.e. that the inner particles are "thermally" shielded by the outer particles from cold ambient gas molecules (so that they cool down slower).

$$d_{\text{eff}} = \left(\frac{N_p}{k_h} \right)^{\frac{1}{D_h}} \cdot d_p \quad (\text{B.2})$$

where k_h is the fractal prefactor, a proportionality constant with order or unity [175]. D_h is the fractal dimension.

Liu et al. [270] used direct simulation Monte Carlo (DSMC) calculations to evaluate the scaling constants k_h and D_h as a function of the thermal accommodation coefficient α_T for aggregates in free-molecular regime.

$$\begin{aligned} k_h &= 1.04476 + 0.22329 \alpha_T + 7.14286 \times 10^{-3} \alpha_T^2 \\ D_h &= 1.99345 + 0.30224 \alpha_T - 0.11276 \alpha_T^2 \end{aligned} \quad (\text{B.3})$$

In continuum regime,

$$\begin{aligned} k_h &= 1.32 \\ D_h &= 2.07 \end{aligned} \quad (\text{B.4})$$

B.2 Heat transfer model

The whole process of laser-induced incandescence starts from heating particles with a laser beam. By absorbing the laser energy, the temperature of the particles rises linearly. Consequently, the particles cool down to ambient temperature. When the peak particle temperature is below the boiling point (sublimation point) of the particles, conduction is the dominant energy loss mechanism by transferring heat to the surrounding medium. Above the boiling point of the particles, vaporization would be the dominant energy loss mechanism, limiting the temperature rise.

These processes contribute to the energy and mass balance of the particle in laser-induced incandescence:

$$\frac{dU_{\text{int}}}{dt} = \dot{Q}_{\text{abs}} + \dot{Q}_{\text{cond}} + \dot{Q}_{\text{vap}} + \dot{Q}_{\text{other}} \quad (\text{B.5})$$

where $\frac{dU_{\text{int}}}{dt}$ is the internal energy change, t is the time, \dot{Q}_{abs} is the energy flux due to laser absorption, \dot{Q}_{cond} is the energy flux due to heat conduction, \dot{Q}_{vap} is the energy flux related to vaporization, \dot{Q}_{other} is the cooling effect from other phenomena like radiation, oxidation, annealing, thermionic effect [268], whose energy transfer rates are orders of magnitude less than the remaining terms and are often omitted in literature. Mass balance can be expressed by:

$$\rho_s c_s \frac{\pi d_p^3}{6} \frac{dT_p}{dt} = \dot{m}_{\text{vap}} \quad (\text{B.6})$$

where ρ_s is the solid nanoparticle density, c_s is the specific heat of particle, d_p is the primary-particle diameter, T_p is the particle temperature, $m_p (= \rho_s \frac{\pi d_p^3}{6})$ is the particle mass. \dot{m}_{vap} is the mass-loss rate from the particle surface during the vaporization process. The time evolution of the particle temperature can be obtained by solving these differential equations with the assumed model for each energy loss term.

For the next part, details on the phenomena and the proposed models to describe each terms in Eq. B.5 and Eq. B.6 are presented. Most of the description is based on the work of Hofmann et al. [397].

B.2.1 Absorption

A laser used for LII generally emits short pulses with a duration of tens of nanoseconds in the gaussian temporal profile. A particle irradiated by the laser absorbs the electromagnetic energy and its temperature increases as a consequence.

For a spherical particle in the Rayleigh regime, where the particle diameter d_p is much smaller than laser wavelength λ_{ex} ($d_p \ll \lambda_{ex}$), the energy flux due to laser absorption is given as:

$$\dot{Q}_{abs} = C_{abs} F q(t) = \frac{\pi^2 d_p^3}{\lambda_{ex}} E(m_{\lambda_{ex}}) F q(t) \quad (B.7)$$

where $C_{abs} = \frac{\pi^2 d_p^3}{\lambda_{ex}} E(m_{\lambda_{ex}})$ is the absorption cross section [398, 174], which is the geometric cross section $\left(\frac{\pi d_p^2}{4}\right)$, multiplied by absorption efficiency ($Q_{abs,\lambda} = E(m_{\lambda_{ex}}) \frac{4\pi d_p}{\lambda_{ex}}$ in Rayleigh regime). λ_{ex} is the excitation laser wavelength, F is the laser fluence (unit: J/cm²), $q(t)$ is the normalized laser power temporal profile.

B.2.2 Conduction

During and after the laser pulse, the particle is cooled by heat transfer to the surrounding gas (conduction), vaporization (sublimation) of material from the particle surface, and thermal radiation. In a low fluence regime without vaporization, conduction heat transfer becomes the principal cause of particle cooling.

Depending on the relation between the mean free path and particle size, the particles experience different conduction regimes; *Free-molecular*, *Continuum*, and *Transition* flow regime. Each regime will be detailed in the following.

Free-molecular flow regime In the free-molecular flow regime, where Knudsen number > 10 , which is valid for flames at atmospheric, the heat conduction rate between the spherical nanoparticle and the surrounding gas is given by [399]:

$$\dot{Q}_{cond} = \alpha_T \pi \left(\frac{d_{eff}}{2}\right)^2 \frac{p_g}{2} \sqrt{\frac{8k_B T_g}{\pi m_g} \frac{\gamma^* + 1}{\gamma^* - 1}} \left(\frac{T_p}{T_g} - 1\right) \quad (B.8)$$

where $\frac{1}{\gamma^* - 1} = \frac{1}{T_p - T_g} \int_{T_g}^{T_p} \frac{dT}{\gamma - 1}$

p_g is the ambient pressure, T_g is the local gas temperature, k_B is the Boltzmann constant, m_g is the mass of the gas molecule, γ is the ratio of heat capacity of local gas.

Continuum flow regime In the continuum region, where the Knudsen number $< \sim 0.01$, the heat transfer between the particle and the surrounding gases is based on diffusion and depends on the gas temperature. The stationary continuum heat transfer equations are given by [399]:

$$\begin{aligned} \dot{Q}_{\text{cond}} &= 2\pi d_{\text{eff}}(T_p - T_g) \left(\frac{1}{\gamma^* - 1} \right) \\ \text{where } \frac{1}{\gamma^* - 1} &= \frac{1}{T_p - T_g} \int_{T_g}^{T_p} \frac{dT}{\gamma - 1} \end{aligned} \quad (\text{B.9})$$

Transition flow regime: Fuchs Fuchs' two-layer theory [399, 400] is based on the transport processes in the free molecular regime within a boundary layer (limiting sphere) closely around the particle, and in the continuum regime outside this layer [401]. Therefore, this approach can be extensively adapted from the free-molecular to the continuum regime.

Inside the limiting sphere, the heat conduction rate from the equivalent sphere to the region within the limiting sphere is calculated using the free-molecular regime expression between the particle temperature T_p and the limiting sphere temperature T_δ .

$$\begin{aligned} \dot{Q}_{\text{cond}} &= \alpha_T \pi \left(\frac{d_{\text{eff}}}{2} \right)^2 \frac{p_g}{2} \sqrt{\frac{8k_B T_g}{\pi m_g} \frac{\gamma^* + 1}{\gamma^* - 1}} \left(\frac{T_p}{T_\delta} - 1 \right) \\ \text{where } \frac{1}{\gamma^* - 1} &= \frac{1}{T_p - T_\delta} \int_{T_\delta}^{T_p} \frac{dT}{\gamma - 1}. \end{aligned} \quad (\text{B.10})$$

In the region outside the limiting sphere, conduction heat loss from the limiting sphere to the surrounding gas is calculated using the continuum regime expression between the gas temperature T_g and the limiting sphere temperature T_δ .

$$\dot{Q}_{\text{cond}} = 4\pi \left(\delta + \frac{d_{\text{eff}}}{2} \right) \int_{T_g}^{T_\delta} k_g dT \quad (\text{B.11})$$

where δ is the boundary layer thickness in the Fuchs approach, $\delta + \frac{d_{\text{eff}}}{2}$ is the radius of the limiting sphere.

The ratio of the radius of the limiting sphere $R_{\text{eff}} (= d_{\text{eff}}/2)$ to the equivalent sphere ($\delta + R_{\text{eff}}$) is given as

$$\frac{\delta + R_{\text{eff}}}{R_{\text{eff}}} = \frac{R_{\text{eff}}^2}{\lambda_\delta^2} \left(\frac{1}{5} \Lambda_1^5 - \frac{1}{3} \Lambda_2 \Lambda_1^3 + \frac{2}{15} \Lambda_2^5 \right) \quad (\text{B.12})$$

where λ_δ is the mean free path of gas molecules in the boundary layer around the equivalent sphere

$$\lambda_\delta = \frac{k_g(T_\delta)\sqrt{T_\delta}(\gamma(T_\delta) - 1)f(T_g)}{k_g(T_g)\sqrt{T_g}(\gamma(T_g) - 1)f(T_\delta)}\lambda_g \quad (\text{B.13})$$

and Λ_1 and Λ_2 are given as

$$\Lambda_1 = 1 + \frac{2\lambda_\delta}{d_p}, \Lambda_2 = 1 + \left(\frac{2\lambda_\delta}{d_p}\right)^2 \quad (\text{B.14})$$

To find T_δ , the Eq. (B.10) and Eq. (B.11) should be in equality since there are no heating sources or heat sinks between two regions. δ can be obtained from the T_δ by solving coupled equations numerically. Then the heat condition rate in the transition regime can be obtained by using either Eq. (B.10) or Eq. (B.11).

Previously the thickness of the limiting sphere where there is no collision was typically defined as the mean free path at the temperature of the boundary sphere. However, a more intricate approach that considers factors such as evaporation, particle curvature, and the directional distribution of gas molecules during their collision has been developed, known as the Wright correction [400]. This method has been evaluated using Direct Simulation Monte Carlo (DSMC) by predicting the Knudsen layer thickness, as demonstrated in [402].

B.2.3 Vaporization

At high laser fluence, the vaporized heat loss can be the most significant endothermic (cooling) mechanism. When the particle temperature reaches the vaporization (sublimation) temperature, it can rapidly decrease the LII signal because of considerable mass loss during the laser pulse with decreasing particle diameter. The energy flux related to vaporization is expressed as:

$$\dot{Q}_{\text{vap}} = -\frac{\Delta H_v}{M_v} \left(\frac{dm_p}{dt}\right)_{\text{vap}} \quad (\text{B.15})$$

where ΔH_v is the enthalpy of formation of the vaporized particles, and M_v is the average molecular weight of the vaporized particles.

The mass-loss rate can be expressed [268]:

$$\left(\frac{dm_p}{dt}\right)_{\text{vap}} = \pi d_p^2 N_v \times \frac{M_v}{N_A} \quad (\text{B.16})$$

where N_v is the molecular flux associated with the particle vaporization in the transition regime [403]. N_A is Avogadro constant 6.022×10^{26} [1/kmol].

The molecular flux N_v is calculated from: $\frac{1}{N_v} = \frac{1}{N_K} + \frac{1}{N_c}$,

with $N_K = \beta n_v \sqrt{\frac{RT_p}{2\pi M_v}}$ and $N_c = \frac{2p_v}{k_B T_p} \frac{\Gamma_{v,s}}{d_p}$

where β (often written as α_M) is the vaporization coefficient, also known as mass accommodation coefficient or sticking coefficient, which is the probability that vapor atoms or molecules will return to the surface. p_v is vapor pressure of the vaporized species, $\Gamma_{v,s}$ is diffusion coefficient. Here T_p indicates the vapor temperature, which is assumed to be identical to the particle temperature in the vaporization process [153].

The diffusion coefficient of the particle vapor $\Gamma_{v,s}$ is given [25]:

$$\Gamma_{v,s} = \frac{fk_B T_p}{4\Sigma_{v,s} p_v} \sqrt{\frac{RT_p}{2\pi M_v}} \quad (\text{B.17})$$

$\Sigma_{v,s}$ is the molecule cross-section of the vapor.

The vapor pressure p_v is related to the latent heat of vaporization through the Clausius-Clapeyron equation, thermal equilibrium between the nanoparticle and the gas.

$$p_v = C_1 \exp\left(-\frac{\Delta H_v}{k_B T_p}\right) \quad (\text{B.18})$$

where C_1 is the material constant related to the reference point, ΔH_v is the latent heat of vaporization at a reference point.

Solving the mass and energy balance from Eq.(B.5) - (B.18), the temperature evolution of the particle can be obtained as the particle passes through the heating and cooling processes.

B.2.4 Thermal radiation

The total energy lost due to radiation can be calculated by integrating the thermal emission (Eq.(4.2)) over all 4π steradians (total surface S) and over all wavelengths.

$$\dot{Q}_{\text{rad}} = \int_0^\infty \int_S C_{\text{abs},\lambda} I_b(\lambda, T_p(t)) \Delta\Omega_{\text{det}} d\Omega d\lambda \quad (\text{B.19})$$

where $C_{\text{abs},\lambda}$ is the absorption cross-section, $I_b(\lambda, T_p(t))$ is blackbody intensity of a body for wavelength λ at absolute temperature $T_p(t)$ of a body and $\Delta\Omega_{\text{det}}$ is the solid angle subtended by the detector as viewed by the nanoparticle.

Attention should be paid attention that Stefan-Boltzmann law (used in the model of [397]) which governs macroscopic objects, can not be applied in nanoscale particles. Still, the cooling loss by thermal radiation is relatively smaller than those of other cooling processes; conduction at atmospheric pressure and vaporization at high laser fluence. Therefore, the radiative cooling effect is often neglected in the energy-mass balance equation [268].

Appendix C

Flame structure parametric study

The fuel and oxidizer flow rates have important roles in the flame structure. In diffusion coflow flame structures, when the fuel rate increases with a constant rate of oxidizer, the flame length becomes longer and the fluctuation at the flame tail increases. In this case, the flame gets richer since the global equivalence ratio ϕ increases. On the other hand, when the oxidizer flow rate in coflow increases with a constant fuel rate, it slightly shortens the flame length, and the flame becomes leaner (ϕ decreases). When the oxidizer increases more, the flame can be lifted. With an even higher oxidizer flow rate, the flame can be blown out due to the excessive oxidizer flow. The same tendency can be found in fuel dilution cases involving inert gas [338]. The overall aspect with the effect of air and fuel rate is shown in Fig. C.1 with the example of CH₄ fuel diluted with N₂ and air coflow in ambient temperature. In a higher temperature environment with a pre-heating system (Sec. 6.1.2), the range of the non-blowout operating region is increased resulting in stronger flame luminescence at the same operating point.

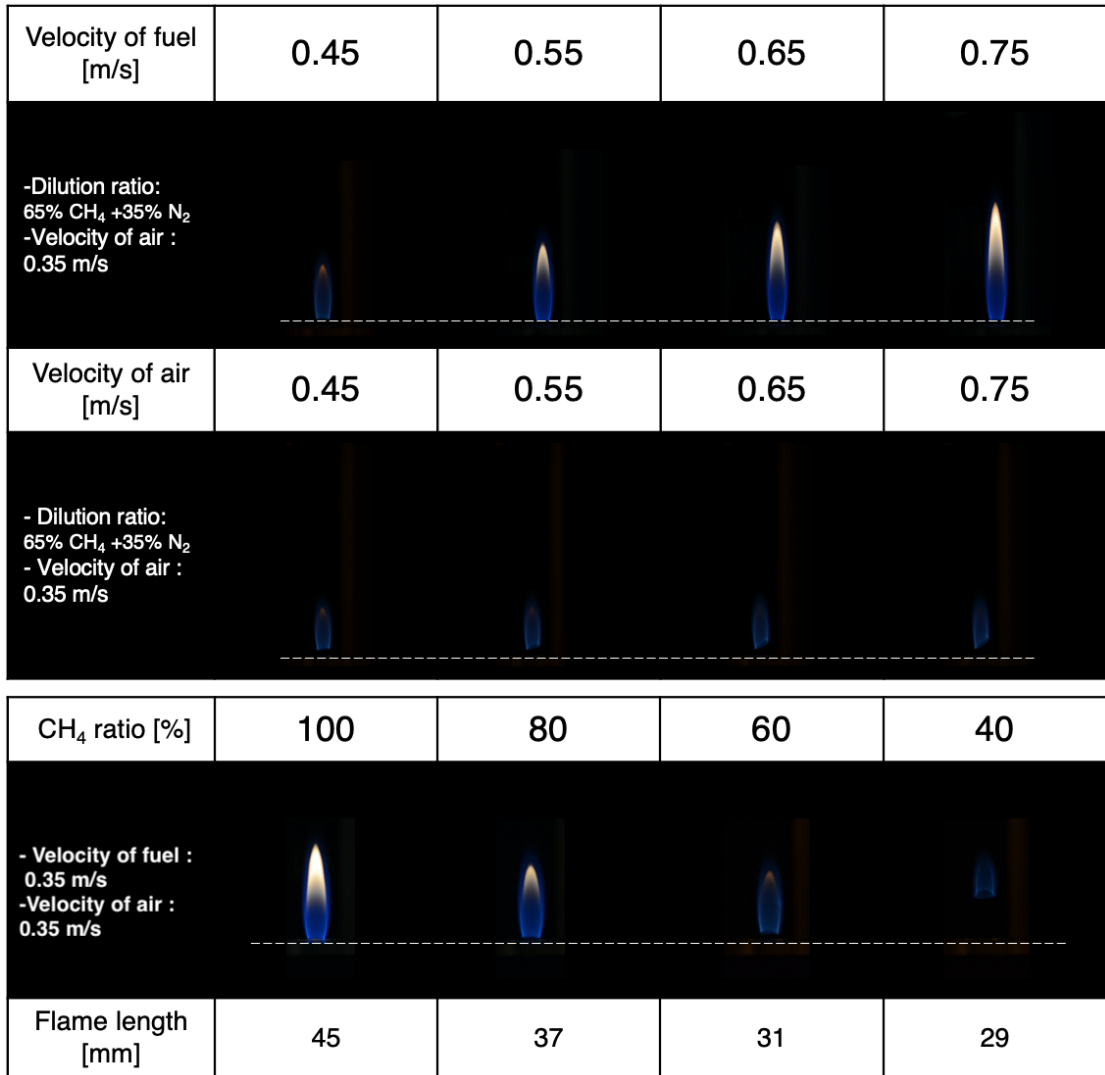


Figure C.1. The effect of fuel rate, oxidizer rate, and dilution ratio on the flame structure in the YDB burner. The fuel is a mixture of CH₄ and N₂, and the coflow is air. The height above the burner (HAB) = 0 mm is marked by a white dashed line.

Appendix D

Characterization of prompt/delayed LIE from flame-generated TiO₂

The prompt emission spectra of flame-generated TiO₂ particles are shown in Fig. D.1. At low fluence ($F = 0.1 \text{ J/cm}^2$ and $F = 0.15 \text{ J/cm}^2$), the emission presents a broadband continuous emission in the visible range without sharp features for all flame heights (except for $F = 0.15 \text{ J/cm}^2$ at HAB = 30 mm, near 500 nm). Compared to these smooth broadband emission, sharp peaks are more significant at $F = 0.19 \text{ J/cm}^2$ than at $F = 0.24 \text{ J/cm}^2$, possibly indicating that LIE contains non-thermal interference from LIF, PS-LIBS.

Figure D.2 shows the laser-induced emission spectra of flame-generated TiO₂ nanoparticles for three heights by considering various acquisition delays from the prompt timing. The emission spectra for three heights all show a red-shift for increasing time delay indicating that the temperature decreases, as expected from LII theory.

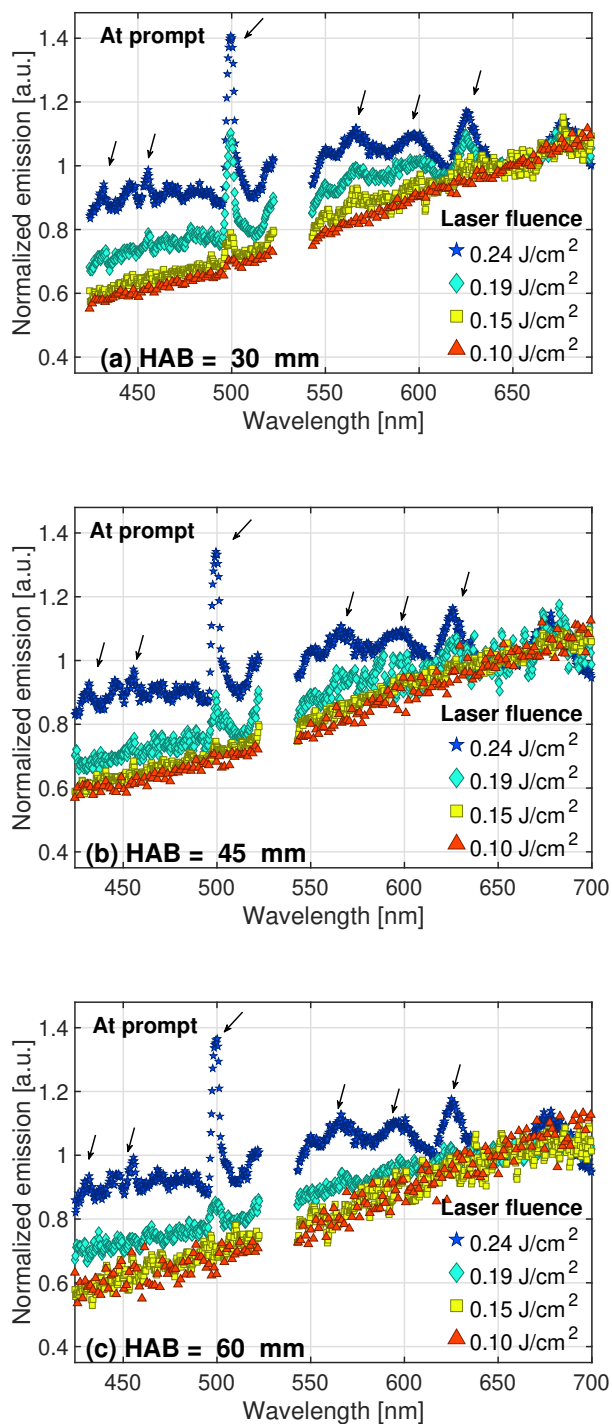


Figure D.1. Effect of laser fluence F on laser-induced emission spectra at prompt for flame-generated TiO_2 nanoparticles. Spectra are normalized by the value of 650 nm.

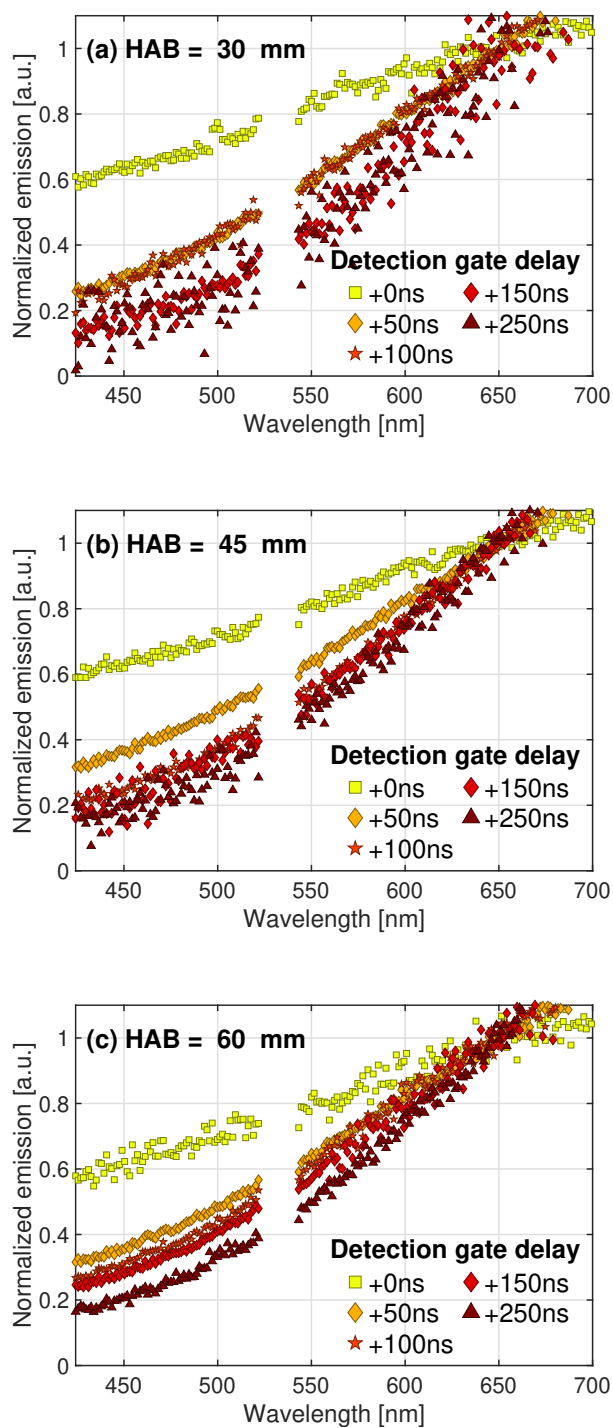


Figure D.2. Effect of gate delay (gate width = 20 ns) on emission spectra of laser-induced emissions of flame-generated TiO₂ nanoparticles at laser fluence $F = 0.15 \text{ J/cm}^2$. Spectra are normalized with the value of the spectrum at 650 nm.

Bibliography

- [1] A. Barhoum, M. L. García-Betancourt, J. Jeevanandam, E. A. Hussien, S. A. Mekkawy, M. Mostafa, M. M. Omran, M. S. Abdalla, and M. Bechelany. Review on natural, incidental, bioinspired, and engineered nanomaterials: history, definitions, classifications, synthesis, properties, market, toxicities, risks, and regulations. *Nanomaterials*, 12(2):177, 2022. p. 1, 9
- [2] M. E. Vance, T. Kuiken, E. P. Vejerano, S. P. McGinnis, M. F. Hochella Jr., D. Rejeski, and M. S. B. Hull. Nanotechnology in the real world: Redeveloping the nanomaterial consumer products inventory. *J. Nanotechnol.*, 5:1769–1780, 2015. p. 1
- [3] H. G. Völz, J. Kischkewitz, P. Woditsch, A. Westerhaus, W.-D. Griebler, M. De Liedekerke, G. Buxbaum, H. Printzen, M. Mansmann, D. Råde, et al. Pigments, inorganic. *Ullmann's Encyclopedia of Industrial Chemistry*, 2000. p. 1, 26, 27, 28, 29, 187
- [4] A. B. Muñoz-García, I. Benesperi, G. Boschloo, J. J. Concepcion, J. H. Delcamp, E. A. Gibson, G. J. Meyer, M. Pavone, H. Pettersson, A. Hagfeldt, et al. Dye-sensitized solar cells strike back. *Chemical Society Reviews*, 2021. p. 1
- [5] M. Cerro-Lopez and M. A. Méndez-Rojas. Application of nanomaterials for treatment of wastewater containing pharmaceuticals. In *Ecopharmacovigilance*, pages 201–219. Springer, 2017. p. xvii, 1, 10
- [6] F. Meierhofer and U. Fritsching. Synthesis of metal oxide nanoparticles in flame sprays: review on process technology, modeling, and diagnostics. *Energy & Fuels*, 35(7):5495–5537, 2021. p. 2, 21, 39, 41, 47, 49
- [7] R. Strobel, A. Baiker, and S. E. Pratsinis. Aerosol flame synthesis of catalysts. *Advanced Powder Technology*, 17(5):457–480, 2006. p. 2
- [8] K. B. Riad, P. M. Wood-Adams, and K. Wegner. Flame-made TiO₂ (B). *Materials Research Bulletin*, 106:276–281, 2018. p. 2, 9, 25, 41
- [9] A. Teleki, S. E. Pratsinis, K. Kalyanasundaram, and P. Gouma. Sensing of organic vapors by flame-made TiO₂ nanoparticles. *Sensors and actuators B: chemical*, 119(2):683–690, 2006. p. 2
- [10] A. C. Eckbreth. Effects of laser-modulated particulate incandescence on raman scattering diagnostics. *Journal of Applied Physics*, 48(11):4473–4479, 1977. p. 2, 69, 183
- [11] L. A. Melton. Soot diagnostics based on laser heating. *Applied optics*, 23(13):2201–2208, 1984. p. 2, 69, 183
- [12] T. A. Sipkens, J. Menser, T. Dreier, C. Schulz, G. J. Smallwood, and K. J. Daun. Laser-induced incandescence for non-soot nanoparticles: recent trends and current challenges.

- Applied Physics B*, 128(4):1–31, 2022. p. xix, xxi, 2, 3, 40, 51, 57, 75, 79, 183
- [13] R. L. Vander Wal, T. M. Ticich, and J. R. West. Laser-induced incandescence applied to metal nanostructures. *Applied optics*, 38(27):5867–5879, 1999. p. 2, 3, 78
- [14] Y. Murakami, T. Sugatani, and Y. Nosaka. Laser-induced incandescence study on the metal aerosol particles as the effect of the surrounding gas medium. *The Journal of Physical Chemistry A*, 109(40):8994–9000, 2005. p. 2
- [15] T. Sipkens, N. Singh, and K. Daun. Time-resolved laser-induced incandescence characterization of metal nanoparticles. *Applied Physics B*, 123(1):1–17, 2017. p. 2, 69
- [16] K. Daun, J. Menser, R. Mansmann, S. T. Moghaddam, T. Dreier, and C. Schulz. Spectroscopic models for laser-heated silicon and copper nanoparticles. *Journal of Quantitative Spectroscopy and Radiative Transfer*, 197:3–11, 2017. p. 2, 79, 185
- [17] I. Altman, D. Lee, J. Chung, J. Song, and M. Choi. Light absorption of silica nanoparticles. *Physical Review B*, 63(16):161402, 2001. p. 2, 186
- [18] T. Lehre, R. Suntz, and H. Bockhorn. Time-resolved two-color LII: size distributions of nano-particles from gas-to-particle synthesis. *Proceedings of the Combustion Institute*, 30(2):2585–2593, 2005. p. 2, 73
- [19] S. Maffi, F. Cignoli, C. Bellomunno, S. De Iuliis, and G. Zizak. Spectral effects in laser induced incandescence application to flame-made titania nanoparticles. *Spectrochimica Acta Part B: Atomic Spectroscopy*, 63(2):202–209, 2008. p. 2, 50, 69, 75, 78, 81
- [20] F. Cignoli, C. Bellomunno, S. Maffi, and G. Zizak. Laser-induced incandescence of titania nanoparticles synthesized in a flame. *Applied Physics B*, 96(4):593–599, 2009. p. 2, 50, 69, 75, 81, 177
- [21] B. Tribalet, A. Faccinnetto, T. Dreier, and C. Schultz. Evaluation of particle sizes of iron-oxide nano-particles in a low-pressure flame-synthesis reactor by simultaneous application of TiRe-LII and PMS. In *5th Workshop on Laser-induced Incandescence*, 2012. p. 2
- [22] T. Sipkens, R. Mansmann, K. Daun, N. Petermann, J. Titantah, M. Karttunen, H. Wiggers, T. Dreier, and C. Schulz. In situ nanoparticle size measurements of gas-borne silicon nanoparticles by time-resolved laser-induced incandescence. *Applied Physics B*, 116(3):623–636, 2014. p. 2, 69
- [23] J. Menser, K. Daun, T. Dreier, and C. Schulz. Laser-induced incandescence from laser-heated silicon nanoparticles. *Applied Physics B*, 122(11):277, 2016. p. 2, 69, 164, 185
- [24] G. Liu, M. Asif, J. Menser, T. Dreier, K. Mohri, C. Schulz, and T. Endres. Spatial distribution of gas-phase synthesized germanium nanoparticle volume-fraction and temperature using combined in situ line-of-sight emission and extinction spectroscopy. *Optics Express*, 29(6):8387–8406, 2021. p. 2, 75, 185
- [25] H. A. Michelsen. Understanding and predicting the temporal response of laser-induced incandescence from carbonaceous particles. *The Journal of chemical physics*, 118(15):7012–7045, 2003. p. xxiv, xxv, 3, 73, 75, 138, 139, 140, 153, 154, 194
- [26] J. C. Miller. Optical properties of liquid metals at high temperatures. *Philosophical Magazine*, 20(168):1115–1132, 1969. p. xxi, 3, 79
- [27] S. Krishnan, J. R. Weber, R. A. Schiffman, P. C. Nordine, and R. A. Reed. Refractive index of liquid aluminum oxide at 0.6328 μm . *Journal of the American Ceramic Society*, 74(4):881–883, 1991. p. 3

- [28] H. Gleiter. Nanostructured materials: state of the art and perspectives. *Nanostructured materials*, 6(1-4):3–14, 1995. p. 9
- [29] K. J. Klabunde and R. M. Richards. *Nanoscale materials in chemistry*. John Wiley & Sons, 2009. p. 9, 14, 28, 80
- [30] G. D. Ulrich. Theory of particle formation and growth in oxide synthesis flames. *Combustion Science and Technology*, 4(1):47–57, 1971. p. 9, 29
- [31] K. Wegner and S. E. Pratsinis. Scale-up of nanoparticle synthesis in diffusion flame reactors. *Chemical Engineering Science*, 58(20):4581–4589, 2003. p. 9, 30
- [32] M. Y. Manuputty, J. A. Dreyer, Y. Sheng, E. J. Bringley, M. L. Botero, J. Akroyd, and M. Kraft. Polymorphism of nanocrystalline TiO₂ prepared in a stagnation flame: formation of the TiO₂-II phase. *Chemical science*, 10(5):1342–1350, 2019. p. 9, 42
- [33] S. E. Pratsinis. Aerosol-based technologies in nanoscale manufacturing: from functional materials to devices through core chemical engineering. *AIChE journal*, 56(12):3028–3035, 2010. p. 9
- [34] H. K. Kammler, R. Mueller, O. Senn, and S. E. Pratsinis. Synthesis of silica-carbon particles in a turbulent H₂-air flame aerosol reactor. *AIChE Journal*, 47(7):1533–1543, 2001. p. 9
- [35] H. K. Kammler and S. E. Pratsinis. Carbon-coated titania nanostructured particles: Continuous, one-step flame-synthesis. *Journal of materials research*, 18(11):2670–2676, 2003. p. 9, 42, 81
- [36] W. Y. Teoh, R. Amal, and L. Mädler. Flame spray pyrolysis: An enabling technology for nanoparticles design and fabrication. *Nanoscale*, 2(8):1324–1347, 2010. p. xvii, 9, 21, 22, 23, 24
- [37] S. Pokhrel and L. Mädler. Flame-made particles for sensors, catalysis, and energy storage applications. *Energy & Fuels*, 34(11):13209–13224, 2020. p. 9, 22, 30
- [38] N. Kumar and S. Kumbhat. *Concise Concepts of Nanoscience and Nanomaterials*. Scientific Publishers, 2018. p. xvii, 10, 11
- [39] G. A. Kelesidis, E. Goudeli, and S. E. Pratsinis. Flame synthesis of functional nanostructured materials and devices: Surface growth and aggregation. *Proceedings of the Combustion Institute*, 36(1):29–50, 2017. p. 11
- [40] E. Comini and G. Sberveglieri. Metal oxide nanowires as chemical sensors. *Materials Today*, 13(7-8):36–44, 2010. p. 11
- [41] Z. Wang, X. Pan, Y. He, Y. Hu, H. Gu, and Y. Wang. Piezoelectric nanowires in energy harvesting applications. *Advances in Materials Science and Engineering*, 2015, 2015. p. 11
- [42] B. C. Steele and A. Heinzl. Materials for fuel-cell technologies. In *Materials for sustainable energy: a collection of peer-reviewed research and review articles from Nature Publishing Group*, pages 224–231. World Scientific, 2011. p. 11
- [43] S. Kango, S. Kalia, A. Celli, J. Njuguna, Y. Habibi, and R. Kumar. Surface modification of inorganic nanoparticles for development of organic–inorganic nanocomposites—a review. *Progress in Polymer Science*, 38(8):1232–1261, 2013. p. 11, 13
- [44] S. Liu, M. M. Mohammadi, and M. T. Swihart. Fundamentals and recent applications of catalyst synthesis using flame aerosol technology. *Chemical Engineering Journal*,

- 405:126958, 2021. p. 11, 30
- [45] E. C. Dreaden, A. M. Alkilany, X. Huang, C. J. Murphy, and M. A. El-Sayed. The golden age: gold nanoparticles for biomedicine. *Chemical Society Reviews*, 41(7):2740–2779, 2012. p. xvii, 12, 13
- [46] D. Guo, G. Xie, and J. Luo. Mechanical properties of nanoparticles: basics and applications. *Journal of physics D: applied physics*, 47(1):013001, 2013. p. 13
- [47] H. Yang, M. Monasterio, D. Zheng, H. Cui, W. Tang, X. Bao, and X. Chen. Effects of nano silica on the properties of cement-based materials: a comprehensive review. *Construction and Building Materials*, 282:122715, 2021. p. 13
- [48] K. Cui, J. Chang, L. Feo, C. L. Chow, and D. Lau. Developments and applications of carbon nanotube reinforced cement-based composites as functional building materials. *Frontiers in Materials*, page 146, 2022. p. 13
- [49] C. A. Charitidis, P. Georgiou, M. A. Koklioti, A.-F. Trompeta, and V. Markakis. Manufacturing nanomaterials: from research to industry. *Manufacturing Review*, 1:11, 2014. p. xvii, 13, 18
- [50] L. P. da Costa. Engineered nanomaterials in the sports industry. In *Handbook of nanomaterials for manufacturing applications*, pages 309–320. Elsevier, 2020. p. 13
- [51] J. N. Anker, W. P. Hall, O. Lyandres, N. C. Shah, J. Zhao, and R. P. Van Duyne. Biosensing with plasmonic nanosensors. *Nature materials*, 7(6):442–453, 2008. p. 13
- [52] M. S. Chavali and M. P. Nikolova. Metal oxide nanoparticles and their applications in nanotechnology. *SN Applied Sciences*, 1(6):607, 2019. p. 13, 14
- [53] W.-Y. Li, L.-N. Xu, and J. Chen. Co_3O_4 nanomaterials in lithium-ion batteries and gas sensors. *Advanced Functional Materials*, 15(5):851–857, 2005. p. 13
- [54] P. Subalakshmi and A. Sivashanmugam. Cuo nano hexagons, an efficient energy storage material for li-ion battery application. *Journal of Alloys and Compounds*, 690:523–531, 2017. p. 13
- [55] M. E. Franke, T. J. Koplín, and U. Simon. Metal and metal oxide nanoparticles in chemiresistors: does the nanoscale matter? *small*, 2(1):36–50, 2006. p. 14
- [56] A. Tricoli, M. Righettoni, and A. Teleki. Semiconductor gas sensors: dry synthesis and application. *Angewandte Chemie International Edition*, 49(42):7632–7659, 2010. p. 14
- [57] S. P. Lee. Electrodes for semiconductor gas sensors. *Sensors*, 17(4):683, 2017. p. xvii, 14
- [58] S. U. Choi and J. A. Eastman. Enhancing thermal conductivity of fluids with nanoparticles. Technical report, Argonne National Lab.(ANL), Argonne, IL (United States), 1995. p. 14
- [59] K. Y. Leong, Z. Najwa, K. Ku Ahmad, and H. C. Ong. Investigation on stability and optical properties of titanium dioxide and aluminum oxide water-based nanofluids. *International Journal of Thermophysics*, 38(5):1–15, 2017. p. 14
- [60] I. Khan, K. Saeed, and I. Khan. Nanoparticles: Properties, applications and toxicities. *Arabian journal of chemistry*, 12(7):908–931, 2019. p. 14
- [61] V. Harish, M. M. Ansari, D. Tewari, M. Gaur, A. B. Yadav, M.-L. García-Betancourt, F. M. Abdel-Haleem, M. Bechelany, and A. Barhoum. Nanoparticle and nanostructure synthesis and controlled growth methods. *Nanomaterials*, 12(18):3226, 2022. p. 15

- [62] D. Williams, M. Amman, H. Autrup, J. Bridges, F. Cassee, K. Donaldson, E. Fattal, C. Janssen, W. De Jong, T. Jung, et al. The appropriateness of existing methodologies to assess the potential risks associated with engineered and adventitious products of nanotechnologies. *Proceedings of the European Commission Health and Consumer Protection Directorate General by the Scientific Committee on Emerging and Newly Identified Health Risks, Brussels, Belgium*, 10, 2006. p. 15
- [63] S. Stankic, S. Suman, F. Haque, and J. Vidic. Pure and multi metal oxide nanoparticles: synthesis, antibacterial and cytotoxic properties. *Journal of nanobiotechnology*, 14(1):73, 2016. p. xvii, 16
- [64] B. Joyce. Molecular beam epitaxy. *Reports on Progress in Physics*, 48(12):1637, 1985. p. 16
- [65] R. Delmdahl and R. Pätzelt. Pulsed laser deposition- UV laser sources and applications. *pulse*, 400(700mJ):650mJ, 2008. p. 16
- [66] H. Kim, J. An, S. Maeng, J.-S. Shin, E. Choi, and J.-Y. Yun. Decomposition characteristics of the TTIP (tetraisopropyl orthotitanate) precursor for atomic layer deposition. *Materials*, 15(9):3021, 2022. p. 16
- [67] M. Nguefack, A. F. Popa, S. Rossignol, and C. Kappenstein. Preparation of alumina through a sol-gel process. synthesis, characterization, thermal evolution and model of intermediate boehmite. *Physical Chemistry Chemical Physics*, 5(19):4279–4289, 2003. p. 17
- [68] C. B. Carter, M. G. Norton, et al. *Ceramic materials: science and engineering*, volume 716. Springer, 2007. p. 17, 28, 64
- [69] C. Raab, M. Simko, U. Fiedeler, M. Nentwich, and A. Gazso. Production of nanoparticles and nanomaterials. *Nano Trust Dossier*, 6:1998–7293, 2011. p. 17
- [70] R. C. Mehrotra and A. Singh. Recent trends in metal alkoxide chemistry. *Progress in Inorganic Chemistry*, 46:239–454, 1997. p. xvii, 17
- [71] A. Nikam, B. Prasad, and A. Kulkarni. Wet chemical synthesis of metal oxide nanoparticles: a review. *CrystEngComm*, 20(35):5091–5107, 2018. p. 18
- [72] E. Hontañón, J. M. Palomares, M. Stein, X. Guo, R. Engeln, H. Nirschl, and F. E. Kruijs. The transition from spark to arc discharge and its implications with respect to nanoparticle production. *Journal of nanoparticle research*, 15(9):1957, 2013. p. 19
- [73] Y. Saito, K. Nishikubo, K. Kawabata, and T. Matsumoto. Carbon nanocapsules and single-layered nanotubes produced with platinum-group metals (Ru, Rh, Pd, Os, Ir, Pt) by arc discharge. *Journal of applied physics*, 80(5):3062–3067, 1996. p. xvii, 19
- [74] S.-B. Wen, X. Mao, R. Greif, and R. E. Russo. Experimental and theoretical studies of particle generation after laser ablation of copper with a background gas at atmospheric pressure. *Journal of Applied Physics*, 101(12):123105, 2007. p. 19
- [75] M. Kim, S. Osone, T. Kim, H. Higashi, and T. Seto. Synthesis of nanoparticles by laser ablation: A review. *KONA Powder and Particle Journal*, page 2017009, 2017. p. 19
- [76] D. Vollath. Plasma synthesis of nanopowders. *Journal of Nanoparticle Research*, 10(1):39, 2008. p. xvii, 20
- [77] S. Tjong and H. Chen. Nanocrystalline materials and coatings. *Materials Science and Engineering: R: Reports*, 45(1-2):1–88, 2004. p. 20

- [78] B. Buesser and S. E. Pratsinis. Design of nanomaterial synthesis by aerosol processes. *Annual review of chemical and biomolecular engineering*, 3:103–127, 2012. p. xviii, 20, 29, 33, 36
- [79] M. J. Hampden-Smith and T. T. Kodas. Chemical vapor deposition of metals: Part 1. an overview of cvd processes. *Chemical Vapor Deposition*, 1(1):8–23, 1995. p. 20
- [80] S. Zhuang, X. Shi, and E. S. Lee. A review on Non-PGM cathode catalysts for polymer electrolyte membrane (PEM) fuel cell. In *International Conference on Fuel Cell Science, Engineering and Technology*, volume 56611, page V001T04A005. American Society of Mechanical Engineers, 2015. p. xvii, 20
- [81] H. K. Kammler, L. Mädler, and S. E. Pratsinis. Flame synthesis of nanoparticles. *Chemical Engineering & Technology: Industrial Chemistry-Plant Equipment-Process Engineering-Biotechnology*, 24(6):583–596, 2001. p. 21, 29
- [82] A. Gurav, T. Kodas, T. Pluym, and Y. Xiong. Aerosol processing of materials. *Aerosol science and technology*, 19(4):411–452, 1993. p. 21
- [83] A. George, R. Murley, and E. Place. Formation of TiO₂ aerosol from the combustion supported reaction of TiCl₄ and O₂. In *Faraday Symposia of the Chemical Society*, volume 7, pages 63–71. Royal Society of Chemistry, 1973. p. 21
- [84] S. C. Jantzi, V. Motto-Ros, F. Trichard, Y. Markushin, N. Melikechi, and A. De Giacomo. Sample treatment and preparation for laser-induced breakdown spectroscopy. *Spectrochimica Acta Part B: Atomic Spectroscopy*, 115:52–63, 2016. p. 21
- [85] H. V. Nguyen and R. C. Flagan. Particle formation and growth in single-stage aerosol reactors. *Langmuir*, 7(8):1807–1814, 1991. p. 21
- [86] K.-S. Kim and S. E. Pratsinis. Manufacture of optical waveguide preforms by modified chemical vapor deposition. *AIChE journal*, 34(6):912–921, 1988. p. 21
- [87] S. E. Pratsinis and K.-S. Kim. Particle coagulation, diffusion and thermophoresis in laminar tube flows. *Journal of Aerosol Science*, 20(1):101–111, 1989. p. 21
- [88] S. E. Pratsinis, H. Bai, P. Biswas, M. Frenklach, and S. V. Mastrangelo. Kinetics of titanium (iv) chloride oxidation. *Journal of the American Ceramic Society*, 73(7):2158–2162, 1990. p. 21
- [89] K. Okuyama, Y. Kousaka, N. Tohge, S. Yamamoto, J. J. Wu, R. Flagan, and J. Seinfeld. Production of ultrafine metal oxide aerosol particles by thermal decomposition of metal alkoxide vapors. *AIChE Journal*, 32(12):2010–2019, 1986. p. 21
- [90] R. Koirala, S. E. Pratsinis, and A. Baiker. Synthesis of catalytic materials in flames: opportunities and challenges. *Chemical Society Reviews*, 45(11):3053–3068, 2016. p. xvii, 22
- [91] C. D. Rosebrock, T. Wriedt, L. Mädler, and K. Wegner. The role of microexplosions in flame spray synthesis for homogeneous nanopowders from low-cost metal precursors. *AIChE Journal*, 62(2):381–391, 2016. p. 22
- [92] L. Mädler, A. Roessler, S. E. Pratsinis, T. Sahm, A. Gurlo, N. Barsan, and U. Weimar. Direct formation of highly porous gas-sensing films by in situ thermophoretic deposition of flame-made Pt/SnO₂ nanoparticles. *Sensors and Actuators B: Chemical*, 114(1):283–295, 2006. p. 22
- [93] W. J. Stark, K. Wegner, S. E. Pratsinis, and A. Baiker. Flame aerosol synthesis of vanadia-

- titania nanoparticles: structural and catalytic properties in the selective catalytic reduction of no by nh₃. *Journal of Catalysis*, 197(1):182–191, 2001. p. xvii, 23
- [94] F. Meierhofer, L. Mädler, and U. Fritsching. Nanoparticle evolution in flame spray pyrolysis—process design via experimental and computational analysis. *AIChE Journal*, 66(2):e16885, 2020. p. 24
- [95] S. Li, Y. Ren, P. Biswas, and D. T. Stephen. Flame aerosol synthesis of nanostructured materials and functional devices: Processing, modeling, and diagnostics. *Progress in Energy and Combustion Science*, 55:1–59, 2016. p. 24, 65, 111
- [96] J. A. Dreyer, S. Pokhrel, J. Birkenstock, M. G. Hevia, M. Schowalter, A. Rosenauer, A. Urakawa, W. Y. Teoh, and L. Mädler. Decrease of the required dopant concentration for δ -Bi₂O₃ crystal stabilization through thermal quenching during single-step flame spray pyrolysis. *CrystEngComm*, 18(12):2046–2056, 2016. p. 25
- [97] L. Wang, A. Teleki, S. E. Pratsinis, and P. Gouma. Ferroelectric WO₃ nanoparticles for acetone selective detection. *Chemistry of Materials*, 20(15):4794–4796, 2008. p. 25
- [98] T. Kogure, T. Umezawa, Y. Kotani, A. Matsuda, M. Tatsumisago, and T. Minami. Formation of TiO₂ (B) nanocrystallites in sol-gel-derived SiO₂-TiO₂ film. *Journal of the American Ceramic Society*, 82(11):3248–3250, 1999. p. 25
- [99] R. Grosjean, M. Fehse, S. Pigeot-Remy, L. Stievano, L. Monconduit, and S. Cassaignon. Facile synthetic route towards nanostructured Fe–TiO₂ (B), used as negative electrode for Li-ion batteries. *Journal of Power Sources*, 278:1–8, 2015. p. 25
- [100] F. Iskandar. Nanoparticle processing for optical applications - a review. *Advanced Powder Technology*, 20(4):283–292, 2009. p. xviii, 25
- [101] R. Mueller, L. Mädler, and S. E. Pratsinis. Nanoparticle synthesis at high production rates by flame spray pyrolysis. *Chemical Engineering Science*, 58(10):1969–1976, 2003. p. xviii, 25
- [102] K. Möls, L. Aarik, H. Mändar, A. Kasikov, A. Niilisk, R. Rammula, and J. Aarik. Influence of phase composition on optical properties of TiO₂: Dependence of refractive index and band gap on formation of TiO₂-II phase in thin films. *Optical Materials*, 96:109335, 2019. p. 26
- [103] T. Feng, L. Li, Q. Shi, Y. Zhang, and G. Li. Heat capacity and thermodynamic functions of TiO₂ (H). *The Journal of Chemical Thermodynamics*, 145:106040, 2020. p. 26
- [104] J. F. Banfield, D. R. Veblen, and D. J. Smith. The identification of naturally occurring TiO₂ (B) by structure determination using high-resolution electron microscopy, image simulation, and distance-least-squares refinement. *American Mineralogist*, 76(3-4):343–353, 1991. p. 26
- [105] S. M. Gupta and M. Tripathi. A review of TiO₂ nanoparticles. *Chinese Science Bulletin*, 56(16):1639, 2011. p. 26
- [106] X. You, F. Chen, and J. Zhang. Effects of calcination on the physical and photocatalytic properties of TiO₂ powders prepared by sol-gel template method. *Journal of sol-gel science and technology*, 34(2):181–187, 2005. p. 26
- [107] Y. Hu, H.-L. Tsai, and C.-L. Huang. Phase transformation of precipitated TiO₂ nanoparticles. *Materials Science and Engineering: A*, 344(1-2):209–214, 2003. p. 26
- [108] D. A. Hanaor and C. C. Sorrell. Review of the anatase to rutile phase transformation.

- Journal of Materials science*, 46(4):855–874, 2011. p. xv, 26, 27
- [109] J. E. Haggerty, L. T. Schelhas, D. A. Kitchaev, J. S. Mangum, L. M. Garten, W. Sun, K. H. Stone, J. D. Perkins, M. F. Toney, G. Ceder, et al. High-fraction brookite films from amorphous precursors. *Scientific reports*, 7(1):1–11, 2017. p. xviii, 26, 27
- [110] V. N. Koparde and P. T. Cummings. Phase transformations during sintering of titania nanoparticles. *ACS nano*, 2(8):1620–1624, 2008. p. 26
- [111] R. J. Lauf. *The Collector's Guide to the Three Phases of Titania : Rutile, Anatase, and Brookite*. Schiffer Publishing, Ltd, 2009. p. xviii, 26
- [112] W. M. Haynes. *CRC handbook of chemistry and physics*. CRC press, 2014. p. xv, 27
- [113] F. J. Bauer, P. A. Braeuer, S. Abmann, M. A. Thiele, F. J. Huber, and S. Will. Characterisation of the transition type in optical band gap analysis of in-flame soot. *Combustion and Flame*, page 111986, 2022. p. 28
- [114] K. Nakata and A. Fujishima. TiO₂ photocatalysis: design and applications. *Journal of photochemistry and photobiology C: Photochemistry Reviews*, 13(3):169–189, 2012. p. 28
- [115] J. Stötzel, D. Lützenkirchen-Hecht, R. Frahm, C. V. Santilli, S. H. Pulcinelli, R. Kaminski, E. Fonda, F. Villain, and V. Briois. Qexafs and uv/vis simultaneous monitoring of the TiO₂-nanoparticles formation by hydrolytic sol-gel route. *The Journal of Physical Chemistry C*, 114(14):6228–6236, 2010. p. 28
- [116] J. Wang, S. Li, W. Yan, D. T. Stephen, and Q. Yao. Synthesis of TiO₂ nanoparticles by premixed stagnation swirl flames. *Proceedings of the Combustion Institute*, 33(2):1925–1932, 2011. p. 28
- [117] K. Tanaka, M. F. Capule, and T. Hisanaga. Effect of crystallinity of TiO₂ on its photocatalytic action. *Chemical Physics Letters*, 187(1-2):73–76, 1991. p. 28
- [118] S. E. Pratsinis and P. T. Spicer. Competition between gas phase and surface oxidation of TiCl₄ during synthesis of TiO₂ particles. *Chemical Engineering Science*, 53(10):1861–1868, 1998. p. 29
- [119] R. Shirley, Y. Liu, T. S. Totton, R. H. West, and M. Kraft. First-principles thermochemistry for the combustion of a TiCl₄ and AlCl₃ mixture. *The Journal of Physical Chemistry A*, 113(49):13790–13796, 2009. p. 29
- [120] K. Okuyama, R. Ushio, Y. Kousaka, R. C. Flagan, and J. H. Seinfeld. Particle generation in a chemical vapor deposition process with seed particles. *AIChE journal*, 36(3):409–419, 1990. p. 29, 111
- [121] A. Kobata, K. Kusakabe, and S. Morooka. Growth and transformation of TiO₂ crystallites in aerosol reactor. *AIChE journal*, 37(3):347–359, 1991. p. 29
- [122] T. Seto, A. Hirota, T. Fujimoto, M. Shimada, and K. Okuyama. Sintering of polydisperse nanometer-sized agglomerates. *Aerosol Science and Technology*, 27(3):422–438, 1997. p. 29
- [123] S. E. Pratsinis. Flame aerosol synthesis of ceramic powders. *Progress in Energy and Combustion Science*, 24(3):197–220, 1998. p. 29, 36
- [124] R. N. Grass, S. Tsantilis, and S. E. Pratsinis. Design of high-temperature, gas-phase synthesis of hard or soft TiO₂ agglomerates. *AIChE journal*, 52(4):1318–1325, 2006. p. 29

- [125] H. Juergen, A. Braun, R. Baidins, and E. Marganski. TiO₂ pigment technology: a review. *Progress in Organic Coatings*, 20(5):109–110, 1992. p. 29
- [126] M. J. Gázquez, J. P. Bolívar, R. Garcia-Tenorio, and F. Vaca. A review of the production cycle of titanium dioxide pigment. *Materials Sciences and Applications*, 2014, 2014. p. 29
- [127] North america titanium dioxide market size, by process (sulfate, chloride), by grade (rutile, anatase), by product (pigmentary, ultrafine), by application (food, paints & coatings, paper & pulp, textiles, plastics & rubber, cosmetics, printing inks), industry analysis report, growth potential, price trends, competitive market share & forecast, 2020 - 2026. p. 29
- [128] Titanium dioxide market by grade (rutile, anatase), process (sulfate, chloride), application (paints & coating, plastics, paper, inks), & region(north america, europe, asia pacific, mea, south america) - trends and forecasts up to 2026. p. 29
- [129] E. Linak and Y. Inoguchi. Chemical economics handbook: Titanium dioxidell. *Mentlo Park, CA, SRI Consulting*, 2005. p. 29
- [130] K. Schumacher, A. Schild, and M. Moerters. Flame-hydrolytically produced titanium dioxide powder, Mar. 30 2010. US Patent 7,686,881. p. 29
- [131] A. Hunt, W. Carter, and J. Cochran Jr. Combustion chemical vapor deposition: A novel thin-film deposition technique. *Applied Physics Letters*, 63(2):266–268, 1993. p. 30
- [132] L. Mädler, H. K. Kammler, R. Mueller, and S. E. Pratsinis. Controlled synthesis of nanostructured particles by flame spray pyrolysis. *Journal of Aerosol Science*, 33(2):369–389, 2002. p. xviii, 30, 43
- [133] K. Wegner, B. Schimmoeller, B. Thiebaut, C. Fernandez, and T. N. Rao. Pilot plants for industrial nanoparticle production by flame spray pyrolysis. *KONA Powder and Particle Journal*, 29:251–265, 2011. p. 30
- [134] N. K. Memon, D. H. Anjum, and S. H. Chung. Multiple-diffusion flame synthesis of pure anatase and carbon-coated titanium dioxide nanoparticles. *Combustion and flame*, 160(9):1848–1856, 2013. p. xviii, 30, 40, 41, 69, 81, 108
- [135] R. Strobel and S. E. Pratsinis. Flame aerosol synthesis of smart nanostructured materials. *Journal of Materials Chemistry*, 17(45):4743–4756, 2007. p. 31
- [136] V. Raman and R. O. Fox. Modeling of fine-particle formation in turbulent flames. *Annual Review of Fluid Mechanics*, 48:159–190, 2016. p. xviii, 31, 36
- [137] H. A. Michelsen, M. B. Colket, P.-E. Bengtsson, A. D’anna, P. Desgroux, B. S. Haynes, J. H. Miller, G. J. Nathan, H. Pitsch, and H. Wang. A review of terminology used to describe soot formation and evolution under combustion and pyrolytic conditions. *ACS nano*, 14(10):12470–12490, 2020. p. 32, 35, 36
- [138] C. Saggese, S. Ferrario, J. Camacho, A. Cuoci, A. Frassoldati, E. Ranzi, H. Wang, and T. Faravelli. Kinetic modeling of particle size distribution of soot in a premixed burner-stabilized stagnation ethylene flame. *Combustion and Flame*, 162(9):3356–3369, 2015. p. 33
- [139] R. I. Patterson and M. Kraft. Models for the aggregate structure of soot particles. *Combustion and Flame*, 151(1-2):160–172, 2007. p. 33
- [140] G. A. Kelesidis, E. Goudeli, and S. E. Pratsinis. Morphology and mobility diameter of

- carbonaceous aerosols during agglomeration and surface growth. *Carbon*, 121:527–535, 2017. p. 34, 44
- [141] M. L. Eggersdorfer and S. E. Pratsinis. Agglomerates and aggregates of nanoparticles made in the gas phase. *Advanced Powder Technology*, 25(1):71–90, 2014. p. xviii, 34, 36
- [142] C. S. Lindberg, M. Y. Manuputty, J. Akroyd, and M. Kraft. A two-step simulation methodology for modelling stagnation flame synthesised aggregate nanoparticles. *Combustion and Flame*, 202:143–153, 2019. p. 35, 164
- [143] M. Y. Manuputty, J. Akroyd, S. Mosbach, and M. Kraft. Modelling TiO₂ formation in a stagnation flame using method of moments with interpolative closure. *Combustion and Flame*, 178:135–147, 2017. p. 35
- [144] S. Friedlander and C. Wang. The self-preserving particle size distribution for coagulation by brownian motion. *Journal of Colloid and interface Science*, 22(2):126–132, 1966. p. 36
- [145] S. K. Friedlander et al. *Smoke, dust, and haze*, volume 198. Oxford university press New York, 2000. p. 36
- [146] S. K. Friedlander and D. Smoke. *Haze: Fundamentals of aerosol dynamics*, 2000. p. 36
- [147] S. Tsantilis and S. E. Pratsinis. Soft-and hard-agglomerate aerosols made at high temperatures. *Langmuir*, 20(14):5933–5939, 2004. p. 36
- [148] C. Liu, J. Camacho, and H. Wang. Phase equilibrium of TiO₂ nanocrystals in flame-assisted chemical vapor deposition. *ChemPhysChem*, 19(2):180–186, 2018. p. xx, 36, 76
- [149] M. L. Eggersdorfer, D. Kadau, H. J. Herrmann, and S. E. Pratsinis. Multiparticle sintering dynamics: from fractal-like aggregates to compact structures. *Langmuir*, 27(10):6358–6367, 2011. p. 37
- [150] H.-K. Ma, T.-J. Pan, P.-T. Cheng, et al. Numerical study of the nanoparticle formation mechanism in a titania flame combustion synthesis process. *Aerosol and Air Quality Research*, 14(1):251–259, 2014. p. 38
- [151] M. K. Akhtar, Y. Xiong, and S. E. Pratsinis. Vapor synthesis of titania powder by titanium tetrachloride oxidation. *AIChE Journal*, 37(10):1561–1570, 1991. p. 38
- [152] G. J. Smallwood, D. Clavel, D. Gareau, R. A. Sawchuk, D. R. Snelling, P. O. Witze, B. Axelsson, W. D. Bachalo, and Ö. L. Gülder. Concurrent quantitative laser-induced incandescence and SMPS measurements of EGR effects on particulate emissions from a TDI diesel engine. *SAE Transactions*, pages 1345–1360, 2002. p. 39, 44
- [153] B. F. Kock, C. Kayan, J. Knipping, H. R. Orthner, and P. Roth. Comparison of LII and TEM sizing during synthesis of iron particle chains. *Proceedings of the Combustion Institute*, 30(1):1689–1697, 2005. p. 40, 194
- [154] T. Yamaguchi, K. Kondo, H. Nishigai, S. Takano, and T. Aizawa. Direct sampling, TEM analysis and optical measurement of soot particles at different axial locations in a transient spray flame. *SAE International Journal of Fuels and Lubricants*, 5(1):316–328, 2012. p. 40
- [155] N. J. Kempema and M. B. Long. Combined optical and TEM investigations for a detailed characterization of soot aggregate properties in a laminar coflow diffusion flame.

- Combustion and Flame*, 164:373–385, 2016. p. 40
- [156] F. Einar Kruijs, J. Van Denderen, H. Buurman, and B. Scarlett. Characterization of agglomerated and aggregated aerosol particles using image analysis. *Particle & particle systems characterization*, 11(6):426–435, 1994. p. 41
- [157] I. Grishin, K. Thomson, F. Migliorini, and J. J. Sloan. Application of the hough transform for the automatic determination of soot aggregate morphology. *Applied optics*, 51(5):610–620, 2012. p. 41
- [158] A. Bescond, J. Yon, F. Ouf, D. Ferry, D. Delhaye, D. Gaffié, A. Coppalle, and C. Rozé. Automated determination of aggregate primary particle size distribution by TEM image analysis: application to soot. *Aerosol Science and Technology*, 48(8):831–841, 2014. p. 41
- [159] R. F. Egerton. *Electron energy-loss spectroscopy in the electron microscope*. Springer Science & Business Media, 2011. p. 41
- [160] M. A. Ismail, N. K. Memon, M. S. Mansour, D. H. Anjum, and S. H. Chung. Curved wall-jet burner for synthesizing titania and silica nanoparticles. *Proceedings of the Combustion Institute*, 35(2):2267–2274, 2015. p. xviii, 42, 43
- [161] P. Jafarkhani, S. Dadras, M. Torkamany, and J. Sabbaghzadeh. Synthesis of nanocrystalline titania in pure water by pulsed Nd: YAG laser. *Applied surface science*, 256(12):3817–3821, 2010. p. 42
- [162] I. Nakamura, N. Negishi, S. Kutsuna, T. Ihara, S. Sugihara, and K. Takeuchi. Role of oxygen vacancy in the plasma-treated TiO₂ photocatalyst with visible light activity for NO removal. *Journal of Molecular Catalysis A: Chemical*, 161(1-2):205–212, 2000. p. 42
- [163] C. B. Almquist and P. Biswas. Role of synthesis method and particle size of nanostructured TiO₂ on its photoactivity. *Journal of Catalysis*, 212(2):145–156, 2002. p. 42
- [164] S. Kumar, N. Verma, and M. Singla. Size dependent reflective properties of TiO₂ nanoparticles and reflectors made thereof. *Digest Journal of Nanomaterials and Biostructures*, 7(2):607–619, 2012. p. 42
- [165] L. G. Bettini, M. V. Dozzi, F. Della Foglia, G. L. Chiarello, E. Selli, C. Lenardi, P. Piseri, and P. Milani. Mixed-phase nanocrystalline TiO₂ photocatalysts produced by flame spray pyrolysis. *Applied Catalysis B: Environmental*, 178:226–232, 2015. p. 42, 43
- [166] A. Kołodziejczak-Radzimska and T. Jesionowski. Zinc oxide—from synthesis to application: a review. *Materials*, 7(4):2833–2881, 2014. p. 42
- [167] H. M. Rietveld. A profile refinement method for nuclear and magnetic structures. *Journal of applied Crystallography*, 2(2):65–71, 1969. p. 42
- [168] R. W. Cheary and A. Coelho. A fundamental parameters approach to X-ray line-profile fitting. *Journal of Applied Crystallography*, 25(2):109–121, 1992. p. 42
- [169] S. Brunauer, P. H. Emmett, and E. Teller. Adsorption of gases in multimolecular layers. *Journal of the American chemical society*, 60(2):309–319, 1938. p. 43
- [170] M. S. Wooldridge, S. A. Danczyk, and J. Wu. Demonstration of gas-phase combustion synthesis of nanosized particles using a hybrid burner. *Nanostructured materials*, 11(7):955–964, 1999. p. 43
- [171] V. Krüger, C. Wahl, R. Hadeif, K. P. Geigle, W. Stricker, and M. Aigner. Comparison of

- laser-induced incandescence method with scanning mobility particle sizer technique: the influence of probe sampling and laser heating on soot particle size distribution. *Measurement Science and Technology*, 16(7):1477, 2005. p. 44
- [172] B. T. Chen, D. Schwegler-Berry, A. Cumpston, J. Cumpston, S. Friend, S. Stone, and M. Keane. Performance of a scanning mobility particle sizer in measuring diverse types of airborne nanoparticles: Multi-walled carbon nanotubes, welding fumes, and titanium dioxide spray. *Journal of occupational and environmental hygiene*, 13(7):501–518, 2016. p. 44
- [173] G. A. Kelesidis and S. E. Pratsinis. Determination of the volume fraction of soot accounting for its composition and morphology. *Proceedings of the Combustion Institute*, 38(1):1189–1196, 2021. p. 44
- [174] C. F. Bohren and D. R. Huffman. *Absorption and scattering of light by small particles*. John Wiley & Sons, 2008. p. 45, 71, 191
- [175] C. Sorensen. Light scattering by fractal aggregates: a review. *Aerosol Science & Technology*, 35(2):648–687, 2001. p. 45, 47, 48, 72, 190
- [176] M. Altenhoff, S. Aßmann, J. F. Perlitz, F. J. Huber, and S. Will. Soot aggregate sizing in an extended premixed flame by high-resolution two-dimensional multi-angle light scattering (2D-MALS). *Applied Physics B*, 125(9):1–15, 2019. p. 45
- [177] Y. Xing, Ü. Ö. Köylü, and D. E. Rosner. Synthesis and restructuring of inorganic nanoparticles in counterflow diffusion flames. *Combustion and Flame*, 107(1-2):85–102, 1996. p. 45
- [178] G. Yang and P. Biswas. Study of the sintering of nanosized titania agglomerates in flames using in situ light scattering measurements. *Aerosol science and technology*, 27(4):507–521, 1997. p. xix, 45, 46
- [179] H. Herbin and P. Dubuisson. *Observation infrarouge de l’atmosphère terrestre*. ISTE Group, 2016. p. xviii, 45
- [180] N.-E. Olofsson, J. Simonsson, S. Török, H. Bladh, and P.-E. Bengtsson. Evolution of properties for aging soot in premixed flat flames studied by laser-induced incandescence and elastic light scattering. *Applied Physics B*, 119(4):669–683, 2015. p. 45
- [181] A. J. Hurd, D. W. Schaefer, and J. E. Martin. Surface and mass fractals in vapor-phase aggregates. *Physical Review A*, 35(5):2361, 1987. p. 46
- [182] M. E. Fisher and R. J. Burford. Theory of critical-point scattering and correlations. i. the ising model. *Physical Review*, 156(2):583, 1967. p. 46
- [183] S. Friedlander. *Smoke, dust and haze. fundamentals of aerosol behavior*, john wiley and sons, 1977. p. xix, 46
- [184] C. Schulz, T. Dreier, M. Fikri, and H. Wiggers. Gas-phase synthesis of functional nanomaterials: Challenges to kinetics, diagnostics, and process development. *Proceedings of the Combustion Institute*, 37(1):83–108, 2019. p. 47
- [185] B. Zhao, Z. Yang, M. V. Johnston, H. Wang, A. S. Wexler, M. Balthasar, and M. Kraft. Measurement and numerical simulation of soot particle size distribution functions in a laminar premixed ethylene-oxygen-argon flame. *Combustion and Flame*, 133(1-2):173–188, 2003. p. 47
- [186] T. L. Farias, Ü. Ö. Köylü, and M. d. G. Carvalho. Range of validity of the rayleigh-

- debye-gans theory for optics of fractal aggregates. *Applied optics*, 35(33):6560–6567, 1996. p. 47
- [187] X. Liu, M. Smith, and S. Tse. In situ raman characterization of nanoparticle aerosols during flame synthesis. *Applied Physics B*, 100(3):643–653, 2010. p. xix, 47, 48
- [188] M. Allendorf, J. Bautista, and E. Potkay. Temperature measurements in a vapor axial deposition flame by spontaneous raman spectroscopy. *Journal of applied physics*, 66(10):5046–5051, 1989. p. 47
- [189] M. Lapp, L. Goldman, and C. Penney. Raman scattering from flames. *Science*, 175(4026):1112–1115, 1972. p. 47
- [190] D. Bersani, P. Lottici, and X.-Z. Ding. Phonon confinement effects in the raman scattering by TiO₂ nanocrystals. *Applied Physics Letters*, 72(1):73–75, 1998. p. 48
- [191] L. Hsu and C. She. Real-time monitoring of crystallization and structural transformation of titania films with raman spectroscopy. *Optics letters*, 10(12):638–640, 1985. p. 48
- [192] C. R. Aita. Raman scattering by thin film nanomosaic rutile TiO₂. *Applied physics letters*, 90(21):213112, 2007. p. 48
- [193] M. P. Moret, R. Zallen, D. P. Vijay, and S. B. Desu. Brookite-rich titania films made by pulsed laser deposition. *Thin Solid Films*, 366(1-2):8–10, 2000. p. 48
- [194] G. Porod, O. Glatter, O. Kratky, et al. Small angle x-ray scattering. *Academic Press, New York*, pages 17–51, 1982. p. 48
- [195] A. Guinier, G. Fournet, and K. L. Yudowitch. Small-angle scattering of x-rays. 1955. p. 48
- [196] J. Hyeon-Lee, G. Beaucage, S. E. Pratsinis, and S. Vemury. Fractal analysis of flame-synthesized nanostructured silica and titania powders using small-angle X-ray scattering. *Langmuir*, 14(20):5751–5756, 1998. p. 48, 49
- [197] F. Ossler, L. Vallenhag, S. E. Canton, J. B. A. Mitchell, J.-L. Le Garrec, M. Sztucki, and S. Di Stasio. Dynamics of incipient carbon particle formation in a stabilized ethylene flame by in situ extended-small-angle-and wide-angle X-ray scattering. *Carbon*, 51:1–19, 2013. p. 48
- [198] H. K. Kammler, G. Beaucage, D. J. Kohls, N. Agashe, and J. Ilavsky. Monitoring simultaneously the growth of nanoparticles and aggregates by in situ ultra-small-angle X-ray scattering. *Journal of applied physics*, 97(5):054309, 2005. p. xix, 49
- [199] H. K. Kammler, R. Jossen, P. W. Morrison Jr, S. E. Pratsinis, and G. Beaucage. The effect of external electric fields during flame synthesis of titania. *Powder technology*, 135:310–320, 2003. p. 49
- [200] H. K. Kammler, G. Beaucage, R. Mueller, and S. E. Pratsinis. Structure of flame-made silica nanoparticles by ultra-small-angle X-ray scattering. *Langmuir*, 20(5):1915–1921, 2004. p. 49
- [201] A. Camenzind, H. Schulz, A. Teleki, G. Beaucage, T. Narayanan, and S. E. Pratsinis. Nanostructure evolution: from aggregated to spherical SiO₂ particles made in diffusion flames, 2008. p. 49
- [202] G. Beaucage, H. K. Kammler, R. Mueller, R. Strobel, N. Agashe, S. E. Pratsinis, and T. Narayanan. Probing the dynamics of nanoparticle growth in a flame using synchrotron radiation. *Nature Materials*, 3(6):370–373, 2004. p. 49

- [203] D. A. Skoog, F. J. Holler, and S. R. Crouch. *Principles of instrumental analysis*. Cengage learning, 2017. p. xix, 50, 59
- [204] A. Braeuer. Laser-induced fluorescence (lif) and phosphorescence (lip) techniques. In *Supercritical Fluid Science and Technology*, volume 7, pages 313–345. Elsevier, 2015. p. 50
- [205] A. Colibaba-Evulet, A. Singhal, and N. Glumac. Detection of AlO and TiO by laser-induced fluorescence in powder synthesis flames. *Combustion science and technology*, 157(1):129–139, 2000. p. xix, 50
- [206] J. Hwang, Y. Gil, J. Kim, M. Choi, and S. Chung. Measurements of temperature and OH radical distributions in a silica generating flame using cars and plif. *Journal of aerosol science*, 32(5):601–613, 2001. p. 50
- [207] N. Glumac, Y. Chen, and G. Skandan. Diagnostics and modeling of nanopowder synthesis in low pressure flames. *Journal of materials research*, 13(9):2572–2579, 1998. p. 50
- [208] H. Kronemayer, P. Ifeacho, C. Hecht, T. Dreier, H. Wiggers, and C. Schulz. Gas-temperature imaging in a low-pressure flame reactor for nano-particle synthesis with multi-line no-lif thermometry. *Applied Physics B*, 88(3):373–377, 2007. p. 50
- [209] C. Hecht, H. Kronemayer, T. Dreier, H. Wiggers, and C. Schulz. Imaging measurements of atomic iron concentration with laser-induced fluorescence in a nanoparticle synthesis flame reactor. *Applied Physics B*, 94(1):119–125, 2009. p. 50
- [210] P. van de Weijer and B. H. Zwerver. Laser-induced fluorescence of OH and SiO molecules during thermal chemical vapour deposition of SiO₂ from silane-oxygen mixtures. *Chemical physics letters*, 163(1):48–54, 1989. p. 50
- [211] M. R. Zachariah and D. R. Burgess Jr. Strategies for laser excited fluorescence spectroscopy. measurements of gas phase species during particle formation. *Journal of aerosol science*, 25(3):487–497, 1994. p. 50
- [212] N. G. Glumac. Formation and consumption of SiO in powder synthesis flames. *Combustion and flame*, 124(4):702–711, 2001. p. 50
- [213] B. K. McMillin, P. Biswas, and M. R. Zachariah. In situ characterization of vapor phase growth of iron oxide-silica nanocomposites: part I. 2-d planar laser-induced fluorescence and mie imaging. *Journal of Materials Research*, 11(6):1552–1561, 1996. p. 50
- [214] S. De Iuliis, F. Migliorini, and R. Dondè. Laser-induced emission of TiO₂ nanoparticles in flame spray synthesis. *Applied Physics B*, 125(11):1–11, 2019. p. xx, xxiv, xxv, xxvi, 50, 52, 69, 75, 76, 77, 78, 81, 83, 85, 142, 143, 145, 154, 155, 156
- [215] S. De Iuliis, R. Dondè, and I. Altman. Light emission of flame-generated TiO₂ nanoparticles: Effect of ir laser irradiation. *Journal of Quantitative Spectroscopy and Radiative Transfer*, 258:107353, 2021. p. xxi, 50, 69, 75, 80, 81, 85
- [216] G. Galbács, A. Kéri, A. Kohut, M. Veres, and Z. Geretovszky. Nanoparticles in analytical laser and plasma spectroscopy—a review of recent developments in methodology and applications. *Journal of Analytical Atomic Spectrometry*, 36(9):1826–1872, 2021. p. 51
- [217] R. Noll. *Laser-Induced Breakdown Spectroscopy*. Springer, Heidelberg, 2012. p. xx, 51, 65, 85
- [218] Z. Gao, L. Han, and J. Li. Investigation of laser induced air breakdown thresholds at 1064, 532, 355, 266 and 248nm. In *Pacific Rim Laser Damage 2019: Optical Materials*

- for High-Power Lasers*, volume 11063, pages 23–27. SPIE, 2019. p. 51, 84
- [219] L. Cabalin and J. Laserna. Experimental determination of laser induced breakdown thresholds of metals under nanosecond q-switched laser operation. *Spectrochimica Acta Part B: Atomic Spectroscopy*, 53(5):723–730, 1998. p. 51
- [220] Y. Ren, J. Wei, and S. Li. In-situ laser diagnostic of nanoparticle formation and transport behavior in flame aerosol deposition. *Proceedings of the Combustion Institute*, 37(1):935–942, 2019. p. 51
- [221] S. Will, S. Schraml, and A. Leipertz. Two-dimensional soot-particle sizing by time-resolved laser-induced incandescence. *Optics letters*, 20(22):2342–2344, 1995. p. 51, 95
- [222] J. E. Dec, A. O. Zur Loye, and D. L. Siebers. Soot distribution in a di diesel engine using 2-D laser-induced incandescence imaging. *SAE transactions*, pages 277–288, 1991. p. 51
- [223] R. Lemaire, S. Bejaoui, and E. Therssen. Study of soot formation during the combustion of diesel, rapeseed methyl ester and their surrogates in turbulent spray flames. *Fuel*, 107:147–161, 2013. p. 51
- [224] R. L. Vander Wal. Soot precursor carbonization: Visualization using LIF and LII and comparison using bright and dark field TEM. *Combustion and flame*, 112(4):607–616, 1998. p. 52
- [225] R. L. Vander Wal. LIF-LII measurements in a turbulent gas-jet flame. *Experiments in fluids*, 23(4):281–287, 1997. p. 52
- [226] S. Talebi Moghaddam and K. Daun. Plasma emission during time-resolved laser-induced incandescence measurements of aerosolized metal nanoparticles. *Applied Physics B*, 124(8):1–14, 2018. p. 52
- [227] J. Menser, K. Daun, and C. Schulz. Interrogating gas-borne nanoparticles using laser-based diagnostics and bayesian data fusion. *The Journal of Physical Chemistry C*, 125(15):8382–8390, 2021. p. 52, 79
- [228] Y. Zhang, G. Xiong, S. Li, Z. Dong, S. G. Buckley, and D. T. Stephen. Novel low-intensity phase-selective laser-induced breakdown spectroscopy of TiO₂ nanoparticle aerosols during flame synthesis. *Combustion and flame*, 160(3):725–733, 2013. p. 52, 66, 67, 68, 85
- [229] J. W. Daily. Laser induced fluorescence spectroscopy in flames. *Progress in energy and combustion science*, 23(2):133–199, 1997. p. 58, 59
- [230] R. Qian, H. Zong, J. Schneider, G. Zhou, T. Zhao, Y. Li, J. Yang, D. W. Bahnemann, and J. H. Pan. Charge carrier trapping, recombination and transfer during TiO₂ photocatalysis: An overview. *Catalysis Today*, 335:78–90, 2019. p. 58
- [231] T. Mouton. *Analyse des processus de nucléation et de croissance des particules de suie dans des flammes par fluorescence induite par laser en jet froid appliquée aux hydrocarbures aromatiques polycycliques et par incandescence induite par laser*. PhD thesis, Lille 1, 2014. p. 58
- [232] A. L. Linsebigler, G. Lu, and J. T. Yates Jr. Photocatalysis on TiO₂ surfaces: principles, mechanisms, and selected results. *Chemical reviews*, 95(3):735–758, 1995. p. 58, 59
- [233] J. Clayden, N. Greeves, and S. Warren. *Organic chemistry*. Oxford university press, 2012. p. 58

- [234] D. K. Pallotti, L. Passoni, P. Maddalena, F. Di Fonzo, and S. Lettieri. Photoluminescence mechanisms in anatase and rutile TiO₂. *The Journal of Physical Chemistry C*, 121(16):9011–9021, 2017. p. 59
- [235] J. Liqiang, Q. Yichun, W. Baiqi, L. Shudan, J. Baojiang, Y. Libin, F. Wei, F. Honggang, and S. Jiazhong. Review of photoluminescence performance of nano-sized semiconductor materials and its relationships with photocatalytic activity. *Solar Energy Materials and Solar Cells*, 90(12):1773–1787, 2006. p. 59
- [236] N. D. Abazović, M. I. Čomor, M. D. Dramićanin, D. J. Jovanović, S. P. Ahrenkiel, and J. M. Nedeljković. Photoluminescence of anatase and rutile TiO₂ particles. *The Journal of Physical Chemistry B*, 110(50):25366–25370, 2006. p. xix, xxi, xxiii, 60, 64, 97, 98, 116, 117
- [237] X. Wang, Z. Feng, J. Shi, G. Jia, S. Shen, J. Zhou, and C. Li. Trap states and carrier dynamics of TiO₂ studied by photoluminescence spectroscopy under weak excitation condition. *Physical Chemistry Chemical Physics*, 12(26):7083–7090, 2010. p. xix, 60, 61, 63
- [238] J. Zhang, X. Chen, Y. Shen, Y. Li, Z. Hu, and J. Chu. Synthesis, surface morphology, and photoluminescence properties of anatase iron-doped titanium dioxide nano-crystalline films. *Physical Chemistry Chemical Physics*, 13(28):13096–13105, 2011. p. xix, xxi, xxiii, 62, 85, 98, 117
- [239] K. Farhadian Azizi and M.-M. Bagheri-Mohagheghi. Transition from anatase to rutile phase in titanium dioxide (tio 2) nanoparticles synthesized by complexing sol–gel process: effect of kind of complexing agent and calcinating temperature. *Journal of sol-gel science and technology*, 65:329–335, 2013. p. 63
- [240] J. Shi, J. Chen, Z. Feng, T. Chen, Y. Lian, X. Wang, and C. Li. Photoluminescence characteristics of TiO₂ and their relationship to the photoassisted reaction of water/methanol mixture. *The journal of physical chemistry C*, 111(2):693–699, 2007. p. xx, 63
- [241] K. Fujihara, S. Izumi, T. Ohno, and M. Matsumura. Time-resolved photoluminescence of particulate TiO₂ photocatalysts suspended in aqueous solutions. *Journal of Photochemistry and Photobiology A: Chemistry*, 132(1-2):99–104, 2000. p. xx, 63
- [242] Y. Zhang, G. Li, Y. Jin, Y. Zhang, J. Zhang, and L. Zhang. Hydrothermal synthesis and photoluminescence of TiO₂ nanowires. *Chemical Physics Letters*, 365(3-4):300–304, 2002. p. 64
- [243] B. Santara, P. Giri, K. Imakita, and M. Fujii. Evidence of oxygen vacancy induced room temperature ferromagnetism in solvothermally synthesized undoped TiO₂ nanoribbons. *Nanoscale*, 5(12):5476–5488, 2013. p. xxi, xxiii, 64, 96, 97, 98, 117
- [244] N. Serpone, D. Lawless, and R. Khairutdinov. Size effects on the photophysical properties of colloidal anatase TiO₂ particles: size quantization versus direct transitions in this indirect semiconductor? *The journal of Physical Chemistry*, 99(45):16646–16654, 1995. p. xx, xxi, xxiii, 64, 98, 117
- [245] Z. Khan, M. H. Ullah, B. Rahman, A. I. Talukder, M. Wahadoszamen, K. Abedin, and A. Haider. Laser-induced breakdown spectroscopy (LIBS) for trace element detection: a review. *Journal of Spectroscopy*, 2022, 2022. p. 65
- [246] S. Yoon, H.-W. Choi, and J. Kim. Analysis of changes in spectral signal according to gas

- flow rate in laser-induced breakdown spectroscopy. *Applied Sciences*, 11(19):9046, 2021. p. xx, 65
- [247] M. Hidalgo, F. Martin, and J. Laserna. Laser-induced breakdown spectrometry of titanium dioxide antireflection coatings in photovoltaic cells. *Analytical chemistry*, 68(7):1095–1100, 1996. p. 65, 68
- [248] R. F. LeBouf, A. L. Miller, C. Stipe, J. Brown, N. Murphy, and A. B. Stefaniak. Comparison of field portable measurements of ultrafine TiO₂: X-ray fluorescence, laser-induced breakdown spectroscopy, and fourier-transform infrared spectroscopy. *Environmental Science: Processes & Impacts*, 15(6):1191–1198, 2013. p. 65, 68, 85, 97
- [249] D. Anglos. Laser-induced breakdown spectroscopy in art and archaeology. *Applied Spectroscopy*, 55(6):186A–205A, 2001. p. 65, 68
- [250] M. Sovago, E.-J. Buis, and M. Sandtke. Nanoparticle detection in aqueous solutions using raman and laser induced breakdown spectroscopy. *Spectrochimica Acta Part B: Atomic Spectroscopy*, 87:182–187, 2013. p. 65, 68
- [251] J. Menneveux, F. Wang, S. Lu, X. Bai, V. Motto-Ros, N. Gilon, Y. Chen, and J. Yu. Direct determination of ti content in sunscreens with laser-induced breakdown spectroscopy: Line selection method for high TiO₂ nanoparticle concentration. *Spectrochimica Acta Part B: Atomic Spectroscopy*, 109:9–15, 2015. p. 65, 68, 85
- [252] Y. Zhang, S. Li, Y. Ren, Q. Yao, and D. T. Stephen. A new diagnostic for volume fraction measurement of metal-oxide nanoparticles in flames using phase-selective laser-induced breakdown spectroscopy. *Proceedings of the Combustion Institute*, 35(3):3681–3688, 2015. p. 66, 67, 68
- [253] Y. Ren, Y. Zhang, S. Li, and C. K. Law. Doping mechanism of vanadia/titania nanoparticles in flame synthesis by a novel optical spectroscopy technique. *Proceedings of the Combustion Institute*, 35(2):2283–2289, 2015. p. 66, 85
- [254] G. Xiong, S. Li, Y. Zhang, S. G. Buckley, and D. T. Stephen. Phase-selective laser-induced breakdown spectroscopy of metal-oxide nanoparticle aerosols with secondary resonant excitation during flame synthesis. *Journal of Analytical Atomic Spectrometry*, 31(2):482–491, 2016. p. 66, 68, 85, 97
- [255] Y. Ren, Y. Zhang, and S. Li. Simultaneous single-shot two-dimensional imaging of nanoparticles and radicals in turbulent reactive flows. *Physical Review Applied*, 13(4):044002, 2020. p. xx, 66, 68
- [256] C. Liu, S. Li, Y. Zong, Q. Yao, and D. T. Stephen. Laser-based investigation of the transition from droplets to nanoparticles in flame-assisted spray synthesis of functional nanoparticles. *Proceedings of the Combustion Institute*, 36(1):1109–1117, 2017. p. 66
- [257] Y. Zhang, S. Li, Y. Ren, Q. Yao, and C. K. Law. Two-dimensional imaging of gas-to-particle transition in flames by laser-induced nanoplasmas. *Applied Physics Letters*, 104(2):023115, 2014. p. 66, 67
- [258] A. Kramida, Yu. Ralchenko, J. Reader, and and NIST ASD Team. NIST Atomic Spectra Database (ver. 5.9), [Online]. Available: <https://physics.nist.gov/asd> [2022, June 2]. National Institute of Standards and Technology, Gaithersburg, MD., 2021. p. xx, xxi, xxiii, 67, 98, 117
- [259] Y. Ren, S. Li, Y. Zhang, D. T. Stephen, and M. B. Long. Absorption-ablation-excitation

- mechanism of laser-cluster interactions in a nanoaerosol system. *Physical review letters*, 114(9):093401, 2015. p. xx, 68, 85, 97
- [260] G. Xiong, S. Li, and D. T. Stephen. Tuning excitation laser wavelength for secondary resonance in low-intensity phase-selective laser-induced breakdown spectroscopy for in-situ analytical measurement of nanoaerosols. *Spectrochimica Acta Part B: Atomic Spectroscopy*, 140:13–21, 2018. p. 68
- [261] J. Yon, R. Lemaire, E. Therssen, P. Desgroux, A. Coppalle, and K. Ren. Examination of wavelength dependent soot optical properties of diesel and diesel/rapeseed methyl ester mixture by extinction spectra analysis and LII measurements. *Applied Physics B*, 104(2):253–271, 2011. p. xxiv, 69, 78, 137, 138, 139, 140
- [262] T. A. Sipkens, P. J. Hadwin, S. J. Grauer, and K. J. Daun. Predicting the heat of vaporization of iron at high temperatures using time-resolved laser-induced incandescence and bayesian model selection. *Journal of Applied Physics*, 123(9):095103, 2018. p. 69
- [263] T. Sipkens, G. Joshi, K. Daun, and Y. Murakami. Sizing of molybdenum nanoparticles using time-resolved laser-induced incandescence. *Journal of heat transfer*, 135(5), 2013. p. 69
- [264] A. Leipertz and S. Dankers. Characterization of nano-particles using laser-induced incandescence. *Particle & Particle Systems Characterization: Measurement and Description of Particle Properties and Behavior in Powders and Other Disperse Systems*, 20(2):81–93, 2003. p. 69, 75
- [265] Y. Ren, K. Ran, S. Kruse, J. Mayer, and H. Pitsch. Flame synthesis of carbon metal-oxide nanocomposites in a counterflow burner. *Proceedings of the Combustion Institute*, 38(1):1269–1277, 2021. p. xxiii, 69, 81, 123, 124
- [266] M. Planck. The theory of heat radiation. *Entropie*, 144(190):164, 1900. p. 69
- [267] F. Goulay, P. E. Schrader, X. López-Yglesias, and H. A. Michelsen. A data set for validation of models of laser-induced incandescence from soot: temporal profiles of LII signal and particle temperature. *Applied Physics B*, 112(3):287–306, 2013. p. xx, 71, 73, 74, 78
- [268] H. Michelsen, C. Schulz, G. Smallwood, and S. Will. Laser-induced incandescence: Particulate diagnostics for combustion, atmospheric, and industrial applications. *Progress in Energy and Combustion Science*, 51:2–48, 2015. p. 72, 78, 96, 189, 190, 193, 194
- [269] F. Liu, B. J. Stagg, D. R. Snelling, and G. J. Smallwood. Effects of primary soot particle size distribution on the temperature of soot particles heated by a nanosecond pulsed laser in an atmospheric laminar diffusion flame. *International Journal of Heat and Mass Transfer*, 49(3-4):777–788, 2006. p. 72
- [270] F. Liu, M. Yang, F. A. Hill, D. R. Snelling, and G. J. Smallwood. Influence of poly-disperse distributions of both primary particle and aggregate size on soot temperature in low-fluence LII. *Applied Physics B*, 83(3):383, 2006. p. 72, 74, 190
- [271] H. Bladh, J. Johnsson, J. Rissler, H. Abdulhamid, N.-E. Olofsson, M. Sanati, J. Pagels, and P.-E. Bengtsson. Influence of soot particle aggregation on time-resolved laser-induced incandescence signals. *Applied Physics B*, 104(2):331–341, 2011. p. 72, 74
- [272] R. Mansmann, T. Terheiden, P. Schmidt, J. Menser, T. Dreier, T. Endres, and C. Schulz. Liisim: a modular signal processing toolbox for laser-induced incandescence measure-

- ments. *Applied Physics B*, 124(4):69, 2018. p. 74
- [273] F. Liu, G. J. Smallwood, and D. R. Snelling. Effects of primary particle diameter and aggregate size distribution on the temperature of soot particles heated by pulsed lasers. *Journal of Quantitative Spectroscopy and Radiative Transfer*, 93(1-3):301–312, 2005. p. 74
- [274] A. Eremin, E. Gurentsov, M. Hofmann, B. Kock, and C. Schulz. TR-LII for sizing of carbon particles forming at room temperature. *Applied Physics B*, 83(3):449–454, 2006. p. 74
- [275] B. F. Kock, B. Tribalet, C. Schulz, and P. Roth. Two-color time-resolved LII applied to soot particle sizing in the cylinder of a diesel engine. *Combustion and Flame*, 147(1-2):79–92, 2006. p. 74
- [276] K. J. Daun, B. Stagg, F. Liu, G. Smallwood, and D. Snelling. Determining aerosol particle size distributions using time-resolved laser-induced incandescence. *Applied Physics B*, 87(2):363–372, 2007. p. 74, 75
- [277] Ü. Ö. Köylü, G. M. Faeth, T. L. Farias, and M. d. G. Carvalho. Fractal and projected structure properties of soot aggregates. *Combustion and Flame*, 100(4):621–633, 1995. p. 74
- [278] K. Daun, T. Sipkens, J. Titantah, and M. Karttunen. Thermal accommodation coefficients for laser-induced incandescence sizing of metal nanoparticles in monatomic gases. *Applied Physics B*, 112(3):409–420, 2013. p. 75, 189
- [279] F. J. Bauer, K. J. Daun, F. J. Huber, and S. Will. Can soot primary particle size distributions be determined using laser-induced incandescence? *Applied Physics B*, 125(6):1–15, 2019. p. 75
- [280] L. Buss, D. Noriler, and U. Fritsching. Impact of reaction chamber geometry on the particle-residence-time in flame spray process. *Flow, Turbulence and Combustion*, 105(4):1055–1086, 2020. p. 75
- [281] Carbon black. CAS common chemistry. cas, a division of the american chemical society, (retrieved 2022-05-06) (CAS RN: 1333-86-4). p. 75
- [282] M. J. O’Neil, A. Smith, P. E. Heckelman, and S. Budavari. *The merck index-An encyclopedia of chemicals, drugs, and biologicals*. Merck, Whitehouse Station, N.J., 2001. p. xxiv, xxv, 75, 85, 112, 141, 142, 144
- [283] R. Weast et al. *CRC handbook of chemistry and physics 69th ed* (Boca Raton, FL: Chemical Rubber). 1988. p. 75
- [284] T. C. Williams, C. R. Shaddix, K. A. Jensen, and J. M. Suo-Anttila. Measurement of the dimensionless extinction coefficient of soot within laminar diffusion flames. *International Journal of Heat and Mass Transfer*, 50(7-8):1616–1630, 2007. p. 75
- [285] H.-Y. Liu, Y.-L. Hsu, H.-Y. Su, R.-C. Huang, F.-Y. Hou, G.-C. Tu, and W.-H. Liu. A comparative study of amorphous, anatase, rutile, and mixed phase TiO₂ films by mist chemical vapor deposition and ultraviolet photodetectors applications. *IEEE Sensors Journal*, 18(10):4022–4029, 2018. p. xvi, xx, xxiv, xxv, xxvi, xxvii, 75, 76, 142, 143, 145, 154, 155, 156, 168, 169, 170, 172, 173
- [286] G. Jellison Jr, L. Boatner, J. Budai, B.-S. Jeong, and D. Norton. Spectroscopic ellipsometry of thin film and bulk anatase (TiO₂). *Journal of Applied Physics*, 93(12):9537–9541,

2003. p. xx, xxvi, 75, 76, 150, 154, 155, 156, 185
- [287] H.-C. Chang and T. Charalampopoulos. Determination of the wavelength dependence of refractive indices of flame soot. *Proceedings of the Royal Society of London. Series A: Mathematical and Physical Sciences*, 430(1880):577–591, 1990. p. xx, xxiv, 76, 77, 137, 138, 139, 140
- [288] A. Coderre, K. Thomson, D. Snelling, and M. Johnson. Spectrally resolved light absorption properties of cooled soot from a methane flame. *Applied Physics B*, 104:175–188, 2011. p. xx, 76, 137
- [289] S. S. Krishnan, K.-C. Lin, and G. M. Faeth. Optical properties in the visible of overfire soot in large buoyant turbulent diffusion flames. *J. Heat transfer*, 122(3):517–524, 2000. p. xx, 76
- [290] B. Stagg and T. Charalampopoulos. Refractive indices of pyrolytic graphite, amorphous carbon, and flame soot in the temperature range 25 to 600 c. *Combustion and flame*, 94(4):381–396, 1993. p. xx, 76
- [291] R. Dobbins, G. W. Mulholland, N. P. Bryner, et al. Comparison of a fractal smoke optics model with light extinction measurements. *Atmospheric Environment*, 28(5):889–900, 1994. p. xx, 76
- [292] J.-S. Wu, S. Krishnan, and G. Faeth. Refractive indices at visible wavelengths of soot emitted from buoyant turbulent diffusion flames. 1997. p. xx, 76
- [293] M. Schnaiter, H. Horvath, O. Möhler, K.-H. Naumann, H. Saathoff, and O. Schöck. Uv-vis-nir spectral optical properties of soot and soot-containing aerosols. *Journal of Aerosol Science*, 34(10):1421–1444, 2003. p. xx, 76
- [294] W. Dalzell and A. Sarofim. Optical constants of soot and their application to heat-flux calculations. 1969. p. xx, 76
- [295] Ü. Ö. Köylü and G. M. Faeth. Spectral Extinction Coefficients of Soot Aggregates From Turbulent Diffusion Flames. *Journal of Heat Transfer*, 118(2):415–421, 05 1996. p. xx, 76
- [296] D. Snelling, K. Thomson, F. Liu, and G. Smallwood. Comparison of lii derived soot temperature measurements with lii model predictions for soot in a laminar diffusion flame. *Applied Physics B*, 96:657–669, 2009. p. xx, 76
- [297] T. Siefke, S. Kroker, K. Pfeiffer, O. Puffky, K. Dietrich, D. Franta, I. Ohlídal, A. Szeghalmi, E.-B. Kley, and A. Tünnermann. Materials pushing the application limits of wire grid polarizers further into the deep ultraviolet spectral range. *Advanced Optical Materials*, 4(11):1780–1786, 2016. p. xx, 76
- [298] P. J. Hadwin, T. Sipkens, K. Thomson, F. Liu, and K. Daun. Quantifying uncertainty in auto-compensating laser-induced incandescence parameters due to multiple nuisance parameters. *Applied Physics B*, 123(4):114, 2017. p. 76, 77
- [299] S. Török, M. Mannazhi, and P.-E. Bengtsson. Laser-induced incandescence (2λ and $2c$) for estimating absorption efficiency of differently matured soot. *Applied Physics B*, 127(7):1–10, 2021. p. 76
- [300] J. Yon, J. J. Cruz, F. Escudero, J. Morán, F. Liu, and A. Fuentes. Revealing soot maturity based on multi-wavelength absorption/emission measurements in laminar axisymmetric coflow ethylene diffusion flames. *Combustion and Flame*, 227:147–161, 2021. p. 76,

177

- [301] Z. Habib and P. Vervisch. On the refractive index of soot at flame temperature. *Combustion science and technology*, 59(4-6):261–274, 1988. p. 76
- [302] T. C. Bond and R. W. Bergstrom. Light absorption by carbonaceous particles: An investigative review. *Aerosol science and technology*, 40(1):27–67, 2006. p. 77, 131
- [303] D. R. Snelling, F. Liu, G. J. Smallwood, and Ö. L. Gülder. Determination of the soot absorption function and thermal accommodation coefficient using low-fluence LII in a laminar coflow ethylene diffusion flame. *Combustion and flame*, 136(1-2):180–190, 2004. p. xxiv, xxv, 77, 138, 139, 140, 153, 154
- [304] F. Goulay, P. E. Schrader, L. Nemes, M. A. Dansson, and H. A. Michelsen. Photochemical interferences for laser-induced incandescence of flame-generated soot. *Proceedings of the Combustion Institute*, 32(1):963–970, 2009. p. 77, 78, 126
- [305] E. Therssen, Y. Bouvier, C. Schoemaeker-Moreau, X. Mercier, P. Desgroux, M. Ziskind, and C. Focsa. Determination of the ratio of soot refractive index function $E(m)$ at the two wavelengths 532 and 1064 nm by laser induced incandescence. *Applied Physics B*, 89(2-3):417–427, 2007. p. xx, 77, 78
- [306] C. S. Moreau, E. Therssen, X. Mercier, J. Pauwels, and P. Desgroux. Two-color laser-induced incandescence and cavity ring-down spectroscopy for sensitive and quantitative imaging of soot and pahn in flames. *Applied Physics B*, 78(3):485–492, 2004. p. 78
- [307] H. A. Michelsen. Laser-induced incandescence of flame-generated soot on a picosecond time scale. *Applied Physics B*, 83(3):443–448, 2006. p. 78, 85
- [308] S. T. Moghaddam and K. Daun. Plasma emission during time-resolved laser-induced incandescence measurements of aerosolized metal nanoparticles. *Applied Physics B*, 124(8):1–14, 2018. p. 78
- [309] S. Talebi-Moghaddam, S. Robinson-Enebeli, S. Musikhin, D. Clavel, J. Corbin, A. Klinkova, G. Smallwood, and K. Daun. Multiphoton induced photoluminescence during time-resolved laser-induced incandescence experiments on silver and gold nanoparticles. *Journal of Applied Physics*, 129(18):183107, 2021. p. 78
- [310] F. Cignoli, S. Benecchi, and G. Zizak. Time-delayed detection of laser-induced incandescence for the two-dimensional visualization of soot in flames. *Applied optics*, 33(24):5778–5782, 1994. p. 78
- [311] R. L. Vander Wal. Laser-induced incandescence: excitation and detection conditions, material transformations and calibration. *Applied Physics B*, 96(4):601–611, 2009. p. 78
- [312] F. Goulay, L. Nemes, P. E. Schrader, and H. A. Michelsen. Spontaneous emission from C_2 ($d^3\Pi_g$) and C_3 ($A^1\Pi_u$) during laser irradiation of soot particles. *Molecular Physics*, 108(7-9):1013–1025, 2010. p. xxi, 78, 80, 81
- [313] Y. Bouvier, C. Mihehan, M. Ziskind, E. Therssen, C. Focsa, J. Pauwels, and P. Desgroux. Molecular species adsorbed on soot particles issued from low sooting methane and acetylene laminar flames: A laser-based experiment. *Proceedings of the Combustion Institute*, 31(1):841–849, 2007. p. 78
- [314] T. Posch, F. Kerschbaum, D. Fabian, H. Mutschke, J. Dorschner, A. Tamanai, and T. Henning. Infrared properties of solid titanium oxides: exploring potential primary dust condensates. *The Astrophysical Journal Supplement Series*, 149(2):437, 2003. p. 78

- [315] D. L. Parry and M. Q. Brewster. Optical constants of Al_2O_3 smoke in propellant flames. *Journal of thermophysics and heat transfer*, 5(2):142–149, 1991. p. xxi, 79
- [316] J. Menser, K. Daun, T. Dreier, and C. Schulz. Laser-induced atomic emission of silicon nanoparticles during laser-induced heating. *Applied optics*, 56(11):E50–E57, 2017. p. 79
- [317] M. A. Green. Self-consistent optical parameters of intrinsic silicon at 300 k including temperature coefficients. *Solar Energy Materials and Solar Cells*, 92(11):1305–1310, 2008. p. 79
- [318] K. Shvarev, B. Baum, and P. Gel'd. Optical properties and electronic characteristics of liquid solutions of nickel in silicon. *Soviet Physics Journal*, 18(4):521–524, 1975. p. 79
- [319] V. K. Bityukov and V. A. Petrov. Absorption coefficient of molten aluminum oxide in semitransparent spectral range. *Applied Physics Research*, 5(1):51, 2013. p. 79, 163
- [320] E. Ching-Prado, A. Watson, H. Miranda, and I. Abrego. Optical properties of multilayers $\text{tio}_2/\text{sno}_2$: F thin films. *MRS Advances*, 1(46):3133–3138, 2016. p. 80
- [321] L. Skowronski, A. Wachowiak, K. Zdunek, M. Trzcinski, and M. Naparty. Tio_2 -based decorative coatings deposited on the aisi 316l stainless steel and glass using an industrial scale magnetron. *Thin Solid Films*, 627:1–8, 2017. p. 80
- [322] D. Saha, R. Ajimsha, K. Rajiv, C. Mukherjee, M. Gupta, P. Misra, and L. Kukreja. Spectroscopic ellipsometry characterization of amorphous and crystalline tio_2 thin films grown by atomic layer deposition at different temperatures. *Applied surface science*, 315:116–123, 2014. p. 80
- [323] A. Lewkowicz, A. Synak, B. Grobelna, P. Bojarski, R. Bogdanowicz, J. Karczewski, K. Szczodrowski, and M. Behrendt. Thickness and structure change of titanium (iv) oxide thin films synthesized by the sol–gel spin coating method. *Optical Materials*, 36(10):1739–1744, 2014. p. 80
- [324] E. Blanco, J. González-Leal, and M. Ramírez-del Solar. Photocatalytic tio_2 sol–gel thin films: optical and morphological characterization. *Solar Energy*, 122:11–23, 2015. p. 80
- [325] H. Fujiwara. *Spectroscopic ellipsometry: principles and applications*. John Wiley & Sons, 2007. p. 80
- [326] G. Jellison Jr and D. Lowndes. Measurements of the optical properties of liquid silicon and germanium using nanosecond time-resolved ellipsometry. *Applied Physics Letters*, 51(5):352–354, 1987. p. 80
- [327] S. Talebi-Moghaddam, T. Sipkens, and K. Daun. Laser-induced incandescence on metal nanoparticles: validity of the rayleigh approximation. *Applied Physics B*, 125:1–16, 2019. p. 80, 146
- [328] E. Cenker, G. Bruneaux, T. Dreier, and C. Schulz. Determination of small soot particles in the presence of large ones from time-resolved laser-induced incandescence. *Applied Physics B*, 118:169–183, 2015. p. 87
- [329] K. A. Kusters, S. E. Pratsinis, S. G. Thoma, and D. M. Smith. Ultrasonic fragmentation of agglomerate powders. *Chemical engineering science*, 48(24):4119–4127, 1993. p. 89
- [330] S. Bejaoui, S. Batut, E. Therssen, N. Lamoureux, P. Desgroux, and F. Liu. Measurements and modeling of laser-induced incandescence of soot at different heights in a flat premixed flame. *Applied Physics B*, 118(3):449–469, 2015. p. 94
- [331] Y. J. Lee, N. W. Song, and S. K. Kim. Photoluminescence of C_{60} and its photofragments

- in the gas phase. *The Journal of Physical Chemistry A*, 106(23):5582–5590, 2002. p. 94
- [332] E. A. Rohlfing. Optical emission studies of atomic, molecular, and particulate carbon produced from a laser vaporization cluster source. *The Journal of chemical physics*, 89(10):6103–6112, 1988. p. 94
- [333] H. Michelsen, F. Liu, B. F. Kock, H. Bladh, A. Boïarciuc, M. Charwath, T. Dreier, R. Hedef, M. Hofmann, J. Reimann, et al. Modeling laser-induced incandescence of soot: a summary and comparison of LII models. *Applied physics B*, 87(3):503–521, 2007. p. 95, 189
- [334] R. L. Vander Wal, G. M. Berger, T. M. Ticich, and P. D. Patel. Application of laser-induced incandescence to the detection of carbon nanotubes and carbon nanofibers. *Applied optics*, 41(27):5678–5690, 2002. p. 96
- [335] K. K. Paul and P. Giri. Role of surface plasmons and hot electrons on the multi-step photocatalytic decay by defect enriched Ag@ TiO₂ nanorods under visible light. *The Journal of Physical Chemistry C*, 121(36):20016–20030, 2017. p. xxi, xxiii, 96, 97, 98, 117
- [336] Y. Lei and L. Zhang. Fabrication, characterization, and photoluminescence properties of highly ordered TiO₂ nanowire arrays. *Journal of Materials Research*, 16(4):1138–1144, 2001. p. xxi, xxiii, 98, 117
- [337] Sooting yale coflow diffusion flames, available at <http://guilford.eng.yale.edu/yalecoflowflames/> (2016). p. xxii, 107, 108
- [338] M. Smooke, M. Long, B. Connelly, M. Colket, and R. Hall. Soot formation in laminar diffusion flames. *Combustion and Flame*, 143(4):613–628, 2005. p. 107, 195
- [339] S. Dworkin, B. Connelly, A. Schaffer, B. Bennett, M. Long, M. Smooke, M. Puccio, B. McAndrews, and J. Miller. Computational and experimental study of a forced, time-dependent, methane–air coflow diffusion flame. *Proceedings of the Combustion Institute*, 31(1):971–978, 2007. p. 107
- [340] D. Bartos, M. Sirignano, M. J. Dunn, A. D’Anna, and A. R. Masri. Soot inception in laminar coflow diffusion flames. *Combustion and Flame*, 205:180–192, 2019. p. 107
- [341] B. Franzelli, M. Roussillo, P. Scouflaire, J. Bonnety, R. Jalain, T. Dormieux, S. Candel, and G. Legros. Multi-diagnostic soot measurements in a laminar diffusion flame to assess the isf database consistency. *Proceedings of the Combustion Institute*, 37(2):1355–1363, 2019. p. 107
- [342] K. Walsh, M. Long, M. Tanoff, and M. Smooke. Experimental and computational study of CH, CH*, and OH* in an axisymmetric laminar diffusion flame. In *Symposium (international) on combustion*, volume 27, pages 615–623. Elsevier, 1998. p. 107
- [343] B. Ma, S. Cao, D. Giassi, D. P. Stocker, F. Takahashi, B. A. V. Bennett, M. D. Smooke, and M. B. Long. An experimental and computational study of soot formation in a coflow jet flame under microgravity and normal gravity. *Proceedings of the Combustion Institute*, 35(1):839–846, 2015. p. 107
- [344] R. W. Schefer, W. D. Kulatilaka, B. D. Patterson, and T. B. Settersten. Visible emission of hydrogen flames. *Combustion and flame*, 156(6):1234–1241, 2009. p. 110
- [345] A. G. Gaydon. Flame spectra in the photographic infra-red. *Proceedings of the Royal Society of London. Series A. Mathematical and Physical Sciences*, 181(985):197–209,

1942. p. 110
- [346] T. Seto, M. Shimada, and K. Okuyama. Evaluation of sintering of nanometer-sized titania using aerosol method. *Aerosol Science and Technology*, 23(2):183–200, 1995. p. 111
- [347] K. Park, M. Ullmann, Y. Suh, and S. Friedlander. Nanoparticle microreactor: application to synthesis of titania by thermal decomposition of titanium tetraisopropoxide. *Journal of Nanoparticle Research*, 3(4):309–319, 2001. p. 111
- [348] P. Buerger, D. Nurkowski, J. Akroyd, S. Mosbach, and M. Kraft. First-principles thermochemistry for the thermal decomposition of titanium tetraisopropoxide. *The Journal of Physical Chemistry A*, 119(30):8376–8387, 2015. p. 111
- [349] K. S. Ershov, S. A. Kochubei, V. G. Kiselev, and A. V. Baklanov. Decomposition pathways of titanium isopropoxide $\text{Ti}(\text{O}i\text{Pr})_4$: New insights from uv-photodissociation experiments and quantum chemical calculations. *The Journal of Physical Chemistry A*, 122(4):1064–1070, 2018. p. 111
- [350] D. Hou, M. Feng, J. Wei, Y. Wang, A. C. van Duin, and K. H. Luo. A reactive force field molecular dynamics study on the inception mechanism of titanium tetraisopropoxide (TTIP) conversion to titanium clusters. *Chemical Engineering Science*, 252:117496, 2022. p. 111
- [351] J. Wei, A. Ostadhosseini, S. Li, and M. Ihme. Kinetics for the hydrolysis of $\text{Ti}(\text{OC}_3\text{H}_7)_4$: A molecular dynamics simulation study. *Proceedings of the Combustion Institute*, 38(1):1433–1440, 2021. p. 111, 164
- [352] A. Shmakov, O. Korobeinichev, D. Knyazkov, A. Paletsky, R. Maksutov, I. Gerasimov, T. Bolshova, V. Kiselev, and N. Gritsan. Combustion chemistry of $\text{Ti}(\text{OC}_3\text{H}_7)_4$ in premixed flat burner-stabilized $\text{H}_2/\text{O}_2/\text{Ar}$ flame at 1 atm. *Proceedings of the Combustion Institute*, 34(1):1143–1149, 2013. p. 111
- [353] W. O. Groves, M. Hoch, and H. L. Johnston. Vapor–solid equilibria in the titanium–oxygen system. *The Journal of Physical Chemistry*, 59(2):127–131, 1955. p. 112, 121, 176
- [354] T. Shinozaki, T. Ooie, T. Yano, J. P. Zhao, Z. Y. Chen, and M. Yoneda. Laser-induced optical emission of carbon plume by excimer and Nd:YAG laser irradiation. *Applied surface science*, 197:263–267, 2002. p. 115
- [355] L. Nemes, A. M. Keszler, C. G. Parigger, J. O. Hornkohl, H. A. Michelsen, and V. Stakhursky. Spontaneous emission from the C_3 radical in carbon plasma. *Applied optics*, 46(19):4032–4040, 2007. p. 115
- [356] F. Goulay, P. Schrader, and H. Michelsen. Effect of the wavelength dependence of the emissivity on inferred soot temperatures measured by spectrally resolved laser-induced incandescence. *Applied Physics B*, 100(3):655–663, 2010. p. xxii, 115
- [357] E. Tognoni, V. Palleschi, M. Corsi, and G. Cristoforetti. Quantitative micro-analysis by laser-induced breakdown spectroscopy: a review of the experimental approaches. *Spectrochimica Acta Part B: Atomic Spectroscopy*, 57(7):1115–1130, 2002. p. 116
- [358] F. Liu, J. Yon, A. Fuentes, P. Lobo, G. J. Smallwood, and J. C. Corbin. Review of recent literature on the light absorption properties of black carbon: Refractive index, mass absorption cross section, and absorption function. *Aerosol Science and Technology*, 54(1):33–51, 2020. p. 131, 148

- [359] W. G. Jacoby. Loess:: a nonparametric, graphical tool for depicting relationships between variables. *Electoral studies*, 19(4):577–613, 2000. p. 135
- [360] D. Snelling, F. Liu, G. Smallwood, and Ö. Gülder. Evaluation of the nanoscale heat and mass transfer model of lii: prediction of the excitation intensity. In *34th National Heat Transfer Conference*, 2000. p. 136
- [361] G. Faeth and Ü. Ö. Köylü. Soot morphology and optical properties in nonpremixed turbulent flame environments. *Combustion science and technology*, 108(4-6):207–229, 1995. p. xxiv, 137, 138, 139, 140
- [362] S. Krishnan, K.-C. Lin, and G. Faeth. Extinction and scattering properties of soot emitted from buoyant turbulent diffusion flames. *J. Heat Transfer*, 123(2):331–339, 2001. p. xxiv, 137, 138, 139, 140
- [363] C. R. Shaddix and T. C. Williams. Soot: Giver and taker of light: The complex structure of soot greatly influences the optical effects seen in fires. *American scientist*, 95(3):232–239, 2007. p. 137
- [364] K. C. Smyth and C. R. Shaddix. The elusive history of $m = 1.57-0.56 i$ for the refractive index of soot. *Combustion and flame*, 107(3):314–320, 1996. p. xxiv, xxv, 138, 139, 140, 153, 154
- [365] A. M. Bennett, E. Cenker, and W. L. Roberts. Effects of soot volume fraction on local gas heating and particle sizing using laser induced incandescence. *Journal of Aerosol Science*, 149:105598, 2020. p. 146, 180
- [366] T. Sipkens and K. Daun. Defining regimes and analytical expressions for fluence curves in pulsed laser heating of aerosolized nanoparticles. *Optics express*, 25(5):5684–5696, 2017. p. 146
- [367] S. Maffi, S. De Iuliis, F. Cignoli, and G. Zizak. Investigation on thermal accommodation coefficient and soot absorption function with two-color TIRE-LII technique in rich premixed flames. *Applied Physics B*, 104(2):357–366, 2011. p. 146
- [368] P. Roth and A. Filippov. In situ ultrafine particle sizing by a combination of pulsed laser heatup and particle thermal emission. *Journal of aerosol science*, 27(1):95–104, 1996. p. 146
- [369] A. Eremin, E. Gurentsov, E. Popova, and K. Priemchenko. Size dependence of complex refractive index function of growing nanoparticles. *Applied Physics B*, 104(2):285–295, 2011. p. 146
- [370] E. V. Gurentsov and A. V. Eremin. Size measurement of carbon and iron nanoparticles by laser induced incandescence. *High Temperature*, 49(5):667–673, 2011. p. 146
- [371] V. Toro, A. Mokhov, H. Levinsky, and M. Smooke. Combined experimental and computational study of laminar, axisymmetric hydrogen–air diffusion flames. *Proceedings of the Combustion Institute*, 30(1):485–492, 2005. p. 147
- [372] M. Asif, J. Menser, T. Endres, T. Dreier, K. Daun, and C. Schulz. Phase-sensitive detection of gas-borne si nanoparticles via line-of-sight UV/VIS attenuation. *Optics Express*, 29(14):21795–21809, 2021. p. 157, 164, 185
- [373] H. Bladh, J. Johnsson, and P.-E. Bengtsson. On the dependence of the laser-induced incandescence (LII) signal on soot volume fraction for variations in particle size. *Applied Physics B*, 90(1):109–125, 2008. p. 159

- [374] F. Liu and G. J. Smallwood. Relationship between soot volume fraction and LII signal in ac-lii: effect of primary soot particle diameter polydispersity. *Applied Physics B*, 112(3):307–319, 2013. p. 159
- [375] D. R. Snelling, G. J. Smallwood, F. Liu, Ö. L. Gülder, and W. D. Bachalo. A calibration-independent laser-induced incandescence technique for soot measurement by detecting absolute light intensity. *Applied optics*, 44(31):6773–6785, 2005. p. 159, 185
- [376] M. R. Lalanne, P. Wollny, M. Nanjaiah, J. Menser, C. Schulz, H. Wiggers, S. Cheskis, I. Wlokas, and I. Rahinov. Early particle formation and evolution in iron-doped flames. *Combustion and Flame*, 244:112251, 2022. p. 163
- [377] A. Cuoci, A. Frassoldati, T. Faravelli, and E. Ranzi. Numerical modeling of laminar flames with detailed kinetics based on the operator-splitting method. *Energy & fuels*, 27(12):7730–7753, 2013. p. 164
- [378] A. Kéromnès, W. K. Metcalfe, K. A. Heufer, N. Donohoe, A. K. Das, C.-J. Sung, J. Herzler, C. Naumann, P. Griebel, O. Mathieu, et al. An experimental and detailed chemical kinetic modeling study of hydrogen and syngas mixture oxidation at elevated pressures. *Combustion and Flame*, 160(6):995–1011, 2013. p. 164
- [379] B. Franzelli, A. Vié, and N. Darabiha. A three-equation model for the prediction of soot emissions in les of gas turbines. *Proceedings of the Combustion Institute*, 37(4):5411–5419, 2019. p. 164
- [380] A. Abdelsamie, F. E. Kruis, H. Wiggers, and D. Thévenin. Nanoparticle formation and behavior in turbulent spray flames investigated by DNS. *Flow, Turbulence and Combustion*, 105(2):497–516, 2020. p. 164
- [381] B. Buesser, A. Grohn, and S. E. Pratsinis. Sintering rate and mechanism of TiO₂ nanoparticles by molecular dynamics. *The Journal of Physical Chemistry C*, 115(22):11030–11035, 2011. p. 164
- [382] B. Derjaguin, A. Storozhilova, and Y. I. Rabinovich. Experimental verification of the theory of thermophoresis of aerosol particles. *Journal of Colloid and Interface Science*, 21(1):35–58, 1966. p. 164
- [383] S. Lai, J. Guo, V. Petrova, G. Ramanath, and L. Allen. Size-dependent melting properties of small tin particles: nanocalorimetric measurements. *Physical review letters*, 77(1):99, 1996. p. 164, 169
- [384] S. Deshpande, S. Patil, S. V. Kuchibhatla, and S. Seal. Size dependency variation in lattice parameter and valency states in nanocrystalline cerium oxide. *Applied Physics Letters*, 87(13):133113, 2005. p. 164, 169
- [385] C. Schulz, B. F. Kock, M. Hofmann, H. Michelsen, S. Will, B. Bougie, R. Suntz, and G. Smallwood. Laser-induced incandescence: recent trends and current questions. *Applied Physics B*, 83(3):333–354, 2006. p. 167
- [386] M. Sirignano, D. Bartos, M. Conturso, M. Dunn, A. D’Anna, and A. R. Masri. Detection of nanostructures and soot in laminar premixed flames. *Combustion and Flame*, 176:299–308, 2017. p. 167
- [387] H. Bladh, J. Johnsson, N.-E. Olofsson, A. Bohlin, and P.-E. Bengtsson. Optical soot characterization using two-color laser-induced incandescence (2C-LII) in the soot growth region of a premixed flat flame. *Proceedings of the Combustion Institute*, 33(1):641–648,

2011. p. 177
- [388] H. Michelsen. Probing soot formation, chemical and physical evolution, and oxidation: A review of in situ diagnostic techniques and needs. *Proceedings of the Combustion Institute*, 36(1):717–735, 2017. p. 177
- [389] F. Schneider, S. Suleiman, J. Menser, E. Borukhovich, I. Wlokas, A. Kempf, H. Wiggers, and C. Schulz. Spraysyn—a standardized burner configuration for nanoparticle synthesis in spray flames. *Review of Scientific Instruments*, 90(8):085108, 2019. p. 183
- [390] D. R. Snelling, K. A. Thomson, G. J. Smallwood, and Ö. L. Gülder. Two-dimensional imaging of soot volume fraction in laminar diffusion flames. *Applied optics*, 38(12):2478–2485, 1999. p. 185
- [391] R. L. Vander Wal. Calibration and comparison of laser-induced incandescence with cavity ring-down. In *Symposium (International) on Combustion*, volume 27, pages 59–67. Elsevier, 1998. p. 185
- [392] A. L. Bodor, A. Cuoci, T. Faravelli, and B. Franzelli. A forward approach for the validation of soot sizing models using laser-induced incandescence (LII). *Applied Physics B*, 126(3):1–19, 2020. p. 186
- [393] D. Kilian, S. Engel, B. Borsdorf, Y. Gao, A. Kögler, S. Kobler, T. Seeger, S. Will, A. Leipertz, and W. Peukert. Spatially resolved flame zone classification of a flame spray nanoparticle synthesis process by combining different optical techniques. *Journal of Aerosol Science*, 69:82–97, 2014. p. 186
- [394] X. Rocquefelte, F. Goubin, H.-J. Koo, M.-H. Whangbo, and S. Jobic. Investigation of the origin of the empirical relationship between refractive index and density on the basis of first principles calculations for the refractive indices of various TiO₂ phases. *Inorganic chemistry*, 43(7):2246–2251, 2004. p. 189
- [395] H. A. Michelsen. Derivation of a temperature-dependent accommodation coefficient for use in modeling laser-induced incandescence of soot. *Applied Physics B*, 94(1):103, 2009. p. 189
- [396] A. Filippov, M. Zurita, and D. Rosner. Fractal-like aggregates: relation between morphology and physical properties. *Journal of colloid and interface science*, 229(1):261–273, 2000. p. 189
- [397] M. Hofmann, B. Kock, and C. Schulz. A web-based interface for modeling laser-induced incandescence (LIISim). *J. Heat Transfer*, 123:814, 2001. p. 190, 194
- [398] M. Kerker. The scattering of light, and other electromagnetic radiation, 27–96 academic press. *New York*, 1969. p. 191
- [399] A. Filippov and D. Rosner. Energy transfer between an aerosol particle and gas at high temperature ratios in the knudsen transition regime. *International journal of heat and mass transfer*, 43(1):127–138, 2000. p. 191, 192
- [400] P. Wright. On the discontinuity involved in diffusion across an interface (the δ of fuchs). *Discussions of the Faraday Society*, 30:100–112, 1960. p. 192, 193
- [401] S.-A. Kuhlmann, J. Reimann, and S. Will. On heat conduction between laser-heated nanoparticles and a surrounding gas. *Journal of aerosol science*, 37(12):1696–1716, 2006. p. 192
- [402] K. Daun and S. Huberman. Influence of particle curvature on transition regime heat con-

- duction from aerosolized nanoparticles. *International journal of heat and mass transfer*, 55(25-26):7668–7676, 2012. p. 193
- [403] D. L. Hofeldt. Real-time soot concentration measurement technique for engine exhaust streams. Technical report, SAE Technical Paper, 1993. p. 193

Titre: Exploration de la capacité de la technique LII à caractériser la synthèse de nanoparticules de dioxyde de titane dans une flamme

Mots clés: flamme pour la synthèse, diagnostics optiques, nanoparticules, dioxyde de titane, incandescence, émission induite par laser

Résumé: Le marché global des nanoparticules représente une production de 11 millions de tonnes par an d'après la Commission européenne. Parmi les différentes méthodes de production, la synthèse de celles-ci dans des flammes est considérée comme une technologie très prometteuse permettant un contrôle fin des caractéristiques des particules produites. Dans ce contexte, l'objectif de ce travail est de développer des diagnostics d'optiques permettant l'étude de l'évolution spatiale des caractéristiques d'une population de particules de TiO_2 produites le long de la flamme ; cela, afin, à la fois de mieux comprendre leur mécanisme de formation, et de créer une base de données pour le développement de modèles numériques. Tout d'abord, l'émission induite par laser (LIE) de nanoparticules de dioxyde de titane (TiO_2) est étudiée pour montrer la faisabilité de la technique d'incandescence induite par laser (LII) sur celles-ci. Cette technique permet de caractériser de façon quasi-non intrusive la fraction volumique des particules f_v et la taille de particules primaire. Elle est classiquement utilisée pour la caractérisation in-situ de la formation de suies dans les flammes, mais sa faisabilité sur de nanoparticules de TiO_2 reste encore à démontrer. Dans le cas où elle le serait, elle pourrait fournir de nouvelles informations sur le processus de synthèse des oxydes métalliques dans les flammes spray et permettre ainsi une description spatiale de la production de nanoparticules de TiO_2 .

Pour vérifier la faisabilité de la technique LII, on considère à la fois des nanoparticules de TiO_2 de haute pureté et des nanoparticules de TiO_2 générées par une flamme d'hydrogène en utilisant deux systèmes de génération de particules : l'un injecte directement des particules dans un milieu non réactif et l'autre synthétise les particules via un milieu réactif. Pour ce dernier, une version inspirée du brûleur de Yale est utilisée. Elle permet la stabilisation de flamme de diffusion pré-vaporisée d'isopropoxyde de titane (TTIP)/ H_2 /Ar. Dans les deux systèmes, les particules sont irradiées à l'aide d'un laser de type top-hat dans la gamme UV, assurant ainsi l'absorption et le chauffage des particules. Un système de détection équipé d'un spectromètre et d'un tube photomultiplicateur (PMT) est également utilisé pour identifier les caractéristiques spectrales et temporelles de LIE des nanoparticules de TiO_2 . Différentes fluences du laser et durées d'acquisition sont prises en compte pour observer les différentes contributions du signal provenant des nanoparticules TiO_2 . La nature du signal est étudiée en la comparant aux résultats théoriques et à des résultats de référence obtenus à partir de nanoparticules de noir de carbone.

Plus précisément, l'émission induite par laser des nanoparticules de TiO_2

présente des composantes non-LII pendant les 100 premières nanosecondes après l'interaction avec le laser. A faible fluence laser, le signal peut être interprété comme une fluorescence induite par laser (LIF). Pour une fluence laser élevée, la spectroscopie par claquage induit par laser sélectif en phase (PS-LIBS) peut se produire en raison d'une éventuelle vaporisation de la surface des particules. Comme les signaux LIF et PS-LIBS sont caractérisés par une courte durée de vie, une acquisition retardée est envisagée pour éviter ces interférences. La nature LII du signal d'émission décalée dans le temps est démontrée premièrement, en confirmant le comportement spectral d'un corps noir. Deuxièmement, l'évolution temporelle du taux de décroissance du signal et de la température inverse est analysée et confirme un comportement du type LII. Dans les configurations considérées, une présence de carbone sur les nanoparticules de TiO_2 est peu probable. De ce fait, la contribution de matériaux carbonés au signal LII peut être supposée négligeable, démontrant ainsi la faisabilité de la technique LII pour des particules de TiO_2 .

Ensuite, une caractérisation quantitative de la production de nanoparticules de TiO_2 dans des flammes a été réalisée. Pour cela, le signal LII est converti en fraction de volume f_v . Cela nécessite donc la connaissance de la température effective Teff atteinte par les particules pendant l'irradiation du laser et de la fonction d'absorption $E(m_\lambda)$. Les deux grandeurs étant fortement liées, il est nécessaire de disposer d'une information sur l'une pour estimer la deuxième. Cependant, une grande variabilité caractérise les données de la littérature pour la fonction $E(m_\lambda)$ pour le TiO_2 , dont les propriétés optiques dépendent fortement des caractéristiques des particules telles que leur géométrie, la structure cristalline et l'état de la matière. Afin de répondre à cette problématique, une nouvelle approche pour estimer la forme spectrale de la fonction d'absorption est proposée à partir des mesures LII. Cette méthode est d'abord validée pour les nanoparticules de noir de carbone pour lesquelles des données sont disponibles dans la littérature. Elle est ensuite appliquée aux nanoparticules de TiO_2 de haute pureté et de TiO_2 synthétisées via la flamme. Une fois l'information sur $E(m_\lambda)$ disponible, la température effective des particules peut être déduite. Enfin, les effets de la distribution spatiale de la température effective et de la fonction d'absorption sur la mesure de la fraction volumique de TiO_2 dans notre flamme de référence ont été étudiés. Les résultats issus des mesures sont comparés à ceux issus d'une simulation numérique représentative de l'état-de-l'art sur le sujet en termes de modélisation. Les comparaisons des champs de f_v normalisés fournissent une première indication pour l'amélioration des modèles numériques.

Title: Exploring the capability of the LII technique to characterize titanium dioxide nanoparticles in flame synthesis

Keywords: Flame synthesis, optical diagnostics, nanoparticles, titanium dioxide, incandescence, laser-induced emission

Abstract:

The global market for nanoparticles represents a production of 11 million tons per year according to the European Commission. Among different production methods, flame synthesis is considered a promising technology for producing nanoparticles with fine control over their characteristics. In this context, the goal of this thesis is to develop optical diagnostics to study the spatial evolution of characteristics of a population of TiO_2 particles produced along the flame, in order to better understand their formation mechanism and create a database for the development of numerical models. First, laser-induced emission (LIE) of titanium dioxide (TiO_2) nanoparticles is studied to demonstrate the feasibility of laser-induced incandescence (LII) technique on these particles. LII is a quasi-non-intrusive technique that characterizes the volume fraction of particles (f_v) and primary particle size. It is traditionally used for in-situ characterization of soot formation in flames, but its feasibility on TiO_2 nanoparticles remains to be demonstrated. If feasible, it could provide new insights into the synthesis process of metal oxide nanoparticles in spray flames and thus allow a spatial description of the production of TiO_2 nanoparticles.

To verify the feasibility of the LII technique, both high-purity TiO_2 nanoparticles and hydrogen flame-generated TiO_2 nanoparticles are considered using two particle-generation systems: the first directly injects particles into a non-reactive environment, and the second synthesizes particles via a reactive environment. The latter applies a new version of the Yale diffusion burner that stabilizes the pre-vaporized diffusion flame of titanium isopropoxide (TTIP)/ H_2 /Ar. In both systems, the particles are irradiated with a top-hat laser in the UV range, thus ensuring absorption and heating of the particles. A detection system equipped with a spectrometer and a photomultiplier tube (PMT) is also used to identify the spectral and temporal characteristics of the LIE of the TiO_2 nanoparticles. Different laser fluences and acquisition times are considered to observe the different signal contributions from the nanoparticles. The nature of the signal is investigated by comparing it to theoretical results and reference results obtained from carbon black nanoparticles.

Specifically, the laser-induced emission of TiO_2 nanoparticles exhibits non-LII

components during the first 100 nanoseconds after the laser interaction. At low laser fluence, these features can be interpreted as laser-induced fluorescence (LIF). With high laser fluence, phase-selective laser-induced breakdown spectroscopy (PS-LIBS) can occur due to possible surface vaporization of the particles. As LIF and PS-LIBS signals are characterized by a short lifetime, delayed acquisition is considered to avoid these interferences. The LII nature of the temporally delayed emission signal is demonstrated first by confirming the spectral behavior of a black body. Secondly, the temporal evolution of the signal decay rate and the inverse temperature is analyzed and confirms as an LII-type behavior. In the considered configurations, the presence of carbon on the nanoparticles of TiO_2 is unlikely. Therefore, the contribution of carbonaceous materials to the LII signal can be assumed negligible, thus demonstrating the feasibility of the LII technique for TiO_2 nanoparticles.

Next, a quantitative characterization of the production of titanium dioxide nanoparticles in flames is carried out. For this, the LII signal is converted into a volume fraction f_v , which requires the knowledge of the effective temperature Teff reached by the particles during the laser irradiation and of the absorption function $E(m_\lambda)$. Since these two quantities are strongly related, it is necessary to have information on one in order to estimate the other. However, there is a large variability in the literature data for the absorption function $E(m_\lambda)$ for TiO_2 , whose optical properties strongly depend on particle characteristics such as geometry, crystalline structure, and state of matter. To address this issue, a new approach to estimate the spectral dependence of the absorption function is proposed from LII measurements. This method is first validated for carbon black nanoparticles, for which data are available in the literature. It is then applied to high-purity and flame-synthesized TiO_2 nanoparticles. Once the information on $E(m_\lambda)$ is available, the effective temperature of the particles can be deduced. Finally, the spatial distribution effects of the effective temperature and the absorption function on the measurement of the volume fraction of TiO_2 in our reference flame are studied. The results of the measurements are compared to those from a numerical simulation representative of state-of-the-art modeling. The comparisons of normalized f_v fields provide a first indication for improving numerical models.